

Ministry of Education and Science of Ukraine  
Sumy State University



# **JOURNAL OF ENGINEERING SCIENCES**

Scientific Journal

**Volume 10, Issue 1 (2023)**

ISSN 2312-2498 (print)  
ISSN 2414-9381 (online)

Founded in 2014

Journal of Engineering Sciences is an open-access, peer-reviewed scientific journal. It covers urgent issues of up-to-date high-tech production in developing new engineering trends and future technologies. The general topics of the journal include manufacturing, mechanical, and chemical engineering. The publication language is English. The editorial board is represented by scientists from different international research institutions covering the journal's topics and evaluating all the submitted articles. The system of double-blinded review provides a high-quality presentation of articles. The editorial policy, including submission, review, acceptance, and publication of articles, is entirely transparent.

The journal was founded in 2014. It is published by Sumy State University of the Ministry of Education and Science of Ukraine under the support of the International Association for Technological Development and Innovations.

**ISSN 2312-2498 (print)**

**ISSN 2414-9381 (online)**

The journal is intended for a wide range of scientists, researchers, practitioners, and others interested in manufacturing, mechanical, and chemical engineering. In 2023, the journal was included in the Scopus database.

*Recommended for publication  
by the Academic Council of Sumy State University,  
(minutes No. 15 of 29.06.2023)*

The journal is the scientific professional edition of Ukraine (Category “B”) in Engineering Sciences ordered by the Ministry of Education and Science of Ukraine, November 7, 2018, No. 1218.

#### **Partners:**

- International Association for Technological Development and Innovations, <http://iatdi.org>;
- Ministry of Education and Science of Ukraine, <https://mon.gov.ua>;
- Faculty of Mechanical Engineering and Management, Poznan University of Technology (Poland), <https://www.put.poznan.pl>;
- Faculty of Manufacturing Technologies with a seat in Prešov, Technical University of Košice (Slovakia), <http://www.fvt.tuke.sk>;
- Faculty of Mechanical Engineering of University of West Bohemia (Czech Republic), <http://www.fst.zcu.cz>.

**Editorial Board:** 2, Rymaskogo-Korsakova St., 40007, Sumy, Ukraine; Apt. M-211

**E-mail:** [jes@teset.sumdu.edu.ua](mailto:jes@teset.sumdu.edu.ua)

**Website:** <http://jes.sumdu.edu.ua>

State registration certificate of the print mass-media No. 20499-10299 PR.



## TOPICS

### **Manufacturing Engineering:**

- Machines and Tools;
- Technical Regulations and Metrological Support;
- Materials Science.

### **Mechanical Engineering:**

- Dynamics and Strength of Machines;
- Computational Mechanics.

### **Chemical Engineering:**

- Processes in Machines and Devices;
- Energy Efficient Technologies;
- Environmental Protection.

## STATISTICS

- **Publication frequency:** biannually (2 issues per year)
- **Acceptance rate:** 25 %
- **Timeline:**
  - days from submission of the manuscript to first decision: 30
  - days from acceptance of the article to publication online: 14
- **Editorial Board:**
  - members: 69
  - institutions: 47
  - cities: 45
  - countries: 24

## **EDITOR-IN-CHIEF**

**Ivan PAVLENKO**, DSc., Professor, Sumy State University, Sumy, Ukraine

## **DEPUTY EDITOR-IN-CHIEF**

**Vitalii IVANOV**, DSc., Professor, Sumy State University, Sumy, Ukraine

## **BOARD OF CO-EDITORS**

### **Manufacturing Engineering**

**Erwin RAUCH**, Ph.D., Professor, Free University of Bozen-Bolzano, Bolzano, Italy

**Jose MACHADO**, Ph.D., Professor, University of Minho, Braga, Portugal

**George-Christopher VOSNIAKOS**, Ph.D., Professor, National Technical University of Athens, Athens, Greece

### **Mechanical Engineering**

**Jan PITEL**, Ph.D., Professor, Technical University of Kosice, Presov, Slovakia

**John MOTTERSHEAD**, DSc., Professor, University of Liverpool, Liverpool, United Kingdom

**Oleksandr POGREBNIYAK**, DSc., Professor, Sumy State University, Sumy, Ukraine

### **Chemical Engineering**

**Alex-Enrich PRAST**, Ph.D., Professor, Linkoping University, Linkoping, Sweden

**Mathieu GAUTIER**, Ph.D., Professor, University of Lyon, Lyon, France

**Kaname TSUTSUMIUCHI**, DSc., Professor, Chubu University, Kasugai, Japan

## **INTERNATIONAL EDITORIAL BOARD**

**Praveen AGARWAL**, Ph.D., Professor, Anand International College of Engineering, Jaipur, India

**Katarzyna ANTOSZ**, DSc., Associate Professor, Rzeszow University of Technology, Rzeszow, Poland

**Peter ARRAS**, DSc., Professor, KU Leuven, Leuven, Belgium

**Viktor ASTAKHOV**, DSc., Professor, Production Service Management Inc., Ann Arbor, USA

**Volodymyr ATAMANYUK**, DSc., Professor, Lviv Polytechnic National University, Lviv, Ukraine

**Eddy BAJIC**, Ph.D., Professor, University of Lorraine, Nancy, France

**Marian BARTOSZUK**, Ph.D., Professor, Opole University of Technology, Opole, Poland

**Jean BOUYER**, Ph.D., Associate Professor, University of Poitiers, Poitiers, France

**Noel BRUNETIERE**, Ph.D., Senior Researcher, University of Poitiers, Poitiers, France

**Robert CEP**, Ph.D., Professor, Technical University of Ostrava, Ostrava, Czech Republic

**Olaf CISAK**, Ph.D., Associate Professor, Poznan University of Technology, Poznan, Poland

**Predrag DASIC**, DSc., Professor, VTMS Trstenik, Trstenik, Serbia

**Kostiantyn DYADYURA**, DSc., Professor, Odessa Polytechnic National University, Odessa, Ukraine

**Milan EDL**, Ph.D., Associate Professor, University of West Bohemia, Pilsen, Czech Republic

**Domenico GUIDA**, Ph.D., Professor, University of Salerno, Salerno, Italy

**Oleksandr GUSAK**, Ph.D., Professor, Sumy State University, Sumy, Ukraine

**Michal HATALA**, Ph.D., Professor, Dr.h.c., Technical University of Kosice, Presov, Slovakia

**Koichi HASEGAWA**, Ph.D., Professor, Chubu University, Kasugai, Japan

**Siamak HOSEINZADEH**, Ph.D., Post Doc., Sapienza University of Rome, Rome, Italy

**Jozef HUSAR**, Ph.D., Assistant Professor, Technical University of Kosice, Presov, Slovakia

**Yury IVANOV**, Ph.D., Associate Professor, Chubu University, Kasugai, Japan

**Fuat KARA**, Ph.D., Assistant Professor, Duzce University, Istanbul, Turkey

**Isak KARABEGOVIC**, DSc., Professor, University of Bihac, Bihac, Bosnia and Herzegovina

**Jakub KASCAK**, Ph.D., Assistant Professor, Technical University of Kosice, Presov, Slovakia  
**Dmytro KRYVORUCHKO**, DSc., Associate Professor, Sumy State University, Sumy, Ukraine  
**Czeslaw KUNDERA**, DSc., Professor, Kielce University of Technology, Kielce, Poland  
**Ivan KURIC**, Ph.D., Professor, University of Zilina, Zilina, Slovakia  
**Milovan LAZAREVIC**, Ph.D., Associate Professor, University of Novi Sad, Novi Sad, Serbia  
**Stanislaw LEGUTKO**, DSc., Professor, Poznan University of Technology, Poznan, Poland  
**Oleksandr LIAPOSHCHENKO**, DSc., Professor, Sumy State University, Sumy, Ukraine  
**Athanasios MAMALIS**, DSc., Professor, Demokritos National Centre for Scientific Research, Athens, Greece  
**Arun MATHEW**, Ph.D., Associate Professor, Vellore Institute of Technology, Vellore, India  
**Thomas MATHIA**, Ph.D., Professor, Ecole Centrale de Lyon, Lyon, France  
**Yurii MATSEVITYI**, DSc., Professor, Podgorny Institute for Mechanical Engineering Problems, National Academy of Sciences of Ukraine, Kharkiv, Ukraine  
**Ronald MERSKY**, Ph.D., Associate Professor, Widener University, Chester, USA  
**Arun NAGARAJAH**, DSc., Professor, University of Duisburg-Essen, Duisburg, Germany  
**Eduard Laurentiu NITU**, Ph.D., Professor, University of Pitesti, Pitesti, Romania  
**Dragan PERAKOVIC**, Ph.D., Professor, University of Zagreb, Zagreb, Croatia  
**Alejandro PEREIRA**, Ph.D., Professor, University of Vigo, Vigo, Spain  
**Yurii PETRAKOV**, DSc., Professor, National Technical University of Ukraine “Kyiv Polytechnic Institute”, Kyiv, Ukraine  
**Roman PETRUS**, DSc., Professor, Rzeszow University of Technology, Rzeszow, Poland  
**Leonid PLYATSUK**, DSc., Professor, Sumy State University, Sumy, Ukraine  
**Frantisek POCHYLÝ**, Ph.D., Professor, Brno University of Technology, Brno, Czech Republic  
**Robert POOLE**, Ph.D., Professor, University of Liverpool, Liverpool, United Kingdom  
**Yimin RONG**, DSc., Professor, South University of Science and Technology, Shenzhen, China  
**Vitalii SIMONOVSKIY**, DSc., Professor, Sumy State University, Sumy, Ukraine  
**Vsevolod SKLABINSKYI**, DSc., Professor, Sumy State University, Sumy, Ukraine  
**Michael STORCHAK**, DSc., Professor, Institute for Machine Tools of Stuttgart University, Stuttgart, Germany  
**Fabio TEIXEIRA**, DSc., Professor, Federal University of Rio Grande do Sul, Porto Alegre, Brazil  
**Justyna TROJANOWSKA**, Ph.D., Assistant Professor, Poznan University of Technology, Poznan, Poland  
**Raul TURMANIDZE**, DSc., Professor, Georgian Technical University, Tbilisi, Georgia  
**Michal VARCHOLA**, Ph.D., Professor, Slovak University of Technology in Bratislava, Bratislava, Slovakia  
**Jinyang XU**, Ph.D., Associate Professor, Shanghai Jiao Tong University, Shanghai, China  
**Jozef ZAJAC**, DSc., Professor, Dr.h.c., Technical University of Kosice, Presov, Slovakia  
**Viliam ZALOGA**, DSc., Professor, Sumy State University, Sumy, Ukraine  
**Lianyu ZHENG**, Ph.D., Professor, Beihang University, Beijing, China

#### **PUBLISHING MANAGER**

**Khrystyna BERLADIR**, Ph.D., Associate Professor, Sumy State University, Sumy, Ukraine

#### **MARKETING AND COMMUNICATION MANAGER**

**Vladyslav KONDUS**, Ph.D., Associate Professor, Sumy State University, Ukraine



**CONTENTS**

**MANUFACTURING ENGINEERING**

**Machines and Tools**

- Sokolov O., Hosovsky A., Ivanov V., Pavlenko I.  
[Movement monitoring system for a pneumatic muscle actuator](#)  
 doi: [10.21272/jes.2023.10\(1\).a1](https://doi.org/10.21272/jes.2023.10(1).a1) A1-A5
- Zaleta O. M., Povstyanoy O. Yu., Ribeiro L. F., Redko R. G., Bozhko T. Ye., Chetverzhuk T. I.  
[Automation of optimization synthesis for modular technological equipment](#)  
 doi: [10.21272/jes.2023.10\(1\).a2](https://doi.org/10.21272/jes.2023.10(1).a2) A6-A14
- Chalyj V., Moroz S., Tkachuk A., Zablotskyi V., Trokhymchuk I., Stelmakh A.  
[Formation of bearings parts waviness in centerless mortise grinding on rigid supports](#)  
 doi: [10.21272/jes.2023.10\(1\).a3](https://doi.org/10.21272/jes.2023.10(1).a3) A15-A21
- Halchuk T. N., Povstyanoy O. Yu., Bembenek M., Redko R. G., Chetverzhuk T. I., Polinkevych R. M.  
[Impact of technological system's characteristics on the machining accuracy of bearing rings](#)  
 doi: [10.21272/jes.2023.10\(1\).a4](https://doi.org/10.21272/jes.2023.10(1).a4) A22-A30
- Stelmakh A., Kostyunik R., Mikosianchyk O., Kushchev A., Ibraimov T., Sydorenko O., Zaichuk N., Shymchuk S.  
[Improvement of operational parameters for precision rolling bearings by cleaning working surfaces from micro pollution of various nature](#)  
 doi: [10.21272/jes.2023.10\(1\).a5](https://doi.org/10.21272/jes.2023.10(1).a5) A31-A40

**Technical Regulations and Metrological Support**

- Prokopovych I. V., Kokhanov A. B., Khamitov V. M., Tikhenko V. M., Dasic P.  
[Standardizing life cycle organization: A synergetic quality management approach](#)  
 doi: [10.21272/jes.2023.10\(1\).b1](https://doi.org/10.21272/jes.2023.10(1).b1) B1-B7

**Materials Science**

- Lebedev V. V., Miroshnichenko D. V., Nyakuma B. B., Moiseev V. F., Shestopalov O. V., Vyrovets S. V.  
[Design of inorganic polymer composites for electromagnetic radiation absorption using potassium titanates](#)  
 doi: [10.21272/jes.2023.10\(1\).c1](https://doi.org/10.21272/jes.2023.10(1).c1) C1-C8
- Kashytskyi V. P., Sadova O. L., Melnychuk M. D., Golodyuk G. I., Klymovets O. B.  
[Structuring of modified epoxy composite materials by infrared spectroscopy](#)  
 doi: [10.21272/jes.2023.10\(1\).c2](https://doi.org/10.21272/jes.2023.10(1).c2) C9-C16

**MECHANICAL ENGINEERING**

**Dynamics and Strength of Machines**

- Uysal M. U.  
[Effects of cryogenically treated CFRP composite on the buckling behavior in the adhesively bonded beam](#)  
 doi: [10.21272/jes.2023.10\(1\).d1](https://doi.org/10.21272/jes.2023.10(1).d1) D1-D7

Voropay A. V., Menshykov O. V., Povaliaiev S. I., Sharapata A. S., Yehorov P. A.  
[Modeling a viscoelastic support considering its mass-inertial characteristics during non-stationary vibrations of the beam](#)  
doi: [10.21272/jes.2023.10\(1\).d2](#) D8-D14

Lymarenko A., Kurgan V., Bazhanova A., Khamray V., Ponomarenko A., Karabegović I.  
[The stress state of a thick-walled hydraulic press cylinder with concentrators](#)  
doi: [10.21272/jes.2023.10\(1\).d3](#) D15-D19

### Computational Mechanics

Javanbakht T.  
[Optimization of graphene oxide's characteristics with TOPSIS using an automated decision-making process](#)  
doi: [10.21272/jes.2023.10\(1\).e1](#) E1-E7

Tigariev V., Lopakov O., Rybak O., Kosmachevskiy V., Cioată V. G.  
[Design in modern information systems by applying cloud technologies](#)  
doi: [10.21272/jes.2023.10\(1\).e2](#) E8-E13

## CHEMICAL ENGINEERING

### Processes in Machines and Devices

Antonyuk V. S., Bondarenko I. Iu., Vislouch S. P., Voloshko O. V., Bondarenko M. O.  
[Heat exchange in a contact zone of nanoinstrumentation with elements of the microsystem technology](#)  
doi: [10.21272/jes.2023.10\(1\).f1](#) F1-F6

Opyatyuk V. V., Kozlov I. L., Karchev K. D., Vistiak S. V., Kozlov O. I., Turmanidze R.  
[Simulation of point defects formation in the fuel element of a nuclear power plant's wave reactor](#)  
doi: [10.21272/jes.2023.10\(1\).f2](#) F7-F10

Spirin A., Borysiuk D., Tsurkan O., Tverdokhlib I., Veselovska N., Edl M.  
[Ways of intensification of grass seed production](#)  
doi: [10.21272/jes.2023.10\(1\).f3](#) F11-F19

### Energy Efficient Technologies

Anyanwu U. O., Okafor O. C., Nkwor C. A.  
[A scheduling model in capturing methane gas from methane clathrates deposits](#)  
doi: [10.21272/jes.2023.10\(1\).g1](#) G1-G13

Sokolov S.  
[Optimization of greenhouse microclimate parameters considering the impact of CO<sub>2</sub> and light](#)  
doi: [10.21272/jes.2023.10\(1\).g2](#) G14-G21

Plotkin J., Levchenko N., Shyshkanova G., Levchenko S.  
[Development of energy enterprises in the context of green transformation](#)  
doi: [10.21272/jes.2023.10\(1\).g3](#) G22-G33

### Environmental Protection

Javanbakht T.  
[A novel automated decision-making process for analysis of ions and organic materials in drinking water](#)  
doi: [10.21272/jes.2023.10\(1\).h1](#) H1-H7



# 7TH INTERNATIONAL CONFERENCE ON DESIGN, SIMULATION, MANUFACTURING: THE INNOVATION EXCHANGE (DSMIE-2024)

JUNE 4-7, 2024 | Pilsen, Czech Republic

**7th International Conference on Design, Simulation, Manufacturing: The Innovation Exchange (DSMIE-2024)** focuses on research challenges in the fields of **Manufacturing Engineering, Materials Engineering, and Mechanical Engineering**, addressing current and future trends in design approaches, simulation techniques, and manufacturing technologies, highlighting the growing role of smart manufacturing systems, artificial intelligence, standards-based integration, and innovations implementation to the transition to a sustainable, human-centric and resilient engineering solutions.

DSMIE brings together researchers from academic institutions, leading industrial companies, and government laboratories worldwide to promote and popularize the scientific fundamentals of engineering.

The conference schedule includes keynote sessions and technical sessions, expert panels, an exhibition of industrial partners, and more.

The working language of the conference (including conference proceedings, presentations, and discussions) is **English**. Authors are welcome to submit original and unpublished research articles. All paper submissions to the DSMIE-2024 should be related to the [Conference Topics](#).

Each paper will be peer-reviewed by at least two program committee members and evaluated based on originality, technical and/or research content/depth, correctness, originality, completeness, contributions, and readability.

After carefully reviewing, all accepted papers will be published as conference proceedings in [Lecture Notes in Mechanical Engineering](#) (Springer Nature) and submitted to the databases **Scopus, Web of Science Core Collection**, and other indexing services. Accepted papers must be presented at the conference by one of their authors who commit to register and attend the conference. The Steering Committee reserves the right to exclude papers not presented from the conference proceedings.

Please feel free to [contact us](#) if you have any questions.

DSMIE-2023 is under the sponsorship of the [International Association for Technological Development and Innovations](#).

## What is DSMIE Conference Series

Where Science, Industry, and Education meet

This is an event where scientists and representatives from industry and academia will meet to exchange ideas, establish business and personal relationships, identify new opportunities for cooperation, find areas of innovation, and make joint efforts to address common projects in Manufacturing Engineering, Materials Engineering, and Mechanical Engineering.





Sokolov O., Hosovsky A., Ivanov V., Pavlenko I. (2023). Movement monitoring system for a pneumatic muscle actuator. *Journal of Engineering Sciences*, Vol. 10(1), pp. A1-A5, doi: 10.21272/jes.2023.10(1).a1

## Movement Monitoring System for a Pneumatic Muscle Actuator

Sokolov O.<sup>1,2\*</sup>[0000-0003-0648-4977], Hosovsky A.<sup>1</sup>[ 0000-0002-8390-7163], Ivanov V.<sup>2</sup>[0000-0003-0595-2660], Pavlenko I.<sup>2</sup>[0000-0002-6136-1040]

<sup>1</sup> Technical University of Kosice, 1, Bayerova, 080 01 Presov, Slovak Republic;

<sup>2</sup> Sumy State University, 2, Rymyskogo-Korsakova, 40007 Sumy, Ukraine

### Article info:

Submitted: November 15, 2022  
 Received in revised form: January 12, 2023  
 Accepted for publication: January 26, 2023  
 Available online: February 1, 2023

### \*Corresponding email:

[o.sokolov@teset.sumdu.edu.ua](mailto:o.sokolov@teset.sumdu.edu.ua)

**Abstract.** Recent advancements in soft pneumatic robot research have demonstrated these robots' capability to interact with the environment and humans in various ways. Their ability to move over rough terrain and grasp objects of irregular shape, regardless of position, has garnered significant interest in developing new pneumatic soft robots. Integrating industrial design with related technologies holds great promise for the future, potentially bringing about a new lifestyle and revolutionizing the industry. As robots become increasingly practical, there is a growing need for sensitivity, robustness, and efficiency improvements. It is anticipated that the development of these intelligent pneumatic soft robots will play a critical role in serving the needs of society and production shortly. The present article is concerned with developing a system for monitoring a pneumatic robot's parameters, including a spatial coordinate system. The focus is on utilizing the relationship between the coordinates and pressure to model the movement of the soft robot within the MATLAB simulation environment.

**Keywords:** soft robotics, process innovation, pneumatic manipulator, monitoring system.

## 1 Introduction

Researchers continue to mimic living things and their materials, morphology, and movements to create robots capable of performing complex tasks in unstructured environments. Soft robotic arms have generated considerable interest over the past few years due to their wide range of potential applications. This is due to their ability to adapt to their surroundings, move dexterously, and manipulate objects of a wide variety of sizes using whole-hand manipulation. In this case, the manipulators can lengthen, contract, and bend at any point in their structure. This allows them to access highly confined spaces and follows complex trajectories. They have unique features compared to rigid-body robots, such as smooth bending, inherent compliance, lighter weight, and increased resiliency [1, 2].

Soft robots and traditional complex robots use different mechanisms to achieve dexterously. Soft robots have distributed deformation, allowing them to have a hyper-redundant configuration space where they can reach any point in the three-dimensional workspace with infinite shapes or configurations. This is in contrast to hard robots, which have a limited number of degrees of freedom

(DOF). Additionally, soft robots generate little resistance to compressive forces, allowing them to conform to obstacles and handle soft and fragile payloads without causing damage. They can also use large strain deformation to squeeze through openings smaller than their nominal dimensions, making them suitable for applications such as personal robots that interact with humans without causing injury, service and painting robots that need high dexterity to access confined spaces, medical robots for use in surgery, and defense and rescue robots that operate in unstructured environments [3].

## 2 Literature Review

The McKibben artificial muscle was Japan's first pneumatic muscle developed in the 1960s. These advantages are high power, low weight, softness, and compliance in terms of material and motion. The McKibben pneumatic artificial muscle is a device that consists of a chemical-fiber sleeve yarn and a rubber tube. When air is introduced into the muscle, the rubber tube expands radially while contracting axially. This deformation process ceases when the braid angle reaches its limiting value. In practical applications, the artificial

muscle is secured at one end by a knot, while the other is connected to an air supply and fixed using a large connector and adhesive. By adjusting the internal air pressure, the actuator contracts and produces a contraction force that is used to power the motion of a manipulator [4]. This paper also contains research on improving a manipulator's mechanical properties based on McKibben's muscles and increasing its wear resistance and strength. This research is based on the similarity of pneumatic artificial and natural muscles [5]. It served as a further development, expanding the scope of the manipulator to industrial applications.

The field of continuum manipulator robots has a history dating back to the 1960s, but more formal research on their design and control began in the 1990s. These robots represent a shift in manipulator design from discrete rigid links to mechanisms with elastic structures that can bend continuously along their entire length. These elastic structures, or "continuum" elements, enable a wide range of motion and conformability, making them suitable for tasks requiring high dexterity and the ability to access confined spaces. [6]

There has been ongoing research to improve and modify pneumatic muscles using pressurized air to generate motion.

The paper [7] presents a soft amphibious robot with three drive links in the legs and four drives in the body (Figure 2). The robot utilizes thin, soft McKibben actuators to achieve two types of bending: in the legs for movement and in the body for added mobility. The body's bending properties are achieved through the deformation of a plastic plate, which helps the robot mimic the locomotion of a salamander during walking. The authors also investigate the effect of changing specific parameters, such as frequency and input pressure, on the speed and stability of the walking movement. The research [8] explained the kinematics of rotation and bending features of the proposed robot arm and illustrated the direction of possible movements. The snake's movement in two directions became the prototype scheme for designing a double-bend pneumatic muscle actuator [9].

This will allow the development of larger underwater swimming robots in the future.

The authors of the work [10] discovered the following advantages of the Pneumatic Muscle Actuators (PMA): low cost, which is about 10 dollars, ease to manufacture, wide dimension grasping ability, safe to low stiffness objects, and it has low mass (0.18 kg). Its inertia is also low, which potentially makes it safer for operation around humans. Generally, the PMA is constructed from an inner rubber tube covered by a braided sleeve with two solid material terminals fixed firmly to ensure no air leakage occurs. One of the terminals has a small hole for the input and output of actuated air [11].

In the paper [12], a two-segment soft robot arm is constructed using simple retractors and extensor actuators. This allows it to expand, contract, and bend in multiple directions. The authors of the work [13] created a robot called "Octarm". Their prototype is the tentacles of an

octopus. Pneumatic extensor muscles powered octarm Continuum robots.

Octarm robots have three independently actuated sections for 9 DOF. Each section is powered by three independently controlled pneumatic pressures fed to the extensor muscles. Therefore, the robot without pressure has a minimum length and continues to its maximum length as a function of actuation.

The research works [11, 16, 17-20] revealed limitations of the traditional soft drive.

These restrictions are:

- a pneumatic artificial muscle creates a contraction force only when pressed;
- the extension drive generates the extension force only when pressure is applied;
- each type of soft drive has a constant stiffness over a certain length.

Therefore, in the study [21], the design of a soft actuator is based on a starfish. The starfish is composed of elements such as connective tissue, calcite bone, and interosseous muscle, which allows it to regulate the structural stiffness of its body actively [22]. Since the movement of the elastic body of the actuator depends on the deformation of the tissue, especially the characteristics of the material used in its construction, this stage compensates for two anisotropic tissues (woven tissue and elastic tissue) and elastomer (silica gel) to develop a contractor and an extensor, respectively. Finally, they are combined into an inner and outer chamber structure and begin as an antagonistic actuator based on the extensors and contractors (ECFA) tissue. If both chambers are pressure controlled, a change in actuator stiffness can be achieved.

### 3 Research Methodology

The paper investigates controlling a soft robot with a pneumatic drive (Figure 1). Such a robot is a manipulator that makes it possible to grab soft objects and move them to specified locations.

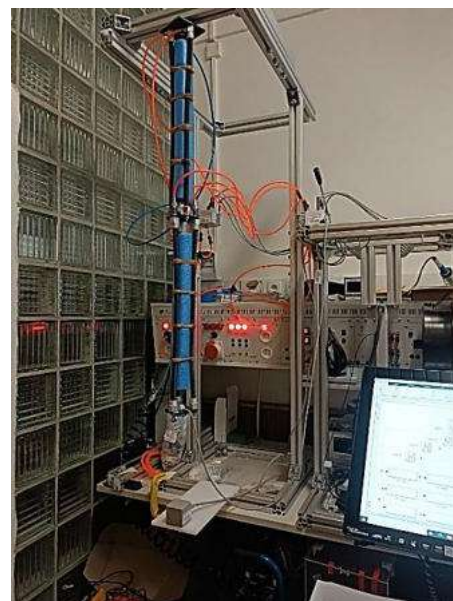


Figure 1 – Stand with the soft pneumatic robot

The movement of the manipulator is controlled by changing the air pressure in six pneumatic actuators. The compressed air source is a pump-compressor that creates an overpressure of 0 to 6 bar. Pressure gauges are used to measure the pressure in the pneumatic actuators, and position sensors are used to control the position. The robot's manipulator's movement is monitored using a computer with the Matlab simulation environment installed (Figure 2).

The set pressure in each of the six pneumatic actuators of the soft robot is set in the Matlab environment using blocks P1-P6. At the output of the circuit in Matlab, the movements of the robot manipulator in three coordinates ( $X$ ,  $Y$ ,  $Z$ ) and three angles ( $\theta$ ,  $\varphi$ , and  $\psi$ ), which are the angles of the rotation coming from the position sensors, are recorded. The experiment determined the dependence of each of the coordinates on the pressure in the pneumatic actuators.

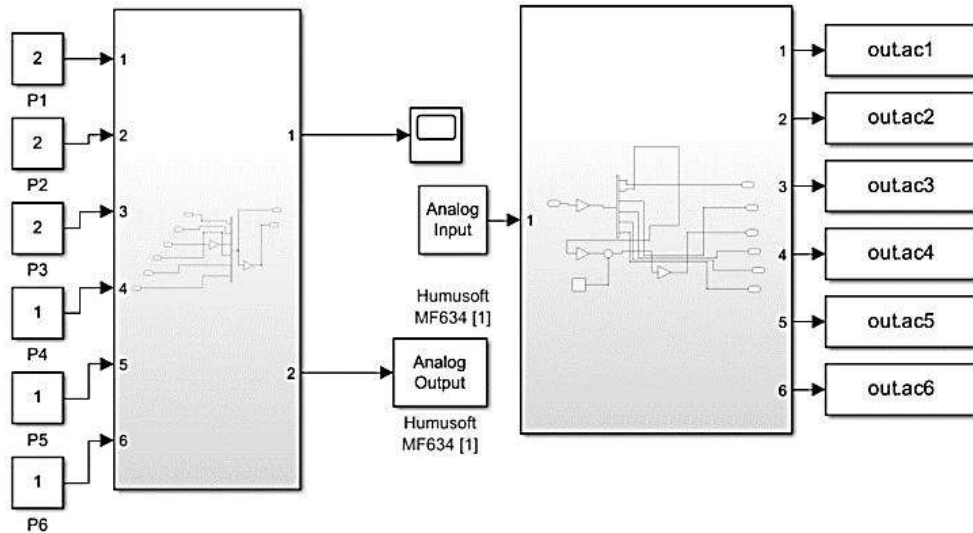
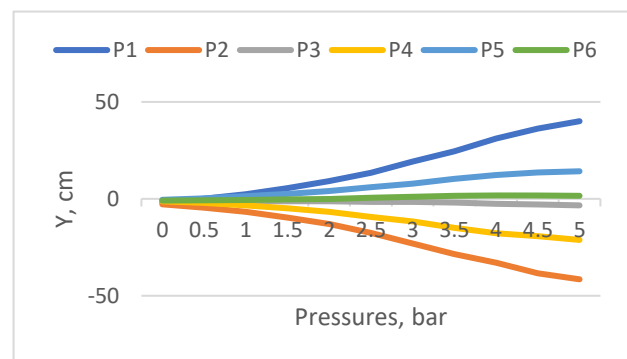


Figure 2 – Pneumatic robot parameters monitoring system

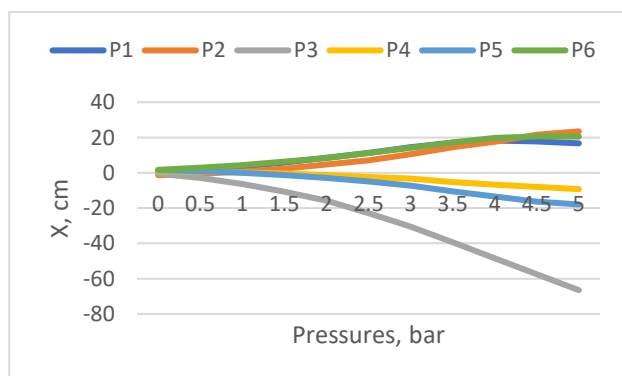
#### 4 Results and Discussion

As a result of the experiment, dependencies were obtained that describe the kinematics of soft robot motion. Figure 3 shows a linear dependence up to a pressure value of 4 bar is observed.

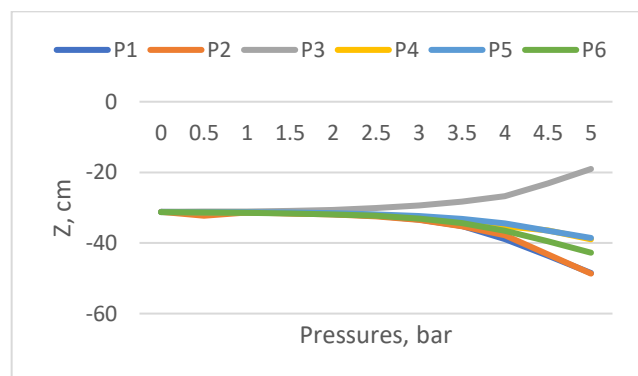
After 4 bars, a non-linear dependency is observed. This relation between the displacement of the soft robot and the pressure is due to the material's properties used to manufacture the soft robot's pneumatic muscles.



b



a



c

Figure 3 – Dependencies of  $X$  (a),  $Y$  (b), and  $Z$  (c) coordinates on pressure

These dependencies can be used to describe the motion model of the pneumatic muscle in three-dimensional space.

These dependencies can be used to describe the motion model of the pneumatic muscle in three-dimensional space, as shown in Figure 4.

One of the biggest problems of pneumatic soft robots is the search for methods and models that would most accurately describe the experimental values. The given graphs (Figures 3, 4) allow for defining the dynamic movements of soft robotics and finding its position at any moment in time.

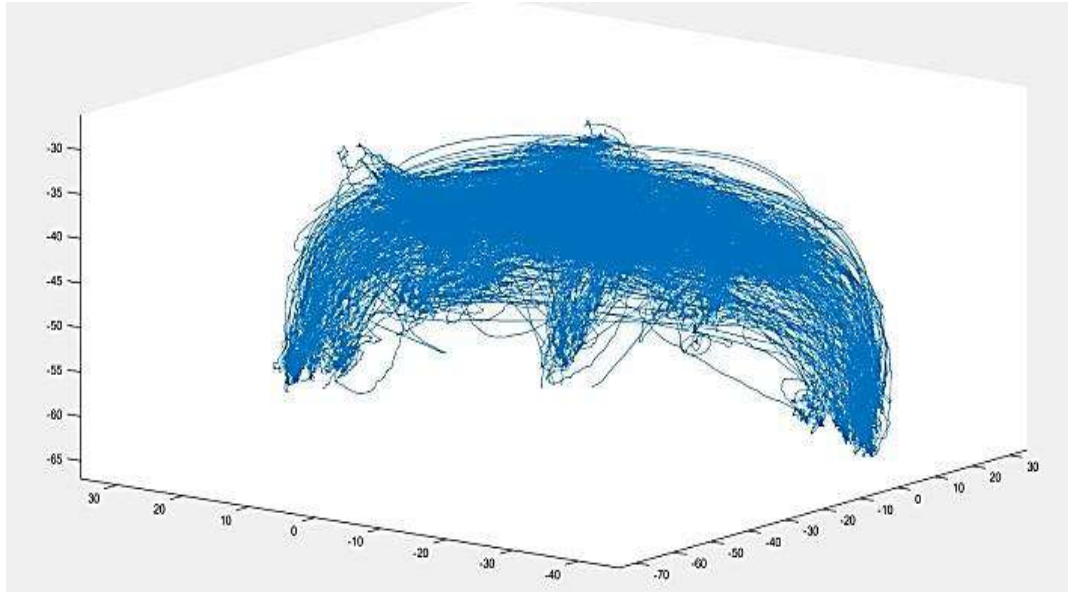


Figure 4 – Simulation model of pneumatic robot movement

## 5 Conclusions

Modern research on pneumatic soft robots has proven that they can interact with people and the environment in various ways, move over unknown terrain, and grasping irregularly shaped objects, regardless of their position.

These basic operations open the door to applications where robots work closely with humans. Therefore, there has been a growing interest in developing new types of pneumatic soft robots in recent decades.

As robots become more practical, sensitivity, robustness, and efficiency improvements become increasingly important. It is believed that shortly, by integrating industrial design with related technologies, advances in this field will create a new lifestyle and change in the industry, enabling intelligent pneumatic soft robots to serve all aspects of society and production.

## References

1. Tang, X., Li, H., Ma, T., Yang, Y., Luo, J., Wang, H., Jiang, P. (2022). A review of soft actuator motion: Actuation, design, manufacturing and applications. *Actuators*, Vol. 11, 331, <https://doi.org/10.3390/act11110331>
2. Sun, C., Chen, L., Liu, J., Dai, J. S., Kang, R. (2020). A hybrid continuum robot based on pneumatic muscles with embedded elastic rods. *Proceedings of the Institution of Mechanical Engineers, Part C: Journal of Mechanical Engineering Science*, Col. 234(1), pp. 318-328, <https://doi.org/10.1177/0954406218822013>
3. Trivedi, D. et al. (2008). Soft robotics: Biological inspiration, state of the art, and future research. *IOS Press*, pp. 99-117, <https://doi.org/10.1080/11762320802557865>
4. Peng, Y., Liu, Y., Yang, Y., Liu, N., Sun, Y., Liu, Y., Pu, H., Xie, S., Luo, J. (2019). Development of continuum manipulator actuated by thin McKibben pneumatic artificial muscle. *Mechatronics*, Vol. 60, pp. 56-65, <https://doi.org/10.1016/j.mechatronics.2019.05.001>

## 6 Acknowledgment

The research was carried out within the project “Intensification of production processes and development of intelligent product quality control systems in smart manufacturing” (State reg. no. 0122U200875, Ministry of Education and Science of Ukraine).

The research was also partially carried out within the project VEGA 1/0061/23, “Research of modeling and control of soft continuum arms based on fluidic muscles using bio-inspired computational methods” (Slovak Republic).

The authors appreciate the International Association for Technological Development and Innovations (IATDI) for the support while conducting the research.

5. Hassanin, A.-F., Davis, S., Nefti-Meziani, S. (2018). The design and mathematical modelling of novel extensor bending pneumatic artificial muscles (EBPAMs) for soft exoskeletons. *Robotics and Autonomous Systems*, Vol. 99, pp. 63-74, <https://doi.org/10.1016/j.robot.2017.10.010>
6. Thuruthel, T. G., Ansari, Y., Falotico, E., Laschi, C. (2018). Control strategies for soft robotic manipulators: A survey. *Soft Robotics*, Vol. 5(2), pp. 149-163, <https://doi.org/10.1089/soro.2017.0007>
7. Faudzi, A. A. M., Razif, M. R. M., Endo, G., Nabae, H., Suzumori, K. (2017). Soft-amphibious robot using thin and soft McKibben actuator. In: *2017 IEEE International Conference on Advanced Intelligent Mechatronics (AIM)*, pp. 981-986, <https://doi.org/10.1109/AIM.2017.8014146>
8. Al-Ibadi, A., Nefti-Meziani, S., Davis, S. (2020). A robot continuum arm inspired by the human upper limb: The pronation and supination rotating behaviour. In: *International Conference on Electrical, Communication, and Computer Engineering (ICECCE)*, pp. 1-6, <https://doi.org/10.3390/robotics7020019>
9. Al-Ibadi, A., Nefti-Meziani, S., Davis, S. (2018). Design, kinematics and controlling a novel soft robot arm with parallel motion. *Robotics*, Vol. 7(2), 19.
10. Al-Ibadi, A., Nefti-Meziani, S., Davis, S. (2018). Active soft end effectors for efficient grasping and safe handling. *IEEE Access*, Vol. 6, pp. 23591-235601, <https://doi.org/10.1109/ACCESS.2018.2829351>
11. Al-Ibadi, A., Nefti-Meziani, S., Davis, S. (2017). Novel models for the extension pneumatic muscle actuator performances. In: *Proceedings of the 23rd International Conference on Automation & Computing, University of Huddersfield, Huddersfield, UK*, pp. 1-6, <https://doi.org/10.23919/ICOnAC.2017.8081973>
12. Al-Ibadi, A., Nefti-Meziani, S., Davis, S., Theodoridis, T. (2018). Design of two segments continuum robot arm based on pneumatic muscle actuator (PMA). In: *2018 24th International Conference on Automation and Computing (ICAC)*, pp. 1-6, <https://doi.org/10.23919/ICOnAC.2018.8749087>
13. Bartow, A., Kapadia, A. D., Walker, I. (2013). A novel continuum trunk robot based on contractor muscles, Vol. 2013. pp. 181-186.
14. Yi, J., Chen, X., Song, C., Wang, Z. (2016). Fiber reinforced origamic robotic actuator. *Soft Robotics*, Vol. 5, pp. 81-92, <https://doi.org/10.1089/soro.2016.0079>
15. Najmuddin, W. S. W. A., Mustaffa, M. T. (2017). A study on contraction of pneumatic artificial muscle (PAM) for loadlifting. *J. Phys. Conf. Ser.*, Vol. 908, 012036, <https://doi.org/10.1088/1742-6596/908/1/012036>
16. Chen, Y., Zhang, J., Gong, Y. (2019). Utilizing anisotropic fabrics composites for high-strength soft manipulator integrating soft gripper. *IEEE Access*, Vol. 7, 127416-127426, <https://doi.org/10.1109/ACCESS.2019.2940499>
17. Xiang, C., Giannaccini, M. E., Theodoridis, T., Hao, L., Nefti-Meziani, S., Davis, S. (2016). Variable stiffness Mckibben muscles with hydraulic and pneumatic operating modes. *Adv. Robot.*, Vol. 30, pp. 889-899, <https://doi.org/10.1088/1742-6596/908/1/012036>
18. Tanaka, D., Kamo, D., Maehara, M., Nakamura, T. (2013). Development of two types of 2DOF wrist joint driven by pneumatic artificial muscles. In: *Proceedings of the 2013 IEEE International Conference on Mechatronics (ICM), Vicenza, Italy*, <https://doi.org/10.1080/01691864.2016.1154801>
19. Belforte, G., Eula, G., Ivanov, A., Sirolli, S. (2014). Soft pneumatic actuators for rehabilitation. *Actuators*, Vol. 3, pp. 84-106, <https://doi.org/10.3390/act3020084>
20. Ferraresi, C., Franco, W., Quaglia, G. (2002). Bi-directional flexible pneumatic actuator. In: *Proceedings of the 5th International Symposium on Fluid Power (JFPS 2002), Nara, Japan*, pp. 25-30, <https://doi.org/10.3390/act9040107>
21. Chen, Y., Zhang, J., Gong, Y. (2020). Novel design and modeling of a soft pneumatic actuator based on antagonism mechanism. *Actuators*, Vol. 9(4), 107, <https://doi.org/10.3390/act9040107>
22. Jeong, H., Kim, J. (2019). Echinoderm inspired variable stiffness soft actuator with connected ossicle structure. In: *Proceedings of the 2019 International Conference on Robotics and Automation (ICRA 2019), Montreal, QC, Canada*, <https://doi.org/10.1109/ICRA.2019.8793545>



Zaleta O. M., Povstyanoy O. Yu., Ribeiro L. F., Redko R. G., Bozhko T. Ye., Chetverzhuk T. I. (2023). Automation of optimization synthesis for modular technological equipment. *Journal of Engineering Sciences*, Vol. 10(1), pp. A6-A14, doi: 10.21272/jes.2023.10(1).a2

## Automation of Optimization Synthesis for Modular Technological Equipment

Zaleta O. M.<sup>1</sup>[0000-0002-0777-9972], Povstyanoy O. Yu.<sup>1</sup>[0000-0002-1416-225X], Ribeiro L. F.<sup>2</sup>[0000-0003-4336-6216], Redko R. G.<sup>1</sup>[0000-0001-5066-0224], Bozhko T. Ye.<sup>1</sup>[0000-0003-2956-2384], Chetverzhuk T. I.<sup>1</sup>[0000-0002-4445-4632]

<sup>1</sup> Lutsk National Technical University, 75, Lvivska St., 43018 Lutsk, Ukraine;

<sup>2</sup> Instituto Politécnico de Bragança, 253, Alameda de Santa Apolónia, 5300-252 Bragança, Portugal

### Article info:

Submitted: March 21, 2023  
 Received in revised form: May 12, 2023  
 Accepted for publication: May 19, 2023  
 Available online: May 22, 2023

### \*Corresponding email:

[o.zaleta@lutsk-ntu.com.ua](mailto:o.zaleta@lutsk-ntu.com.ua)

**Abstract.** Technological equipment design based on functionally modular methods is widely used in various technical fields. The designed object can be a technological machine, a production line, or a manufacturing complex. Special attention is paid to the optimization of its structure. The sequence of performing all stages of the optimization synthesis problem is presented in the article. To find a solution to this task, the developer should apply the complete or directed search of acceptable structure options and determine the best one using some optimization criteria to evaluate their quality. It can be simple enough if the designed technical system structure consists of no more than several elements. For example, if the number of alternative elements options is several dozen, it takes much time to accomplish the search correctly. Thus, the greater the number of components considered, the more difficult it is to do all the necessary calculations manually. In this case, machine resources should be involved. This scientific work aims to identify procedures of optimization synthesis that can be automated. Also, appropriate software has to be developed. Our computer program is based on the algorithm of a complete search of all options of the technical system structure. It can process an extensive array of input data and produce all possible and logically permissible results in the form the designer can analyze using the Pareto method to choose the best one. This software can be used for any technical system with a modular structure.

**Keywords:** equipment structure, optimization problem, software, industrialization, innovation, productivity.

## 1 Introduction

Modern technological equipment is a set of unified nodes, which designers often classify as a technical system with a functionally modular structure. Also, the same principle can be used for the equipment that structurally makes the production line or manufacturing complex.

It is effective enough to apply classical methods of synthesis and analysis, optimization, and predicate logic, when the object is considered from the point of view of its discrete structure with functional relations between components.

The idea of a modular approach to considering the structure of technological equipment is determined by production requirements. The technological process is divided into elementary technological operations. Then the functional module type for each operation's implementation can be selected. The functional module here is a functionally independent and structurally

complete set of mechanisms that are united by a mutual functional purpose [1, 2].

If a machine implements the technological process, functional modules include assembly units, mechatronic systems, and transport mechanisms.

If a production line implements the technological process, functional modules include machines, conveyors, manipulators, systems for accumulating workpieces, and semi-finished products.

Based on the modular approach, the following essential tasks have been solved.

Structural and parametric optimization for synthesizing technological layout structures during multi-tool processing is considered in [3].

The definition of the maximum period of use of unified nodes (modules) is proposed in [4].

The research work [5] proposes an approach to machine tool frames that can be reused and adapted multiple times is presented.

Geometric requirements from the selected scenarios of the use of machine structures are determined by dividing the structures into their ideal mechanical equivalents [6].

This article uses the modular principle for applying optimization synthesis as a kind of technological equipment design. It implies creating options of the technical system structure by combining functional modules of the necessary nomenclature in a specific order according to the technological process.

The subject of this investigation is a technical system such as a technological machine, production line, or manufacturing complex, the elements of which can be represented as a set of functional modules connected by functional relations.

The object of the study is the optimization synthesis methods, which help to determine the best option of the technical system among possible alternatives during its development. Particular attention focuses on identifying tasks that can be automated because the optimization is very time-consuming in general, so its execution using machine resources is in demand.

The aim of the study is the analysis of various optimization synthesis methods for the determination of the procedures, which can be carried out by computer. The obtained results became the basis for software development that implements our idea of partial automation of the optimization synthesis problem of modular technological equipment.

## 2 Literature Review

In modern industry, the choice of equipment for various purposes is so large that several options can represent each functional module. They may have different construction and are characterized by various technical and economic parameters, affecting the system's efficiency [7]. Of course, choosing those functional modules with the best parameter values is justified, but often the improvement of some of them is accompanied by a worse performance of others.

To include one alternative functional module in the designed system's overall structure, it is necessary to solve the optimization synthesis problem [8]. That means the designer should consider all possible combinations of functional modules, evaluate their quality and choose the best one [9-11].

In general, the optimization synthesis of any technological equipment is divided into the following stages (Figure 1) [1, 12].

The designer should formulate the design task at the "Problem formulation" stage. The functional purpose of the system and which quality characteristics will be evaluated should be considered.

The stage "Decomposition of the technological process" aims to divide the technological process into technological operations that should be implemented.

The decomposition algorithm of the technological process into operations was described in detail in the previous research work [1].

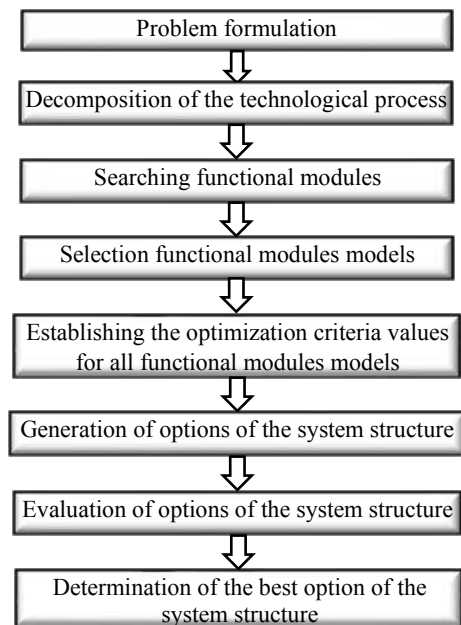


Figure 1 – Stages of optimization synthesis of modular technological equipment

"Searching functional modules" leads to finding the technological machines, devices, and mechanisms types that should perform all operations from the previous stage. It should be noted that depending on the design, some functional modules can perform two or more operations. Therefore, the number of operations is not always the same as the number of devices that implement the technological process.

"Selection functional modules models" means that any number of functional modules of the same functional purpose can be selected for further consideration.

"Establishing the optimization criteria values" lies in the determination of numerical values of technical or economic parameters, which were accepted as optimization criteria in the 1st stage and can be used for the efficiency evaluation of the entire system.

The formed set of equipment models with numerical values of the optimization criteria is the necessary initial data for solving the optimization problem.

The above stages represent an intellectual task, which implies searching and processing the array of data for compliance with the requirements.

They may be executed by one specialist, such as a design engineer, or by a group of experts (for example, to select optimization criteria, if the task is complex, and if it is more efficient to involve more than one point of view).

The next step is solving the structural optimization problem, as the most essential and complicated procedure of optimization synthesis.

Structural optimization aims to find the best option for the system structure among all alternatives obtained while solving the problem. The optimal solution is determined by finding the extremum of the objective function.

The stages "Generation of versions of the system structure", "Evaluation of versions of the system

structure”, and “Determination of the best version of the system structure” are implemented using the appropriate known methods of structural optimization.

There are two groups of methods for this purpose: complete search and directed search [10-16].

The formalization of optimization synthesis procedures is performed according to one of the following principles:

1) one-stage optimization synthesis, which suggests the synthesis of possible versions of the object’s structure without their intermediate evaluation. Next, all received options are evaluated, and the best (optimal) is selected. One-stage optimization synthesis characterizes the methods of complete search. As a rule, these are methods of combinatorics that allow forming all the possible combinations of elements among themselves [10]. Often a genetic algorithm is used too as a tool for solving various combinatorial optimization problems, including the modular design problem [13];

2) multi-stage optimization synthesis. According to it, the increase in the number of elements within the generated options alternates at each step with its evaluation. This principle characterizes the methods of directed search, which are based on the evaluation of intermediate structures, and if they do not satisfy the task conditions, they are rejected. Eliminating unpromising initial parts of options from further consideration saves computational costs. Thus, sequential algorithms make it possible to reduce a large-dimensional problem to a set of small-dimensional problems [14, 15].

The choice of the most acceptable method for solving the specific task depends on the dimension of the problem and the designer’s knowledge and capabilities.

In general, it is best when the method satisfies two main requirements:

1) makes it possible to select a set of dominant alternatives from all the results;

2) excludes the possibility of exclusion of potentially more effective options compared to those accepted for the final choice.

If the dimension of the problem is small, the designer can make the necessary conclusions empirically without using complicated mathematical algorithms. In the opposite case, the more the initial data of the problem, the more difficult it is to get the correct calculations. In this case, computer resources should be used.

Many engineering problems can be solved using appropriate software for designing various technological equipment.

In particular, designers can widely use CAD, CAM, and CAE technologies to create 3D models of equipment and its elements or execution of some standard calculations of equipment parameters [16, 17].

Specialized programs such as Mathcad or MATLAB can be used for complex mathematical calculations [18, 19].

There are also program tools for solving local problems of limited application, such as automatic tool path generation [20], digital twin development of robotized manufacturing systems [21], reverse digitizing for entire part geometry [22], obtaining optimal parameters of the

milling process [23], determination of the relationship between the technological regimes and operational characteristics of materials [24], and developing mathematical models of device operation [25].

These programs can be applied to some optimization tasks, but none is acceptable for solving the problem of optimization synthesis.

We considered it expedient to develop such software based on a functionally modular approach, which would perform the mathematical part of the structural optimization task.

Two main factors determine the relevance of this task. Firstly, today’s modern assortment of technological equipment is extensive and provides great opportunities for engineers to choose different equipment to implement the same technological process. Therefore, much of the time is spent on data search and analysis. The more information the engineer accepts as the initial data of the problem, the more complex the optimization task becomes.

Secondly, optimization synthesis methods are mathematically complicated enough for manual calculations.

Methods of directed search help to reject part of the results without their analysis and decrease the range of possible alternatives, but there is a risk that the optimal result will be mistakenly rejected as unpromising. The complete search methods avoid this problem and are algorithmically simpler but require much more calculations quantitatively. However, automation of these calculations can improve the efficiency of obtaining results, both from the point of view of their accuracy and saving time and resources.

### 3 Research Methodology

To implement the idea of partial automation of the process of solving the optimization problem, we developed the software “OptiTech”. It can process an array of parameter values of functional modules (input data), produce all possible and logically permissible results (output data) according to the complete search algorithm and present them conveniently for further processing.

It is necessary to start using the program when the results of the first five optimization synthesis stages described above (Figure 1) have already been carried out.

The sequence of solving the structural optimization problem is fully illustrated below by a practical example.

Suppose a task is to collect a production line for packing liquid products (e.g., water and juice) in glass bottles.

At the initial design stage, optimization criteria for evaluating the quality of structural elements of the line and the result of its structural synthesis should be selected. Anyone or two can do it, but no more than three characteristics that are most important from the developer’s point of view. It is important to note that each parameter must be additive since the program determines the sum of values of each criterion for each generated option of the structure.



From the point of view of saving cost, workshop space, and energy resources, we have chosen the following quality criteria respectively:

- 1) price ( $P$ , USD);
- 2) area ( $S$ ,  $m^2$ );
- 3) energy consumption ( $E$ ,  $\frac{kw \cdot s}{pc}$ ).

Energy consumption is determined by considering the power of the equipment, as below:

$$E_i = P_i \cdot T_i, \quad (1)$$

where  $E_i$  – energy spent by the functional module during time  $T$ , MJ;  $P_i$  – the power of the functional module, kW;  $T_i$  – the time required to produce a unit of a product.

At  $1 \text{ kW} \cdot \text{s} = 1000 \text{ W} \cdot 1 \text{ s} = 1 \text{ MJ}$

$$T = \frac{1}{Q}, \quad (2)$$

where:  $Q_i$  – productivity of the functional module, pc/s. Then

$$E_i = \frac{P_i}{Q_i}. \quad (3)$$

The values of these parameters should be as small as possible. It means that we need to solve a multicriteria minimization problem:

$$F(X) = (f_1(X), f_2(X), f_3(X)) \rightarrow \min,$$

where  $F(X)$  – the general objective function;  $f_i(X)$  – the partial objective function [1].

As a result of the decomposition of a technological process of packing liquids into glass bottles, we got a list of main operations (Table 1).

Table 1 – Compliance of functional modules with operations

Technological operation	Code	Functional module	Code
Cleaning and disinfection of bottles	O <sub>1</sub>	Bottle washing machine	FM <sub>1</sub>
Product bottling	O <sub>2</sub>	Dosing machine	FM <sub>2</sub>
Capping of bottles	O <sub>3</sub>	Capping machine	FM <sub>3</sub>
Labeling	O <sub>4</sub>	Labeling machine	FM <sub>4</sub>
Marking the date of manufacture	O <sub>5</sub>	Marking machine	FM <sub>5</sub>

Auxiliary operations (input empty bottles, inspecting them after washing, moving between working positions of the equipment, checking tightness after capping, and removing finished products and their packaging in transport containers) are not included in the optimization synthesis in this case. We accept that the appropriate equipment is presented in a single quantity so that it may be added to the main structure of the line after its optimizations.

The next step is data formalization.

The plural of implemented operations will be:

$$O = \{O_1, O_2, \dots, O_n\} = \{O_1, O_2, O_3, O_4, O_5\},$$

where  $O$  – technological operation;  $n$  – the sequence number of the operation in the technological process.

To perform the specified operations, applying appropriate functional modules – technological machines is necessary. They are shown in Table 1.

Thus, the technological process is realized by generalized structure  $X$  of the production line:

$$X = \{FM_1, FM_2, FM_3, FM_4, FM_5\}.$$

The set of the models of machines will be:

$$FM_n = \{E_{nm}\},$$

where:  $m$  – the sequence number of the model of  $n^{\text{th}}$  functional module.

The alternative models of defined functional modules are presented in coded form (Table 2). The manufacturers of the equipment set the values of optimization criteria.

Table 2 – Base of initial data of the problem of structural optimization of the production line for packing liquids

Functional module	Functional module model	Price $P$ , USD	Area $S$ , $m^2$	Energy consumption $E$ , $\text{kW} \cdot \text{s}/\text{pc}$
Bottle washing machine	E11	21700	24.5	13.2
	E12	20100	25.8	15.3
	E13	19300	27.4	14.1
Dosing machine	E21	15300	10.1	7.8
	E22	14800	13.7	8.5
	E23	16100	12.5	7.1
	E24	15400	11.6	7.6
Capping machine	E31	8700	9.8	6.4
	E32	9100	8.7	6.7
	E33	8200	9.1	6.2
Labeling machine	E41	5400	4.2	5.6
	E42	6300	3.6	5.9
	E43	6800	5.2	6.1
Marking machine	E51	750	1.6	3.8
	E52	900	1.2	4.2

So, we accept that the technological process includes five operations, which are implemented by five separate types of technological machines.

The next stage is generation of possible options of the structure of the entire production line.

Iteration is executed in the order from E11 to E52 with the step-by-step addition of the next element within  $FM_n$  to the formed structure until the complete set of modules is completed.

For example,

- $$X_1 = \{E11, E21, E31, E41, E51\};$$
- $$X_2 = \{E12, E21, E31, E41, E51\};$$
- $$X_3 = \{E13, E21, E31, E41, E51\};$$
- $$X_4 = \{E11, E21, E31, E41, E51\};$$
- $$X_5 = \{E11, E22, E31, E41, E51\}, \text{ and so on.}$$

In the described case, the number of such sets will be:

$$N = 3 \cdot 4 \cdot 3 \cdot 3 \cdot 2 = 216.$$

The last solution should be represented by the set:

$$X_{216} = \{E13, E24, E33, E43, E52\}.$$

However, we consider that the model E43 of the labeling machine can mark the product's date of manufacture (the notches, which are made on the labels, indicate the date of production). That is, E43 can implement operations  $O_4$  and  $O_5$ . Therefore, it should not be combined with elements E51 or E52 in the same structure.

The sequence of work with the program using the received information is described below.

## 4 Results

### 4.1 Description of the software

Work with the program "OptiTech" starts with creating a new document (Figure 2). To view an already created database, it can be loaded into the program using the command "Open" in the same menu.

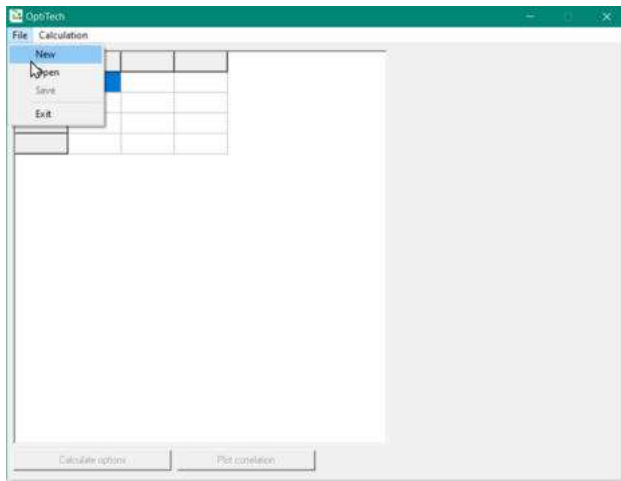


Figure 2 – The main program window

Next, the functional modules count (Figure 3a), models of each module count (Figure 3b), the optimization criteria count (Figure 3c), and the names of these criteria (Figure 3d) should be entered at the request of the program.

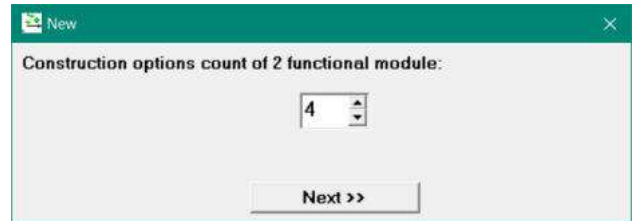
Then, it is necessary to fill in the table on the screen (Figure 4) with the appropriate criteria values for each element.

The next action is to specify the logical relations between elements. A logical relation should be understood as a condition that excludes the possibility of having more than one module that performs the same operation in the object structure. To mark that the element E43 should not be combined with element E51 or E52 in one structure the following actions should be done:

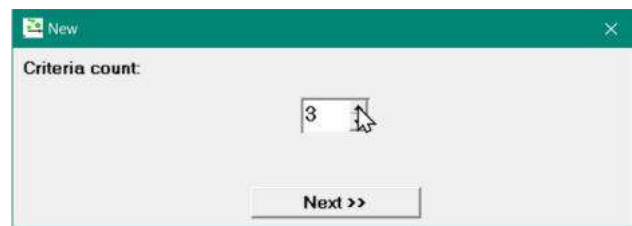
- 1) select the "Calculation - Logical relations" menu item;
- 2) using the drop-down lists, select the elements that are incompatible with each other (Figure 5).



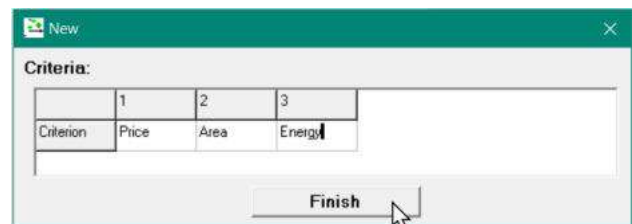
a



b



c



d

Figure 3 – The program window for entering data: a – functional modules count; b – the model of each module count; c – count of optimization criteria; d – names of optimization criteria

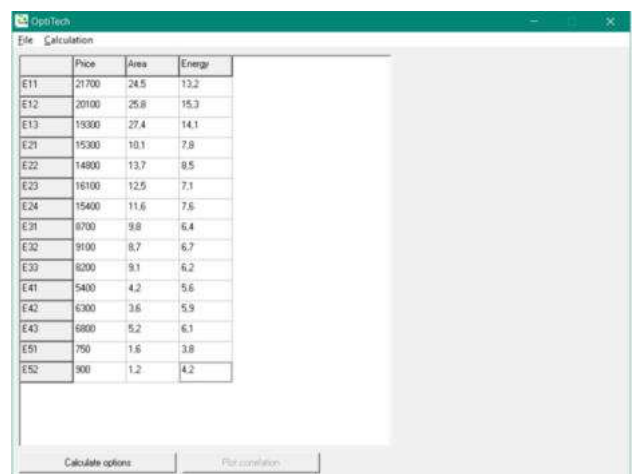


Figure 4 – The program window for entering criteria values

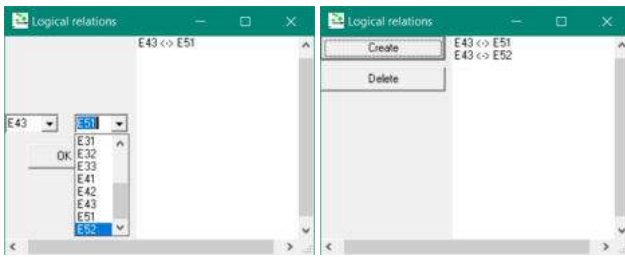


Figure 5 – The program window for entering the logical relations between functional modules

In this case, the program will count the criteria values for such modules in the same structure one by one, and the values of the alternative module will be counted as zero.

After clicking the “Calculate options” tab, a table with all the calculated results will appear in the right part of the program window (Figure 6), the sums of values for each criterion appropriate to a specific option of the problem solution.

In order to display the results of the calculation, it is necessary to click “Plot correlation”. The window that opens coordinate axes should be marked with the criteria names. For this purpose, drop-down lists placed in the upper left (axis Z), lower left (axis X), and lower right (axis Y) corners of the program window are used.

	Price	Area	Energy
E11	21700	24.5	13.2
E12	20100	25.8	15.3
E13	19300	27.4	14.1
E21	15300	10.1	7.8
E22	14800	13.7	8.5
E23	16100	12.5	7.1
E24	15400	11.6	7.6
E31	8700	9.8	6.4
E32	9100	8.7	6.7
E33	8000	9.1	6.2
E41	5400	4.2	5.6
E42	6300	3.6	5.9
E43	6800	5.2	6.1
E51	750	1.6	3.8
E52	900	1.2	4.2

	Price	Area	Energy
199	50400	54.2	33.5
199	48950	54.6	37.5
200	49700	54.2	37.9
201	50450	54	37.8
202	50600	53.6	38.2
203	50200	54	34.2
204	50200	54	34.2
205	49950	53.5	37.8
206	50100	53.1	38.2
207	50850	52.5	38.1
208	51000	52.5	38.5
209	50600	52.9	34.5
210	50600	52.9	34.5
211	49650	53.9	37.3
212	45200	53.5	37.7
213	49950	53.3	37.6
214	50100	52.9	38
215	49700	53.3	34
216	49700	53.3	34

Figure 6 – The program window with the calculated results

After performing the specified actions, a set of calculated results (solutions) will be displayed on a 3D graph (Figure 7).

For convenient work with the results, the program can show the projections of these points in the Cartesian coordinate system.

To divide the three-dimensional graph into planes with the possibility of viewing each of them, it is necessary to remove the 3D mark in the upper part of the window.

Next, it is possible to switch the marker in the upper left part of the window to the desired pair of axes.

The obtained results are presented in Figure 8. In particular, it can be seen, how the result window looks like for a point (Figure 8a). It shows information about the set of functional modules for this option of the structure and the total values for each criterion. To see it just click on any point.

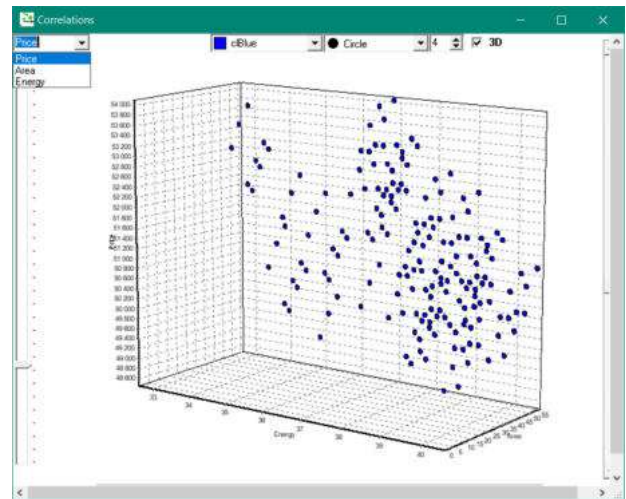
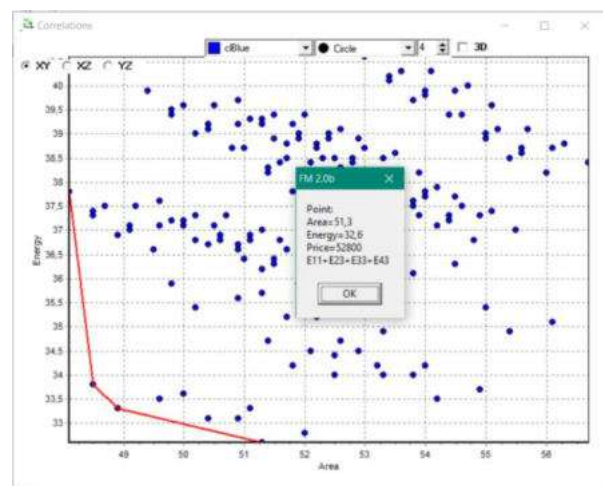


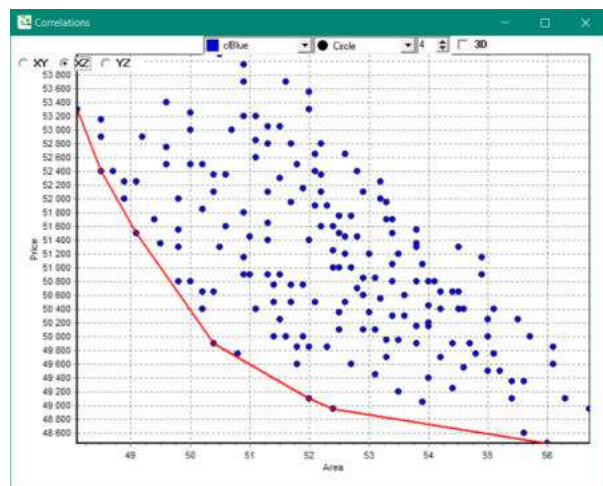
Figure 7 – 3D correlation graph of optimality criteria

Next, we highlight the Pareto set in the program.

To connect the desired points on each graph, it is necessary to select the “Add line” item with the right mouse button, click on the desired points, open the menu again and select the “Finish” item. An explanation of which points should be selected is given below



a



b

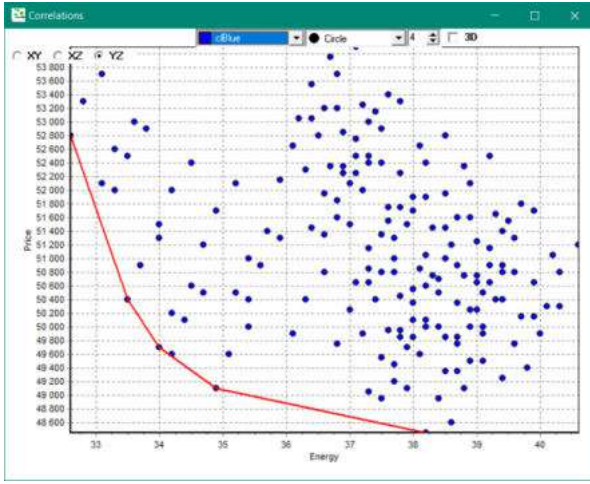


Figure 8 – Projection of points on planes: a – “Energy-Area” (XY); b – “Price-Area” (XZ); c – “Price-Energy” (YZ)

## 4.2 Program results interpretation

Further on the concept of criteria space  $\{F\}$ , which has dimension  $s$  (according to the optimal criteria count) and is formed by  $s$  orthogonal axes on which the values are marked  $f_k(X)$ ,  $k \in [1, s]$  is used.

We are using the language of predicate logic for description [26].

The priority relationship  $>$  should be determined on the set  $D_X$ . Then, under conditions  $F(X) \rightarrow \min$  and  $f_k(X^1) \leq f_k(X^2)$ ,  $k \in [1, s]$  vector  $X^1 \in D_X$  has priority over the vector  $X^2 \in D_X$ , which we denote as  $X^1 > X^2$ . Similarly, we define the dominance relation  $\triangleleft$ . If  $X^1 > X^2$  vector optimality criterion  $F(X^1) \in D_X$  dominates over  $F(X^2) \in D_X$ , that is  $F(X^1) \triangleleft F(X^2)$ .

The defined relations of priority and dominance are transitive. That is, if  $X^1 > X^2$  and  $X^2 > X^3$ , then  $X^1 > X^3$ . Similarly, if  $F(X^1) \triangleleft F(X^2)$  and  $F(X^2) \triangleleft F(X^3)$ , then  $F(X^1) \triangleleft F(X^3)$ .

So, we can define the set  $D_X$  a subset of points  $D_X^* \in D_X$ , for which no points are dominating them. The indicated set  $D_X^*$  is the Pareto one. Accordingly, the value of any partial optimization criteria can be improved only by worsening the other.

All the specified criteria must be minimized, so the Pareto set will be a set of points located in the extreme left lower position in the graphs.

In Figure 8a, the Pareto set includes the following solutions (options for the production line structure):

$$\begin{aligned} X^1 &= \{E_{11}, E_{21}, E_{32}, E_{42}, E_{52}\}; \\ X^2 &= \{E_{11}, E_{21}, E_{32}, E_{43}\}; \\ X^3 &= \{E_{11}, E_{21}, E_{33}, E_{43}\}; \\ X^4 &= \{E_{11}, E_{23}, E_{33}, E_{43}\}. \end{aligned}$$

In Figure 8b, the Pareto set includes the following solutions:

$$\begin{aligned} X^4 &= \{E_{11}, E_{21}, E_{32}, E_{42}, E_{52}\} \\ &\text{(the same as in the plane “XY”);} \\ X^5 &= \{E_{11}, E_{21}, E_{33}, E_{42}, E_{52}\}; \end{aligned}$$

$$\begin{aligned} X^6 &= \{E_{11}, E_{21}, E_{33}, E_{41}, E_{52}\}; \\ X^7 &= \{E_{12}, E_{21}, E_{33}, E_{41}, E_{52}\}; \\ X^8 &= \{E_{13}, E_{21}, E_{33}, E_{41}, E_{52}\}; \\ X^9 &= \{E_{13}, E_{21}, E_{33}, E_{41}, E_{51}\}; \\ X^{10} &= \{E_{13}, E_{22}, E_{33}, E_{41}, E_{51}\}. \end{aligned}$$

In Figure 8c, the Pareto set includes the following solutions:

$$\begin{aligned} X^4 &= \{E_{11}, E_{23}, E_{33}, E_{43}\} \\ &\text{(the same as in the plane “XY”);} \\ X^{11} &= \{E_{13}, E_{23}, E_{33}, E_{43}\}; \\ X^{12} &= \{E_{13}, E_{24}, E_{33}, E_{43}\}; \\ X^{13} &= \{E_{13}, E_{22}, E_{33}, E_{43}\}; \\ X^{10} &= \{E_{13}, E_{22}, E_{33}, E_{41}, E_{51}\} \\ &\text{(the same as in the plane “XZ”).} \end{aligned}$$

## 4.3 Determination of the optimal solution

The results show that some points of the Pareto set are projected onto two planes at once, so we get 13 solutions that dominate the rest of the 203 in terms of quality.

The total numerical values of the optimality criteria are summarized in Table 3.

We conclude that the program does not give a single solution to the problem, and the Pareto method only narrows the search circle but does not give a final result.

The designer’s task is to choose the best (optimal) solution by going through the points belonging to the Pareto set. We should proceed to mathematical calculations of the integral optimality criterion for this.

In this case, it is the simplest to search for the values of the additive criterion [15].

When applying the additive criterion, the objective function is obtained by summing up the normalized values of the partial criteria.

Table 3 – Values of optimization criteria for options of the production line structure

Criterion Solution	Price $P$ , USD	Area $S$ , m <sup>2</sup>	Energy consumption $E$ , kW·s/pc
X <sup>1</sup>	53300	48.1	37.8
X <sup>2</sup>	52900	48.5	33.8
X <sup>3</sup>	52000	48.9	33.3
X <sup>4</sup>	52800	51.3	32.6
X <sup>5</sup>	52400	48.5	37.3
X <sup>6</sup>	51500	49.1	37.0
X <sup>7</sup>	49900	50.4	39.1
X <sup>8</sup>	49100	52.0	37.9
X <sup>9</sup>	48950	52.4	37.5
X <sup>10</sup>	48450	56.0	38.2
X <sup>11</sup>	50400	54.2	33.5
X <sup>12</sup>	49700	53.3	34.0
X <sup>13</sup>	49100	55.4	34.9

The objective function is:

$$F(X^j) = \sum_i^k C_i \frac{f_i(X^j)}{f_i^0(X^j)} = \sum_i^k C_i f_i^*(X^j) \rightarrow \min, \quad (4)$$

where:  $j$  – the number of points in the Pareto set;  $C_i$  – weight coefficient of the  $i$ -th partial criterion;  $f_i(X^j)$  – the

value of the  $j$ -th partial criterion;  $f_i^0(X^j)$  –  $i$ -th normalizing divisor (minimum) value of  $i$ -th criterion;  $f_i^*(X^j)$  – a normalized value of the  $i$ -th partial criterion.

Thus, we assigned the weighting coefficients  $C_i$  for each value of the partial criteria (Table 4). We did it according to the principle of increasing values of partial criteria since we have a minimization problem for all optimization criteria.

Table 4 – Evaluation of options of the production line structure by weighting coefficients

Solution \ Criterion	Price $P$ , USD	Area $S$ , m <sup>2</sup>	Energy consumption $E$ , kW·s/pc	The value of the additive criterion $F(X^j)$
$X^1$	12	1	10	25.8
$X^2$	11	2	4	18.2
$X^3$	8	3	2	13.7
$X^4$	10	6	1	18.3
$X^5$	9	2	8	12.9
$X^6$	7	4	7	17.4
$X^7$	5	5	13	25.9
$X^8$	3	7	11	22.9
$X^9$	2	8	9	21.1
$X^{10}$	1	12	12	29.0
$X^{11}$	6	10	3	20.6
$X^{12}$	4	9	5	19.3
$X^{13}$	3	11	6	22.1

So, substituting the relevant data in (4), we get:

$$F(X^1) = 12 \cdot \frac{53300}{48450} + 1 \cdot \frac{48.1}{48.1} + 10 \cdot \frac{37.8}{32.6} = 25.79;$$

...

$$F(X^{13}) = 3 \cdot \frac{49100}{48450} + 11 \cdot \frac{55.4}{48.1} + 6 \cdot \frac{34.9}{32.6} = 22.13.$$

The results of all calculations are listed in Table 4.

The optimal option of the structure of the designed production line among all possible is  $X^5$  because its additive criterion is the smallest.

## 5 Discussion

Many scientific works are aimed at improving the equipment at the design stage. Solving engineering problems based on a modular approach is widespread [2, 4-7, 9, 17]. Structural optimization issues are also well investigated [3, 8, 10-12, 14, 15, 18].

Some studies are devoted to automating various design tasks [16, 19-25].

A review of these studies confirms that structural optimization is one of technological equipment design's most essential and challenging stages. Mistakes made in

its early stages irreversibly affect the quality of the object and the efficiency of its operation. Therefore, the development result should be technically rational and economically justified as possible.

Regardless of the effectiveness of the chosen optimization method, the quality of the solution depends directly on the accuracy of calculations. So special attention should be paid to its correctness.

In this article, we offer to increase the efficiency of solving the optimization problem by software to automate its stages.

As can be seen from the presented materials, our software "OptiTech" has a few features:

- does not limit the number of elements (models of the equipment) of the designed system structure;
- executes the combinatorial part of the optimization task;
- determines problem solutions with high mathematical precision;
- is suitable for a wide range of equipment with a discrete structure regardless of its functional purpose.

Based on the above results, it can be stated that the research aim is completely achieved.

## 6 Conclusions

In the article, an analysis of optimization synthesis methods to determine the procedures which computer resources can carry out is conducted. The obtained results became the basis for software development that implements the idea of partial automation of the optimization synthesis problem of modular technological equipment.

The suggested software "OptiTech" is developed using the complete search algorithm. It generates all logically admissible options of the system structure, counts the values of selected criteria, and visualizes the set of all solutions. The obtained correlation is convenient for applying the Pareto method. The optimal option is determined using the generalized optimality criterion.

The efficiency of this research is confirmed by the presented optimization synthesis of a production line for packing liquid products in glass bottles. Automation of the calculation procedures ensures adequate accuracy of results. The dimension of the data to be calculated manually is reduced significantly. For the presented task, the number of solutions, which should be processed at the final stage, decreased from 216 to 13 (by 16 times).

Software "OptiTech" is acceptable for structural optimization of any technical system with a functionally modular structure (technological machines, production lines, or manufacturing complexes) regardless of its functional purpose.

## References

1. Zabolotnyi, O., Zaleta, O., Bozhko, T., Chetverzhuk, T., Machado, J. (2022). Algorithmization of Functional-Modular Design of Packaging Equipment Using the Optimization Synthesis Principles. In: Innovations in Mechatronics Engineering II. ICIENG 2022. *Lecture Notes in Mechanical Engineering*. Springer, Cham, [https://doi.org/10.1007/978-3-031-09385-2\\_13](https://doi.org/10.1007/978-3-031-09385-2_13)
2. Shaik, A.M., Rao, V.V.S.K., Rao, C.S. (2015). Development of modular manufacturing systems – A review. *Int J Adv Manuf Technol*, Vol. 76, pp. 789–802 (2015), <https://doi.org/10.1007/s00170-014-6289-2>

3. Yakovenko, I., Permyakov, A., Prihodko, O., Basova, Y., Ivanova, M. (2020). Structural Optimization of Technological Layout of Modular Machine Tools. In: Advanced Manufacturing Processes. InterPartner 2019. *Lecture Notes in Mechanical Engineering*. Springer, Cham, [https://doi.org/10.1007/978-3-030-40724-7\\_36](https://doi.org/10.1007/978-3-030-40724-7_36)
4. Yakovenko, I., Permyakov, A., Ivanova, M., Basova, Y., Shepeliev, D. (2022). Lifecycle Management of Modular Machine Tools. In: Tonkonogyi, V., Ivanov, V., Trojanowska, J., Oborskyi, G., Pavlenko, I. (eds) Advanced Manufacturing Processes III. InterPartner 2021. *Lecture Notes in Mechanical Engineering*. Springer, Cham, [https://doi.org/10.1007/978-3-030-91327-4\\_13](https://doi.org/10.1007/978-3-030-91327-4_13)
5. Uhlmann, E., Saoji, M., Peukert, B. (2016). Principles for interconnection of modular machine tool frames. *Procedia CIRP*, Vol. 40, pp. 413–418, <https://doi.org/10.1016/j.procir.2016.01.081>
6. Peukert, B., Saoji, M., Uhlmann, E. (2015). An evaluation of building sets designed for modular machine tool structures to support sustainable manufacturing. *Procedia CIRP*, Vol. 26, pp. 612–617, <https://doi.org/10.1016/j.procir.2014.07.175>
7. Yakovenko, I., Permyakov, A., Naboka, O., Prihodko, O., Havryliuk, Y. (2020). Parametric Optimization of Technological Layout of Modular Machine Tools. In: Ivanov V., Trojanowska J., Pavlenko I., Zajac J., Peraković D. (eds) Advances in Design, Simulation and Manufacturing III. DSMIE 2020. *Lecture Notes in Mechanical Engineering*. Springer, Cham, [https://doi.org/10.1007/978-3-030-50794-7\\_9](https://doi.org/10.1007/978-3-030-50794-7_9)
8. Usubamatov, R., Alwaise, A.M.A., Zain, Z.M. (2013). Productivity and optimization of section-based automated lines of parallel-serial structure with embedded buffers. *Int J Adv Manuf Technol*, Vol. 65, pp. 651–655, <https://doi.org/10.1007/s00170-012-4204-2>
9. Pavlov, K.S., Khobotov, E.N. (2015). Models for equipment selection and upgrade in manufacturing systems of machine building enterprises. *Autom Remote Control*, Vol. 76, pp. 292–303, <https://doi.org/10.1134/S0005117915020083>
10. Marmion, M.E. (2013). Local search and combinatorial optimization: from structural analysis of a problem to efficient algorithms design. *4OR-Q J Oper Res*, Vol. 11, pp. 99–100, <https://doi.org/10.1007/s10288-012-0204-1>
11. Guo, X., Cheng, G.D. (2010). Recent development in structural design and optimization. *Acta Mech Sin*, Vol. 26, pp. 807–823, <https://doi.org/10.1007/s10409-010-0395-7>
12. Saliba, M.A., Azzopardi, S., Pace, C. et al. (2019). A heuristic approach to module synthesis in the design of reconfigurable manufacturing systems. *Int J Adv Manuf Technol*, Vol. 102, pp. 4337–4359, <https://doi.org/10.1007/s00170-019-03444-4>
13. Kamrani, A.K., Gonzalez, R. (2003). A genetic algorithm-based solution methodology for modular design. *Journal of Intelligent Manufacturing*, Vol. 14, pp. 599–616, <https://doi.org/10.1023/A:1027362822727>
14. Allen-Zhu, Z., Li, Y., Singh, A. et al. (2021). Near-optimal discrete optimization for experimental design: a regret minimization approach. *Math. Program.*, Vol. 186, pp. 439–478, <https://doi.org/10.1007/s10107-019-01464-2>
15. Wang, K., Zhou, Y., Tian, G. et al. (2021). A structured solution framework for fuzzy minimum spanning tree problem and its variants under different criteria. *Fuzzy Optim Decis Making*, Vol. 20, pp. 497–528, <https://doi.org/10.1007/s10700-021-09352-1>
16. Chetverzhuk, T., Zabolotnyi, O., Sychuk, V., Polinkevych, R., Tkachuk, A. (2019). A method of body parts force displacements calculation of metal-cutting machine tools using CAD and CAE technologies. *Annals of Emerging Technologies in Computing*, Vol. 3(4), pp. 37–47, <https://doi.org/10.33166/AETiC.2019.04.004>
17. Wen, X., Liu, J., Du, C. et al. (2022). The key technologies of machining process design: a review. *Int J Adv Manuf Technol*, Vol. 120, pp. 2903–2921, <https://doi.org/10.1007/s00170-022-08982-y>
18. Kudryavtsev, Y.M. (2018). Structurally-parametrical optimization technological process by Dijkstra’s method in system Mathcad. *Materials Science Forum*. Vol. 931, pp. 1238–1244, <https://doi.org/10.4028/www.scientific.net/msf.931.1238>
19. Calusdian, J., Yun, X. (2019). A simple and highly portable MATLAB interface for learning robotics. *SN Appl. Sci.*, Vol. 1, 890, <https://doi.org/10.1007/s42452-019-0941-2>
20. Xu, T., Chen, Z., Li, J. et al. (2015). Automatic tool path generation from structuralized machining process integrated with CAD/CAPP/CAM system. *Int J Adv Manuf Technol*, Vol. 80, pp. 1097–1111, <https://doi.org/10.1007/s00170-015-7067-5>
21. Saavedra Sueldo, C., Perez Colo, I., De Paula, M. et al. (2023). ROS-based architecture for fast digital twin development of smart manufacturing robotized systems. *Ann Oper Res*, Vol. 322, pp. 75–99, <https://doi.org/10.1007/s10479-022-04759-4>
22. Lan, H., Ding, Y., Hong, J. et al. (2008). A re-configurable cross-sectional imaging system for reverse engineering based on a CNC milling machine. *Int J Adv Manuf Technol*, Vol. 37, pp. 341–353, <https://doi.org/10.1007/s00170-007-0962-7>
23. Krimpenis, A.A., Fountas, N.A., Ntalianis, I. et al. (2014). CNC micromilling properties and optimization using genetic algorithms. *Int J Adv Manuf Technol*, Vol. 70, pp. 157–171, <https://doi.org/10.1007/s00170-013-5248-7>
24. Obertyukh, R., SlabkyiA., Polishchuk, L., Povstianoi, O., Kumargazhanova, S., Satymbekov, M. (2022). Dynamic and mathematical models of the hydroimpulsive vibro-cutting device with a pressure pulse generator built into the ring spring. *Informatyka, Automatyka, Pomiar w Gospodarce i Ochronie Środowiska*, Vol. 12(3), pp. 54–58, <https://doi.org/10.35784/iapgos.3049>
25. Povstyanoy, O., Zabolotnyi, O., Kovalchuk, O., Somov, D., Chetverzhuk, T., Gromaszek, K., Amirgaliyeva, S., Denissova, N. (2021). *Analysis, Development, and Modeling of New Automation System for Production of Permeable Materials from Machining Waste*. Mechatronic Systems, Vol. 1. Taylor & Francis Group, London, UK, <https://doi.org/10.1201/9781003224136-14>
26. Nikitchenko, N.S. (2003). Equitone predicate algebras and their applications. *Cybernetics and Systems Analysis*, Vol. 39, pp. 97–112, <https://doi.org/10.1023/A:1023829327704>



Chalyj V., Moroz S., Tkachuk A., Zablotskyi V., Trokhymchuk I., Stelmakh A. (2023). Formation of bearings parts waviness in centerless mortise grinding on rigid supports. *Journal of Engineering Sciences*, Vol. 10(1), pp. A15-A21, doi: 10.21272/jes.2023.10(1).a3

## Formation of Bearings Parts Waviness in Centerless Mortise Grinding on Rigid Supports

Chalyj V.<sup>1</sup>[0000-0002-6592-6715], Moroz S.<sup>2</sup>[0000-0003-4677-5170], Tkachuk A.<sup>2\*</sup>[0000-0001-9085-7777], Zablotskyi V.<sup>2</sup>[0000-0002-2921-0031], Trokhymchuk I.<sup>2</sup>[0000-0002-0737-6452], Stelmakh O.<sup>3</sup>[0000-0002-9132-6334]

<sup>1</sup> PSC "SKF Ukraine", 34, Bozhenka St., 43017 Lutsk, Ukraine;

<sup>2</sup> Lutsk National Technical University, 75, Lvivska St., 43018 Lutsk, Ukraine;

<sup>3</sup> Beijing Institute of Technology, 5, Zhongguancun St., Haidian Qu, China

### Article info:

Submitted: January 31, 2023  
 Received in revised form: May 10, 2023  
 Accepted for publication: May 22, 2023  
 Available online: June 1, 2023

### \*Corresponding email:

[a.tkachuk@lntu.edu.ua](mailto:a.tkachuk@lntu.edu.ua)

**Abstract.** The formation of waviness on the working surfaces of bearing parts is associated with fluctuations in the size of the cut layer of metal and changes in the components of the cutting force. Laplace operators were used to model the centerless grinding system based on the construction of the transfer function and the characteristic equation. It was found that the formation of waviness depends on the position of the hodograph of the movement of the vector of the center of the part in the complex plane, which in turn depends on the geometric parameters of the rigid supports of the centerless grinder machine. This makes it possible, based on hodographs and the angular orientation of their asymptotes, to determine the geometric stability of the process depending on the angles of adjustment of the rigid supports of the grinder machine. Two methodological approaches were used to confirm the correctness of the hypotheses. The first one is a multiplication of wave's hodographs. The second one is regeneration displacement and the coincidence of the combined hodograph of regeneration and waviness displacement mechanisms with the hodograph of infinitely rigid machine displacement. The diagrams which allow choosing geometry of adjustment of rigid support that allows to increase or decrease parameters of certain harmonics are developed. The 3D diagram allows setting the local minima, characterized by acceptable geometric adjustment conditions, providing regulated waviness of the working surfaces of bearing parts.

**Keywords:** process innovation, adjustment, asymptote, harmonic analysis, hodograph, waviness.

## 1 Introduction

During the manufacture of roller bearings, the quality of treated rolling surfaces is essential [1]. When grinding the functional rolling surfaces of roller bearing rings, it is necessary to ensure rapid removal of allowance and high processing performance, the final macro-and micro geometric accuracy of the treated surface, and compliance with physical and mechanical requirements [2]. The size of the cut layer during grinding is proportional to the normal grinding force [3]. The formation of the waviness of the details is caused by deviations in the size of the cut layer or changes in the grinding force [4]. Surface roughness depends on the material of the part and the grinding wheel, the productivity of the allowance removal, and the relative speed between the part and the grinding wheel. The

grinding force is the main variable for the machining process analysis [5].

The scheme of the dynamic model, which was used to predict both static (geometric) and dynamic stability of the process of centerless grinding on rigid supports, is shown in Figure 1. During the centerless grinding process study, the tangential force vectors of supports  $A$  and  $B$  were not considered since they have small values and do not significantly affect the modeling. The components of the grinding forces  $F_n$ ,  $F_t$ , taking into account the force  $F_G$  arising from the weight of the part and the force  $F_M$  from magnetic retention, form the formation of force vectors of the reactions of the supports  $F_A$ ,  $F_B$ , which is necessary to ensure the static balance of the grinding system. As seen in Figure 1, the center of the part is shifted relative to the center of the support by a small amount ( $\Delta X$ ;  $\Delta Y$ ). This is done to ensure permanent contact with the supports of the part. One of the main

parameters of the centerless grinding process that can be controlled is the angles of inclination of the supports ( $\varphi_1$  and  $\varphi_2$ ).

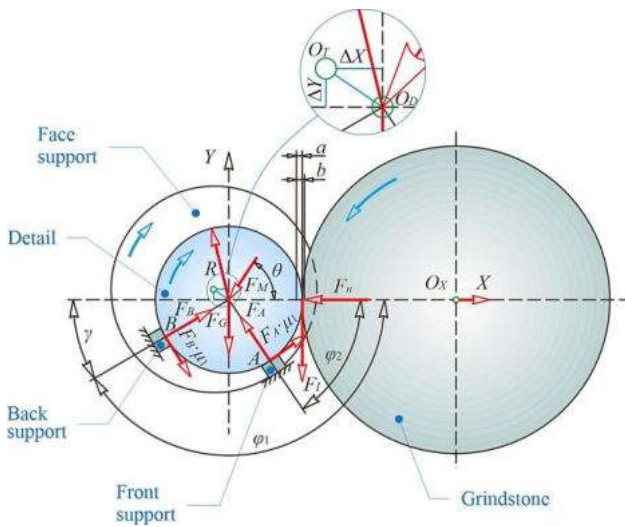


Figure 1 – Scheme of a dynamic model for predicting the stability of the centerless grinding [6]

That is why production requires recommendations for choosing the value of the angles of the supports and obtaining the final regulated harmonics, thanks to this. However, such recommendations require research and scientific justification of their results [6].

## 2 Literature Review

To research the grinding processes, there are mathematical models used by Laplace operators to analyze the centerless grinding system.

The research of the transfer function and the solution of the characteristic equation is carried out using graph-analytical methods [7]. The formation of waviness depends on the position of the hodograph of the movement of the vector of the center of the detail in the complex plane, which in turn depends on the geometric parameters of the rigid supports of the grinder machine [8, 9]. Adjustment angles  $\varphi_1$  or  $\varphi_2$  directly affect the normal component of grinding force, cutting depth, stability in the cutting zone, and, consequently, the harmonics of the newly formed waviness of bearing details [10].

In the Laplace region, multiplication is required to combine the mechanism of waviness and the mechanism of regeneration. For graphical analysis, the mechanism of the combined effect is determined by multiplying the vector by the corresponding value of  $s = \sigma + jn$ . In this case, the coordinate origin vector for both ripple and regeneration mechanisms is at the same frequency and  $\sigma$  (here,  $\sigma = 0$ ). In vector multiplication, the values of each vector are multiplied, and angles from the positive real axis are added. For example, Figure 2 shows the vector's multiplication at a frequency of  $n = 7.5$ . The waveform has a magnitude of 2 and an angle of  $-45^\circ$ , and the regeneration vector has a magnitude of 3 and an angle of  $120^\circ$ . The combined vector for this condition is shown in Figure 2b, where the value of  $n = 7.5$  is the vector 6 (2, 3), and the angle is  $75^\circ$  ( $120^\circ + (-45^\circ)$ ).

The part of the hodograph of the harmonic vector 6 to 8 shows the general picture of the combined hodograph of the vector for different harmonics and conditions set up.

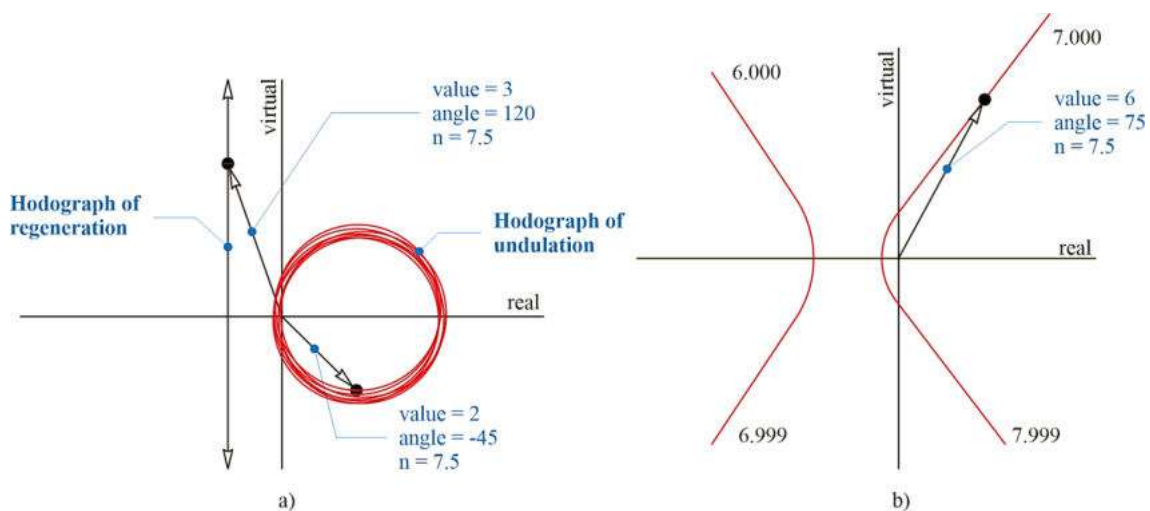


Figure 2 – Vector multiplication scheme (a) and combined hodograph of the vector from 6th to 8th harmonics (b) [6]

Elements of the sample of the combined operation of the hodograph mechanism from the 2nd to the 10th harmonic under a specific debugging condition [11]. These forms of hodograph hyperbola are concentrated

around a point  $(-0.5; 0)$  in the complex plane and have infinite asymptotes covering the range from  $0^\circ$  to  $360^\circ$  (Figure 3).



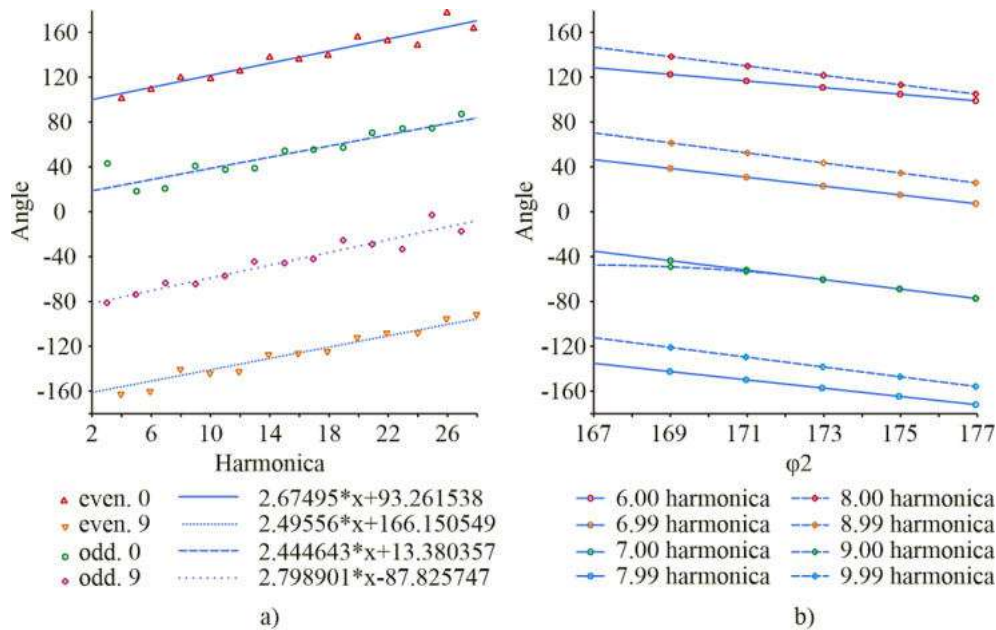


Figure 3 – Vector multiplication scheme (a) and combined hodograph of the vector from 6th to 8th harmonics (b) [11]

Asymptotes have imaginary components, starting with positive infinity for integers numbered harmonics (e.g., 5.000, 6.000) and ending with negative infinity for numbers of smaller integers (e.g., 5.999, 6.999). It is established that the most variable for these hodographs is the angular orientation of the asymptotes. This confirms that the asymptotes around  $0^\circ$  mean the geometric instability of the process [12].

### 3 Research Methodology

We will analyze the change in waviness harmonics depending on the geometry of the setup of rigid supports (Figure 3a). The asymptotes increase by  $2.5^\circ$  per harmonic with even and odd, grouping at approximately  $180^\circ$  from each other [13, 14].

Figure 3b shows the trends of the asymptotes of the angles with a change in the angle  $\varphi_2$  for some harmonics if the angle of the front support is constant,  $\varphi_1 = 55^\circ$ . This graph shows a decrease in the asymptote of the angle if  $\varphi_2$  is increased. It is also possible to observe even and odd, whole, and next-to-whole asymptotes of angles approximately  $180^\circ$  apart. Since the asymptotes of angles are clear arrays, we need the interpretation of angles to explain the geometry of centerless grinding processes [15, 16].

The study proposes to use two methodologies. The first is the multiplication procedure of hodographs of waviness displacement and regeneration. The second is analyzing the graphic coincidence of the combined hodograph of regeneration and waviness movement mechanisms with the hodograph of infinitely rigid machine movement [17]. The analysis showed that the displacement hodograph has a negative real part, so the mechanism of the waviness effect on the process is

unstable [18]. At the same time, the angle of such hodograph movement of the waviness mechanism will acquire a value greater than  $90^\circ$  or less than  $-90^\circ$  from the positive real axis. Since the hodograph of the movement of the regeneration mechanism is in a certain area, the angle of the hodograph will be similar at a given frequency. If the waviness and regeneration mechanisms coincide at a certain frequency (geometric angles are compensated), the combined displacement hodograph forms a hyperbola with an asymptote of  $0^\circ$  ( $-360^\circ$ ). Such a compensation mechanism indicates the geometric instability of the asymptotes for some harmonics [19]. For an infinitely rigid machine, the hodograph of displacement in the complex plane is located at the point at the origin of the coordinates. At the same time, the hodograph of waviness movement and regeneration enters the area around the point  $(-0.5; 0)$ . The displacement hodographs, which have an asymptote near  $0^\circ$ , usually intersect with the machine displacement hodograph. The fact that the results fall in the system of the process mechanism corresponding to the interaction for this indicated frequency of the ripple allows the growth of this harmonic due to instability in the processing zone [20]. The given interpretation involves an infinitely rigid machine, so the study points to the geometric instability of the waviness frequency, which consists of a vector coincidence in the complex plane. It has been established that the asymptote angles largely depend on the number of harmonics and the geometry of tuning angles, so it allows for predicting which harmonics will be unstable in a given range of tuning angles [21]. Suppose a certain angle of the asymptote of one harmonic is changed and investigated during the full complex of tuning geometry. In that case, it is observed that the theoretical geometric instability of the specified number of harmonics will manifest if the asymptote's

angle is a multiple of the value in radians –  $2\pi$ . During the research, a contour diagram of the asymptote angle was obtained, and the 14th harmonics were studied within the standard geometry of centerless grinding on rigid supports (Figure 4).

The angular shift from  $2\pi$  to 0 radians leads to a high density of contours, allowing one to see places where the asymptotes are multiples of  $2\pi$  easily. This graph shows that the 14th harmonic is theoretically unstable at  $\varphi_1 = 52^\circ, 78^\circ$ , and  $\varphi_2 = 143^\circ, 168^\circ$ . Although only one line in each of these regions will be exactly  $0^\circ$ , instability ripples are common for harmonics whose numbers are away from the whole due to a phase shift in the regeneration of waviness regeneration during grinding. Therefore, looking only at the general region, where the whole harmonic is unstable, is best. For example, in Figure 4, an ellipse can be drawn around each area of the concentrated contour lines to represent the main zones where 14th harmonics are theoretically unstable.

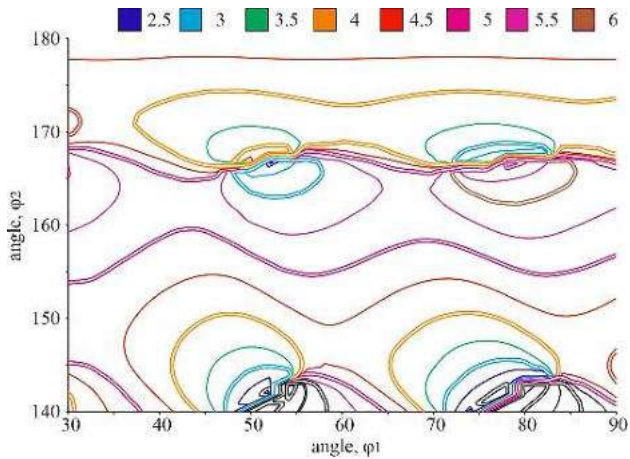


Figure 4 – Contour diagram of asymptote angles in radians for the 14th harmonic within the typical geometry of centerless grinding

During the research, results were obtained that made it possible to construct a diagram of the geometric instability of the waviness for a specific range of harmonics (2–22) for the standard conditions of the geometry of the grinding process adjustment based on the asymptote angles. The diagram confirms that the vast majority of combinations during adjustment of the angles of rigid supports are in the region of geometric instability, and the instability of harmonics corresponds to a particular array of values. For example, consider the 12th harmonic, which is geometrically unstable in the region of  $\varphi_1 = 60^\circ$  and  $\varphi_2 = 165^\circ$ . The 14th harmonic is geometrically unstable in the region above and to the left near the values of  $\varphi_1 = 52^\circ$  and  $\varphi_2 = 168^\circ$ . This diagram allows selecting the geometry of the grinding adjustment on rigid supports, which increases or decreases the parameters of a particular harmonic.

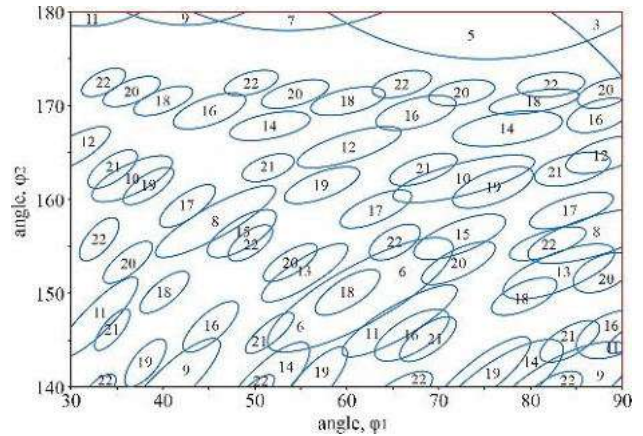


Figure 5 – The geometric instability wave diagram constructed using angular analysis of the combined displacement hodograph at the stability limit within the typical debug geometry

Analysis of Figure 5 makes it possible, with high probability, to predict the geometric instability in the cutting zone during grinding, thereby predicting the growth or reduction of a harmonic ripple.

## 4 Results

### 4.1 Impact diagram based on angular analysis of the hodograph

To maintain the stability and relative speed of rotation between the part and the grinding wheel during the machining process, the magnetic force of the end support must be equal to or exceed the tangential grinding force (Figure 1):

$$F_M \geq F_t. \quad (1)$$

The angle of the magnetic force application is equal to

$$\theta \geq \arcsin\left(\frac{1}{2 \cdot \cos(\gamma)}\right). \quad (2)$$

The geometry of the setup of rigid supports affects the parameters of the waviness of the working surfaces of the roller bearing rings, and different angles of the supports have different effects on the different harmonics of the waviness.

When the combined hodograph of the displacement and regeneration mechanisms for any harmonic had an asymptote at  $0^\circ$ , this harmonic was geometrically unstable. The angles of the asymptotes followed the main trends depending on the machine's adjustment conditions. Given this fact, it is fair to assume that the closer the angle of the asymptote to  $0^\circ$ , the less stable the harmonic becomes. The summary diagram is defined as an indicator of the degree of instability for each debugging condition. When performing this action, there is a need for a parameter that would be proportional to the angle of the asymptote, and angles around 0 or  $2\pi$  should have a significant effect on it, and angles far from 0 or  $2\pi$  have little effect. The cosine function satisfies the established requirements. If we take the values of the cosines of the radians shown in Figure 4, the results

diagram suggests a relative level of instability for 14th harmonics under different debugging conditions. In this diagram (Figure 6), contours with levels close to zero (0.1, 0.2) are much more stable than levels around 1.0.

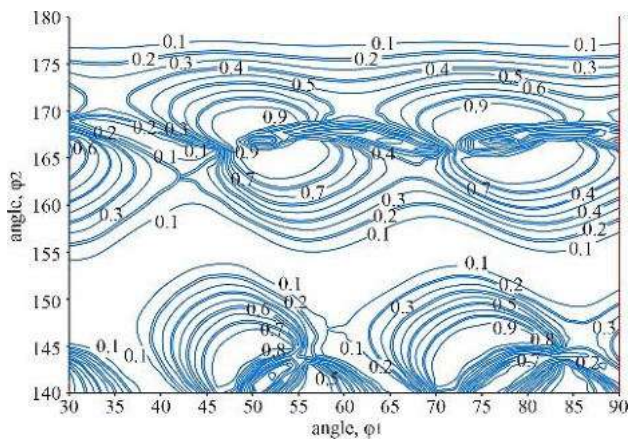


Figure 6 – Contour diagram of cosines of asymptote angles for the 14th harmonic within the typical geometry of centerless grinding

If the performance analysis is similar to Figure 6 for each harmonic from 2 to 30 within the usual geometry of the centerless grinding, we obtain a general diagram of the geometric stability results, shown in Figure 7.

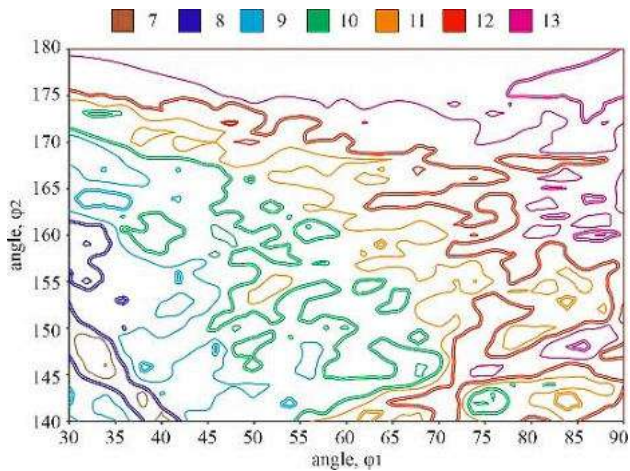


Figure 7 – Contour diagram of all cosines of asymptote angles from 2nd to 30th harmonics within the typical geometry of centerless grinding

#### 4.2 Non-zero sigma, impact diagram based on hodograph diameter analysis

If we analyze the combined hodograph of undulating displacement and regeneration with a non-zero growth rate,  $\sigma$ , its graphical representation changes dramatically. Non-zero  $\sigma$  changes the hodograph of regeneration movement from a straight line to a circle. For a positive  $\sigma$ , the circles are centered closer to the point  $(-1; 0)$ , while the negative  $\sigma$  forms circles centered around the origin  $(0; 0)$ .

The size of the hodograph responds faster than the exponential function so that only at the slightest change in the value of  $\sigma$  does it significantly change the appearance of the combined hodograph of waviness displacement and regeneration.

Figure 8 shows a combined hodograph of waviness displacement and regeneration with different positive  $\sigma$  from 6.000 to 7.999 harmonics under a given debugging condition. Thus, the hyperbola rotates around itself, forming cyclic spirals. As the sigma value increases, the size of the spirals decreases. With an absolute increase in the sigma, the size of the spirals decreases.

An infinitely rigid machine in the complex plane is the point at the origin. When the hodograph of the movement of the waviness and regeneration intersects with the hodograph of the movement of this machine, the result is a geometric instability in the grinding zone. If a particular spiral intersects with the hodograph of the machine movement, it should be small enough to be near the origin. Therefore, any value of  $\sigma$  that can make the spiral small enough to intersect with the hodograph of the machine movement will form individual harmonics of unstable level. That is, if one helix is large compared to another at a certain  $\sigma$ , it is clear that a larger helix will need a larger  $\sigma$  to become small enough to intersect with the hodograph of machine movement. On the other hand, the best condition for grinding will result from the debugging condition, the spirals of which form a very small instability (small  $\sigma$ ) intersecting with the hodograph of the machine movement. Based on this analysis, the debugging condition with large spirals is less desirable than with smaller spirals at a certain unstable  $\sigma$ .

After using these features, an estimate of the geometric stability of the grinder is obtained based on the size of the combined hodograph of waviness displacement and regeneration at constant, non-zero  $\sigma$ . If we consider in the complex plane of the spiral of all harmonics under all debugging conditions with some non-constant  $\sigma$ , the total size of the spirals will be proportional to the instability under each debugging condition. Figure 9 illustrates the sum of the total size of the spirals from the 2nd to 30th harmonics for each debugging condition within the normal geometry of debugging centerless grinding.

A 3D diagram is shown for the conceptual interpretation of research results.

To analyze the waviness of the raceways of the bearing rings, it is advisable to use the Fourier series, which describes it as a complex periodic function consisting of simple harmonic oscillations with frequencies that are multiples of the fundamental one. The sequence number of a simple harmonic determines the number of irregularities highlighted on the part's surface. In particular, the second term of the Fourier series corresponds to the second harmonic and reflects the ovality of the part's surface, the third term - the third harmonic - reflects the trihedron, and so on.

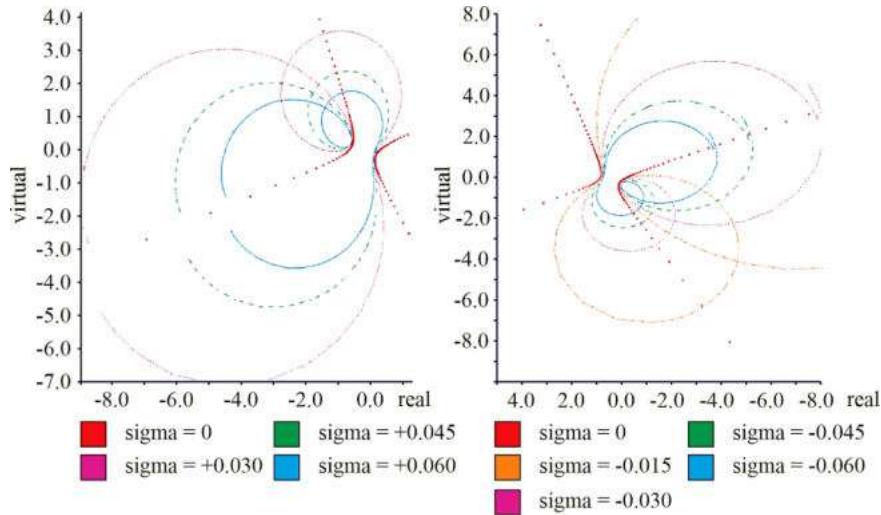


Figure 8 – Scheme of change of the combined hodograph of movement in a spiral at +sigma (a) and at -sigma (b)

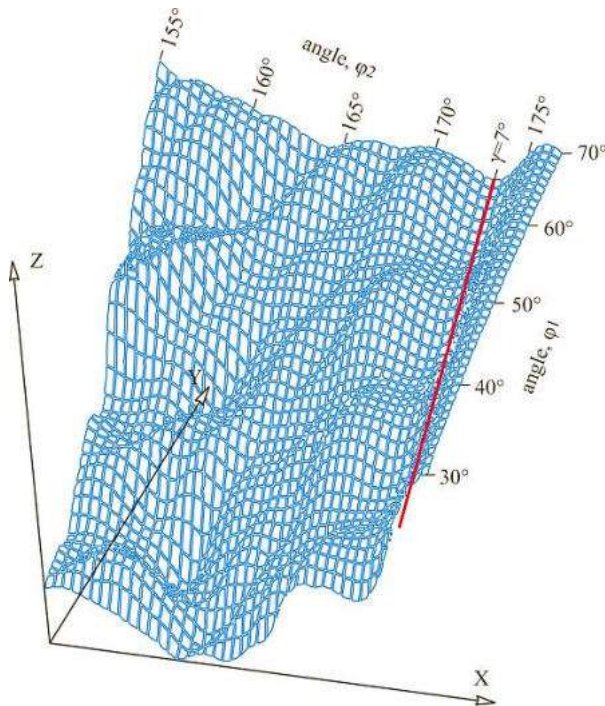


Figure 9 – Scheme of change of the combined hodograph of movement in a spiral at +sigma (a) and at -sigma (b)

## 5 Conclusions

So, as a result of the conducted research, it was established that the characteristics of the waviness of the working surfaces of the roller bearing rings are influenced by the geometry of the setup of rigid supports during centerless grinding. It is shown that different support angles during processing have different effects on

the harmonics of the waviness of the working surfaces of roller bearings.

The mechanism of waviness on the surface of the part in the process of centerless mortise grinding depends on many additional factors (characteristics of the grinding wheel, machine vibration, grinding force, initial and time-varying waviness of the part), which must be considered to ensure stable quality.

The geometry of the rigid supports influences the stability of the centerless grinding process. The corresponding diagrams show this. In particular, on the influence diagram based on the angular analysis of the hodograph, provided that the system finds a stability limit  $\sigma = 0$ , lower values of the adjustment angles  $\varphi_1$  and  $\varphi_2$  lead to greater geometric stability.

In the impact diagram based on the angular analysis of the hodograph, under some level of system instability, it is also observed that smaller adjustment angles  $\varphi_1$  and  $\varphi_2$  provide greater geometric stability and should lead to improved surface roughness on a dynamically stable machine. In particular, there is a constant local depression about  $\varphi_2 = 173^\circ$  ( $\gamma = 7^\circ$ ), which may be the most optimal condition for centerless grinding. There are several local minima in the diagram, which indicate the presence of several acceptable geometric debugging conditions that provide regulated waviness of the detail.

If the machine is dynamically stable from the point of view of vibration, then according to the general diagram of geometric stability, it is possible to predict trends of final waviness parameters based on the geometry of adjustment of rigid supports at centerless mortise grinding. The results of this study create the preconditions for controlling the parameters of the waviness of bearing detail. It will stabilize bearing parameters such as noise and vibration.

## References

1. Yue, Q., Li, L., Zhang, X. (2023). Failure mechanism and bearing capacity analysis of the underpinning structure with relative displacement. *Engineering Failure Analysis*, Vol. 148, 107205, <https://doi.org/10.1016/j.engfailanal.2023.107205>
2. Gu, Q., Deng, Z., Lv, L., Liu, T., Teng, H., Wang, D., Yuan, J. (2021). Prediction research for surface topography of internal grinding based on mechanism and data model. *International Journal of Advanced Manufacturing Technology*, Vol. 113(3-4), pp. 821-836, <https://doi.org/10.1007/s00170-021-06604-7>
3. Zhao, B., Wang, X., Ding, W., Wang, Y., Fu, Y., Zhao, Y., Zhu, J. (2023). Grain erosion wear properties and grinding performance of porous aggregated cubic boron nitride abrasive wheels. *Chinese Journal of Aeronautics*, <https://doi.org/10.1016/j.cja.2022.08.005>
4. Wu, Z., Zhang, L. (2023). Analytical grinding force prediction with random abrasive grains of grinding wheels. *International Journal of Mechanical Sciences*, Vol. 250, 108310, <https://doi.org/10.1016/j.ijmecsci.2023.108310>
5. Kishore, K., Sinha, M. K., Chauhan, S. R. (2023). A comprehensive investigation of surface morphology during grinding of Inconel 625 using conventional grinding wheels. *Journal of Manufacturing Processes*, Vol. 97, pp. 87-99 <https://doi.org/10.1016/j.jmapro.2023.04.053>
6. Chalyj, V., Moroz, S., Ptachenchuk, V., Zablotskyj, V., Prystupa, S. (2020). Investigation of waveforms of roller bearing's working surfaces on centerless grinding operations. In: *Ivanov V. et al. (eds) Advances in Design, Simulation and Manufacturing III. DSMIE 2020. Lecture Notes in Mechanical Engineering, Springer, Cham*, Vol. 1, pp. 349-360, [https://doi.org/10.1007/978-3-030-50794-7\\_34](https://doi.org/10.1007/978-3-030-50794-7_34)
7. Kalchenko, V., Yeroshenko, A., Oyko, S. (2017). Mathematical modeling of abrasive grinding working process. *Naukovyi Visnyk Natsionalnoho Hirnychoho Universytetu*, Vol. 6, pp. 76-82.
8. Zhang, X.-M., Zhang, Q.-J. (2010). Research on the simulation of centerless grinding process. *Proceedings of the 29th Chinese Control Conference*, Vol. 2010, pp. 5310-5313.
9. Chunjian, H., Qiuju, Z., Yubing, X. (2010). Research on the computer simulation technique of cylindrical centerless grinding process. *2010 Second International Workshop on Education Technology and Computer Science*, pp. 431-433, <https://doi.org/10.1109/ETCS.2010.551>
10. Yang, H., Zhang, L., Li, D., Li, T. (2011). Modeling and analysis of grinding force in surface grinding. *2011 IEEE International Conference on Computer Science and Automation Engineering*, pp. 175-178, <https://doi.org/10.1109/CSAE.2011.5952448>
11. Zablotskyi, V., Tkachuk, A., Prozorovskyi, S., Tkachuk, V., Waszkowiak, M. (2022). Influence of turning operations on waviness characteristics of working surfaces of rolling bearings. In: *Ivanov, V., Trojanowska, J., Pavlenko, I., Rauch, E., Peraković, D. (eds) Advances in Design, Simulation and Manufacturing V. DSMIE 2022. Lecture Notes in Mechanical Engineering. Springer, Cham*, pp. 345-354, [https://doi.org/10.1007/978-3-031-06025-0\\_34](https://doi.org/10.1007/978-3-031-06025-0_34)
12. Shah, H., Taha, E. H. (2022). Busemann functions in asymptotically harmonic Finsler manifolds. *Journal of Mathematical Physics, Analysis, Geometry*, Vol. 18(4), pp. 546-561, <https://doi.org/10.15407/mag18.04.546>
13. Zhuang, J., Cao, Y., Jia, M., Zhao, X., Peng, Q. (2023). Remaining useful life prediction of bearings using multi-source adversarial online regression under online unknown conditions. *Expert Systems with Applications*, Vol. 227, 120276, <https://doi.org/10.1016/j.eswa.2023.120276>
14. Gabor, M., Zdunek, R., Zimroz, R., Wodecki, J., Wylomanska, A. (2023). Non-negative tensor factorization for vibration-based local damage detection. *Mechanical Systems and Signal Processing*, Vol. 198, <https://doi.org/10.1016/j.ymsp.2023.110430>
15. Chen, J., Lin, C., Yao, B., Yang, L., Ge, H. (2023). Intelligent fault diagnosis of rolling bearings with low-quality data: A feature significance and diversity learning method. *Reliability Engineering and System Safety*, Vol. 237, <https://doi.org/10.1016/j.res.2023.109343>
16. Bai, X., Zeng, S., Ma, Q., Feng, Z., An, Z. (2023). Intelligent fault diagnosis method for rolling bearing using WMNRS and LSSVM. *Measurement Science and Technology*, Vol. 34(7), <https://doi.org/10.1088/1361-6501/acc3b9>
17. Zhu, D., Yin, B., Teng, C. (2023). An improved spectral amplitude modulation method for rolling element bearing fault diagnosis. *Journal of the Brazilian Society of Mechanical Sciences and Engineering*, Vol. 45(5), <https://doi.org/10.1007/s40430-023-04184-z>
18. Chen, S., Xie, B., Wang, Y., Wang, K., Zhai, W. (2023). Non-stationary harmonic summation: A novel method for rolling bearing fault diagnosis under variable speed conditions. *Structural Health Monitoring*, Vol. 22(3), pp. 1554-1580, <https://doi.org/10.1177/14759217221110278>
19. Lin, S., Jiang, S. (2022). Rotordynamics of an improved face-grinding spindle: Rotational stiffness of thrust bearing increases radial stiffness of spindle. *Journal of Manufacturing Science and Engineering, Transactions of the ASME*, Vol. 144(8), <https://doi.org/10.1115/1.4053458>
20. Zmarzły, P. (2022). Analysis of technological heredity in the production of rolling bearing rings made of AISI 52100 steel based on waviness measurements. *Materials*, Vol. 15(11), <https://doi.org/10.3390/ma15113959>
21. Brosed, F. J., Zaera, V. A., Padilla, E., Cebrián, F., Aguilar, J. J. (2018). In-process measurement for the process control of the real-time manufacturing of tapered roller bearings. *Materials*, Vol. 11(8), <https://doi.org/10.3390/ma11081371>



Halchuk T. N., Povstyanoy O. Yu., Bembenek M., Redko R. G., Chetverzhuk T. I., Polinkevych R. M. (2023). *Impact of technological system's characteristics on the machining accuracy of bearing rings*. *Journal of Engineering Sciences*, Vol. 10(1), pp. A22-A30, doi: 10.21272/jes.2023.10(1).a4

## Impact of Technological System's Characteristics on the Machining Accuracy of Bearing Rings

Halchuk T. N.<sup>1</sup>[0000-0003-3474-9848], Povstyanoy O. Yu.<sup>1\*</sup>[0000-0002-1416-225X], Bembenek M.<sup>2</sup>[0000-0002-7665-8058], Redko R. G.<sup>1</sup>[0000-0001-5066-0224], Chetverzhuk T. I.<sup>1</sup>[0000-0002-4445-4632], Polinkevych R. M.<sup>1</sup>[0000-0002-4243-5585]

<sup>1</sup> Lutsk National Technical University, 75, Lvivska St., 43018 Lutsk, Ukraine;

<sup>2</sup> AGH University of Science and Technology, 30, Adama Mickiewicza Ave., 30-059, Krakow, Poland

### Article info:

Submitted: March 2, 2023  
 Received in revised form: April 28, 2023  
 Accepted for publication: May 30, 2023  
 Available online: June 5, 2023

### \*Corresponding email:

[povstjanoj@ukr.net](mailto:povstjanoj@ukr.net)

**Abstract.** The article shows the influence of the technological system of an automated lathe, in particular cam chucks, on the accuracy of machining bearing rings for production conditions. The value of the deformation during machining, i.e., the non-circularity of the ring of a single row tapered roller bearing 32017X in outer diameter, was investigated. For the study, samples were selected that were processed under the same conditions directly in the production unit of PJSC "SKF Ukraine" without interference with the technological process. The use of replaceable floating cams in the chuck design was proposed to increase the accuracy and productivity of machining. Experimental studies have shown that the machined surface's ovality depends on the chuck cams' clamping force. The effectiveness of computer processing of statistical data on the accuracy control of engineering products was shown. Implementing machining accuracy control in production using the Minitab computer program was presented. It was proven that the quality of products is formed under the influence of the use of modern computer technologies at all stages of manufacturing and control of parts, which ensures research in a wide range of changes in technological parameters and comparison of individual studies with actual machining conditions on the machine, with the results of a sufficient level of reliability.

**Keywords:** turning, machining errors, production, workpiece, cam chuck, product innovation.

## 1 Introduction

In modern mechanical engineering, the requirements for improving machining accuracy are constantly growing, and the problems of achieving accuracy are characterized by extreme multifactorial. A number of factors practically do not change in the process of processing: deformation of the workpiece and elements of the technological system under the influence of fastening forces; errors of the base surfaces of the workpiece and its installation on the machine; errors in the manufacture and installation of the tool; geometric errors of the machine. Other factors change significantly in the processing under the influence of variable forces, variable stiffness, changes in temperature conditions, and parameters of cutting and friction processes [1, 2].

Machining of bearing rings on turning operations is associated with the deflection of machined surfaces under the cutting and fixing forces with the subsequent formation of related processing errors. During the clamping of thin-walled rings in the chucks, the deformation of the workpiece is formed, which depends, in particular, on the number of points of application of force and the magnitude of the clamping force. The part is compressed, and at the points of mechanical contact in the material, there are increased stresses caused solely by changes in the wall thickness of the workpiece. This leads to a processing error of the ring - non-roundness. The roundness of the rings affects the performance. In particular, it reduces the durability of rolling bearings several times [3]. The magnitude of this error depends on the number of cams and the extent to which the shape of their clamping surface approaches the shape of the part.

The more cams and their clamping surface corresponds to the shape of the part, the smaller the error will be.

Moreover, even with perfectly correct machining, the part after removing from the machine, as a result of relaxation of stresses in the metal, acquires a cut (partial case of non-roundness) with the number of faces by the number of cams. To reduce it, choosing a suitable scheme of installation and fastening of workpieces is necessary, which primarily ensures the accuracy of the final processing of parts and increases the productivity of metalworking [4]. In these conditions, the problem of identifying reserves to improve the accuracy of machined surfaces is actual, in particular, the rings of roller bearings during their manufacture in automated production.

The study aims to ensure the accuracy of turning bearing rings due to the selection of the optimal cartridge design for production conditions.

## 2 Literature Review

A review of literature sources is engaged in researching and describing this problem [5, 6]. Their works are devoted to research on analytical calculations of machining error, ensuring the accuracy of cutting parts, improving the accuracy of machines, developing and testing clamping structures, and their drives for fixing and processing non-rigid parts. However, at the same time, it is essential to study the accuracy of operations for the conditions of a particular production. Machining of products with a given accuracy and surface quality depends not only on the machine tool but also on the entire technological processing system (TPS). The tool, workpiece, chuck, and cutting modes are included in the TPS [7]. For the most part, errors due to deformations of the TPS make up a significant part of the overall machining error. In particular, it is advisable to consider in more parts the error due to the clamping force of the workpiece. These forces cause elastic deformations of the workpieces, which generates errors in the shape of the processed workpieces.

Large deformations can occur when clamping thin-walled, non-rigid workpieces such as rolling bearing rings. Non-roundness rings can reduce the service life of rolling bearings by several times. To reduce the error, choosing the correct installation and clamping scheme for the workpieces is necessary. The amount of error also depends on the number of cams and how close the shape of their clamping surface is to the shape. The above allows us to conclude that roughing and finishing machining should be performed for precision parts. Furthermore, take measures to reduce the machining error, which is essential for finishing operations and roughing.

One of these factors in improving the quality of parts is the timely elimination of errors during machining. This problem can be solved by identifying reserves for improving the accuracy of machined surfaces. This can be done by introducing analytical processing with the

help of quality management software, detection, and avoiding errors in manufacturing various products.

In [8], a dynamic model of a flexible rotor supported by ball bearings with rubber damping rings was proposed by combining the finite element and the mass-centralized method. In the proposed model, the rotor was built with the Timoshenko beam element, while the supports and bearing outer rings were modeled by the mass-centralized method.

To verify the correctness of the modeling method [9, 10], theoretical and experimental analysis is carried out by a rotor-bearing test platform, where the error rate between the theoretical and experimental studies is less than 10 %. Besides that, the influence of the rubber damping ring on the dynamic properties of the rotor-bearing coupling system was also analyzed.

This paper [11] presents a practical approach for failure mode prediction using multiple sensors installed in a bearing ring grinder for process control and condition monitoring.

A number of researchers have studied the design of clamping chucks for fixing and machining non-rigid parts [12, 13]. It has been established that all clamping chucks for fixing such parts are made with clamping elements made precisely to the diameter of the clamp and have systems for distributing forces between the cams. When choosing any design of a clamping chuck, it is necessary to solve the problem of finding the distributed loads in its elements. In addition, it is also necessary to know the displacement values of individual points of the selected design, both under static external loads and under variable loads.

The process of mechanical processing of bearing rings creates a surface layer of plastically deformed material, which acts as a source of residual stresses in the cross-section of the workpiece. These stresses significantly impact the physical, mechanical, and chemical properties of the surface layer of the workpiece. During mechanical processing, plastically deformed material from the previous stages of production is removed, which causes deformation of the blank of the bearing rings. At the next stages of production, residual stresses and shape deviations during mechanical processing can affect the deformation of the workpiece.

In addition, clamping forces lead to elastic deformation of the ring. In the case of a 3-jaw cartridge, the triangle occurs after unzipping. Basically, these shape deviations depend on the clamping forces and the number of cams [8, 9]. Elastic deformations due to chuck clamping affect the stability of processing [10-12].

The structure of the pattern recognition process will be introduced, this includes the signal pre-processing, the selection of the most suitable features for this specific application using Minitab [13].

In particular, the determination of deformations of the part in the process of roughing and the definition of indicators that reduce the impact of the error of deformation of the workpiece on the accuracy of processing.

### 3 Research Methodology

For bearing rings, high requirements are set for the geometric shape after turning. Parameters such as the inconsistency of the inner diameter of the ring, the angle of the inner diameter, the inconsistency of the outer diameter and its conicity, the inconsistency of the width of the ring, as well as deviations from the roundness of the shape (the ring cut) are controlled. When the thin-walled ring is fixed in the cartridge, its elastic deformation occurs, which causes a form error in the processing process, both in roughing and finishing operations. The part will examine the technological heredity, and the geometric shape in cross-sections obtained after the processing stage. Therefore, it is essential to minimize the value of the deviation of the roundness of the bearing ring shape not only during grinding but also during turning.

To determine the amount of deformation of the part during machining, it was decided to investigate the accuracy of the shape of the ring of the roller bearing on the outer diameter - the cut that occurs after turning. The bearing ring, the machining of which was studied, is a ring of single-row roller tapered roller bearing 32017X, manufactured by PJSC "SKF Ukraine". The bearing consists of two clips (outer and inner) and bodies of rotation (conical rollers) connected by a separator (Figure 1a).

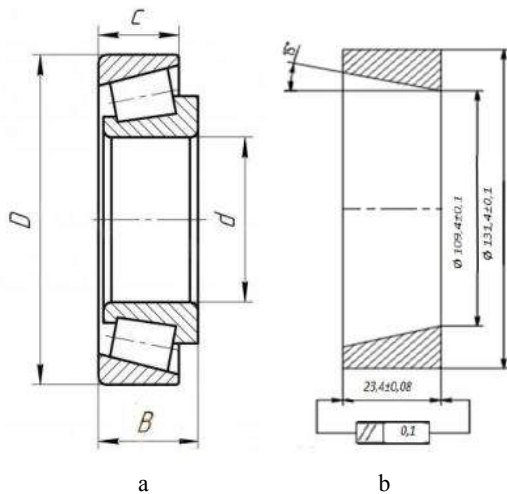


Figure 1 – The design scheme: a – bearing 32017X; b – layout of the ring

The outer diameter of the bearing  $D = 130$  mm, the inner diameter  $d = 85$  mm, the total height  $B = 29$  mm, and the height of the holder  $C = 22$  mm.

Bearing 32017X is used in the automotive industry of trucks, e.g., models of Mercedes-Benz (Atego, Atego 2), Fiat, MAN, Renault, Volvo, and Isuzu. The billet ring is made by forging (Figure 1b) from steel grade SHKH15SG DSTU 4738:007.

Parts with the set roundness on external diameter were used for tests:  $0.27$  mm – 5 pieces. Each workpiece in the dividing head was divided into 12 numbered parts. A thin-walled workpiece with a diameter of  $130^{+0.5}$  mm (Figure 1b) was installed in the expanded cartridge and clamped by axial forces  $P_0 = 25$  kN to check the accuracy of the centering of the workpiece when an axial force pressed it. From the rear headstock side of the lathe, through the dynamometer DS-10, the workpiece was loaded with this effort, which simulated the axial component of the cutting forces, respectively 50, 100, 200, 300, and 400 N.

The experiment used a turning three-jaw chuck with pneumatic cylinder pistons  $\text{Ø}150$  mm and  $\text{Ø}95$  mm and a floating six-jaw chuck with a pneumatic cylinder piston  $\text{Ø}95$  mm (Figure 2a-b) mounted on a machine 1B265NP-6K (Figure 2c), characterized by high requirements serial production. As a result of research, it was necessary to establish the best variant of a cam cartridge that would provide the minimum deformation of preparation.

To determine the amount of deformation of the part during machining, it was decided to investigate the accuracy of the shape of the bearing ring in terms of outer diameter. The test parameter of the shape deviation is not roundness but rather its special case of faceting, which occurs after turning the ring when it is clamped in a turning chuck. The parts for the study were selected directly in the production unit - the turning department of PJSC "SCF Ukraine" in the order of processing without interference with the process. All parts were processed under the same machining conditions, without cooling and with the same clamping force in the chuck [16, 17].

For the study, samples of rings were taken:

- sequentially, at regular intervals;
- with the same number of parts in the group;
- with covering as many specific causes of variability as possible.

Groups of parts with the same number of 130 pieces each were studied. The parts were selected after turning with clamping in a 3-jaw chuck with a pneumatic cylinder with piston diameters of  $\text{Ø}150$  mm and  $\text{Ø}95$  mm and a floating 6-jaw chuck with a pneumatic cylinder with a piston diameter of  $\text{Ø}95$  mm. The measuring system described above was used for the measurements.

Measurements of the characteristics of the groups of parts were carried out in the sequence of their selection. All parts under study were stored until the statistical evaluation was completed.

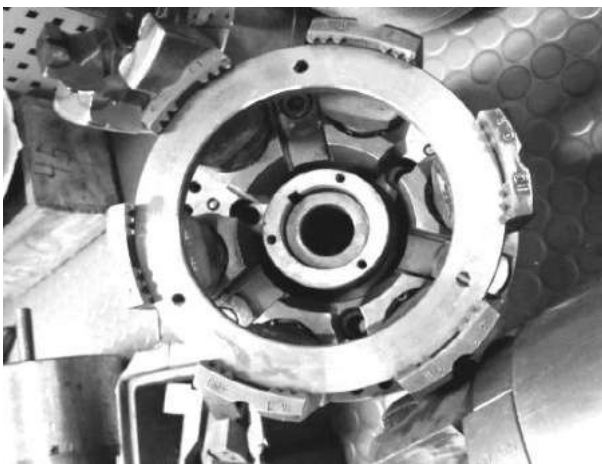
For further data analysis, we additionally recorded:

- the start and end time of data collection;
- each intervention in the process of processing parts;
- all stops in the operation of the equipment;
- shift(s)/operator(s);
- unexpected interruptions in the machining process;
- change of workpiece batch.





a



b



c

Figure 2 – Clamping of a ring preparation: a – 3 cam cartridges; b – 6-cam lathe chuck; c – general view of the machine 1B265NP-6K

#### 4 Results

Fixing of the workpiece in the cartridges was performed 10 times because the cut has a practical effect on the diameter measurement and may give an erroneous result during the measurement, affecting the actual size of the part during its manufacture. Therefore, it is necessary to rotate the workpiece to measure the correctness of the

shape. When measuring the size of the ring, there is a difference between the measured and the actual size for any odd number of faces, so the deviation of the shape of the part can significantly affect its size, measured by the usual method. Determining the correctness of the shape requires measuring the instability – the cut, which is expressed by regularly recurring inequalities. This is especially important to ensure the required accuracy because the cut is essential to any machine tooling [14].

After each clamp, the workpiece was drilled on a machine 1B265NP-6K with a cutting depth  $t = 0.5$  mm, speed  $n = 378$  rpm, and feed  $S = 0.3$  mm/rev. In the process of machining parts, ensuring compliance with the form is almost impossible, so during the control of the outer diameter of the ring was used the method of control using microcator IGPV and installation of the ring in the device PP-1M, which guarantees measurement accuracy (Figure 3).

The IHPV microcator is inserted into the spring measuring head. This gives advantages during the measurement (absence of “dead running” and low friction in the links of the mechanism). Thus, the measuring system used for the measurements was acceptable.

The cut of the workpiece was measured at 12 points on the outer diameter (Figure 4). The roundness of the treated surface was up to 0.15 mm [15]. The obtained values of deviations are within the tolerance and, in some cases, significantly smaller than those provided on the control chart (Table 1).



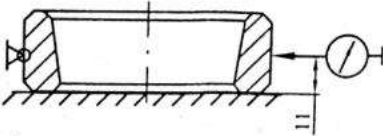
a



b

Figure 3 – General view: a – device PP-1M; b – measuring the bearing ring cut

Table 1 – Accuracy control chart for turning the outer ring of the bearing

Measuring scheme	Measuring mean	Parameters		
		Name	Abbreviation	Tolerance, mm
	PP-1 10IHPV	T-shape deviation-cut	V3D	0.27

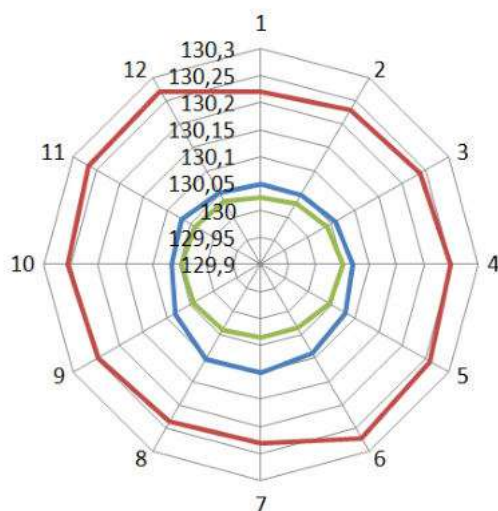


Figure. 4 – Cut the ring at 12 points

- Ø95 mm 3-jaw chuck;
- Ø150 mm 3-jaw chuck;
- Ø95 mm 6-jaw chuck

At the production site, 3 batches of workpieces were sampled with a sample of 130 pieces each, machined on a lathe with clamping in cam chucks of different types. The sample size for the batch of ring blanks is shown in Table 2.

Table 2 – the batch of ring blanks

Lathe chuck	Minimum cut value, $\mu\text{m}$	Maximum cut value, $\mu\text{m}$	Span of the sample, $\mu\text{m}$
3-jaw chuck with 95 mm piston	40	110	60
3-jaw chuck with 150 mm piston	210	290	80
6-jaw chuck with 95 mm piston with replaceable floating cams	20	80	60

After the measurements were taken, the calculations were carried out using the Minitab computer program. Based on the research data, graphs were drawn, one showing the difference between the values of the previous and next samples (a batch of 5 consecutive measured parts), and the absolute value is taken (Figure 5a).

In another graph (Figure 5b), the total number of measurements is also divided into samples of 5 parts, but the difference between the maximum and minimum measurement values is taken from each sample (for example, the processed data for 3-jaw cartridges with piston diameters of 95 mm and 150 mm are shown).

The statistical analysis of the data shows that, according to the criteria of statistical uncontrollability, the production of the ring machining accuracy in the turning operation is maximized when it is clamped in a 6-jaw chuck with a 95 mm piston with replaceable floating cams (Table 3).

Table 3 – Criteria for statistical unmanageability

Criteria for statistical unmanageability	Lathe chuck		
	3-jaw chuck with 95 mm piston	3-jaw chuck with 150 mm piston	6-jaw chuck with 95 mm piston*
Point beyond / on the border of the control boundary	2	1	–
Consecutive dots above or below the midline	5	4	2
The upward or downward trend of consecutive dots	6	4	3
Consecutive dots are close to the midline	6	7	11

\* with replaceable floating cams.

For work using the Minitab program, we filled in:  
 – for the map of medians X-maps of ranges R (Figure 6a);  
 – the map of individual values of X-maps of displaced ranges mR (Figure 6b).

The actual deviations of the controlled parameter are as close as possible to the middle of the tolerance field. However, there are cases when unusual curve behavior is detected (both on the R-value/shifted mR map and on the X-value/individual X-value map), characterized by one or more criteria of statistical uncontrollability of the process. For example, in Figure 5, there are cases (marked in red) when the measured value exceeds the values provided by the scale, particularly for workpieces fixed in a 3-jaw chuck with a piston diameter of 150 mm. This indicates the need for immediate intervention in the technological process [18].

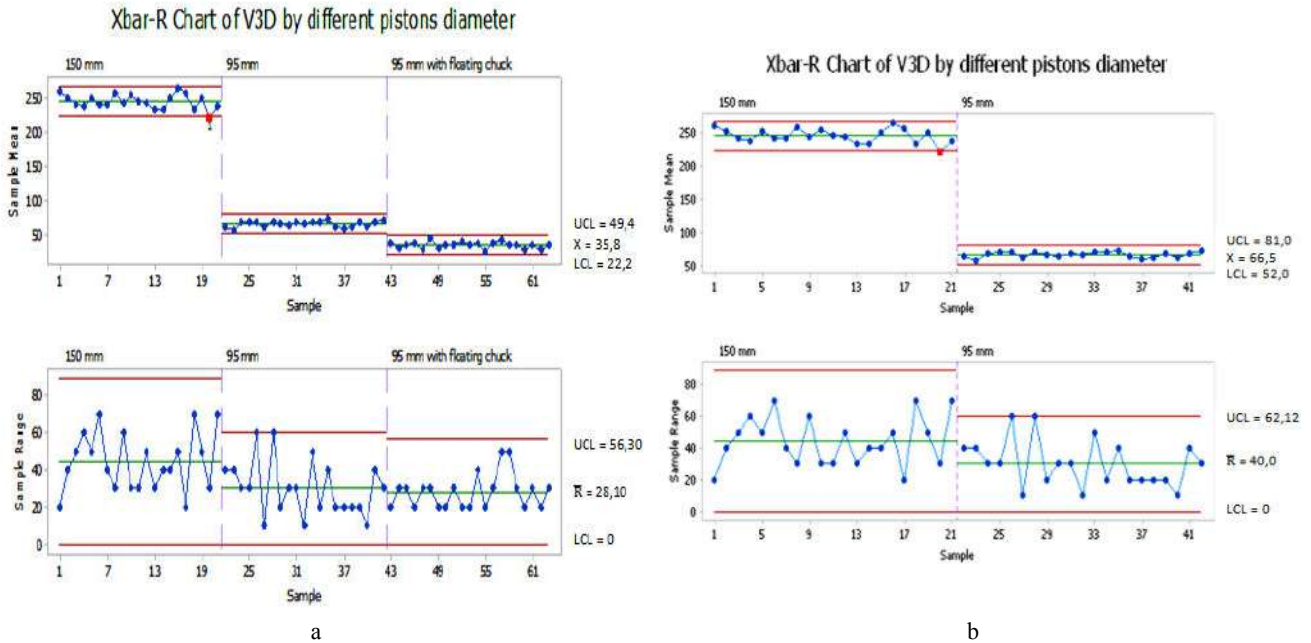


Figure 5 – Probability plots for the study of faceting considering the absolute value (a) and the total number of measurements (b)

In order to prevent such phenomena, shortcomings have been identified, and many recommendation measures have been developed to improve the accuracy of turning.

Potential cause of mechanical failure:

- 1) clamping force is significantly higher than required;
- 2) incorrectly adjusted pressure in the hydraulic system;
- 3) imperfect design of the chuck for clamping non-rigid rings.

Recommendations for elimination cause of mechanical failure:

- 1) use lathe chuck for new designs;
- 2) replace pistons with a diameter of 150 mm with 95 mm;
- 3) use a chuck design with a uniform clamping force (floating cams).

## 5 Discussion

After analyzing the obtained experimental data, it can be argued that the workpiece in the three-cam cartridge takes a triangular shape, and during the clamp in the 6-cam - hexagonal. Thus, the part obtained after turning will acquire some technological inheritance due to the deformation forces arising during the clamping of the workpiece in the device, which will inevitably affect both the accuracy of finishing and the accuracy and quality of the finished product.

Up to 30 % of the non-roundness of the turning surface treated by turning can be transferred to the finished surface by grinding for the wall thickness of the workpiece within 9 mm. Tests in machining with high cutting forces were performed on manufactured in the amount of 3 parts with increased allowance (cutting depth – 2.5 mm, feed – 0.3 mm/rpm, spindle speed of the machine – 376 rpm, and pressure in the hydraulic system – 10–15 kg/cm<sup>2</sup>), cutting workpieces before turning is 0.5 mm.

Various designs of clamping cartridges are used for processing parts [1, 4]. In the conditions of automated production of turning chucks, it is necessary to ensure high accuracy and productivity of turning processing [21-24]. In some literature and patent sources, there is insufficient data on the influence of cartridge parameters on the processing error. Using chucks with floating jaws for clamping the workpiece, which also uses a Ø95 mm piston, is advisable. This allows reducing the number of passes, thereby reducing the processing time.

The obtained deviation values are within the tolerance range, and in some cases, the values are significantly lower than those provided by the scale of the sample range. As a result, losses due to defects are reduced by 0.2 % due to increased stability and reliability of fixing parts, and increased processing accuracy.

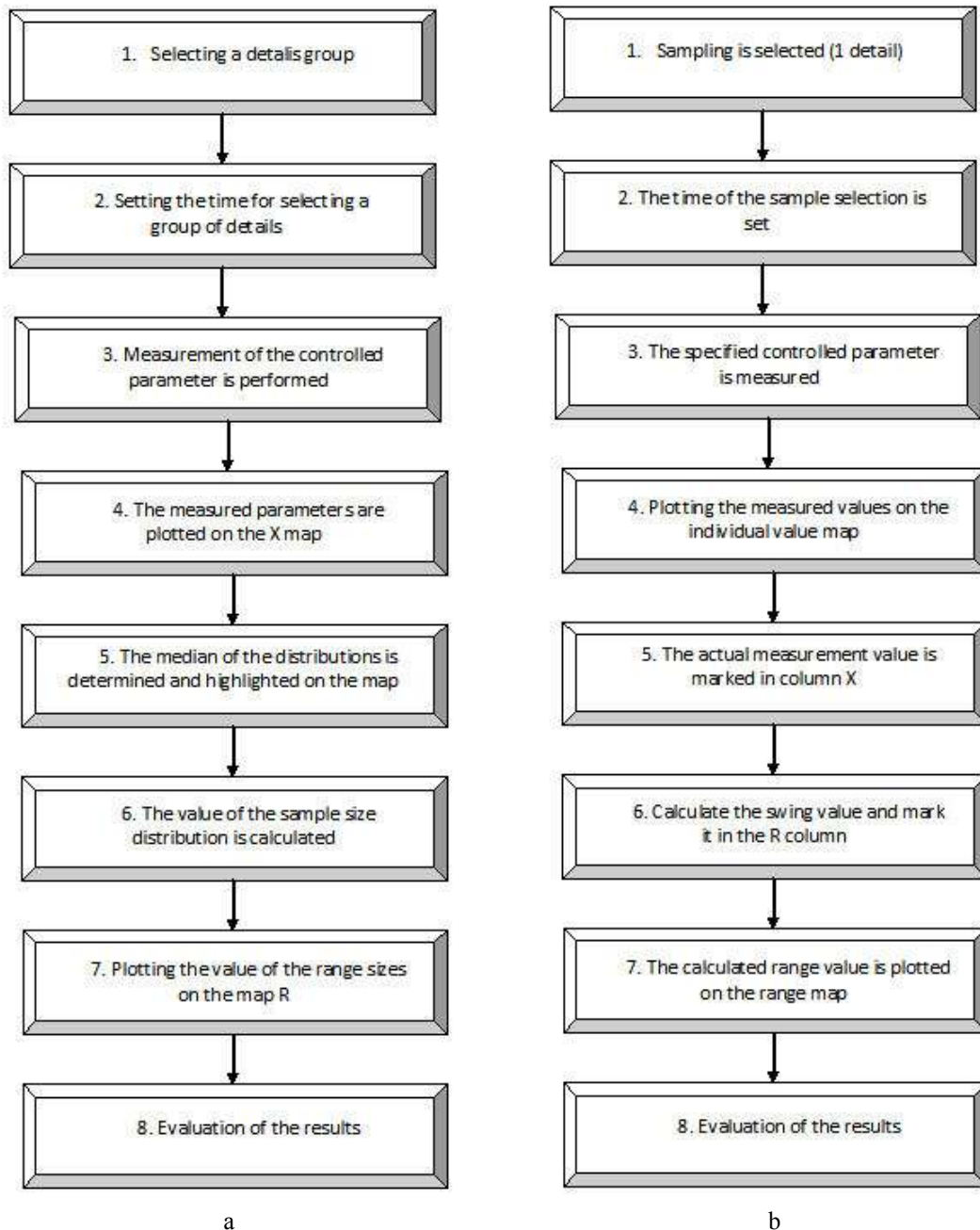


Figure 6 – Sequence of filling: a – map of medians for  $\bar{X}$ -map of ranges R; map of individual values for X-map of shifted ranges mR

## 6 Conclusions

To increase the accuracy of machining the outer ring of single-row roller tapered roller bearing 32017X on automated lathes for the conditions of PJSC “SKF Ukraine” it is proposed to use replaceable floating cams in the chuck design.

Based on the analysis of experimental and production tests, it was found that the ovality of the treated surface depends on the clamping force on the cams of the chuck. This is determined by the fact that lower clamping forces reduce the friction forces through which the cams move differently, and there is a deformation of the part's surface. In this regard, it is recommended to carry out

machining with the minimum clamping forces of the workpiece (25 kN), which are allowed by the cutting force. The stability of centering the workpiece is 0.04–0.05 mm. The best cut size and roundness results are obtained when clamping the workpiece in the piston chuck of a pneumatic cylinder with Ø95 mm.

For chucks with 6 floating cams for clamping the workpiece, which uses a Ø95 mm piston, the obtained values of the deviations of the cut are within tolerance (0.27 mm), and in some places, the values are significantly smaller (up to 0.15 mm) than those provided by the scale sample size. The shape accuracy achieved during the installment is higher in a 6-cam chuck with replaceable floating cams than in a three-cam chuck

under the same machining conditions. It was established that up to 30 % of the out-of-roundness of the turned surface could be transferred by grinding the finished surface with a workpiece wall thickness of 9 mm.

The studied quality of bearing ring machining was formed by modern computer technologies, which is especially important for flexible automated engineering production. The accuracy parameters of successively processed parts were checked to confirm the correctness of the machine setup and to establish optimal machining

modes (cutting depth – 2.5 mm, feed – 0.3 mm/rpm, spindle speed of the machine – 376 rpm). The actual deviations of the monitored parameters obtained are as close as possible to the middle of the dimensional tolerance field.

Experimental studies can be used to ensure and stabilize the accuracy of the shape of roller bearing rings in turning operations for the conditions of the enterprise PJSC “SCF Ukraine”.

## References

1. Lee, S. H., Lee, H. J., Lee, K. H. et al. (2020). A novel variable stiffness scotch yoke series elastic actuator for enhanced functional stiffness. *Microsyst Technol*, Vol. 26, pp. 3395-3402, <https://doi.org/10.1007/s00542-020-04893-8>
2. Marchuk V., Mykhalevytch V. (2008). Deviation of the shape of surfaces and their influence on the dimensional accuracy of bodies of rotation. *Scientific Notes: Interuniversity Collection. Series “Engineering Mechanics”*, Vol. 23, pp.197-202.
3. Raghu, A., Melkote, S. N. (2005). Modeling of workpiece location error due to fixture geometric error and fixture-workpiece compliance. *J. Manuf. Sci. Eng.*, Vol. 127(1), pp. 75-83, <https://doi.org/10.1115/1.1828052>
4. Alquraan, T., Kuznetsov, Y., Tsyvd, T. (2016). High-speed clamping Mechanism of the CNC lathe with compensation of centrifugal forces. *Procedia Engineering*, Vol. 150(2016), pp. 689-695, <https://doi.org/10.1016/j.proeng.2016.07.081>
5. Kuznetsov, Y.M., Lutsiv, I.V., Shevchenko, A.V., Voloshin, V.N. (2011). *Technological Equipment for High Speed and a Precision Machining on Lathes*. Technograph, Kyiv, Ukraine.
6. Gal’chuk, T. (2017). Computer processing of static information accuracy control products of mechanical engineering computer-integrated technologies. *Education, Science, Production*, Vol. 26, pp.42-47.
7. Yuze, M., Liqin, W., Chi, Z. (2018). Influence of ring deformation on the dynamic characteristics of a roller bearing in clearance fit with housing. *International Journal of Mechanical Sciences*, Vol. 138(139), pp. 122-130, <https://doi.org/10.1016/j.ijmecsci.2018.01.042>
8. Jang, G., Jeong, S.-W. (2004). Vibration analysis of a rotating system due to the effect of ball bearing waviness. *Journal of Sound and Vibration*. Vol. 269(3-5), pp. 709-726.
9. Sölter, J., Nowag, L., De Rocha, A., Walter, A., Brinksmeier, E., Hirsch, T. (2004). Einfluss von Maschinenstellgrößen auf die Eigenspannungszustände beim Drehen von Wälzlagering. *HTM*, Vol. 59(3), pp.169-175.
10. Bernatskyi, A., Sydorets, V., Berdnikova, O., Krivtsun, I., Chinakhov, D. (2020). Pore formation during laser welding in different spatial position. *Solid State Phenomena*. Vol. 303, pp.47-52, <https://doi.org/10.4028/www.scientific.net/SSP.303.47>
11. Dobrotvor, I., Stukhlyak, P., Mykytyshyn, A., et al. (2021). Influence of thickness and dispersed impurities on residual stresses in epoxy composite coatings. *Strength Mater*, Vol. 53, pp. 283-290, <https://doi.org/10.1007/s11223-021-00287-x>
12. Zhu, H., Chen, W., Zhu, R., et al. (2020). Dynamic analysis of a flexible rotor supported by ball bearings with damping rings based on FEM and lumped mass theory. *J. Cent. South Univ.*, Vol. 27, pp. 3684-3701, <https://doi.org/10.1007/s11771-020-4510-z>
13. Wang, H., Gong, J., Chen, G. (2017). Characteristics analysis of aero-engine whole vibration response with rolling bearing radial clearance. *Journal of Mechanical Science and Technology*. Vol. 37, pp. 2129-2141, doi: <https://doi.org/10.1007/s12206-017-0409-5>
14. Liu, X., Liu, Y., Wang, S., Yan, H., Liao, P. (2019). Bifurcation analysis of a magnetically supported rigid rotor in auxiliary bearings. *Chaos, Solitons & Fractals*, Vol. 118, pp. 328-336, <https://doi.org/10.1016/j.chaos.2018.11.034>
15. Ahmer, M., Sandin, F., Marklund, P., et al. (2022). Failure mode classification for condition-based maintenance in a bearing ring grinding machine. *Int J Adv Manuf Technol*, Vol. 122, pp. 1479-1495, <https://doi.org/10.1007/s00170-022-09930-6>
16. Kulišek, V., Kolar, P., Vrba, P., et al. (2021). On passive damping in machine tool hybrid structural parts. *Int J Adv Manuf Technol*, Vol. 114, pp. 1925-1952, <https://doi.org/10.1007/s00170-021-06865-2>
17. D’Emiliaa, G., Gasparia, A., Hohwielerb, E., Laghmouchib, A., Uhlmannb, E. (2018). Improvement of defect detectability in machine tools using sensor-based condition monitoring applications. *Procedia CIRP*, Vol. 67, pp. 325-331, <https://doi.org/10.1016/j.procir.2017.12.221>
18. Kocovic, V., Vukelic, D., Kostic, S., et al. (2023). Micro-cutting of holes by centrifugal force. *Int J Adv Manuf Technol*, Vol. 124, pp. 1437-1455, <https://doi.org/10.1007/s00170-022-10581-w>
19. Obertyukh, R., SlabkyiA., Polishchuk, L., Povstianoi, O., Kumargazhanova, S., Satymbekov, M. (2022). Dynamic and mathematical models of the hydroimpulsive vibro-cutting device with a pressure pulse generator built into the ring spring. *Informatyka, Automatyka, Pomiar w Gospodarce i Ochronie Środowiska*, Vol. 12(3), pp. 54-58, <https://doi.org/10.35784/iapgos.3049>

20. Povstyanoy, O., Zabolotnyi, O., Kovalchuk, O., Somov, D., Chetverzhuk, T., Gromaszek, K., Amirgaliyeva, S., Denissova, N. (2021). Analysis, development, and modeling of new automation system for production of permeable materials from machining waste. *Mechatronic Systems*, Vol. 1(2021), 12, <https://DOI:10.1201/9781003224136-14>
21. Maiß, O., Denkena, B., Grove, T. (2016). Hybrid machining of roller bearing inner rings by hard turning and deep rolling. *J. of Mat. Pr. Tech.*, Vol. 230, pp. 211-216.
22. Ma, C., Liu, J., Wang, S. (2020). Thermal contact conductance modeling of bearing outer ring/bearing housing interface. *International Journal of Heat and Mass Transfer*, Vol. 150, pp. 789-799, <https://doi.org/10.1016/j.ijheatmasstransfer.2019.119301>
23. Ruihong, J., Shulin, L., Youfu, T., Yinghui, L. (2015). A novel method of fault diagnosis for rolling element bearings based on the accumulated envelope spectrum of the wavelet packet. *Journal of Vibration and Control*, Vol. 21(8), pp. 1580-1593, <https://doi.org/10.1177/1077546313499391>
24. Fredriksson, M. J., Petersson, P., Axelsson C. S., Bylund, D. (2015). An automatic peak finding method for LC-MS data using Gaussian second derivative filtering. *Journal of Separation Science*, Vol. 32(22), pp. 3906-3918, <https://doi.org/10.1002/jssc.200900395>



*Stelmakh A., Kostyunik R., Mikosianchyk O., Kushchev A., Ibraimov T., Sydorenko O., Zaichuk N., Shymchuk S. (2023). Improvement of operational parameters for precision rolling bearings by cleaning working surfaces from micro pollution of various nature. Journal of Engineering Sciences, Vol. 10(1), pp. A31-A40, doi: 10.21272/jes.2023.10(1).a5*

## Improvement of Operational Parameters for Precision Rolling Bearings by Cleaning Working Surfaces from Micro Pollution of Various Nature

Stelmakh A.<sup>1,2</sup>[0000-0002-9132-6334], Kostyunik R.<sup>2</sup>[0000-0003-0232-9208], Mikosianchyk O.<sup>2</sup>[0000-0002-2438-1333],  
Kushchev A.<sup>2</sup>[0009-0003-9056-0123], Ibraimov T.<sup>2</sup>[0009-0003-1637-4541], Sydorenko O.<sup>2</sup>[0000-0002-3051-8703],  
Zaichuk N.<sup>3</sup>[0000-0001-6258-4820], Shymchuk S.<sup>3\*</sup>[0000-0002-1293-560X]

<sup>1</sup> Beijing Institute of Technology, 5, Zhongguancun St, Haidian Qu, China;

<sup>2</sup> National Aviation University, 1, Liubomyra Huzara Ave., 03058 Kyiv, Ukraine;

<sup>3</sup> Lutsk National Technical University, 75, Lvivska St., 43018 Lutsk, Ukraine

### Article info:

Submitted: February 28, 2023  
Received in revised form: May 4, 2023  
Accepted for publication: May 31, 2023  
Available online: June 6, 2023

### \*Corresponding email:

[s.shimchuk@lntu.edu.ua](mailto:s.shimchuk@lntu.edu.ua)

**Abstract.** In manufacturing high-precision rolling bearings for aviation and urban machinery, the key tasks are to reduce the cost of production of such products, increase their efficiency and resource, and ensure their reuse after performing appropriate repair work. The results of many years of research show that these tasks can be successfully solved by cleaning the working surfaces of the parts of such precision tribonodes by non-contact pulse methods, particularly by using variable electromagnetic fields. The article describes the process of deep cleaning the working surfaces of parts of various high-precision ball bearings (from overall to miniature). During this cleaning, ferromagnetic and other impurities in the form of micro-, sub-micro- and nanoparticles were removed on a developed stand that can be used on an industrial scale. Further studies of cleaned bearings showed improved operational parameters such as reduced noise and vibration and the degree of magnetization. To achieve the specified results, appropriate cleaning methods were developed and tested.

**Keywords:** miniature ball bearings, nanopollution particles, vibration speed, vibration acceleration, pulse-magnetic-turbulent cleaning, ultrasonic method.

## 1 Introduction

The performance, reliability, and resource of modern land and aviation equipment, technological machines, and various devices and equipment depend on the accuracy and quality of bearing assemblies and rolling bearings. In addition, with a high accuracy class of bearings, their final cleaning operations at manufacturing enterprises do not always ensure the declared quality. First, precise bearings of small sizes (including miniature ones) used in aircraft engineering and instrument-making fall into this problem. One of the ways to increase it is to increase the efficiency of removing production micro-, sub-micro- and nanoparticles caused by new bearings and operational parts, one of such types of nature [1, 2]. Along with rolling bearings, this approach is appropriate for precision parts of complex shapes, which are widely used in mechanical systems of aviation, space technology, the machine-building industry in general and engine-building industries. As in mechanical processinare while ensuring

the necessary accuracy of various types of parts and the quality of processed surfaces [3-5], effective cleaning of such micro metal products is not always ensured, which in the process of work worsens the occurrence of various types of unwanted noises and vibrations [6, 7], accelerates the initial surface wear and affects its naturey [8, 9].

Traditional cleaning methods are used to remove industrial contaminants from the working surfaces of machine parts and mechanisms. Today's most effective methods are based on ultrasonic waves, which cause cavitation in the liquid. This makes it possible to destroy the integrity of the pollution film and destroy them from the place of deposition in the zone of action of the flow of this medium. However, even such highly effective methods do not allow for the qualitative removal of micro- and nano-ferromagnetic particles of damage from bearing surfaces. The one-vector nature of the action of activating and destructive pollution fields and forces, the static nature of the cleaning object, and its design features

lead to the creation of certain areas of shading of working surfaces by structural elements. Based on this, the nature of micro- and nano-particle damage and the mechanisms of their retention by fairly massive ferromagnetic parts of ball bearings [10] are not sufficiently studied. However, appropriate practical monitoring and diagnostic possibilities are offered [11], which facilitates the collection of statistical data. Modern lubrication systems of aircraft engines include dozens and two ball bearings of an open type, the lubrication of which is implemented by circulating the lubricating fluid.

The requirements for the latter are extremely high. The size of the contamination particles must be less than 3  $\mu\text{m}$ , which meets the requirements of the 12th class according to the international purity classification for aviation lubricants. No less responsibility should be applied to plastic lubricants, which fasten bearings [12].

It is evident that during the assembly of, for example, a gas turbine engine, all parts, including non-dismountable ball bearings, must be subjected to pre-operational preparation, which aims to diagnose and maximally remove existing contaminants of various natures and sizes. Therefore, the problem of highly effective cleaning of ball bearings, working surfaces of precision spools, and distributors, which are part of the corresponding units and systems of precision devices, especially in aircraft engine construction, remains relevant not only during repairs but also during the manufacture and assembly of new units and nodes of gas turbine engines.

## 2 Literature Review

A thorough literature analysis shows that during the production and operation of machines and mechanisms, on the working surfaces and between the parts of the friction nodes, small particles of dirt are collected and accumulated, sticking to the edges of the seals, which can be separated from the liquid mechanically or with the help of force fields. In the first case, various filters are widely used for filtering working fluids. In the second, pollution particles are removed from fluids by gravitational, centrifugal, magnetic, electric, and other fields.

It is known that the deposition of small particles smaller than 10  $\mu\text{m}$  in a gravitational field can last several days, even with a small height of the liquid column.  $m$  of particles by tens and hundreds of thousands of times, carrying out a controlled filtration process. The results of experiments on removing micro-pollution from the working surfaces of miniature bearings show the weak effectiveness of these methods concerning micro-, sub-micro- and nano-sized pollution particles.

Currently, in addition to traditional methods of cleaning parts, such as cleaning with alkaline aqueous solvents [15], various solutions and compositions that allow cleaning of its parts and ball bearings without disassembling the mechanism before the scheduled replacement of lubricant [16], new technologies for cleaning surfaces from mechanical burrs are being

created, hydraulic methods, as well as using ultrasound [17].

Today's most common and effective methods are based on ultrasonic waves, which cause cavitation in the liquid. Nevertheless, even such highly effective methods sometimes fail to remove sub-micro dirt from ball bearings. The reason for this is the single-vector nature of the action of fields and forces that activate and destroy pollution, as well as the static nature of the cleaning object and its design features. This contributes to the formation of particular zones of shading of the working surfaces by structural elements and leads to the fact that it is challenging to clean ball bearings without detailed disassembly effectively, and when using non-disassemble ones, it is impossible.

There are ways and methods [18, 19] that realize the forced mutual movement of the structural elements of the bearing when creating ultrasonic vibrations in a constant flow of washing liquid. Forced contact rotation or movement reduces the time of action of the liquid on the working surfaces, and a complex mechanical drive can become a source of additional contamination. All these charges lead to the insignificant efficiency of such devices.

The most extensive are the theoretical and experimental ones, which reveal the malfunction of rolling bearings at the initial stage of their operation by analyzing the fluctuation of the amplitude of vibration signals [20] using the so-called performance indicators [21, 22] or using the methods of investigating bearing defects by electrical methods based on resonance [23]. However, such methods are more adapted to laboratory research and are very complex and not consistently effective for practical use and an actual increase in durability and service life of high-precision rolling bearings.

Almost all types of precision ball bearings design a small cross-section of gaps between elements, thin channels of the complex primary profile, and mutual overlap of working surfaces due to design features forming a unique set of problems, the solution of which requires a special approach.

## 3 Research Methodology

In modern tribotechnics, a special place is occupied by the problems of precise mechanics, in connection with which the requirements for their functionality, in addition to the standard requirements for the quality of wear resistance and anti-friction, are constantly increasing: in terms of noise level – in particular underwater, aviation and land systems and complexes; by the level of vibrations and noise – in highly sensitive electromechanical systems. At the same time, all rolling tribosystems are constantly being asked to increase their service life. Taking into account the experience of previous studies obtained in the course of scientific and research work, the team of authors developed a method and stand for cleaning the contacting surfaces of friction nodes, which is based on the idea of excitation and



removal of micro- and submicron-ferromagnetic particles by acting on them by pulsed variable magnetic fields, which remove them from the surfaces, move them, pulling them on themselves and keeping them in the zone of the fields of most significant stress. This method has been implemented in the technological process of cleaning aviation non-dismantling ball bearings of gas turbine engines at leading enterprises of the world level: “Ivchenko-PROGRES ZMKB”, OJSC “Motor Sich” (Zaporizhia), and repair plant “Motor” (Lutsk), as it has been repeatedly proven in industrial conditions, that the method of non-contact cleaning of the surfaces of rolling tribosystems with a source of pulsed magnetic-turbulent fields is the most effective in comparison with traditional mechanical and ultrasonic methods and gives a positive economic effect from its use.

Using the developed method and stand for pre-operational preparation of bearings (Figure 1), the mechanism of holding ferromagnetic micro- and submicron-particles on the surfaces of ferromagnetic parts by magnetic fields at the boundary of the domain grains was determined for the first time. The existing methods of cleaning the working surfaces of parts: ultrasonic, cavitation, and pulsating hydraulic are not effective enough because they do not consider the fundamentally different retention mechanisms of removing magnetically susceptible microparticles.



Figure 1 – Stand for pre-operational preparation of bearings: a – appearance of the stand; b – a chamber for cleaning and drying the ball bearings

Considering the high cost of special aviation bearings (from 100 USD to 15 000 USD) and their relatively high service life compared to the inter-repair service life of gas turbine engines (10–15 times), it is economically feasible to use them repeatedly, subject to appropriate pre-operational preparation with control of specific quality indicators, for example, by the general level of vibrations.

At the first stage of the study of the influence of micro- and nano-pollution on the performance and service life of miniature sliding ball bearings, modernized laboratory devices for determining the general level of vibration (Figure 2) are used as the primary operating characteristics of sliding bearings.

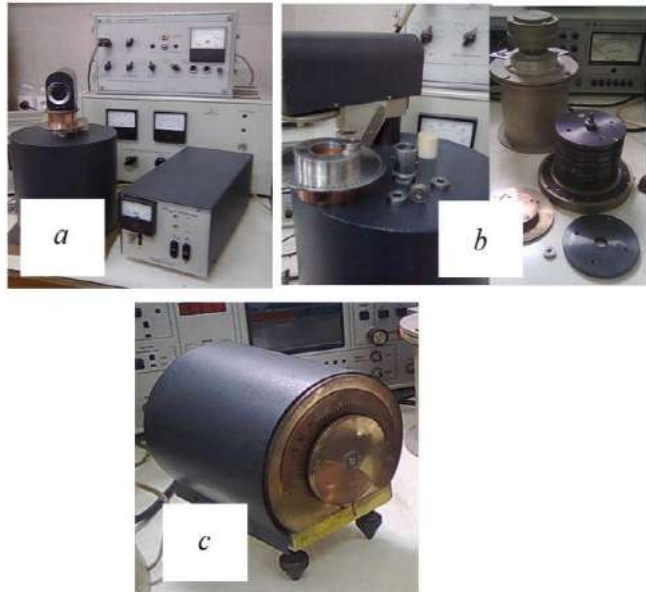


Figure 2 – The appearance of the laboratory stands for the assessment of the general level of vibration: a – the stand for vibration and noise studies; b – rolling device; c – a device for measuring the moment of friction

The laboratory complex allows for assessing vibration speed, acceleration, and friction moment in rolling tribosystems. The set of loading disks and mandrels, included in its composition, significantly expands the nomenclature of the investigated bearings.

The following requirements were established experimentally: the total vibration level of the bearings should not exceed 67 dB, and the friction moment at a rotation frequency of 1500 rpm and a radial load of 200 g should not exceed 0.23 N·mm.

After the preparatory work, the bearings are positioned in the appropriate order and undergo the pre-operational preparation operation, which includes cleaning and checking the vibration characteristics on the pre-operational preparation stand (Figure 1).

## 4 Results

### 4.1 Study of vibration characteristics

Since the general vibration level is a dynamic quantity with a relatively high level of oscillations, several experimental studies showed that vibration stabilization occurs after one minute of bearing operation at a normal load (Figure 3).

Notably, most researchers show vibrations in bearings as non-linear and non-stationary characteristics [24, 25].

Vibroacoustic characteristics were evaluated in the delivery state by the manufacturer and after cleaning and replacing the lubricant with a new one in 0.25 g for each ball bearing.

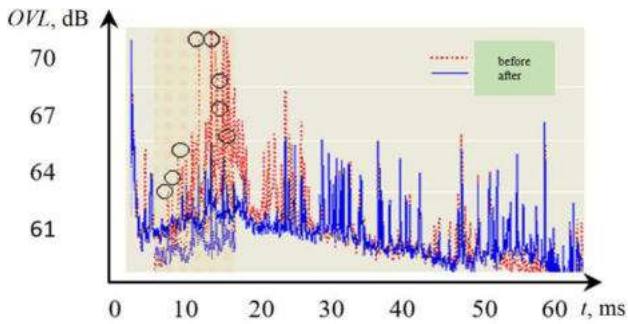


Figure 3 – Oscillograms of the general vibration level of ball bearings and their extremes (marked with a circle) before and after cleaning

Based on the results of measuring the friction moment and the general level of vibrations, the graphs shown in (Figures 4, 5) were drawn, which reveal the effect of cleaning and replacing the lubricant on the change in the MT friction moment and the average value of the overall vibration level (OVL).

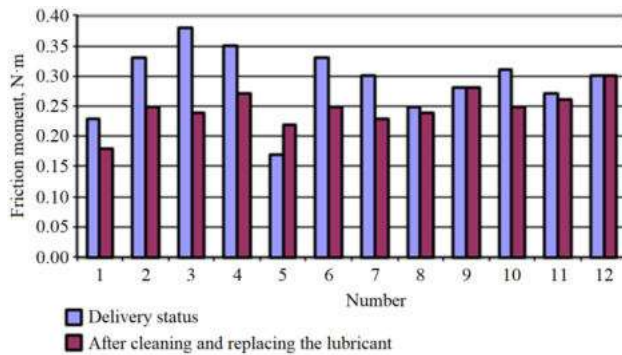


Figure 4 – The graph of the change in the friction moment of the MT after cleaning and applying a new lubricant

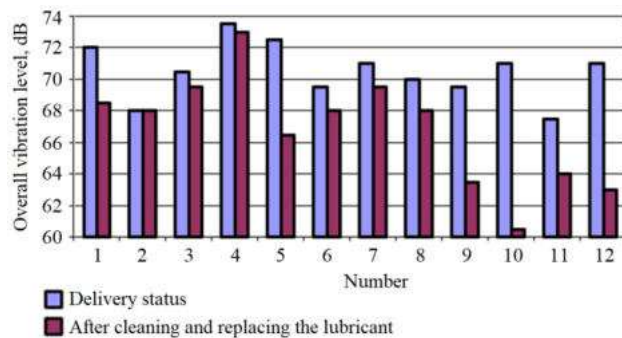


Figure 5 – Graph of the effect of cleaning and replacing the lubricant on the average value of the overall vibration level

The studies showed the effectiveness of the modernized laboratory complex and the possibility of conducting a comparative assessment of the vibroacoustic characteristics of precision rolling tribosystems before and after their cleaning.

The research results showed the objectivity of quality control of ball bearings by the general level of vibrations, which in its case, allows for developing new methods and devices for cleaning model rolling bearings and

withstanding a comparative assessment of their effectiveness.

The main feature of non-dismountable miniature rolling bearings used in various precision mechanical systems of aviation, space, and other special equipment is their overall dimensions, the diameter of which is less than 25 mm, which is orders of magnitude smaller than the diameters of gas turbine engine bearings. Such dimensions of the cleaning objects required more in-depth research into the cleaning processes to determine the optimal parameters of the alternating magnetic field sources for effective removal of ferromagnetic and other particles of contamination from the rolling surface.

Through numerous experimental studies carried out on the developed stand for pre-operational preparation of rolling bearings (Figure 1), using a modernized set of instruments for determining the general level of vibrations (Figure 2), the dependence of the amplitude and frequency of rotation of an alternating pulsed magnetic field on the distance to it in the environment was determined aviation gas This made it possible to determine and adjust the working location of the pulsed magnetic field source in such a way that with one-sided positioning for a magnetic field with an amplitude of 20 mm, effective cleaning will be for bearings with a ring height of up to 15 mm.

With two-way positioning, effective cleaning will be for an experimental ball bearing with a ring height of up to 30 mm when switching from one side to the other. Simultaneously, the magnetic field strength for effectively cleaning bearings from ferromagnetic particles at half the width of the bearing should be at least 0.1 mT. Testing showed that the most effective removal of microparticles of ferromagnetic and other nature from all surfaces of a non-dismantling rolling bearing occurs when the amplitude of the magnetic induction of the moving S/N field is 0.35–0.45 mT and at a constant speed of rotation. Measurements were made using an EM 4305 Tesla meter.

It was experimentally determined that the minimum time for cleaning the bearings within the determined optimal amplitude of magnetic induction and the frequency of rotation of the variable magnetic field source is 2 minutes (one minute on each positioning side). The possibility of positioning rolling bearings in up to 100 pieces has been revealed. At the same time, the amplitude of the magnetic induction of the source of the alternating magnetic field was 150 mT, and the rotation frequency of the S/N field was maintained at the level of 1800 pulses per minute, which is within the range of the frequency that ensures contactless rotation of the bearing and the critical frequency. The critical frequency of rotation of the magnetic field source is when the washing liquid flows in the middle of the rolling path, and when it exceeds the frequency, the liquid is pushed away from the bearing by centrifugal forces.

## 4.2 Investigation of the nature of contamination of rolling bearings

Ball bearings No. 4-1080096 were used for the research. They passed all stages of industrial cleaning and were provided by the manufacturer in hermetically sealed packaging. After deconservation, the bearings were installed on the appropriate bearings at the bottom of the chamber of the cleaning stand, and under the conditions of optimal amplitude and frequency of the alternating magnetic field, they were subjected to cleaning for 1-2 minutes. During the cleaning process, impurities of various natures (metal particles of various sizes and lint) accumulated on the bottom of the chamber, which had a characteristic shine and moved opposite to the movement of alternating magnetic fields. It was visually observed that most of these particles carried out a rolling motion, which indicates the occurrence of a magnetic moment in

microparticles, which is created by the difference in the intensity of the magnetic field in the lowest (contact) and highest areas of the pollution particles.

After cleaning a batch of 4-1080096 bearings in 10 pieces in the TS-1 washing liquid, it was filtered through a fine filter element, and the selected microparticles were subjected to fractographic analysis. With the help of electron microscopy and X-ray spectral analysis, the average size and composition of impurities removed from experimental miniature ball bearings was established (Figure 6).

Studies have shown that the most significant number of pollution particles recorded on filter elements had a size of up to 5  $\mu\text{m}$ , while particles larger than 50  $\mu\text{m}$  were observed much less often. Especially many of the smallest particles, less than 1  $\mu\text{m}$ , were recorded (Figure 6).

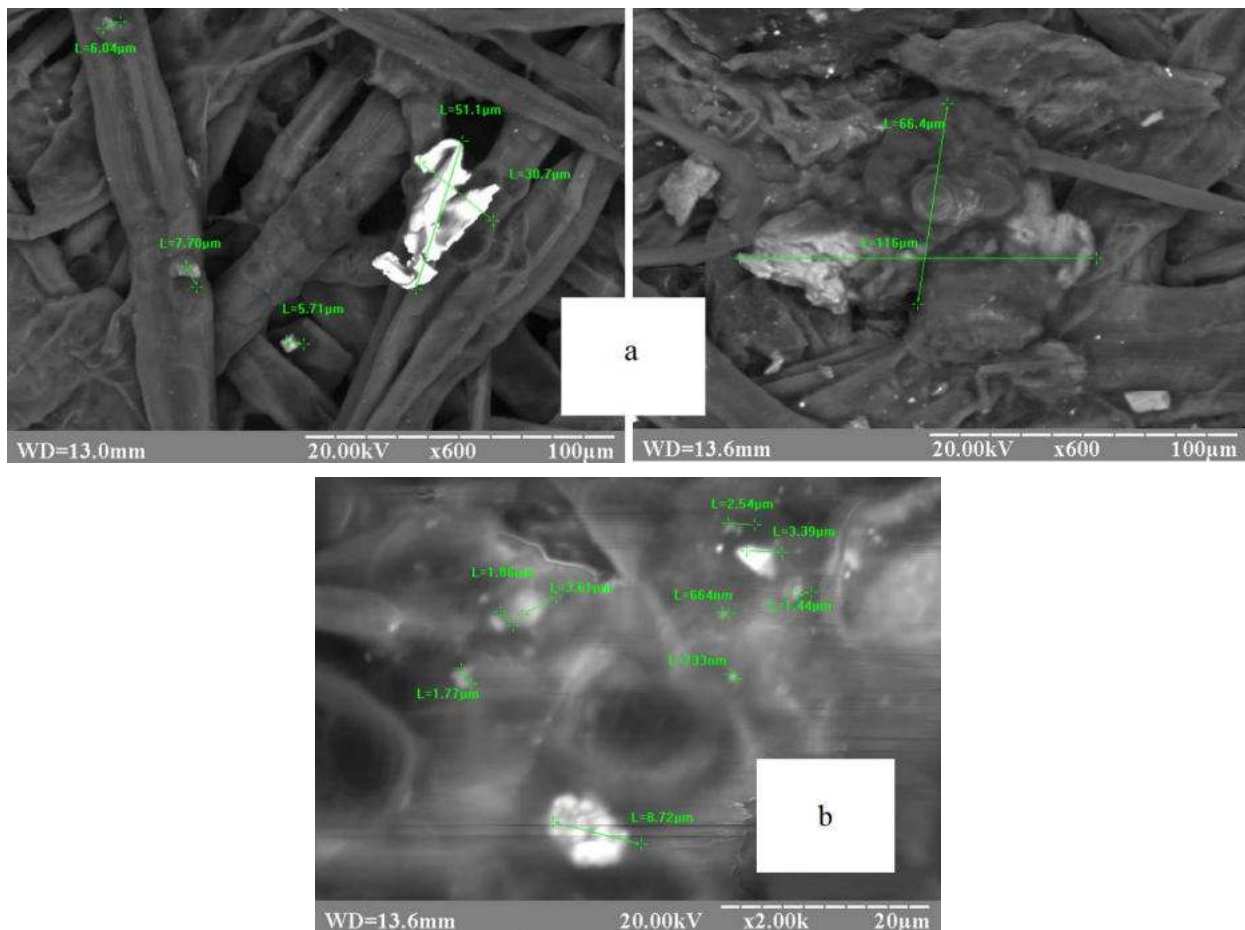


Figure 6 – Samples of contaminants that were removed from new bearings: a – large fragments of metal shavings; b – small particles of pollution of various nature

## 4.3 Research of the chemical composition of rolling bearing contaminants

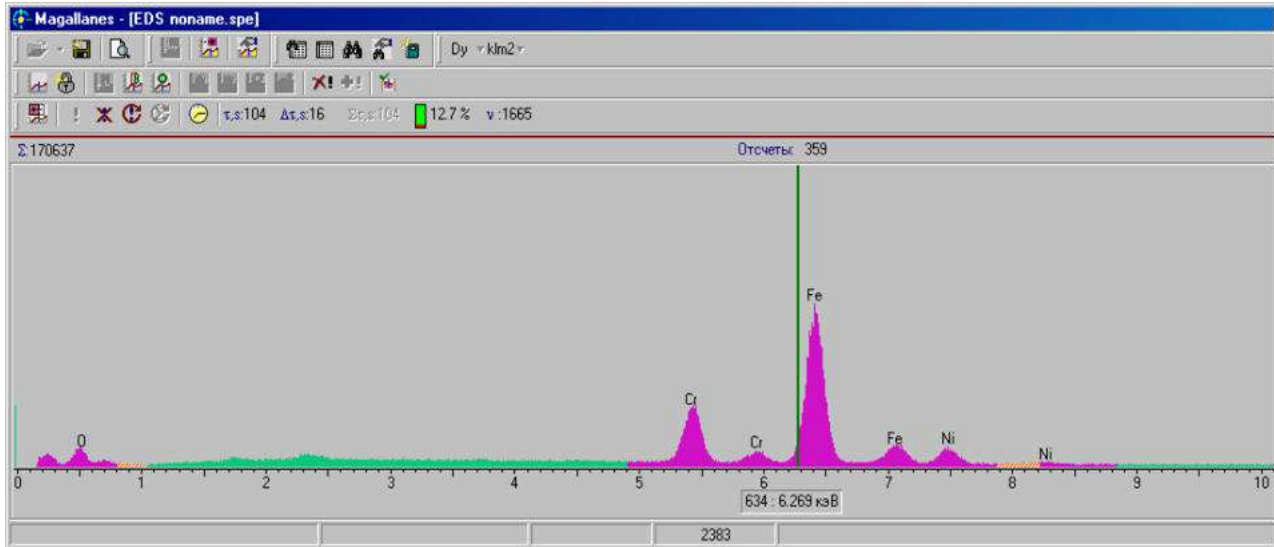
The chemical composition of most metal contamination particles is close to steel 1.3505 (EU), some of which had a composition characteristic of bronze and brass, which collectively indicates the nature of micro-contamination of rolling bearings, closely related

to their production. That is the very atmosphere of bearing production, which is permeated with micrometallic dust during the production of each part (grinding, polishing, stamping, and cutting) at all stages of assembly and assembly of bearings, brings to their surface micro- and nanoparticles that are naturally produced in bearings. Among this group, there are those whose composition coincides with the composition of the

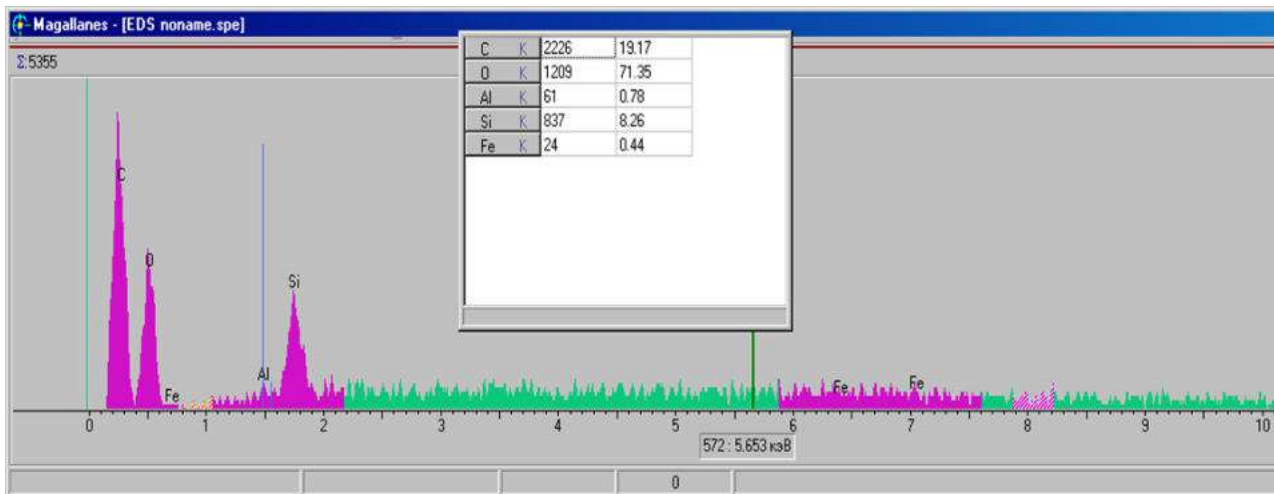
materials from which the structural elements are directly made (steel 1.3505 (EU) of the rolling elements and the bracket, bronze, or brass of the separator) and those that are not directly related to the design of rolling tribosystems, which were subject to research. The extracted non-ferromagnetic pollution particles (Figure 7) are mainly represented by abrasive materials, such as carbide and silicon oxide (they have a characteristic

crystal appearance). A significant part of non-metallic contamination is composed of fragments of polymerized fuel and lubricant materials, which may be the remains of preservation material.

Research on the chemical composition of contaminants (Figure 7) showed that most are ferromagnetic metal fragments in the form of metal particles and shavings.



a



b

Figure 7 – Spectra of the chemical composition of metallic (a) and non-metallic (b) contaminants removed from the new bearings under study

#### 4.4 Study of geometric parameters of contamination of rolling bearings

A careful study of the geometrical parameters of the removed microparticles is called on the REM-106I electron microscope about their asymmetric shape, which is characterized by the presence of the maximum and minimum size of each particle.

The dependence of the size of the removed particles of pollution fixed on the filter elements *R*, considering their type, is indicated in Figure 8.

The nature of the distribution is the same for ferromagnetic and non-ferromagnetic particles (the main part is less than 5 μm). It can be seen from the graphs that when the size of the removed impurities decreases, their number increases many times, especially for sizes smaller than 3 μm.

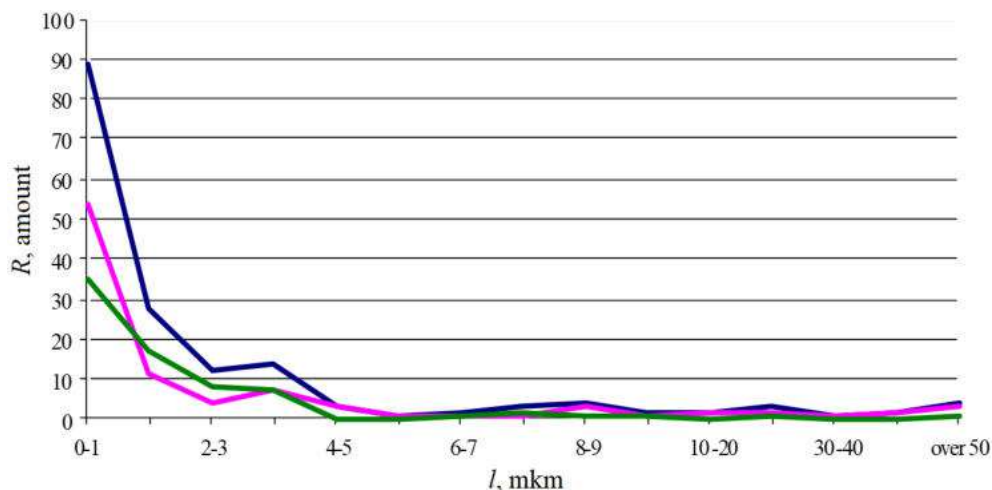


Figure 8 – Graph of dependence of the number of removed pollutants  $R$  on their type and maximum linear size  $l$ : 1 – total number of pollutants; 2 – pollution of ferromagnetic nature; 3 – pollution of a non-ferromagnetic nature

#### 4.5 Approval of the method of cleaning non-dismountable rolling bearings

Using numerous experimental studies, as well as observations of the processes of removing ferromagnetic micropollutants on the stand created for non-contact magnetic-turbulent cleaning of ball bearings in assembly (Figure 1), a generalized method of non-contact cleaning of miniature ball bearings in assembly was developed and tested, which consists of the following.

De-preservation of both new and used ball bearings. This happens by immersing them in desiccators filled with TS-1 aviation fuel, where they are kept for 1-2 h. Previously, by repeatedly rotating the free ring of the bearing in different directions, the maximum removal of preservative oil from the working surfaces of the experimental bearing was achieved.

Depending on the standard size of the ball bearing, a template with inserts with the corresponding diameter of the inner ring is selected (Figure 9). After that, the bottom of the cleaning chamber, the safety gasket, and all surfaces of the template with the bearings are thoroughly wiped with alcohol and positioned accordingly on the working surface of the cleaning chamber.

All ball bearings to be cleaned are checked for free rotation of the outer rings before installation on the corresponding bearings by turning them easily by hand. If the free ring does not rotate or periodically jams, this bearing is re-immersed in the TS-1 aviation gas environment.

After installing the bearings on the housing, the cleaning chamber is closed with a lid.

Selection of the number and duration of cycles of reverse rotation of the bearings is performed by the operator as follows. The cycle duration and their number are set on the control panel (experimentally established and recommended cleaning duration of 1-3 minutes in each direction and 3-5 cycles).

The mode switch of the experimental model of the non-contact magnetic-turbulent cleaning of rolling surfaces of ball bearings assembly is set to the “Automatic” position, after which the “Start” button is pressed.

After cleaning according to the selected program, the ball bearings are turned over, the cover is closed, and the bearings are cleaned according to the selected program.

At the end of the cleaning procedure, the substrate and bearings are carefully removed from the cleaning chamber and installed in the demagnetization and pre-drying chamber, and the lid is closed.

The “Demagnetization” button is pressed on the control panel, which occurs in the automatic mode of operation.

After the preliminary drying and demagnetization procedure, all bearing surfaces are lyophilized with a working fluid (e.g., IPM-10 oil) by injecting the working fluid into the rolling path of the ball bearing. After that, the bearing is packed in a polyethylene hermetic bag and transferred to this state for cleaning efficiency evaluation according to their operational vibroacoustic parameters.

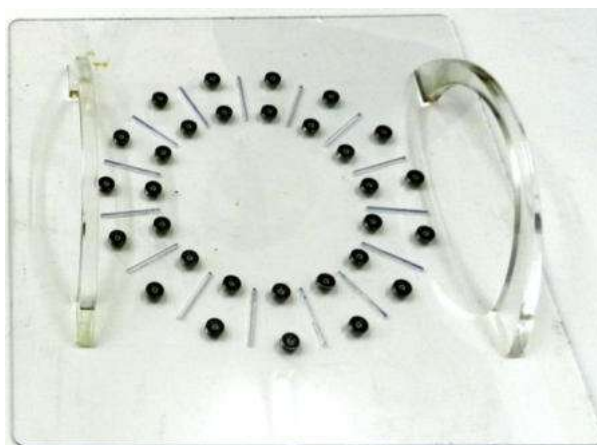


Figure 9 – Designed and manufactured prototype of a pad with bearings for positioning ball bearings

All microparticles removed from the rolling path of the experimental non-dismantling ball bearings during cleaning according to the developed method of non-contact pulse-magnetic-turbulent cleaning at the stand for pre-operational preparation of bearings were subject to examination with a scanning electron microscope REM-1061.

The results of measurement and research of non-dismantling bearings of the 1st category after each stage of technological action and research of removed microparticles.

After removing the preservative grease of unpacked ball bearings in the environment of TS-1 aviation gas, the average values are vibration acceleration of 5.2 m/s<sup>2</sup> and vibration speed of 3.4 m/s<sup>2</sup>.

After cleaning the ball bearings according to the technology used at the customer's enterprise, their

vibration characteristics improved: vibration acceleration – 3.1 m/s<sup>2</sup>; vibration speed – 1.8 m/s<sup>2</sup>.

After cleaning the ball bearings according to the developed method of cleaning non-dismountable ball bearings on the stand for pre-operational preparation of bearings, their vibration characteristics improved significantly: vibration acceleration – 1.7 m/s<sup>2</sup>; vibration speed – 1.1 m/s<sup>2</sup>.

It is important to note that after applying the method of non-contact pulse-magnetic-turbulent cleaning of non-dismountable ball bearings on the created prototype of the stand at the operating rotation speed of the inner rings of 1800 min<sup>-1</sup>, the level of vibration (vibration speed) decreased by 40–45 %.

Results of studies of the chemical composition of the extracted microparticles of pollution are presented in Figure 10.

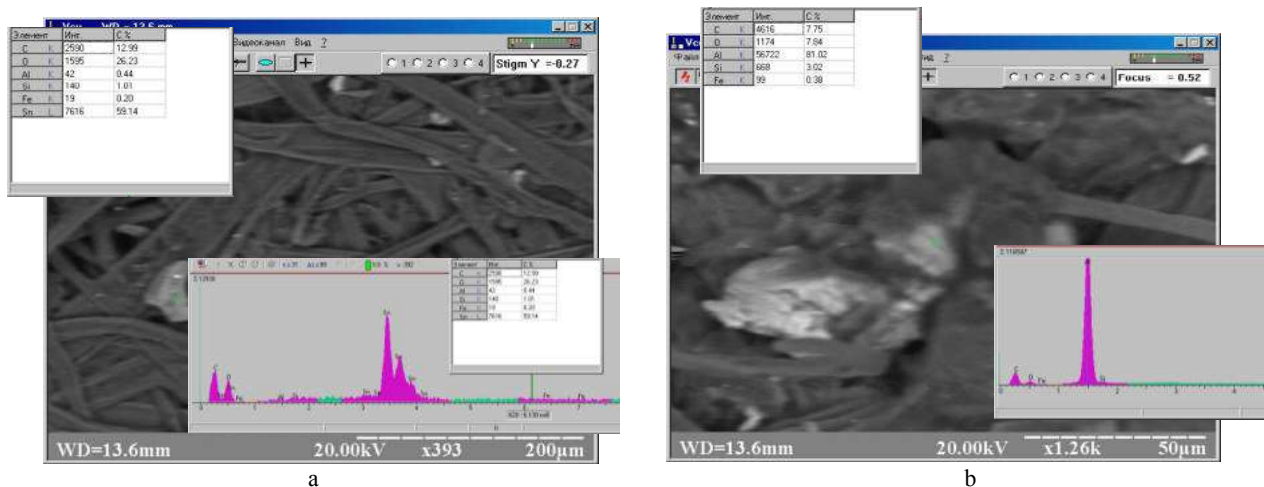


Figure 10 – Results of studies of the chemical composition of the extracted microparticles of pollution: a – 200 μm; b – 50 μm

## 5 Discussion

The study of the size and chemical composition of microparticles removed in the process of non-contact cleaning of non-dismountable ball bearings of the 1st category on the stand showed that microparticles were separated from the rolling path: 30–50 μm in size – 8 %; 10–30 μm – 12 %; 5–10 μm – 50 %, the rest (30 %) – particles up to 5 μm in size.

X-ray spectral analysis of remote microparticles after using the method of non-contact pulse-magnetic-turbulent cleaning of non-dismantling ball bearings on the created test sample of the stand showed that 80 % of the remote particles have a ferromagnetic ferrocement nature and contained on the boundaries of the domain structure of the surfaces of the bearing parts (Figure 10).

It is worth noting that about 5 % of the removed solid microparticles are metal-ceramic conglomerates, characteristic of the wear process of the abrasive processing tool during the finishing of surfaces in the conditions of bearing production. These particles are the most dangerous for ball bearings during operation and especially for all friction pairs of oil systems.

A comparative evaluation of the cleaning of non-disassembled small rolling bearings on the pre-operational preparation stand with new parameters of the pulse variable magnetic field source, which takes into account the features of the standard dimensions according to the developed method in laboratory conditions, showed high efficiency compared to the known ones, as contamination from the working surfaces of the rolling elements was removed after their previous cleaning on the most effective special ultrasonic equipment. The vibration level decreased by 10–27 % on average and on some ball bearings – by 40–65 %.

The criterion for the effectiveness of cleaning model rolling bearings based on the overall vibration level was the presence of a sufficiently large amount of dirt removed from newly preserved ball bearings produced by AFG and SKF, as well as from those that were in use after their preliminary cleaning by ultrasonic methods on modern equipment.

After cleaning the ball bearings according to the technology used at specialized enterprises using their special ultrasonic equipment, the developed method removed enough microparticles smaller than 10 μm. However, the ultrasonic cleaning method has become

widely used in various industries due to its ability to activate impurities. The occurrence of cavitation processes under the action of ultrasonic waves in liquids allows the breaking of the integrity and adhesion of the most complex and robust contaminants [26-28].

Therefore, ultrasonic is widely used in machine building, precision manufacturing, instrument making, radio electronics, and medicine [29, 30].

After analyzing the comparative tests results, it can be noted that the complexity of the structure and the static, especially of prairie ball bearings, are significant obstacles when cleaning by the ultrasonic method, considering many zones shielded from the access of ultrasonic waves, as well as the magnetic component of retention of impurities of a ferromagnetic nature on the working surfaces of the ball bearing. Therefore, when applied, this method does not work effectively enough when cleaning miniature ball bearings in an assembly. However, it can be used with our developed pulsed magnetic-turbulent cleaning method, having previously selected power of the combined pulsed-magnetic source.

## 6 Conclusions

A method of researching the main operating parameters of non-dismountable ball bearings by vibroacoustic characteristics and their cleaning from microparticles of ferromagnetic and other nature has been developed.

It was established that with one-sided positioning for a magnetic field with an amplitude of 20 mm, effective cleaning would be for bearings with a ring height of up to 15 mm. With double-sided positioning, when moving the bearing from one side to the other, effective cleaning will be for bearings with a ring height of up to 30 mm.

The optimal values of the amplitude of the moving magnetic field at a constant speed for the most effective removal of microparticles of ferromagnetic and other nature from all surfaces of a non-separable rolling bearing are 0.35–0.45 mT.

The criterion for the effectiveness of the developed method of cleaning model rolling bearings in terms of the general level of vibration is the presence of a sufficiently large amount of dirt removed from newly preserved ball bearings manufactured by AFG and SKF, as well as from those that were in use after their preliminary cleaning by ultrasonic methods on modern equipment.

Based on the results of the experimental tests, the optimal rotation frequency of the source of the magnetic S/N field for ball bearings with an outer ring diameter of up to 25 mm was determined, which is within 1800 pulses per minute.

The minimum time for cleaning bearings of various standard sizes when ensuring the determined optimal values of the amplitude of tension and frequency of rotation S/N of the magnetic field is up to 2 minutes.

The principal possibility of using the effect of non-contact magnetic-turbulent cleaning of the surfaces of miniature rolling ball bearings when cleaning them with standard sizes up to 30 mm has been experimentally proven.

The method of non-contact magnetic-turbulent cleaning of rolling surfaces of miniature ball bearings was developed and tested.

Joint comparative tests of the developed method of pulse-magnetic-turbulent non-contact cleaning of non-disassemble ball bearings on the bench in the laboratory showed its high efficiency: the level of vibration decreased on average by 10–27 %, and on some ball bearings – by 40–65 %.

## References

1. Jeevanandam, J., Barhoum, A., Chan, Y. S., Dufresne, A., Danquah, M. K. (2018). Review on nanoparticles and nanostructured materials: History, sources, toxicity and regulations. *Beilstein J Nanotechnol.*, Vol. 9, pp. 1050-1074, <https://doi.org/10.3762/bjnano.9.98>
2. Yang, L., Wei, J., Ma, Z., Song, P., Ma, J., Zhao, Y., Huang, Z., Zhang, M., Yang, F., Wang, X. (2019). The fabrication of micro/nano structures by laser machining. *Nanomaterials (Basel)*, Vol. 9(12), 1789, <https://doi.org/10.3390/nano9121789>
3. Chalyj, V., Moroz, S., Ptachenchuk, V., Zablotskyj, V., Prystupa, S. (2020). Investigation of waveforms of roller bearing's working surfaces on centerless grinding operations. In: *Ivanov V. et al. (eds) Advances in Design, Simulation and Manufacturing III. DSMIE 2020. Lecture Notes in Mechanical Engineering. Springer, Cham*, Vol. 1, pp. 349-360, [https://doi.org/10.1007/978-3-030-50794-7\\_34](https://doi.org/10.1007/978-3-030-50794-7_34)
4. Zablotskyi, V., Tkachuk, A., Moroz, S., Prystupa, S., Svirzhevskiy, K. (2021). Influence of technological methods of processing on wear resistance of conjugated cylindrical surfaces. In: *Tonkonogyi V. et al. (eds) Advanced Manufacturing Processes II. InterPartner 2020. Lecture Notes in Mechanical Engineering. Springer, Cham*, pp. 477-487, [https://doi.org/10.1007/978-3-030-68014-5\\_47](https://doi.org/10.1007/978-3-030-68014-5_47)
5. Zablotskyi, V., Tkachuk, A., Senyshyn, A., Trokhymchuk, I., Svirzhevskiy, K. (2022). Impact of turning operations on the formation of rolling bearing's functional surfaces. In: *Tonkonogyi V., Ivanov V., Trojanowska J., Oborskyi G., Pavlenko I. (eds) Advanced Manufacturing Processes III. InterPartner 2021. Lecture Notes in Mechanical Engineering. Springer, Cham*, pp. 229-238, [https://doi.org/10.1007/978-3-030-91327-4\\_23](https://doi.org/10.1007/978-3-030-91327-4_23)
6. Yaroshevich, N., Yaroshevych, O., Lyshuk, V. (2021). Drive dynamics of vibratory machines with inertia excitation. In: *Balthazar J. M. (eds) Vibration Engineering and Technology of Machinery. Mechanisms and Machine Science, Springer, Cham*, Vol. 95, pp. 37-47, [https://doi.org/10.1007/978-3-030-60694-7\\_2](https://doi.org/10.1007/978-3-030-60694-7_2)
7. Yaroshevich, N., Gursky, V., Puts, V., Yaroshevych, O., Martyniuk, V. (2022). On the dynamics of vibrational capture of rotation of an unbalanced rotor. *Vibroengineering Procedia*, Vol. 42, pp. 1-6, <https://doi.org/10.21595/vp.2022.22413>
8. Stelmakh, A., Kostunik, R., Radzievskiy, V., Shymchuk, S., Zaichuk, N. (2022). An increase in tribocharacteristics for highly loaded friction units of modern equipment. In: *Ivanov, V., Trojanowska, J., Pavlenko, I., Rauch, E., Peraković, D. (eds)*

9. Stelmakh, A., Kostunik, R., Shymchuk, S., Zaichuk, N., Tkachuk, A. (2023). Improvement of operational parameters for high-precision tribosystems. In: *Tonkonogyi V. et al. (eds) Grabchenko's International Conference on Advanced Manufacturing Processes InterPartner-2023, Lecture Notes in Mechanical Engineering*. Springer, Cham, pp. 370-379, [https://doi.org/10.1007/978-3-031-16651-8\\_35](https://doi.org/10.1007/978-3-031-16651-8_35)
10. Lv, Y., Yuan, R., Wang, T., Li, H., Song, G. B. (2018). Health degradation monitoring and early fault diagnosis of a rolling bearing based on CEEMDAN and improved MMSE. *Materials*, Vol. 11, 1009, <https://doi.org/10.3390/ma11061009>
11. Lu, S., Zhou, P., Wang, X., Liu, Y., Liu, F., Zhao, J. (2018). Condition monitoring and fault diagnosis of motor bearings using undersampled vibration signals from a wireless sensor network. *Journal of Sound and Vibration*, Vol. 414, pp. 81-96.
12. Khan, T., Voevodin, A., Yerokhin, A., Matthews, A. (2023). Fretting wear and fretting fatigue. Fundamental principles and applications. *Elsevier Series on Tribology and Surface Engineering*, Vol. 2023, pp. 173-199, <https://doi.org/10.1016/B978-0-12-824096-0.00009-3>
13. Baumann, D., Meinig, U. (2011). *Centrifuge For Cleaning a Liquid*. Patent of USA, No. US7959547B2.
14. Doyle, M. P., Richards, G. (2021). *Purification of Renewable Oils*. Patent of USA, No. US10961466B2.
15. Smith, G. H. (1991). Cleaning with alkaline aqueous solutions. *Metall Finish.*, Vol. 9, pp. 9-11.
16. Eggen, M., Wooton, D. L., Erdek, P. J. (2021). *Bearing Flushing Compositions and Methods*. Patent of USA, No. US11021671B2.
17. Kumar, A. Sravan, Deb, Sankha, Pau, S. (2021). Ultrasonic-assisted abrasive micro-deburring of micromachined metallic alloys. *Journal of Manufacturing Processes*, Vol. 66, pp. 595-607.
18. Jiangsu Kunzhou Precision Electromechanical Co Ltd. (2021). *Bearing Cleaning Machine*. Patent of China, No. CN113714198A.
19. French, J. (1998). *An Ultrasonic Cleaning Method of Bearing Balls and Device*. Patent of France, No. WO1998031478A1.
20. Xue, L., Li, N., Lei, Y., Li, N. (2017). Incipient fault detection for rolling element bearings under varying speed conditions. *Materials*, Vol. 10, 675, <https://doi.org/10.3390/ma10060675>
21. Zhang, S., Zhang, Y., Li, L., Wang, S., Xiao, Y. (2018). An effective health indicator for rolling elements bearing based on data space occupancy. *Structural Health Monitoring*, Vol. 17(1), pp. 3-14, <https://doi.org/10.1177/1475921716682432>
22. Liang, G., Naipeng, L., Feng, J., Yaguo, L., Jing, L. (2017). A recurrent neural network based health indicator for remaining useful life prediction of bearings. *Neurocomputing*, Vol. 240, pp. 98-109, <https://doi.org/10.1016/j.neucom.2017.02.045>
23. Shahriar, M. R., Borghesani, P., Tan, A. C. C. (2018). Electrical signature analysis-based detection of external bearing faults in electromechanical drivetrains. *IEEE Transactions on Industrial Electronics*, Vol. 65(7), pp. 5941-5950, <https://doi.org/10.1109/TIE.2017.2782240>
24. Li, Y. B., Wang, X. Z., Liu, Z. B., Liang, X. H., Si, S. B. (2018). The entropy algorithm and its variants in the fault diagnosis of rotating machinery: A review. *IEEE Access*, Vol. 6, pp. 66723-66741, <https://doi.org/10.1109/ACCESS.2018.2873782>
25. Rostaghi, M., Ashory, M. R., Azami, H. (2019). Application of dispersion entropy to status characterization of rotary machines. *J. Sound Vib.*, Vol. 438, pp. 291-308, <https://doi.org/10.1016/j.jsv.2018.08.025>
26. Weller, R. N., Brady, J. M., Bernier, W. E. (2013). Efficacy of ultrasonic cleaning. *Journal of Endodontic*, Vol. 6(9), pp. 740-743.
27. Fuchs, F. J. (1995). Ultrasonic cleaning: Fundamental theory and application. *NASA. Marshall Space Flight Center, Aerospace Environmental Technology Conference*, pp. 369-378.
28. Mason, T. J. (2016). Ultrasonic cleaning: A historical perspective. *Ultrasonics Sonochemistry*, Vol. 29, pp. 519-523.
29. Vetrimurugan, M. G., Lim, S. T., Nagarajan, J. S. (2013). Experimental investigation of ultrasonic and megasonic frequency on cleaning of various disk drive components. *International Journal of Chemical Engineering and Applications*, Vol. 4(4), pp. 174-177.
30. Verhaagen, B., Rivas, D. F. (2016). Measuring cavitation and its cleaning effect. *Ultrasonics Sonochemistry*, Vol. 29, pp. 619-628.





Prokopovych I. V., Kokhanov A. B., Khamitov V. M., Tikhenko V. M., Dašić P. (2023). Standardizing life cycle organization: A synergetic quality management approach. *Journal of Engineering Sciences*, Vol. 10(1), pp. B1-B7, doi: 10.21272/jes.2023.10(1).b1

## Standardizing Life Cycle Organization: A Synergetic Quality Management Approach

Prokopovych I. V.<sup>1\*</sup>[0000-0002-8059-6507], Kokhanov A. B.<sup>1</sup>[0000-0002-7197-6380], Khamitov V. M.<sup>1</sup>[0009-0005-3494-8304], Tikhenko V. M.<sup>1</sup>[0000-0003-1040-9160], Dašić P.<sup>2</sup>[0000-0002-9242-274X]

<sup>1</sup>Odessa Polytechnic National University, 1, Shevchenko Ave., 65044 Odessa, Ukraine;

<sup>2</sup>High Technical Mechanical School of Professional Studies, 19, Radoja Krstića St., 37240 Trstenik, Serbia

### Article info:

Submitted: February 21, 2023  
 Received in revised form: May 9, 2023  
 Accepted for publication: May 19, 2023  
 Available online: May 25, 2023

### \*Corresponding email:

[igor.prokopovich@gmail.com](mailto:igor.prokopovich@gmail.com)

**Abstract.** Standardization is essential for innovation (on the impacts on design, manufacturing, and operation processes) and its dissemination, both within a country and internationally. A phenomenological information model has been developed for the system of standards, which will be used as an information base for integrated quality management systems, environmental safety, and energy saving depending on the type of products, requirements of technical regulations, and conformity assessment procedures. Phase portraits of the life cycle system of complex products were constructed, and a general expression for the Lyapunov exponents characterizing the overall behavior of the dynamic system in phase space was obtained. The presence of particular areas to which, regardless of the initial conditions, all phase trajectories rapidly evolve has been established. The critical conditions for the control parameters were found. A diagram was constructed that determines the stability of the system states of the life cycle of complex products. It was found that the processes of the life cycle of complex products are carried out in two stages: in the first, there is a rapid evolution of components and parameters of technical and software tools, as well as energetic elements of functional subsystems, which is reflected in a specific attractive section of phase portraits, in the second, further slow development along it.

**Keywords:** additive manufacturing, industrial growth, production function, state parameter, synergetic order parameter.

## 1 Introduction

Energy efficiency and environmental impact of applied technologies are relevant for various industries and (to a large extent) related to the effectiveness of the use of technical and economic information in ensuring the quality of complex products (CP) [1, 2]. The ISO 9000 standards cover various aspects of quality management [3]. The standards provide guidance and tools for companies and organizations that want their products and services to meet customer requirements and consistently improve quality. This is especially true for products for industrial purposes (various production equipment) used to manufacture the final finished product. ISO has several quality management system standards developed from ISO 9001 and adapted to specific industrial sectors [4].

The growing awareness of the importance of the problem of environmental protection and the possible impacts associated with manufactured and consumed

products has increased interest in developing methods to understand and study these impacts. One method being developed for this purpose is life cycle assessment (LCA). The standard ISO 14044 details the requirements for LCA [5]. The ISO man-agreement system helps organizations improve their performance by developing specific design, manufacturing, and operation steps that organizations will follow during their activities to achieve their goals and create an organizational culture.

Understanding and caring for mutually related processes at these stages as a system for judging the effectiveness and efficiency of the organization in the reach of planned results. Simulation is a recognized method for planning and optimizing production systems. Existing standards (e.g., ISO 14040/44), data sources, and software support LCA.

In paper [6], two approaches to the modeling of prospective resource reserves at the stages of the life cycle of the CP are distinguished, namely, predictive

scenarios and ranges of scenarios both for the near term (current state of the life cycle) and for background modeling of the system (future state). The first approach depicts likely events with the status quo in mind. Technology learning curves can be used to build predictive scenarios [7]. The second approach includes extreme scenarios that can be obtained using stoichiometric ratios to analyze the best scenario [8]. These works propose including TRL and production readiness level (MRL) in assessing new technologies' life cycle to indicate technology maturity. The authors of these works define the problem of the functionality of the observed system. However, there is still no consistency in the perspective methodology of evaluating residential buildings.

Further research in this area is needed to develop scaling schemes for new technologies. Thus, emphasis should be placed on uncertainty analysis. An assessment of the reliability of scaling methods can be established by analyzing assumptions and scaling models as the technology evolves. In this way, the quality of the scaling scheme can be assessed, evaluated, and verified. For example, due to the static nature of LCA data and standard data gaps, only averages from databases are often used in conjunction with generic black box models to define processes, materials, and resources.

Traditional LCAs cannot account for the dynamic effects of time-dependent variables. The number of input parameters and their uncertainties influence life cycle modeling, making it complex and challenging. As practice proves, the majority (55 %, according to [9]) of unsuccessful projects for the development and production of products is connected precisely with the lack of scientific approaches and appropriate regulatory and methodological support based on the use of system-wide evolutionary models. Such models should consider the large size and complexity of the data during the design, manufacture, and operation of the CP, depending on the dynamic change of the internal and external environment. As a result, there are significant unjustified costs of information, material, and energy resources when meeting the requirements of customers and other interested parties.

The purpose of this study is to develop, based on the principles of synergy, a phenomenological information model for improving the integrated system of quality management standards, environmental safety, and energy saving at the stages of the LCA of CP, depending on the requirements of technical regulations, conformity assessment procedures.

## 2 Literature Review

This paper analyzes the theoretical, methodological, and normative-methodical foundations of the formation and effective use of technical and economic information at the stages of the life cycle of complex products and objects of military equipment, taking into account the self-coordinated interaction of processes as an open system, the self-organization of which affects the

achieved results in terms of satisfying customer requirements. In the work of [10], when assessing the sustainability of LC, economic aspects are combined with technical preparation of production (TPV), technological features, and environmental and social impacts.

A more detailed discussion of the various modes of operation of the LCA CP processes, including the future states of technical systems, is given in the results of the research works [12, 13], presents the results of studies of economic growth models based on production functions, which show realistic dynamic interdependencies associated with resource consumption, growth and structural changes at the LC stages. In models of economic growth [14], the production function describing the dependence of output on factors of production is usually assumed to be smooth everywhere. However, due to this limitation, the qualitative parameters affecting CP manufacturing cannot be included in the model.

The article [15] discusses the peculiar features of quality management in modern manufacturing and technological systems with consideration for risk-based thinking, which characterizes quality as a measurable and estimable factor, its indices, existing major categories of quality management, how and when they are applied, as well as their distinctive features.

In the article [16], the proposed approach emphasizes the relevance of the influence of dynamic effects in production systems at the life cycle stages of a complex product. This article introduces the concept of combining LCA and production system modeling, explains the types of models for each methodology, and provides an example of applying the combined methodology to analyze the case of integrating volatile energy sources into production control.

The research [17] addresses the problem of using machine learning methods to provide LCA solutions. The general hypothesis is this: LCA, backed up by machine learning and based on dynamic data, paves the way for a more accurate LCA, supporting decision-making throughout the Favi, C. [18] suggest including TRL and production readiness level (MRL) when evaluating the life cycle of new technologies as an indicator of technology maturity. The research works [19, 20] define the problem of the functionality of the observed system. Thus, the characteristic features of CP are the presence of emergent properties, inherent both to the elements of hierarchical structures of CP, which are diverse in their configurations, and to the processes that accompany them at the stages of CP; the need to take into account the influence of all factors of the external environment on the CP and the system of processes at the stages of the LC, which can change the composition, structure, and condition of the CP, cause deviations from the established requirements. In this regard, this research sets out the task of creating scientifically based bases for making decisions on ensuring compliance with the established requirements of CP in mechanical engineering based on life cycle (LC) management technologies and models of self-coordinated interaction of processes during design, manufacturing, and operation.

### 3 Research Methodology

Based on the main provisions of the theory of self-organization, the open system of the LC CP is represented by self-consistent nonlinear equations, which allows us to consider possible variants of phase transitions between modes of process implementation during design, manufacture, and operation. According to the synergistic approach, a self-organizing system is defined by self-consistent equations that relate the intensity of execution of the design processes  $dF/d\tau$ , manufacturing  $dG/d\tau$  and operation  $dQ/d\tau$  with the values of the functions  $F$ ,  $G$ ,  $Q$ , which can be considered as a control parameter, conjugate field and synergetic order parameter [21].

The analysis has been made in [22] demonstrations that in the process of the transition between low- and high-performance modes of realization of mutual interaction between the processes of design, manufacturing, and operation of CP for production and technical purpose, the characteristic time  $\tau_Q$  of the production function change  $Q(t)$  has a constant value. Inherently response of the system to the increase of  $Q$  can result in a scale increase of  $\tau_Q$ , which can be represented using approximation [23]:

$$\tau_Q = \tau_0 \left( 1 + \frac{k}{1 + \frac{Q^2}{Q_\tau^2}} \right)^{-1}, \quad (1)$$

which is characterized by positive constants of  $\tau_0$ ,  $k$ , and  $Q_\tau$ .

The following expression can represent synergetic potential:

$$V = \frac{Q^2}{2} \left\{ 1 - \frac{F_e}{F_{c0}} \left( \frac{Q}{Q_m} \right)^{-2} \ln \left[ 1 + \left( \frac{Q}{Q_m} \right)^2 \right] \right\} + \frac{kQ_\tau^2}{2} \ln \left[ 1 + \left( \frac{Q}{Q_\tau} \right)^2 \right], \quad (2)$$

where  $F_{c0} \equiv (a_Q a_G)^{-1}$ .

According to Figure 1, for small values of  $F_e$ , the dependence  $V(Q)$  has a monotone increasing form (curve 1) with its minimum in point  $Q = 0$ . This case corresponds to the low-performance realization of mutual interaction between design, manufacturing, and operation processes. In the following case, when the value of

$$F_c^0 = F_{c0} \left[ 1 + \frac{Q_\tau^2}{Q_m^2} (k-1) + 2 \frac{Q_\tau}{Q_m} \sqrt{k \left( 1 - \frac{Q_\tau^2}{Q_m^2} \right)} \right], \quad (3)$$

a plateau (curve 2) appears, which becomes transformed into a minimum.

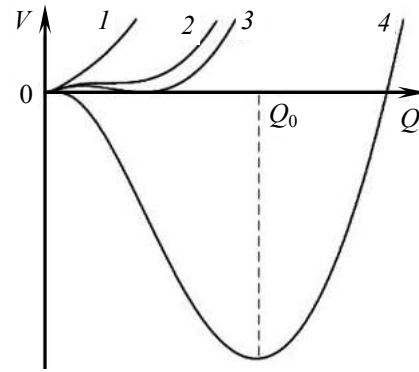


Figure 1 – Form of the dependence of synergetic potential upon the synergetic order parameter under different  $F_e$  values: 1 –  $F_e < F_c^0$ ; 2 –  $F_e = F_c^0$ ; 3 –  $F_c^0 < F_e < F_c$ ; 4 –  $F_e \geq F_c$

This case corresponds to the value of the production function  $Q_0 \neq 0$  (high-performance mode) and maximum (unstable state), which separate minima  $Q_0 = 0$ ,  $Q_0 \neq 0$  (curve 3).

With further increasing of  $F_e$  level, the minimum high-performance mode of realization deepens, and the height of the barrier, which separates stationary states, drops and reaches zero under the following critical value:

$$F_c = F_{c0} (1+k). \quad (4)$$

If  $F_e \geq F_c$  (Figure 1, curve 4),  $V(Q)$  dependence has the same form as the analyzed above continuous transition. Stationary values of a production function  $Q$  here have the following form (Figure 2):

$$Q_0 = Q_{00} \left\{ 1 - \left[ 1 + \left( \frac{Q_m Q_\tau}{Q_{00}^2} \right)^2 \frac{F_e - F_c}{F_{c0}} \right]^{1/2} \right\}, \quad (5)$$

$$Q_{00}^2 \equiv \frac{1}{2} \left[ \left( \frac{F_e}{F_{c0}} - 1 \right) Q_m^2 - (1+k) Q_\tau^2 \right]. \quad (6)$$

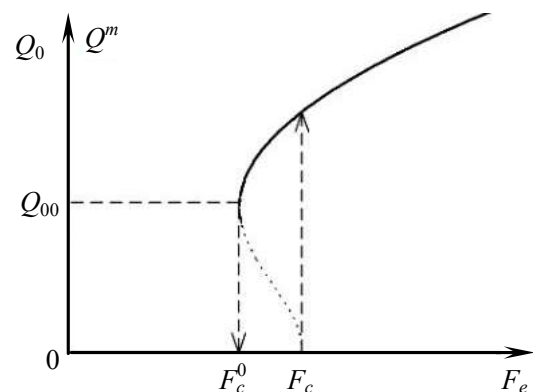


Figure 2 – Dependence of stationary values of the synergetic order parameters upon  $F_e$  rating parameter (solid curve corresponds to stable state  $Q_0$ , dotted – to unstable state  $Q_m$ )

The upper index corresponds to the unstable state  $Q_m$ , when synergetic potential reaches maximum, and lower one corresponds to stable state  $Q_0$  in its minimum.

The control parameter

$$F_0 = \frac{(1+Q_0^2) - \sqrt{(1+Q_0^2)^2 - (1-Q_\tau^2) \frac{F_e}{F_{c0}}}}{1-Q_\tau^2} \quad (7)$$

fall freely with increasing the value

$$F_{c0} = 1 + Q_\tau \sqrt{\frac{k}{1-Q_\tau^2}}, \quad (8)$$

that corresponds to  $F_e = F_c^0$  up to  $F_c$  under  $F_e \rightarrow \infty$ .

From Figure 2, under free scientific and technological development in point  $F_e = F_c$  a sudden change of the stationary value of production function  $Q_0$  from zero up to  $\sqrt{2} \cdot Q_{00}$  occurs, and then its value increases freely according to the law (5).

In the inverse case, when  $F_e$  decreases, the stationary value of production function  $Q_0$  decreases freely according to the dependence (5) up to the point  $F_e = F_c^0$ ,  $Q_0 = Q_{00}$ . Then it reaches zero value by sudden change.

The stationary value of the production function  $F_0$  coincides with the level of engineering and design information  $F_e$  only within interval  $0 < F_e < F_c^0$ .

In case when the level of scientific and technological development  $F_e > F_c^0$ , the production function  $F_0$  becomes double-valued, following the descending curve, which decreases freely from the value  $F_{c0}$  (8) under  $F_e = F_c^0$  condition up to  $F_c$  under  $F_e \rightarrow \infty$  condition.

In case of a free increase of the level of scientific and technological development  $F_e$  from 0 up to  $F_c$ , the stationary value of the production function  $F$  increases linearly within the same interval. After a sudden drop in  $F_e = F_c$  The value of  $F_0$  decreases freely according to the dependence (7). In the inverse case, when the level of scientific and technological information  $F_e$  decreases, the stationary value of production function  $F_0$  suddenly increases in  $F_c^0$  the point from  $F_{c0}$  value up to  $F_c^0$  value.

Thus, we observe hysteresis, which is conditioned by the availability of the barrier for the effective potential (2) and is revealed under  $Q_\tau/Q_m < 1$  condition when changing  $Q$  and  $F$  production functions. The hysteresis loop gets narrow as the rate of non-equilibrium parameter change increases.

#### 4 Results

Measuring  $Q$ ,  $G$ , and  $F$  values in such units of measurement  $Q_m = (a_G a_F)^{-1/2}$ ,  $G_m \equiv (a_Q^2 a_G a_F)^{-1/2}$ , and  $F_c \equiv (a_Q a_G)^{-1}$ , we are to analyze different boundary relations of the characteristic times  $\tau_0, \tau_G, \tau_F$ , as we have already analyzed them for continuous phase transition. Here, the characteristic time  $\tau_Q$  of the production function change is set by the equation (1). The carried-out investigation shows that Lorentz's combined equations (9)-(11) allow representing principal features of phase transitions between modes of realization of simultaneous functioning of the design, manufacturing, and operation processes (Figure 3).

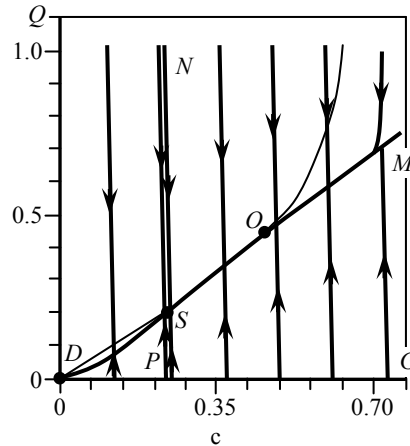
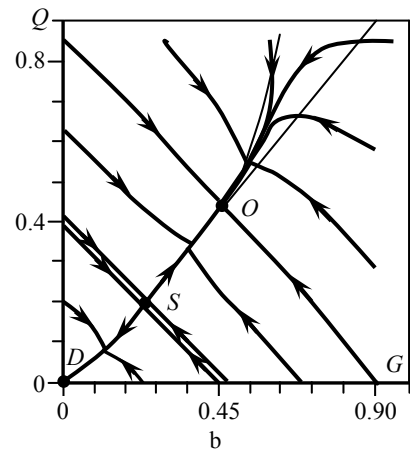
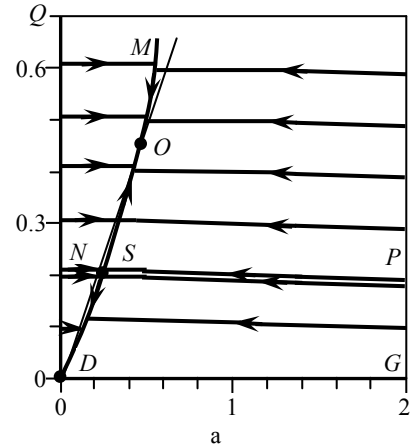


Figure 3 – Phase portraits of discontinuous transition ( $k = 1, Q_\tau = 0.1Q_c, F_e = 1.25F_c$ ): a –  $\tau_F \ll \tau_0 = 100\tau_G$ ; b –  $\tau_F \ll \tau_0 = \tau_G$ ; c –  $\tau_F \ll \tau_0 = 10^2\tau_0$

According to phase portraits of discontinuous transition (Figure 3), at  $F_e = F_c^0$  bifurcation takes place, and there appears a saddle  $S$  corresponding to the energy barrier on  $V(Q)$  dependence and attracting vertex/focus  $O$ , which characterizes the high-performance mode of realization because of bifurcation. At that, attracting vertex  $D$ , which again corresponds to low-performance mode, remains changeless. With increasing of control parameter within the interval  $(F_c^0, F_c)$ , a saddle  $S$  shifts to vertex  $D$  assimilating it in point  $F_c$ , and vertex/focus  $O$

shifts towards increasing synergetic order parameter and conjugate field. The type of singular point  $O$ , which corresponds to a high-performance mode of the system of joint functioning of the design, manufacturing, and operation processes, depends upon the relation of characteristic times  $\tau_Q$ ,  $\tau_G$ , and  $\tau_F$ .

We consider the time of change  $\tau_0$ , which belongs to dependence (1), as the value of change of production function of operation functional subsystem  $\tau_Q$  for discontinuous transition [7]. If values  $\tau_Q$ ,  $\tau_G$ , and  $\tau_F$  are not equal, we can distinguish six specific modes [8]:

$$\begin{aligned} a) t_G \ll t_F \ll t_Q; \quad d) t_F \ll t_Q \ll t_G; \\ b) t_Q \ll t_F \ll t_G; \quad e) t_G \ll t_Q \ll t_F; \\ c) t_F \ll t_G \ll t_Q; \quad f) t_Q \ll t_G \ll t_F. \end{aligned} \quad (9)$$

As the carried-out analysis shows, in cases (9 a-d), point  $O$  is an attractive vertex. In a short time, the trajectory of the system of joint functioning of the design, manufacturing, and operation processes exits onto a universal area (“stream of a big river”), which location is determined by external conditions (by the value of  $F_e$ ). The availability of such an area causes the universal character of the system’s evolution. In the given phase portraits “stream of a big river” is represented in parametric space  $Q$ ,  $G$ , and  $F$  in such a way that when projecting onto planes  $F-Q$ ,  $F-G$ , it has a form of monotonously falling curve of *MOD-type* [9] or *MOS-type* (discontinuous transition).

Projection onto plane  $G-Q$  is close to bisectrix (Figure 3a). Universal area *NSP*, which corresponds to the system’s transition over the energy barrier, occurs in case of discontinuous transition (Figure 3). The presented phase portraits let us see that for the modes (9 a-d), exit to universal area occurs along almost linear paths, practically parallel to axes, corresponding to minimum relaxation time. Thus, in mode (9 a), the point moves rapidly in the beginning along the straight line parallel to the  $G$ -axis, then it shifts onto the segment parallel to the  $F$ -axis and moves along it with speed  $\tau_F/\tau_G$  times less than before, but  $\tau_Q/\tau_F$  times higher than the speed of further moving within the universal area. After this, the shift onto the “stream of a big river” occurs.

For relations of relaxation times, which characterize cases (9 e-f), the system gets decaying oscillations within the plane corresponding to two maximum values of these times. For both cases, the characteristic time of change of the control parameter ( $F$ ) has the most significant value. Critical increasing of times  $\tau_Q$ ,  $\tau_G$  in compliance with relations of the type  $\tau_Q/(F_e - F_c)$ ,  $\tau_G/(F_e - F_c)$  is a cause of oscillation origination. Near to critical point  $F_c$ , it secures parity of values  $\tau_Q|F_e - F_c|^{-1}$  and  $\tau_F$  (in case (9 e)), as well as  $\tau_G|F_e - F_c|^{-1}$  and  $\tau_F$  (in case (9 f)), in consequence of that relation between respective values  $Q$ ,  $F$  and  $G$ ,  $F$  gets resonance character. As to evolution along  $G$  and  $Q$  axes, which correspond to minimum times in cases (9 e-f), it preserves the same character, as for transition to universal mode: the system with speed  $\tau_F/\tau_G$  and  $\tau_F/\tau_Q$  times higher than oscillation frequency, (cases

(9 e) and (9 f), respectively), shifts to the corresponding plane along the perpendicular axis.

In the general case, the kinetic pattern of transition from a low-performance state of the system of joint functioning of the design, manufacturing, and operation processes to a high-performance one is defined by a set of three synergetic and kinetic parameters. The key role in the first group belongs to the external factor (level of engineering and design provision)  $F_e$ , which relates to critical value  $F_c$  defines the type of the system state (Figure 3).

Two other synergetic parameters ( $k$  and  $Q_1 \equiv Q_\tau/Q_c$ ), which values are set by law (1) of dispersion of change time of production function  $Q$ , define the area of discontinuous transition. It is limited by minimum value  $k = Q_1^2/(1 - Q_1^2)$ , moving away from, which increases this area. Characteristic of discontinuous transition lies in the fact that separatrix appears in phase portrait, and the availability of separatrix results in the critical dependence of the system evolution upon the choice of its initial state.

Characteristic times  $\tau_0$ ,  $\tau_G$ ,  $\tau_F$  of changes of functions  $Q$ ,  $G$ , and  $F$  in independent modes are kinetic parameters that define the system behavior. The carried-out investigations show that the universal representation of the evolution of the system of joint functioning of the design, manufacturing, and operation processes realizes if the last of the abovementioned times get the minimum value. At that, the system for a short time  $\tau_F$  exits onto universal area *MOS* (Figure 3), which position depends only upon synergetic parameters but not upon the relation of scales  $\tau_0$ ,  $\tau_G$ ,  $\tau_F$ . Such a situation is realized for the high-performance mode of realization of the system of joint functioning of the design, manufacturing, and operation processes. Under the anomalous increasing of times of change of function  $F$ , twisting of phase portraits takes place near the high-performance mode of realization, obtained through a series of drops and jumps.

Moreover, under  $\tau_G \sim \tau_Q \ll \tau_F$  condition, when the level of scientific and technical development gets overcritical value  $(F_e - F_c) \sim \tau_Q/\tau_F \sim \tau_G/\tau_F \ll 1$  the system of joint functioning of the design, manufacturing, and operation processes shifts to the mode of strange attractor, where evolution becomes unpredictable. This is evidence of the extreme risk of regulation of the level of engineering and design provision under the conditions of self-consistent development of the system of joint functioning of the design, manufacturing, and operation processes.

## 5 Discussion

The large-scale behavior of the life cycle and CP depends on a specific case, and a lower impact on the environment at the advanced technological stage cannot be taken for granted. In addition, the consequences of a scaled life cycle system are not often compared with the consequences of a mature alternative technology. In addition, there is still no formal and strict definition of a complex or large technical system. Based on the content

analysis results, we identified the following four challenges: comparability, scaling issues, data availability, and uncertainty. However, we included the scaling issue in the data call because scaling is required to create inventory data for a scaled product system.

## 6 Conclusions

Based on models of production functions, a method of evaluating the effectiveness of the compatible interaction of functional subsystems (design, manufacturing, and operation) is proposed, each of which can have an independent nature of applying its results in the life cycle stages. Application of a choice model of effective modes of realization of mutual interaction between functional subsystems allows estimation of each variant of CP design from the point of view of expenditures for its design, manufacturing, and operation.

One can choose the most optimal from the market standpoint by analyzing the advantages and disadvantages of these variants. The joint functioning of

the design, manufacturing, and operation processes can be represented as an open interaction system between corresponding functional subsystems. Each of them can have an independent pattern of use of the results.

Integration into the general system provides a new qualitative sense, combination of characteristics and degree of utility of machine-building products, and improves technical and economic indices when designing and manufacturing.

Modes of the system realization are defined by a combination of conditions and means of many economic, technical, and social processes, which are unequally influenced by the external environment and have various persistence levels.

## 7 Acknowledgments

The research presented in this paper was supported by the international grant project Jean Monnet Actions under ERASMUS+ Programme ERASMUS-JMO-2021-HEI-TCH-RSCH EUGreeCon – 101047527.

## References

1. Zaloga, V., Dyadyura, K., Rybalka, I., Pandova, I. (2019). Implementation of integrated management system in order to enhance equipment efficiency. *Management Systems in Production Engineering*, Vol. 27(4), pp. 221-226.
2. Zaloga, V., Dyadyura, K., Rybalka, I., Pandova, I., Zaborowski, T. (2020). Enhancing efficiency by implementation of integrated management system in order to align organisational culture and daily practice. *Management Systems in Production Engineering*, Vol. 28(4), pp. 304-311.
3. ISO 9001:2015 Quality Management Systems – Requirements.
4. ISO/TS 9002:2016 Quality Management Systems – Guidelines for the Application of ISO 9001:2015.
5. ISO 14044:2006 Environmental Management – Life Cycle Assessment – Requirements and Guidelines.
6. Krenicky, T., Hrebenyk, L., Chernobrovchenko, V. (2022). Application of concepts of the analytic hierarchy process in decision-making. *Management Systems in Production Engineering*, Vol. 30(4), pp. 304-310.
7. Dyadyura, K., Hovorun, T.P., Pylypenko, O.V., Hovorun, M.V., Pererva, V.I. (2017). Influence of roughness of the substrate on the structure and mechanical properties of TiAlN nanocoating condensed by DCMS. *Proceedings of the 2017 IEEE 7th International Conference on Nanomaterials: Applications and Properties, NAP 2017*, 01FNC10.
8. Sukhodub, L.F., Dyadyura, K. (2018). Design and fabrication of polymer-ceramic nanocomposites materials for bone tissue engineering. *Journal of Nano- and Electronic Physics*, Vol. 10(6), 06003.
9. Blind, K., Von Laer, M. (2022). Paving the path: Drivers of standardization participation at ISO. *J Technol Transf*, Vol. 47, pp. 1115-1134.
10. Jemghili, R., Ait Taleb, A., Mansouri, K. (2023). A collaborative multidisciplinary design methodology for additive manufacturing with a left-handed mouse as a case study. *Int J Adv Manuf Technol*, Vol. 125, pp. 4925-4951.
11. Santolaya, J.L., Lacasa, E., Biedermann, A. et al. (2019). A practical methodology to project the design of more sustainable products in the production stage. *Res Eng Design*, Vol. 30, pp. 539-558.
12. Ghoroghi, A., Rezgui, Y., Petri, I. et al. Advances in application of machine learning to life cycle assessment: A literature review. *Int J Life Cycle Assess*, Vol. 27, pp. 433-456.
13. França, W.T., Barros, M.V., Salvador, R. et al. (2021). Integrating life cycle assessment and life cycle cost: A review of environmental-economic studies. *Int J Life Cycle Assess*, Vol. 26, pp. 244-274.
14. King, C.W. (2022). Interdependence of growth, structure, size and resource consumption during an economic growth cycle. *Biophys Econ Sust.*, Vol. 7, 1.
15. Malik, A.I., Kim, B.S. (2021). Coordination supply chain management under flexible cleaner production system and stochastic conditions. *Ann Oper Res*, Vol. 21, <https://doi.org/10.1007/s10479-021-04303-w>
16. Sadler, H. (2020). ER<sup>2</sup>C SDMLC: Enterprise release risk-centric systems development and maintenance life cycle. *Software Qual J.*, Vol. 28, pp. 1755-1787.

17. Priarone, P.C., Catalano, A.R. Settineri, L. (2023). Additive manufacturing for the automotive industry: On the life-cycle environmental implications of material substitution and light-weighting through re-design. *Prog Addit Manuf*, <https://doi.org/10.1007/s40964-023-00395-x>
18. Favi, C., Campi, F. Germani, M. (2019). Comparative life cycle assessment of metal arc welding technologies by using engineering design documentation. *Int J Life Cycle Assess.*, Vol. 24, pp. 2140-2172.
19. Yanıkoğlu, İ., Albey, E., Okçuoğlu, S. (2022). Robust parameter design and optimization for quality engineering. *Oper. Res. Forum*, Vol. 3, 8 (2022).
20. Siran, K.C., Dipendra, G. (2021). Progress in sustainable structural engineering: a review. *Innov. Infra-struct. Solut.*, Vol. 6, 68.
21. Dyadyura, K., Hrebenyk, L., Krenicky, T., Zaborowski, T. (2021). Modeling of the manufacturing systems state in the conditions of the lean production. *MM Science Journal*, Vol. 2021(June), pp. 4408-4413.
22. Cao, Y., Liu, Y., Ye, X. et al. (2020). Software-physical synergetic design methodology of mechatronic systems based on formal functional models. *Res Eng Design*, Vol. 31, pp. 235-255.
23. Zhang, X., Dong, S. (2019). Analysis on supply-demand system of automotive manufacturer-supplier with synergetics. *Cluster Comput.*, Vol. 22(3), pp. 6817-6826.



*processes*

an Open Access Journal by MDPI



## Monitoring and Control of Processes in the Context of Industry 4.0

Guest Editors:

**Prof. Dr. Ján Pitel**

Department of Industrial Engineering and Informatics, Faculty of Manufacturing Technologies with a seat in Presov, Technical University of Kosice, 080 01 Presov, Slovakia

jan.pitel@tuke.sk

**Prof. Dr. Ivan Pavlenko**

Department of Computational Mechanics named after V. Martsynkovskyy, Sumy State University, 40007 Sumy, Ukraine

i.pavlenko@cm.sumdu.edu.ua

**Dr. Sławomir Luściński**

Department of Production Engineering, Kielce University of Technology, Faculty of Management and Computer Modelling, Aleja Tysiąclecia Państwa Polskiego 7, 25-314 Kielce, Poland

luscinski@tu.kielce.pl

### Message from the Guest Editors

This Special Issue, titled “Monitoring and Control of Processes in the Context of Industry 4.0”, aims to highlight the novel advances in process monitoring and control according to Industry 4.0 requirements. Topics will include, but are not limited to:

- The real-time monitoring of processes;
- Advanced control of processes using soft computing;
- Digitalization of processes, interfaces and digital twins;
- Smart sensors and smart metering in processes and signal processing;
- Vision and measuring systems for quality control;
- Data acquisition, storage and processing;
- Virtual, augmented and mixed reality in processes.

Deadline for manuscript submissions:

**10 October 2023**



mdpi.com/si/136613

**Special Issue**





Lebedev V. V., Miroshnichenko D. V., Nyakuma B. B., Moiseev V. F., Shestopalov O. V., Vyrovets S. V. (2023). Design of inorganic polymer composites for electromagnetic radiation absorption using potassium titanates. *Journal of Engineering Sciences*, Vol. 10(1), pp. C1-C8, doi: 10.21272/jes.2023.10(1).c1

## Design of Inorganic Polymer Composites for Electromagnetic Radiation Absorption Using Potassium Titanates

Lebedev V. V.<sup>1\*</sup>[0000-0001-6934-2349], Miroshnichenko D. V.<sup>1</sup>[0000-0002-6335-8742], Nyakuma B. B.<sup>2</sup>[0000-0001-5388-7950], Moiseev V. F.<sup>1</sup>[0000-0002-3217-1467], Shestopalov O. V.<sup>1</sup>[0000-0001-6268-8638], Vyrovets S. V.<sup>1</sup>[0000-0002-1944-0677]

<sup>1</sup> National Technical University “Kharkiv Polytechnic Institute”, 2, Kyrpychova St., 61002 Kharkiv, Ukraine;

<sup>2</sup> Hydrogen & Fuel Cell Laboratory, Institute of Future Energy, Universiti Teknologi Malaysia, BLOK S19 UTM Johor Bahru, 81310 Skudai, Johor Darul Takzim, Malaysia

### Article info:

Submitted: February 24, 2023  
 Received in revised form: May 8, 2023  
 Accepted for publication: May 15, 2023  
 Available online: May 19, 2023

### \*Corresponding email:

[vladimirlebedev1980@ukr.net](mailto:vladimirlebedev1980@ukr.net)

**Abstract.** This paper investigated the synthesis of inorganic polymer composites for electromagnetic radiation absorption using potassium titanates. The selected polyamide 6 and potassium polytitanate materials contain  $\text{TiO}_2$ ,  $\text{K}_2\text{CO}_3$ , and  $\text{KCl}$  obtained by charge sintering. Results showed that modification of polyamide 6 with sintering products in the form of a fine powder of potassium polytitanate that contains different phases  $\text{K}_2\text{O} \times 2\text{TiO}_2$ ,  $\text{K}_2\text{O} \times 4\text{TiO}_2$ , and  $\text{K}_2\text{O} \times 6\text{TiO}_2$  which increased their strength properties. With increased potassium titanates (PTT) synthesis, a gradual transition from di to potassium hexatitanates occurs  $\text{K}_2\text{O} \times 2\text{TiO}_2 - \text{K}_2\text{O} \times 4\text{TiO}_2 - \text{K}_2\text{O} \times 6\text{TiO}_2$ . The optimal content of potassium polytitanate was over 20 % by mass. To fully ensure the reinforcing effect due to the filling of potassium polytitanate polyamide 6, it is necessary to use whiskers  $\text{K}_2\text{O} \times 6\text{TiO}_2$ , which can be collected by the additional crystallization of the amorphous charge sintering product. By designing experimental-statistical mathematical models in equal regressions, mathematical optimization of inorganic polymer composites for electromagnetic radiation absorption using PTT was carried out.

**Keywords:** polymer, composite, potassium titanates, synthesis, electromagnetic radiation, absorption, strength properties.

## 1 Introduction

Nowadays, the production of various radio-electronic equipment is actively expanding. The main direction is radio-electronic equipment improving properties: reducing the size and energy losses, better accuracy, and speed, among others.

Many technologies are already in transit to a higher frequency range. So, there is a need for materials with appropriate electromagnetic characteristics, which can match and protect various electromagnetic ranges components.

Scientific progress and technological development have significantly increased electromagnetic pollution (EP) with significant costs to human health, safety, and the environment. This challenge is exacerbated by new sources of electromagnetic radiation (EMR) and energy transmission, such as cellular, satellite radio communication, navigation and radar systems, radio

engineering installations, medical devices, household appliances, and other technical equipment [1, 2].

The EMR generated by various sources also causes equipment and machinery malfunctions [3,4]. It should be noted that the presented division by types is conditional since most materials are systems that combine features of functioning different types [5, 6]. By their composition, most known radioabsorbing materials (RAM) are composite materials that include a dispersed absorber of electromagnetic waves and a dielectric matrix that creates absorber particles with volumetric distribution [7].

The absorber use can solve the problem of EMR dissipation in the material structure by one of two possible mechanisms: due to dielectric type losses (conductive fibers, dispersed graphite, and carbon black) and dielectric and magnetic simultaneous losses (e.g., ferromagnets and ferrites).

There are various measures aimed at protecting biological and technical objects from EMR exposure, which can be divided into several types [1-3]:

- organizational, such as distance protection (location at the maximum allowable distance from the EMR area action); time protection (restriction staying in the EMR zone); quantity protection (the EMR sources capacity must be the minimum necessary);
- therapeutic and preventive – increasing the body's resistance to EMR exposure; sanitary and preventive provision; treatment in emergencies;
- engineering and technical – particular protective materials use; individual and collective protection use; structures improvement.

The most significant scientific and practical interest is engineering and technical measures. Design and creation of special protective materials for shielding can help us. Two types of shielding are generally considered: shielding EMR sources from humans and shielding humans from EMR sources [6]. The screen's protective properties are based on the tension-weakening effect and electric field distortion in the space near the grounded metal object. Protection against the industrial frequency magnetic field is possible only at the product development or object design stage.

The field level reduction is achieved due to vector compensation since other shielding industrial frequency magnetic field methods are highly complicated and expensive [1]. Various radio reflectors (RR) and radio-absorbing materials are used for EMR shielding in radio frequency ranges. RR materials include various metals – iron, steel, copper, brass, and aluminum.

To protect against UHF, thin or perforated sheets, conductive films, metalized fabrics, or metal meshes are used, which have sufficient attenuation but differ from sheet materials in lower weight and cost.

Many materials that provide a high EMR shielding level have been designed to create flexible screens, protective clothing, and covers to ensure biological protection and electromagnetic compatibility of radio-electronic equipment [1, 7].

The RR materials' disadvantages for human protection include EMR reflection from curved surfaces of the protected object leads to interference of waves with different amplitudes and phases and, as a result, individual body parts irradiation [1]. This circumstance necessitates the RR materials used to reduce the EMR impact.

The radio-absorbing material reduces the overall EMR level reflection in the radio range due to the electromagnetic energy conversion [8].

EMR energy dissipation in its propagation in the material is due to the conduction, magnetization, and polarization processes [2]. From a technological point of view, radio-absorbing materials can be divided into two large groups.

The first group is materials or radio-absorbing coatings (RAC), and the second is structural radio-absorbing materials (RAM). Most often, the initial components

composition, the intended structure, and the structural RAC and RAM purpose are equal [2].

According to the operation principles, the representative class of designed RAC and RAM can be conditionally divided into the following types [1, 8, 9]:

1) gradient materials, the outer layer of which has radiophysical properties as close as possible to the free space characteristics, and the magnetic and dielectric permeability change values continuously in the direction of increase from the material surface layer to the depth;

2) materials, which action is based on the electrodynamic swamp principle, the distinguishing feature of which is uniformity, that is, the radiophysical characteristics practically do not change in the direction from the material surface to the depth (cellular, fibrous, and foam composites can be classified as such materials);

3) multiplanar, which are structures consisting of a large number of thin conductive or ferromagnetic films, separated by dielectric and interference-absorbing layers, which action is based on the total or partial mutual quenching of the electromagnetic wave incident and reflected from the metal substrate.

In most cases, anthropogenic electromagnetic pollution sources use energy in the entire UHF range of wavelengths, and absorbing materials should reduce the incident EMR reflection in a wide frequency range. In contrast, the effective reflection level should not exceed minus 15 dB (3 % of incident EMR capacity).

At the same time, an essential factor is the reduction of RAM's weight and size characteristics and the increase of resistance to environmental impact [10]. These requirements implementation is an urgent and complex scientific and applied task.

Today, a lot of radio-absorbing coatings and materials have been designed based on polymer binders and dispersed conductive (semiconductor) carbon-containing, metal (alloys and oxides), and magnetic fillers [11]. As a rule, multi-component systems are used to achieve the best radiophysical properties. It can be elastomers filled with dielectric and absorbing fillers. A metalized surface (substrate) is required for RAC to function. At the same time, a layer or several layers of RAC must be applied directly to the protected object, which is a complex and time-consuming technological process. Individual protective elements can be made from structural RAMs, produced separately from the object [1].

Depending on the purpose, such materials can be conventionally divided into rigid and flexible (elastic). The rigidity or flexibility degree will depend on the polymer matrix type and structure [11].

Rigid screens are used in mobile screens construction to locate service personnel in repair places, limit local UHF sources' impact, and separate or shield individual elements or blocks inside radio technical devices [12].

Flexible materials are used for the equipment covers and capes production and protective clothing for household and particular purposes production. It is essential that all materials, regardless of their composition and construction, are designed based on the specified requirements achievement [13].

Specified requirements are defined by the frequency band within which the effective level of EMR absorption is achieved. Different RAM types are well-known, but their receiving often challenging technological processes with low productivity. Thus, in works [2], RAM was received by the polymer melt extrusion method with structure fixation by cooling. A polyethylene terephthalate and polypropylene mixer modified by different conductive fillers was used as a polymer matrix.

Modern technologies are implemented on composite materials with different filler combinations, as no single-component material could achieve a high absorption capacity in a wide frequency band. Such composite materials are used for: biological object protection, electromagnetic device compatibility [14], and electromagnetic wave reflection reduction [15].

Various composite materials are actively used to protect against electromagnetic radiation, which corresponds to the sustainable development concept.

The main feature of composite materials is that they consist of two or more constituent components, which possess properties different from the component materials. Composites are easy to produce and provide new and unique physical-chemical properties (e.g., flexibility, high strength, and elasticity) unattainable for traditional materials.

## 2 Literature Review

According to the literature, typical materials for absorbing electromagnetic radiation are [3, 4]:

1) conductive powdered materials (coal, carbon black, graphite, metals – steel, cast iron, iron, aluminum, cobalt, lead, zinc, tin, copper, and metal salts) with spherical, cylindrical, flaky, and shaped particles.

2) conductive carbon, metal, and metal-carbon fibers, carbon fabrics, metal threads, plates, foil strips, wire scraps, meshes of a complex shape, gratings, resonant elements in the form of cross-shaped dipoles or closed conductors (rings) [6, 7];

3) metalized carbon and polymer fibers, fabrics, films, and microspheres;

4) magnetic fillers – ferrites of different chemical composition (mostly magnetically soft), as well as magnetic powders of metals and amorphous Fe alloys, Fe-Co-Ni alloys, and perm);

5) dispersed semiconductors – metal oxides, carbides and sulfides, silicon carbide, ferroceramics, charred organic silicon fabrics, and fibers;

6) dielectrics, in particular, easily polarized organic substances (retinyl Schiff salts) and biopolymers (chitin).

Many compositions of ferrite components used as absorbers of various ranges are described in modern scientific literature. In addition, such absorbers have an insufficiently wide band of operating frequencies [5].

By varying fillers concentration, it is possible to achieve the required electromagnetic properties such as high absorption coefficient, complex dielectric, magnetic permeability, and shielding level. In modern scientific

sources, there is much research on receiving materials for protection against electromagnetic radiation.

Most research concerns the design of effective materials for protection against electromagnetic radiation based on mixtures and composites of fillers with magnetic properties (such as ferrites [3,4], metals [5,6]) and various dielectrics – ceramic, polymer, and other matrices [7].

As an active phase (filler) of composites, carbon-containing materials (carbon nanotubes, graphite, carbonyl iron, and fullerenes) [7, 8] and ferrite powders [9, 10] are used widely. The composite materials research based on ferroelectrics and multiferroics is actively developing [11, 12].

Thermo-reactive polymer composites containing silicon carbide [12], carbon fibers [13], carbon black [14], and carbon nanotubes [15, 16] are also effective. The materials act as radio shielding materials and coatings due to the combination of absorption mechanisms.

This is due to their natural ferromagnetic resonance, the resonance of domain boundaries movement, multiple imprints, eddy current losses, and repolarization, among others. Such materials effectively protect against electromagnetic radiation, but their disadvantages include the complexity of synthesis and high cost.

Therefore, polymer composites for protection against electromagnetic radiation based on various thermoplastic matrices (polyvinyl butyral [17], polypropylene [18], and polyvinylidene chloride [19]) have been recently designed. Inorganic ferromagnetic fillers are used in polymer composites due to their better technological, operational, and economic characteristics.

Creating inorganic polymer composites (PIC) for electromagnetic radiation absorption using potassium titanates presents a unique perspective. Potassium titanates (PTT) with the general formula  $K_2Ti_nO_{2n+1}$ , consisting of titanium oxide layers and cations interlayers, form unique layered and tunnel crystal structures due to their high ion exchange, intercalation capacity, and photocatalytic activity properties. Depending on synthesis conditions and chemical composition, PTT is either an amorphous compound with a layered (flaky) structure or crystalline submicron- and nanofibers (potassium tetra-, hexa-, or octatitanate).

The layered structures of PTT are characterized by low interlayer shear energy and high reflection and absorption values in the visible and infrared spectral regions. Fibrous materials have high mechanical strength, low thermal conductivity, and good reflectivity in a wide spectral range. These properties make PTT a prospective material for producing functional materials, including fillers for polymeric materials.

Polyamide 6 hybrid composites reinforced with PTT whiskers  $K_2Ti_6O_{13}$  and liquid crystalline polymer have been reported in the literature [20]. The static tensile measurements showed that the tensile strength and modulus of the composite increased with increasing whisker content.

As potential fillers for composite materials that can absorb electromagnetic radiation, PTT with amorphous

layered structures is exciting due to their low interlayer shear energy and high values of [21-24].

Other characteristics of PPT include reflection coefficient and absorption radiation coefficient in the visible and infrared spectral regions as well as high intercalation ability and catalytic activity.

PTT's ability to absorb ultraviolet radiation or visible light with photosensitized modifications enhances its potential application in solar photovoltaic manufacture. Photoelectric characteristics of Nb-doped titanates were investigated in [25]. There is a high potential for using PTTs with various morphologies and structures to obtain composite materials for electromagnetic radiation absorption.

Researchers have designed and investigated polymer composites using complex filler systems such as graphite and humic substances [16, 26]. Similarly, our previous work [27] examined polymer composites for absorbing electromagnetic radiation based on thermoplastic polyamide 6 and silicon carbide. The proposed composite was relatively transparent in the millimeter frequency range and characterized by a small absorption coefficient. Hence, it is essential to consider using PTT for effective composite materials development for electromagnetic radiation absorption.

The article aims to design and characterize inorganic polymer composites for electromagnetic radiation absorption using PTT. To achieve this aim, the following tasks were set:

- to research sintering products of titanium oxide  $\text{TiO}_2$ , potassium carbonate  $\text{K}_2\text{CO}_3$  and potassium chloride KCl at different temperature conditions;
- to determine the influence of the modification of polyamide 6 with PPT on their strength properties;
- to design experimental-statistical mathematical models of strength properties of inorganic polymer composites for electromagnetic radiation absorption using PTT.

### 3 Research Methodology

The following materials were used to design the inorganic polymer composites for electromagnetic radiation absorption:

- polyamide 6 (Grodnamid PA6-L-211/311). It is the baseline injection moulding polymer composite material on the base of PA-6 with modifying additives that improve its injection properties: surface quality of moulded articles, filling of the mould, and easier demoulding of finished articles;
- titanium oxide  $\text{TiO}_2$ ;
- potassium carbonate  $\text{K}_2\text{CO}_3$ ;
- potassium chloride KCl.

Polymer inorganic composites for electromagnetic radiation absorption were synthesized by extruding pre-prepared raw materials in a single-screw laboratory extruder at 170-200 °C and a screw speed of 30-100 turns per minute.

The study of impact strength and breaking stress during the bending of the samples was carried out on a

pendulum head according to ISO 180 and ISO 178, respectively, without notching at a temperature of 20 °C.

Microscope analysis was performed on the Olympus GX Inverted Microscope LECO Corporation (USA).

PTT was received by charge sintering that contains  $\text{TiO}_2$ ,  $\text{K}_2\text{CO}_3$ , and KCl. The  $\text{TiO}_2$ : $\text{K}_2\text{O}$  was used in the ratio (in moles) from 4:1 to 7:1 with the addition from the mass S  $\text{TiO}_2$ : $\text{K}_2\text{O}$  20 % wt. KCl.

The materials were first crushed, mixed, passed through a sieve of 60-300  $\mu\text{m}$  and then heated in a muffle furnace under oxidative conditions (Air) for 1-3 hours at 900 °C (product diameter is 0.005-0.100  $\mu\text{m}$  and a length is 1-10  $\mu\text{m}$ ).

Next, the temperature was ramped to 1000 °C (product diameter 0.1-0.6  $\mu\text{m}$  and length 5-60  $\mu\text{m}$ ) and then finally at 1100 °C (product diameter 0.6-2.0  $\mu\text{m}$  and length 60-600  $\mu\text{m}$ ). The salt matrix (KCl) separated from unreacted particles by leaching with a slightly acidic solution with stirring or deionized water at 90 °C.

The precipitate was then filtered and washed until the chloride ion was removed entirely. Lastly, it was dried at 105-120 °C to a residual moisture content of 0.5-1.0 % wt.

### 4 Results and Discussion

Figures 1, 2 show the batch sintering stage, the resulting sintering products, and the finished product after drying.



Figure 1 – Photo of the charge sintering process (A) and the finished product after drying (B)

As observed in Figure 2, the sintering product after drying is a fine powder of PTT with a particle size of 1-5  $\mu\text{m}$ .

Figure 3 shows a microscope image of PTT received by different temperature sintering of composition  $\text{TiO}_2$ ,  $\text{K}_2\text{CO}_3$ , and KCl. From microscopic images of PTT obtained at different temperature conditions, it can be seen that with an increase in the synthesis temperature, a crystalline phase is formed along the edges of PTT particles in the form of filamentous crystals.



Figure 2 – Photo of the finished product of PTT after synthesis (A) and after drying (B)

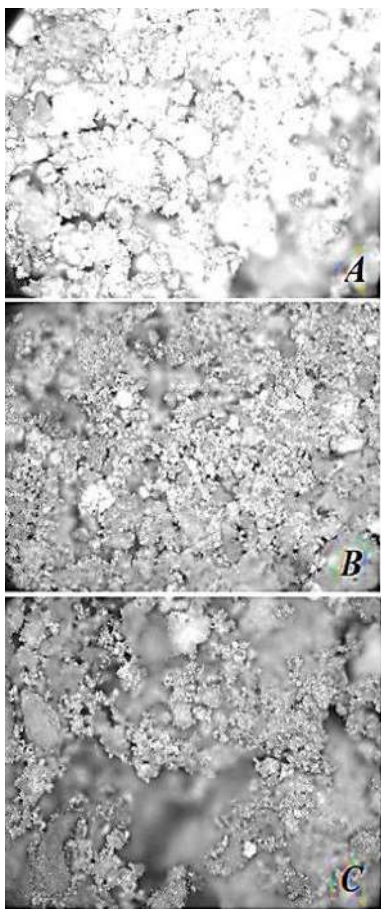


Figure 3 – Microscope image (the degree of increase – 100) of PTT obtained at different sintering temperatures for  $\text{TiO}_2$ ,  $\text{K}_2\text{CO}_3$ , and  $\text{KCl}$  compositions: A – 900 °C; B – 1000 °C; C – 1100 °C

This observation could be ascribed to the direct formation of an amorphous phase in the PTT, which also correspondent with data in the articles [21, 22]. With an increase in the process of PTT synthesis, a gradual transition from di to potassium hexatitanates occurs  $\text{K}_2\text{O} \times 2\text{TiO}_2 - \text{K}_2\text{O} \times 4\text{TiO}_2 - \text{K}_2\text{O} \times 6\text{TiO}_2$  [24, 25].

Next, the influence of PTT and the introduction of the polyamide 6 strength properties complex was examined, as shown in Figures 4-5.

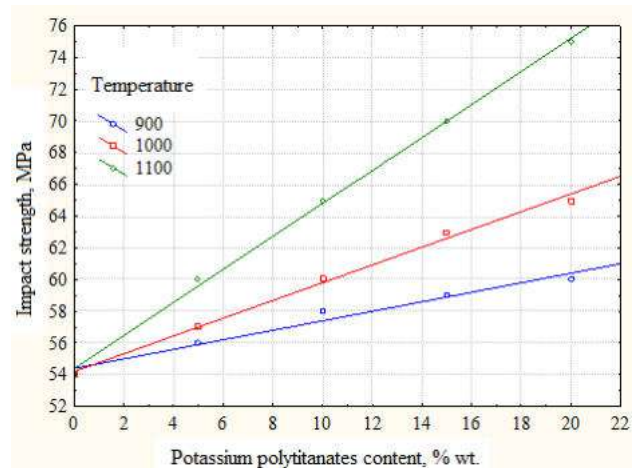


Figure 4 – Effect of on impact strength of polyamide 6 PPT particles at different temperature conditions with regression equations:  $\text{Impact strength}_{900} = 54.4 + 0.3 \cdot \text{PTT}$ ;  $\text{Impact strength}_{1000} = 54.2 + 0.56 \cdot \text{PTT}$ ;  $\text{Impact strength}_{1100} = 54.4 + 1.04 \cdot \text{PTT}$

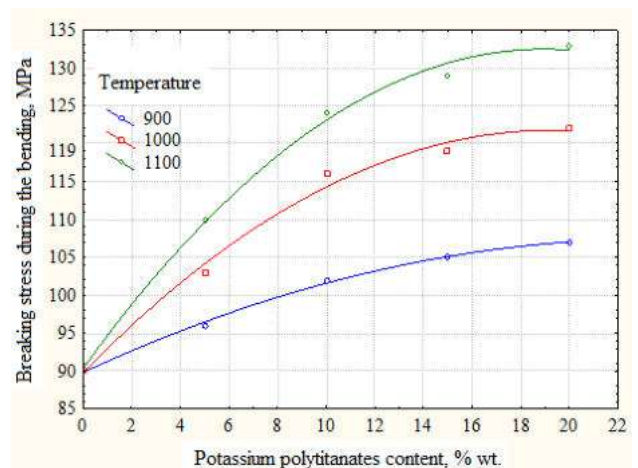


Figure 5 – Effect of breaking stress during the bending of polyamide 6 PPT particles at different temperature conditions with regression equations:  $\text{Breaking stress during the bending}_{900} = 89.8 + 1.49 \cdot \text{PTT} - 0.031 \cdot \text{PTT}^2$ ;  $\text{Breaking stress during the bending}_{1000} = 89.7 + 3.31 \cdot \text{PTT} - 0.086 \cdot \text{PTT}^2$ ;  $\text{Breaking stress during the bending}_{1100} = 90.3 + 4.44 \cdot \text{PTT} - 0.117 \cdot \text{PTT}^2$

From Figures 4, 5, polyamide 6 with PPT modification increased their strength properties. Concurrently, the reinforcing effect of PTT concerning the strength properties of polyamide 6 increased with

higher PTT synthesis temperatures due to the formation of crystalline filamentous phases, which also corresponds with data in the article [28]. It was also observed that the optimal PTT content is over 20 % wt.

It is necessary to introduce a dispersed conductive filler into its composition to provide inorganic polymer composites for electromagnetic radiation absorption high strength properties [15]. Different geometric shapes and sizes of particles are used as conductive fillers. The particles' shapes are spherical (soot, metal powders, colloidal graphites, metalized microspheres), lamellar (expanded graphite, metal powders after attrition treatment, metalized mica), and needle-like (carbon fibers, metalized fibers, needles) [1, 2].

Figures 6, 7 present the 3D plot of the mathematical model based on regression equations developed in MathCad Prime 6.0. For this model, theoretical calculations of the predicted impact strength and breaking stress values during bending inorganic polymer composites for electromagnetic radiation absorption were performed. The results are presented in 3D graphics for forecasting the strength properties of inorganic polymer composites for electromagnetic radiation absorption using PTT in different synthesis temperatures.

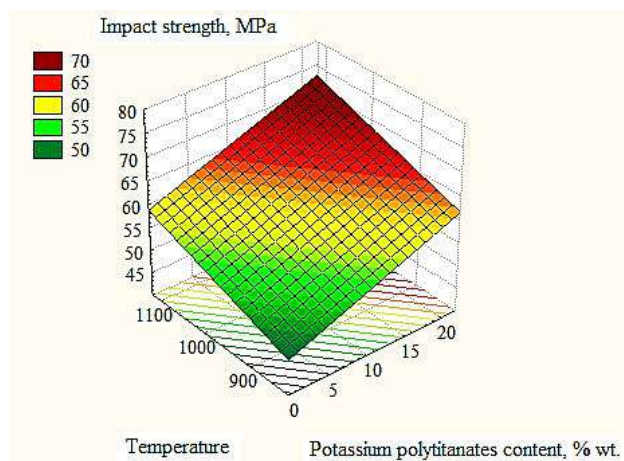


Figure 6 – The 3D plot for forecasting the impact strength of inorganic polymer composites for electromagnetic radiation absorption using PTT with regression equations: Impact strength =  $17.3 + 0.63 \cdot \text{PTT} + 0.037 \cdot \text{Temperature}$

The results indicate that depending on the PTT content, the impact of synthesis temperature is the most effective in terms of increasing the polymer inorganic composites for electromagnetic radiation absorption strength properties. Forecasting researches on definition the most effective structure of the polymer inorganic composites for electromagnetic radiation absorption are carried out.

The possibility of forming various products of inorganic polymer composites for electromagnetic radiation absorption is shown, with particular attention to its deserved composition with a content of PTT over 20 % wt.

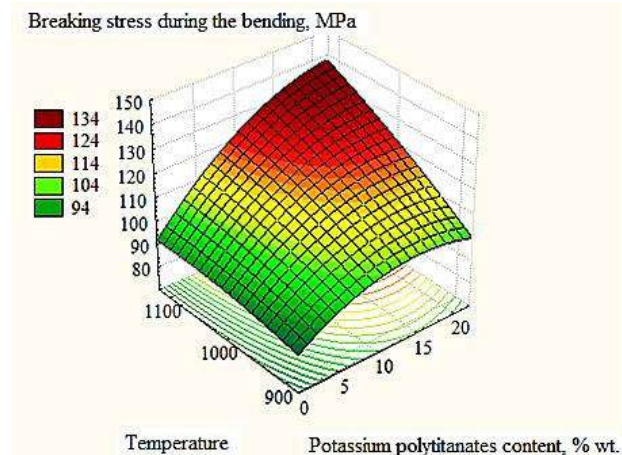


Figure 7 – The 3D plot for forecasting the breaking stress during the bending of inorganic polymer composites for electromagnetic radiation absorption using PTT with regression equations: Breaking stress during the bending =  $-73.1 - 3.12 \cdot \text{PTT} + 0.304 \cdot \text{Temperature} - 0.0781 \cdot \text{PTT}^2 + 0.0062 \cdot \text{PTT} \cdot \text{Temperature} - 0.0001 \cdot \text{Temperature}^2$

The increase of breaking stress during bending also indicates the manufacturability of the inorganic polymer composites for electromagnetic radiation absorption. In addition, it even slightly «softens» the original rather rigid polyamide 6. The simulation allowed obtaining models for forecasting the strength properties of inorganic polymer composites for electromagnetic radiation absorption depending on their chemical composition, which can be adapted to any content and temperature synthesis of PTT.

## 5 Conclusions

The study proposed using inorganic polymer composites for electromagnetic radiation absorption using PTT. The charge-sintered PTT containing  $\text{TiO}_2$ ,  $\text{K}_2\text{CO}_3$ , and KCl were utilized as fillers in the polyamide 6 polymer composite. The sintering products were found to consist of a fine powder of potassium polytitanate containing different phases  $\text{K}_2\text{O} \times 2\text{TiO}_2$ ,  $\text{K}_2\text{O} \times 4\text{TiO}_2$ , and  $\text{K}_2\text{O} \times 6\text{TiO}_2$ . With an increase in the PTT synthesis process, a gradual transition from di to potassium hexatitanates occurs  $\text{K}_2\text{O} \times 2\text{TiO}_2 - \text{K}_2\text{O} \times 4\text{TiO}_2 - \text{K}_2\text{O} \times 6\text{TiO}_2$ .

Modifying polyamide 6 with PTT increased their strength properties, whereas the optimal content of PTT was over 20 % by mass. By designing experimental-statistical mathematical models in equal regressions, mathematical optimization of strength properties of inorganic polymer composites for electromagnetic radiation absorption using PTT was performed. The results are presented in the 3D plot to forecast the strength properties of inorganic polymer composites for electromagnetic radiation absorption using PTT at different synthesis temperatures. The simulation 3D graphic allowed to forecasting the strength properties of polymer inorganic composites for electromagnetic radiation absorption depending on their chemical

composition, which can be adapted to any content and temperature synthesis of PTT.

Perspective directions for future research are to determine the degree of absorption of electromagnetic radiation developed polymer composites based on polyamide 6 and PTT and also to explore the potential applications of these composites in various industries.

## References

1. Tong, X.C. (2008). *Advanced materials and design for electromagnetic interference shielding* (1st ed.). CRC Press, Boca Raton, USA, doi: 10.1201/9781420073591.
2. Yu, W.C., Zhang, G.Q., Liu, Y.H., Xu, L., Yan, D.X., Huang, H.D., Tang, J.H., Xu, J.Z., Li, ZM (2019). Selective electromagnetic interference shielding performance and superior mechanical strength of conductive polymer composites with oriented segregated conductive networks. *Chemical Engineering Journal*, Vol. 373, pp. 556-564, doi: 10.3390/nano10040768.
3. Wang, F., Wang, X., Zhu, J.F., Yang, H.B., Kong, X.G., Liu, X. (2016). Lightweight NiFe<sub>2</sub>O<sub>4</sub> with controllable 3D network structure and enhanced microwave absorbing properties. *Scientific Reports*, Vol. 6, pp. 37892, doi: 10.1038/srep37892.
4. Lv, R., Kang, F., Gu, J., Gui, X., Wei, J., Wang, K., Wu, D. (2008). Carbon nanotubes filled with ferromagnetic alloy nanowires: lightweight and wide-band microwave absorber. *Applied Physics Letters*, Vol. 93, pp. 223105, doi: 10.1063/1.3042099.
5. Liu, Q.H., Xu, X.H., Xia, W.H., Che, R.C., Chen, C., Cao, Q., He, J. (2015). Dependency of magnetic microwave absorption on surface architecture of Co<sub>20</sub>Ni<sub>80</sub> hierarchical structures studied by electron holography. *Nanoscale*, Vol. 7, pp. 1736–43, doi: 10.1039/c4nr05547k.
6. Lv, H.L., Jia, G.B., Wang, M., Shang, C.M., Zhang, H.Q., Du, Y.W. (2014). Hexagonal-cone like of Fe<sub>50</sub>Co<sub>50</sub> with broad frequency microwave absorption: effect of ultrasonic irradiation time. *Journal of Alloys and Compounds*, Vol. 615, pp. 1037–42, doi: 10.1016/j.jallcom.2014.07.118.
7. Menga, F., Wanga, H., Huang, F., Guoa, Y., Wanga, Z., Huib, D., Zhou, Z. (2018). Graphene-based microwave absorbing composites: A review and prospective. *Composites Part B*, Vol. 137, pp. 260–277, doi:10.1016/j.compositesb.2017.11.023
8. Bibi, M., Abbas, S.M., Ahmad, N., Muhammad, B., Iqbal, Z., Rana, U.A., Khane, S.U. (2017). Microwaves absorbing characteristics of metal ferrite/multiwall carbon nanotubes nanocomposites in X-band. *Composites Part B: Engineering*, Vol. 114, pp. 139–48, doi: 10.1016/j.compositesb.2017.01.034.
9. Rusly, S.N.A., Matori, K.A., Ismail, I., Abbas, Z., Awang, Z., Zulkimi, M.M.M., Idris, F.M., Zaid, M.H.M., Zulfikri, N.D. (2018). Microwave absorption properties of single- and double-layer coatings based on strontium hexaferrite and graphite nanocomposite. *Journal of Materials Science: Materials in Electronics*, Vol. 29, pp. 14031-14045, doi:10.1007/s10854-018-9535-9.
10. Wanasinghe, D., Aslani, F. (2019). A review on recent advancement of electromagnetic interference shielding novel metallic materials and processes. *Composites Part B: Engineering*, Vol. 176, pp. 107207, doi: 10.1016/j.compositesb.2019.107207.
11. Rusly, S.N.A., Ismail, I., Matori, K.A., Abbas, Z., Shaari, A.H., Awang, Z., Ibrahim, I.R., Idris, F.M., Mohd Zaid, M.H., Mahmood, M.K.A., Hasan, I.H. (2020). Influence of different BFO filler content on microwave absorption performances in BiFeO<sub>3</sub>/epoxy resin composite. *Ceramics International*, Vol. 4, pp. 737-746, doi: 10.1016/j.ceramint.2019.09.027.
12. Shah, A., Wang, Y.H., Huang, H., Zhang, L., Wang, D.X., Zhou, L., Duan, Y.P., Dong, X.L., Zhang, Z.D. (2015). Microwave absorption and flexural properties of Fe nanoparticle/carbon fiber/ epoxy resin composite plates. *Composite Structures*, Vol. 131, pp. 1132–41, doi: 10.1016/j.compstruct.2015.05.054.
13. Al-Ghamdi, A.A., Al-Hartomy, O.A., A-Solamy, F.R., Dishovsky, N., Malinova, P., Atanasova, P., Atanasovde, N. (2016). Conductive carbon black/magnetite hybrid fillers in microwave absorbing composites based on natural rubber. *Composites Part B: Engineering*, Vol. 96, pp. 231–41, doi:10.1016/j.compositesb.2016.04.039.
14. Hu, J.T., Zhao, T.K., Peng, X.R., Yang, W.B., Ji, X.L., Li, T.H. (2018). Growth of coiled amorphous carbon nanotube array forest and its electromagnetic wave absorbing properties. *Composites Part B: Engineering*, Vol. 134, pp. 91–7, doi: 10.1016/j.compositesb.2017.09.071.
15. Makarova, T.L., Geydt, P., Zakharchuk, I., Lahderanta, E., Komlev, A.A., Zyrianova, A.A., Kanygin, M.A., Sedelnikova, O.V., Suslyayev, V.I., Bulusheva, L.G., Okotrub, A.V. (2016). Correlation between manufacturing processes and anisotropic magnetic and electromagnetic properties of carbon nanotube/polystyrene composites. *Composites Part B: Engineering*, Vol. 91, pp. 505–12, doi: 10.1016/j.compositesb.2016.01.040.
16. Lebedev, V., Miroshnichenko, D., Z. Xiaobin, Pyshyev, S., Savchenko, D., Nikolaichuk, Y. (2021). Use of Humic Acids from Low-Grade Metamorphism Coal for the Modification of Biofilms Based on Polyvinyl Alcohol. *Petroleum and Coal*, Vol. 63(4), pp. 953-962.

17. Zhu, G., Cui, X., Zhang, Y., Chen, S., Dong, M., Liu, H., Shao, Q., Ding, T., Wu, S., Guo, Z. (2019). Poly (vinyl butyral)/graphene oxide/poly (methylhydrosiloxane) nanocomposite coating for improved aluminum alloy anticorrosion. *Polymer*, Vol. 172, pp. 415-422, doi:10.1016/j.polymer.2019.03.056.
18. Lai, H., Li, W., Xu, L., Wang, X., Jiao, H., Fan, Z., Lei, Z., Yuan, Y. (2020). Scalable fabrication of highly crosslinked conductive nanofibrous films and their applications in energy storage and electromagnetic interference shielding. *Chemical Engineering Journal*, Vol. 400, pp. 125322, doi: 10.1016/j.cej.2020.125322.
19. Liang, C., Hamidinejad, M., Ma, L., Wang, Z., Park, C.B. 2020. Lightweight and flexible graphene/SiC-nanowires/poly(vinylidene fluoride) composites for electromagnetic interference shielding and thermal management. *Carbon*, Vol. 156, pp. 58-66, doi:10.1016/j.carbon.2019.09.044.
20. Tjong, S.C., Meng, Y.Z. (1999). Properties and morphology of polyamide 6 hybrid composites containing potassium titanate whisker and liquid crystalline copolyester. *Polymer*, 40(5), pp. 1109-1117, doi: 10.1016/S0032-3861(98)00340-1.
21. Kim, T.W., Hur, S.G., Hwang, S.-J., Choy, J.-H. (2006). Layered titanate-zinc oxide nanohybrids with mesoporosity. *Chemical Communications*, Vol. 23, pp. 220-222, doi:10.1039/b511471c.
22. Kim, T.W., Hwang, S.-J., Park, Y., Choi, W., Choy, J.H. (2007). Chemical bonding character and physicochemical properties of mesoporous zinc oxide-layered titanate nanocomposites. *The Journal of Physical Chemistry C*, Vol. 111, pp. 1658-1664, doi: 10.1039/b511471c.
23. Kim, T.W., Han, A.R., Hwang, S.-J., Choy, J.-H. (2007). Local atomic arrangement and electronic configuration of nanocrystalline zinc oxide hybridized with redoxable 2D lattice of manganese oxide. *The Journal of Physical Chemistry C*, Vol. 111, pp. 16774-16780, doi: 10.1021/jp012704g.
24. Kim, T.W., Ha, H.-W., Paek, M.-J., Hyun, S.H., Baek, I., Choy, J., Hwang, S. (2008). Mesoporous iron oxide-layered titanate nanohybrids: soft-chemical synthesis, characterization, and photocatalyst application. *The Journal of Physical Chemistry C*, Vol. 112, pp. 14853-14862, doi: 10.1021/jp805488h.
25. Long, L., Wu, L., Yang, X., Li, X. (2014). Photoelectrochemical Performance of Nb-doped TiO<sub>2</sub> Nanoparticles Fabricated by Hydrothermal Treatment of Titanate Nanotubes in Niobium Oxalate Aqueous Solution. *Journal of Materials Science & Technology*, Vol. 30(8), pp. 765-769, doi: 10.1016/j.jmst.2014.03.010.
26. Lebedev, V., Miroshnichenko, D., Xiaobin, Z., Pyshyev, S., Savchenko, D. (2021). Technological Properties of Polymers Obtained from Humic Acids of Ukrainian Lignite. *Petroleum and Coal*, Vol. 63(3), pp. 646-654.
27. Lebedev, V., Kryvobok, R., Cherkashina, A., Bliznyuk, A., Lisachuk, G., Tykhomyrova, T. (2022). Design and research polymer composites for absorption of electromagnetic radiation. *2022 IEEE 3rd KhPI Week on Advanced Technology (KhPIWeek)*. National Technical University "Kharkiv Polytechnic Institute", Kharkiv, Ukraine, pp. 1-4, doi: 10.1109/KhPIWeek57572.2022.9916467.
28. Yu, D., Wu, J., Zhou, L., Xie, D., Wu, S. (2000) The dielectric and mechanical properties of a potassium-titanate-whisker-reinforced PP/PA blend. *Composites Science and Technology*, Vol. 60, pp. 499-508, doi: 10.1016/S0266-3538(99)00149-9.





*Kashytskyi V. P., Sadova O. L., Melnychuk M. D., Golodyuk G. I., Klymovets O. B. (2023). Structuring of modified epoxy composite materials by infrared spectroscopy. Journal of Engineering Sciences, Vol. 10(1), pp. C9-C16, doi: 10.21272/jes.2023.10(1).c2*

## Structuring of Modified Epoxy Composite Materials by Infrared Spectroscopy

Kashytskyi V. P. <sup>[0000-0003-2346-912X]</sup>, Sadova O. L. <sup>[0000-0002-6152-5447]</sup>, Melnychuk M. D. <sup>[0000-0001-6813-250X]</sup>,  
Golodyuk G. I. <sup>[0000-0002-9740-5498]</sup>, Klymovets O. B. <sup>[0009-0002-6889-1199]</sup>

Lutsk National Technical University, 75, Lvivska St., 43018 Lutsk, Ukraine

### Article info:

Submitted: March 2, 2023  
Received in revised form: May 8, 2023  
Accepted for publication: May 18, 2023  
Available online: May 25, 2023

### \*Corresponding email:

[v.kashytskyi@lntu.edu.ua](mailto:v.kashytskyi@lntu.edu.ua)

**Abstract.** A comparative evaluation of the structuring processes of the epoxy polymer system with epoxy polymers modified with polyvinyl chloride solution and epoxy composites filled with finely dispersed titanium oxide powder was carried out. Analysis of the infrared (IR) absorption spectra of the studied epoxy polymer and epoxy composite materials showed the presence of deformation and valence vibrations of certain groups of atoms. The oscillations of groups of atoms with double bonds and regions of existence of triple bonds were also revealed. In the region of high frequencies, absorption bands correspond to valence vibrations of groups containing a hydrogen atom. The presence of triple bonds in the epoxy polymer system was determined, indicating unreacted functional groups. This fact corresponds to the low content of the gel fraction of unmodified epoxy polymers after heat treatment and indicates the formation of a system with insufficient chemical bonds. The absorption bands of the epoxy composite material filled with titanium oxide powder are characterized by a lower optical density and a larger peak area compared to the bands of the unmodified epoxy polymer, which indicates the formation of a higher number of crosslinking nodes of the epoxy composite material. The introduction of polyvinyl chloride into the composition of the epoxy polymer system increases the degree of structuring of epoxy polymers. However, a smaller number of formed chemical bonds of the modified epoxy polymer was recorded compared to epoxy composites containing titanium oxide particles. The highest degree of structuring is provided in polyvinyl chloride-modified epoxy composites containing titanium oxide powder due to intensive structuring and formation of double and triple bonds.

**Keywords:** particle surface modification, finely dispersed filler, titanium oxide powder, polyvinyl chloride solution, optical density, infrared spectrum.

## 1 Introduction

Increasing the service life of military and transport aviation equipment is strategically essential for developing the economy and ensuring the country's defense capability. The complex impact of atmospheric factors, abrasive particles, and aggressive environments causes intense destruction of the surface of aviation equipment parts, which leads to a loss of structural strength and functionality, requiring the replacement of parts or restoration of damaged surfaces.

The most common way to protect aviation equipment from the complex impact of atmospheric factors is by using polymer-based composite coatings, which have a low density and high resistance to aggressive environments. In particular, compositions on an epoxy binder are technological, which allows modifying the structure of the polymer mesh, introducing dispersed

fillers, and forming a coating of a complex profile without using specific and expensive equipment. Epoxy composite coatings provide high adhesive strength, hardness, and chemical resistance, allowing them to protect the outer surface of fuselages and jet engine housings from destruction.

The importance of the work is the study of the peculiarities of structuring the developed wear-resistant epoxy composite coatings intended for aviation equipment, which will increase the service life of the products and reduce the costs of repair and maintenance.

## 2 Literature Review

According to scientific and technical literature, the most effective way to increase thermal resistance is to create a low-permeable protective layer on the surface of the filler containing refractory compounds resistant to oxidation.

Necessary conditions for choosing finish substances are thermodynamic compatibility with all components of the composite and oxidation resistance in the entire working temperature range [1, 2].

Finish substances must provide the following:

- reduction of the level of residual stresses (due to reduction of binder shrinkage);
- complete wetting of the surface of the filler;
- displace water vapor and air from microcracks;
- fill microdefects in the surface layer of the filler.

Finishing treatment in the technology of creating polymer composites is a critical stage since the formed protective layer must relax cracks at the “filler-matrix” interface, transfer mechanical load from the matrix to the filler, maintain chemical and microstructural stability in the entire working temperature range, and be resistant to oxidation. Therefore, the finishing treatment creates an optimal ratio between high and very low matrix adhesion with the filler. High adhesion will contribute to the realization of the physical and mechanical properties characteristic of the matrix with its high crack resistance and fragility. Low adhesion will not lead to the dissipation of fracture energy at the “filler-matrix” interface, which will also not increase mechanical properties [3, 4].

In the last stage, finishing is carried out and used as reinforcing additives. The finishing treatment aims to improve technological properties: facilitate the formation process, protect against mechanical damage during processing, and improve the adhesion of the polymer matrix to the filler when used as a reinforcing component of polymer composite materials. Surface modification of nanofillers can increase the hydrophobicity of fillers, improve interfacial adhesion due to chain entanglement or chemical bonding, and eliminate the loose structure of filler agglomerates [5]. The composition of coupling agents, usually, is an emulsion or suspension consisting of polymer components – emulsifiers, film-forming, antistatic and coupling agents that contribute to the leveling and protection of the filler, improving its wettability.

In order to improve the interphase interaction of composite components, chemical modifications of wood fibers with alkalis and coupling agents are used. When processing fillers with coupling agents, their concentrations are the main parameters. Insufficient content of coupling agents leads to poor adhesion between the fillers and the matrix. On the contrary, an overdose will lead to severe agglomeration of fillers. Therefore, the optimal content of coupling agents is necessary for the best characteristics of composite materials [4].

The surface of metal powders is often covered with silane finishes to increase the adhesive interaction on the interface and reduce moisture adsorption [6]. Treatment of hemp fibers with an alkali solution and then with a solution of  $\text{KMnO}_4$  or silane (Si69) increases composites' tensile strength and density based on natural rubber without changing their thermal stability [7]. Polyvinyl alcohol strengthens the interfacial bond between the polymer

matrix and fillers, increasing mechanical properties, thermal stability, and fire resistance [8].

An effective way to improve adhesion between components is to treat fillers with oxidation or ozonation [9]. Ozone treatment is one of the most promising surface treatment methods, as it requires low costs and is an environmentally friendly surface treatment. Ozone treatment can control the amount of oxygen functional groups on the surface of carbon nanotubes according to the concentration of ozone [10].

According to published data, polyimides are widely used as finish substances. After combining with polyimide binders, these finishes ensure the performance of polymer composite materials at elevated temperatures. In the case of using an epoxy binder, the polyimide finish substance contributes to a better hardening of the resin in the boundary layers [11].

The problem of surface modification of fillers is relevant in connection with the wide use of thermosetting resins as binders, particularly epoxy resins [12], the problem of surface modification of fillers is relevant. Information on the surface treatment of fillers for this binder is limited. Also, there is no specific data on the compositions of the decorated compositions and the conditions of their application.

### 3 Research Methodology

The epoxy-diane resin of the ED-20 (DSTU 2093-92) was selected as the starting material for forming the polymer matrix. Polyethylene polyamine – PEPA (TU 20.1-22944575-002-2017) was used to harden epoxy compositions. Additives-reinforced epoxy polymers are finely dispersed titanium oxide powder ( $\text{TiO}_2$ ), polyvinyl chloride powder, and cyclohexanone.

Infrared (IR) spectra were recorded on an IRAffinity-1S spectrophotometer (Japan) in the frequency range of 400-4000  $\text{cm}^{-1}$  by the single-beam method in reflected light. The spectrum sweep by wave numbers  $\lambda^{-1} = \nu$  was carried out on the diagram within 225 mm in the range of selected frequencies. Wave numbers were determined using the IRsolution computer program. The error in determining the wave number  $\nu = \pm 0.01 \text{ cm}^{-1}$ , determining the accuracy of the peak location  $\pm 0.125 \text{ cm}^{-1}$ . The photometric accuracy was  $\pm 0.2 \%$  with software control of the slit and the integration duration  $t = 10 \text{ s}$ . The integration step  $\Delta\lambda = 4.0 \text{ cm}^{-1}$ . The material was pre-dried at a temperature  $T = (373 \pm 2) \text{ K}$  for 20 min and mixed in an agate mortar with KBr powder. Then on a hydraulic press with a force  $F = 20 \text{ MPa}$ , samples were formed in the ratio: material under study – 1 mg, KBr – 300 mg.

Quantitative and qualitative analysis (presence of active groups and segments in the structure) of epoxy composite materials was carried out using IR spectroscopy. Most of the IR absorption bands of polymers correspond to specific vibrations of atoms in the polymer chain. IR absorption bands of the same types of vibrations of the atomic group of various substances are located in a specific range of the IR spectrum. The position of absorption maxima on IR spectra characterizes the nature of the substance. The

number of absorption bands, their width, shape, and intensity are determined by the structure and chemical composition of the substance. In order to study the relative content of specific functional groups in polymers, the “internal standard” method is used, that is, the ratio of the absorption intensities of two bands, expressed in terms of the optical density ( $D$ ) and the value of the half-width of the absorption band ( $b$ ,  $\text{cm}^{-1}$ ) [13].

The content of the gel-sol fraction determined the degree of hardening of materials and coatings. The method is based on the ability of a part of the material (a film) not bound into a polymer mesh to be washed out by an organic solvent in a Soxhlet extractor, which operated in automatic mode.

## 4 Results

The IR absorption spectra of the developed epoxy polymer and epoxy composite materials were analyzed (Table 1).

Table 1 – Composition and formation technology of epoxy composite materials

Composition No.	Composition and formation technology
1	ED-20 + PEPA
2	(ED-20 + PEPA) + $\text{TiO}_2$
3	(ED-20 + PEPA) + (PVH + Cyclohexanone) for 1 hour
4	(ED-20 + PEPA) + (PVH + Cyclohexanone) for 1 hour + $\text{TiO}_2$
5	(ED-20 + PEPA) + [(PVH + Cyclohexanone) 1 hour + $\text{TiO}_2$ ] from surface modification of filler particles within 10 min

IR spectra revealed deformation and valence vibrations of certain groups of atoms. In a  $400\text{-}1500\text{ cm}^{-1}$  frequency range, there are deformation vibrations of  $\text{-N-H-}$ ,  $\text{-O-H-}$ , and  $\text{-C-H-}$  and valence vibrations of  $\text{-C-C-}$ ,  $\text{-C-O-}$ , and  $\text{-C-N-}$  groups. Group vibrations of

compounds with double bonds ( $\text{C=C}$ ,  $\text{C=O}$ , and  $\text{C=N}$ ) are present in a  $1500\text{-}1800\text{ cm}^{-1}$  frequency range. These oscillations are not purely valence since adjacent angles and bonds play a large part. The frequency interval of  $2000\text{-}2300\text{ cm}^{-1}$  corresponds to the region of existence of triple bonds ( $\text{C}\equiv\text{C}$  and  $\text{C}\equiv\text{N}$ ). In a high-frequency region ( $2700\text{-}4000\text{ cm}^{-1}$ ), absorption bands correspond to valence vibrations of groups containing a light hydrogen atom ( $\text{C-H}$ ,  $\text{N-H}$ , and  $\text{O-H}$ ).

For the epoxy polymer sample No. 1, containing an epoxy oligomer and a polyethylene polyamine hardener, the following absorption bands were detected in the area of deformation vibrations (Figure 1):

- optical density  $D = 0.39$  and a peak area  $S = 13.8\%$  at frequency  $\nu = 561.3\text{ cm}^{-1}$ ;
- optical density  $D = 0.31$  and peak area  $S = 44.8\%$  at frequency  $\nu = 827.5\text{ cm}^{-1}$ ;
- optical density  $D = 0.32$  and peak area  $S = 26.0\%$  at frequency  $\nu = 1035.8\text{ cm}^{-1}$ ;
- optical density  $D = 0.31$  and peak area  $S = 19.7\%$  at frequency  $\nu = 1182.4\text{ cm}^{-1}$ ;
- optical density  $D = 0.30$  and peak area  $S = 16.8\%$  at frequency  $\nu = 1247.9\text{ cm}^{-1}$ ;
- optical density  $D = 0.28$  and peak area  $S = 10.3\%$  at frequency  $\nu = 1454.3\text{ cm}^{-1}$ .

In the range of valence vibrations, there are absorption bands corresponding to double bonds:

- optical density  $D = 0.27$  and peak area  $S = 10.3\%$  at frequency  $\nu = 1514.1\text{ cm}^{-1}$ ;
- optical density  $D = 0.35$  and peak area  $S = 11.8\%$  at frequency  $\nu = 1606.7\text{ cm}^{-1}$ ;
- optical density  $D = 0.48$  and peak area  $S = 3.5\%$  at frequency  $\nu = 1747.5\text{ cm}^{-1}$ .

They also correspond to triple-bond tongues:

- optical density  $D = 0.51$  and peak area  $S = 12.0\%$  at frequency  $\nu = 2069.6\text{ cm}^{-1}$ ;
- optical density  $D = 0.51$  and peak area  $S = 24.2\%$  at frequency  $\nu = 2320.4\text{ cm}^{-1}$ .

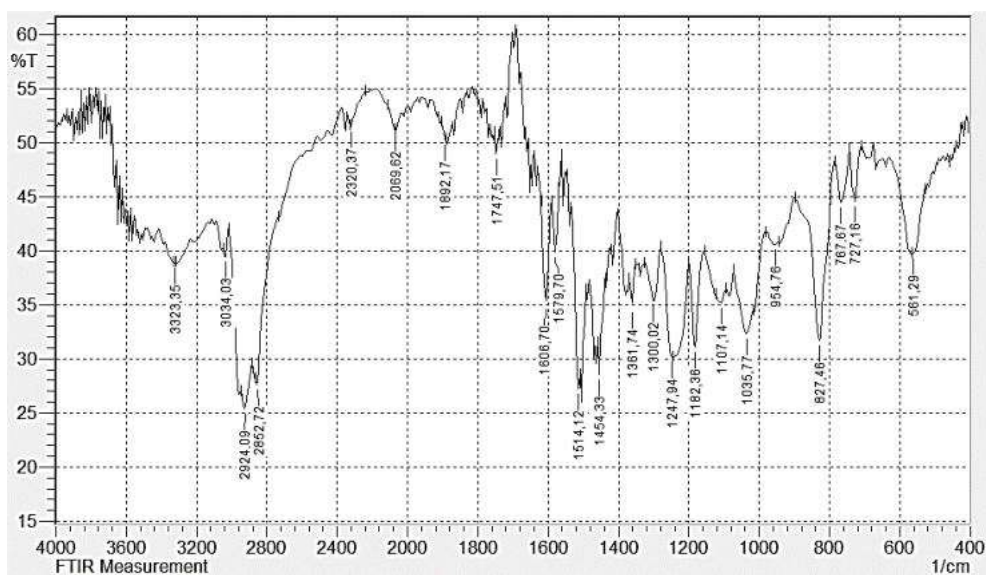


Figure 1 – IR spectrum of epoxy composite No. 1

In the high-frequency areas, oscillations with optical density  $D = 0.25$  and peak area  $S = 36.2\%$  at frequency  $\nu = 2924.1\text{ cm}^{-1}$  were detected. The detected vibrations indicate the presence of  $-\text{CH}-$  and methylene  $-\text{CH}_2-$  valence vibrations.

Absorption at frequency  $\nu = 3323.4\text{ cm}^{-1}$  with optical density  $D = 0.38$  and peak area  $S = 4.8\%$  indicates valence vibrations of  $-\text{OH}-$ ,  $-\text{NH}-$ , and  $-\text{CH}-$  groups.

For the epoxy composite material filled with  $\text{TiO}_2$  powder (composition No. 2), the following absorption bands were detected (Figure 2):

- optical density  $D = 0.30$  and peak area  $S = 23.8\%$  at frequency  $\nu = 567.1\text{ cm}^{-1}$  in the region of low frequencies;

- optical density  $D = 0.26$  and peak area  $S = 50.3\%$  at frequency  $\nu = 829.4\text{ cm}^{-1}$ ;

- optical density  $D = 0.26$  and peak area  $S = 30.1\%$  at frequency  $\nu = 1037.7\text{ cm}^{-1}$ ;

- optical density  $D = 0.25$  and peak area  $S = 22.9\%$  at frequency  $\nu = 1182.4\text{ cm}^{-1}$  (the same frequency as the epoxy polymer band);

- optical density  $D = 0.24$  and peak area  $S = 44.1\%$  at frequency  $\nu = 1246.0\text{ cm}^{-1}$ ;

- optical density  $D = 0.24$  and peak area  $S = 12.7\%$  at frequency  $\nu = 1456.3\text{ cm}^{-1}$ .

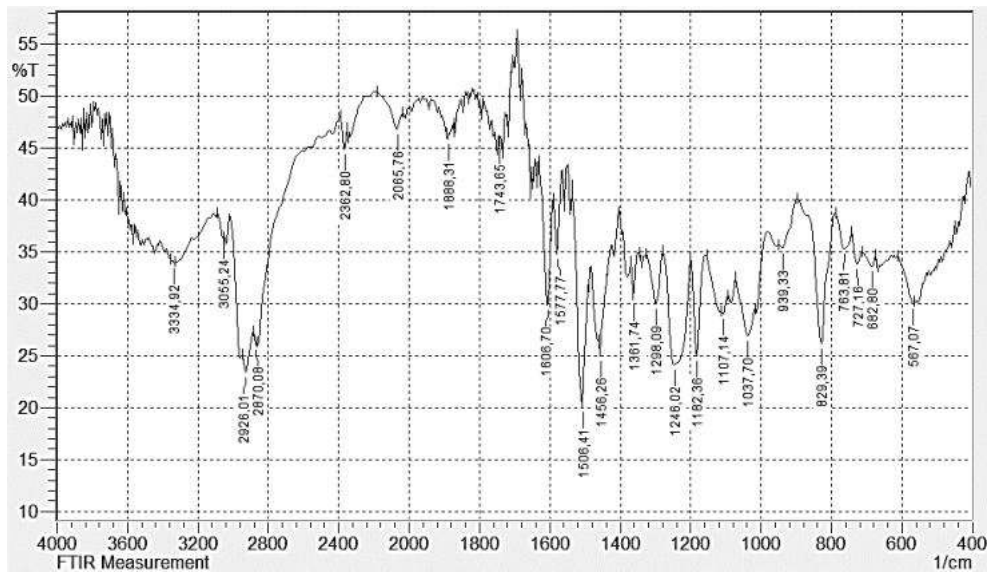


Figure 2 – IR spectrum of epoxy composite No. 2

Absorption bands characterize the areas of double bonds shifted toward smaller wave numbers with the following:

- optical density  $D = 0.20$  and peak area  $S = 25.4\%$  at frequency  $\nu = 1506.4\text{ cm}^{-1}$ ;

- optical density  $D = 0.45$  and peak area  $S = 1.3\%$  at frequency  $\nu = 1743.7\text{ cm}^{-1}$ .

An absorption band is present at the identical frequency ( $\nu = 1606.7\text{ cm}^{-1}$ ) with sample No. 1 but with a lower optical density  $D = 0.29$  and peak area  $S = 18.7\%$ .

In the areas of triple bonds, two absorption bands were detected:

- optical density  $D = 0.46$  and peak area  $S = 45.7\%$  at frequency  $\nu = 2065.8\text{ cm}^{-1}$ ;

- optical density  $D = 0.44$  and peak area  $S = 12.9\%$  at frequency  $\nu = 2362.8\text{ cm}^{-1}$ .

The following shifted absorption bands also characterize the high-frequency areas:

- optical density  $D = 0.23$  and peak area  $S = 39.4\%$  at frequency  $\nu = 2926.0\text{ cm}^{-1}$ ;

- optical density  $D = 0.33$  and peak area  $S = 10.8\%$  at frequency  $\nu = 3334.9\text{ cm}^{-1}$ .

The absorption bands of identical frequencies  $\nu = 561.3\text{ cm}^{-1}$  ( $D = 0.34$ ,  $S = 15.0\%$ ),  $\nu = 1247.9\text{ cm}^{-1}$  ( $D = 0.22$ ,  $S = 46.6\%$ ), and  $\nu = 1454.3\text{ cm}^{-1}$  ( $D = 0.25$ ,  $S = 11.4\%$ ) with bands of the epoxy polymer sample of composition No. 1 are presented in Figure 3.

There are also bands absorption of the identical frequency  $\nu = 1037.7\text{ cm}^{-1}$  ( $D = 0.24$ ,  $S = 31.5\%$ ) with epoxy composite material composition No. 2, and an absorption band – at the same frequency  $\nu = 1182.4\text{ cm}^{-1}$  ( $D = 0.23$ ,  $S = 23.8\%$ ).

In the areas of double bonds, the absorption bands are shifted towards smaller values of  $\nu = 1504.5\text{ cm}^{-1}$  ( $D = 0.18$ ,  $S = 10.8\%$ ) and  $\nu = 1712.8\text{ cm}^{-1}$  ( $D = 0.30$ ,  $S = 5.7\%$ ). The absorption band is available at the same frequency  $\nu = 1606.7\text{ cm}^{-1}$  ( $D = 0.26$ ,  $S = 14.6\%$ ).

In the region of triple bonds, two absorption bands were detected:

- optical density  $D = 0.43$  and peak area  $S = 32.3\%$  at frequency  $\nu = 2069.6\text{ cm}^{-1}$ ;

- optical density  $D = 0.41$  and peak area  $S = 11.3\%$  at frequency  $\nu = 2351.2\text{ cm}^{-1}$ .

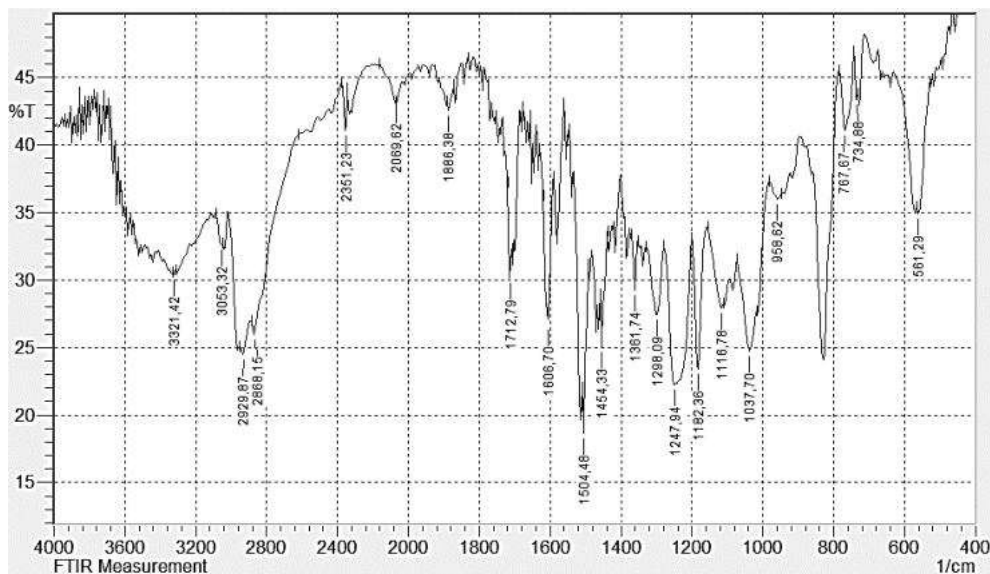


Figure 3 – IR spectrum of epoxy composite No. 3

The high-frequency areas have the following absorption bands:

- optical density  $D = 0.24$  and peak area  $S = 38.8\%$  at frequency  $\nu = 2929.9\text{ cm}^{-1}$ ;
- optical density  $D = 0.30$  and peak area  $S = 9.9\%$  at frequency  $\nu = 3321.4\text{ cm}^{-1}$ .

The obtained results indicate that introducing polyvinyl chloride as a modifying additive (epoxy polymer composition No. 3) increases the degree of structuring of epoxy polymers.

For epoxy composite material composition No. 4 in the frequency range  $400\text{--}1500\text{ cm}^{-1}$ , the following absorption bands were found (Figure 4):  $\nu = 567.1\text{ cm}^{-1}$  ( $D = 0.46$ ,  $S = 3.9\%$ );  $\nu = 763.8\text{ cm}^{-1}$  ( $D = 0.53$ ,  $S = 8.4\%$ );  $\nu = 829.4\text{ cm}^{-1}$  ( $D = 0.40$ ,  $S = 21.7\%$ );  $\nu = 1037.7\text{ cm}^{-1}$  ( $D = 0.41$ ,  $S = 19.3\%$ );  $\nu = 1182.4\text{ cm}^{-1}$  ( $D = 0.39$ ,  $S = 14.6\%$ );  $\nu = 1246.0\text{ cm}^{-1}$  ( $D = 0.37$ ,  $S = 29.1\%$ );  $\nu = 1456.3\text{ cm}^{-1}$  ( $D = 0.43$ ,  $S = 7.5\%$ ).

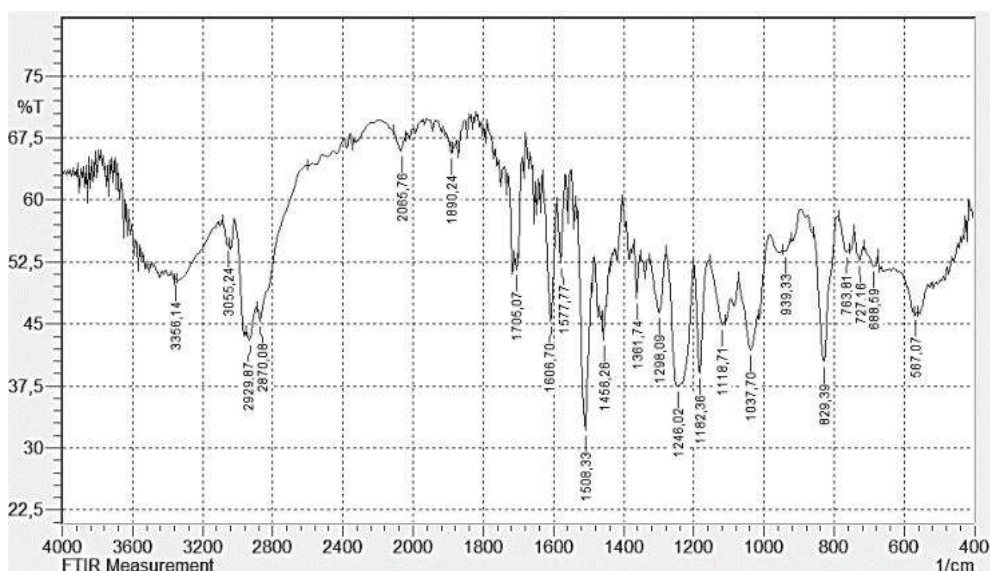


Figure 4 – IR spectrum of epoxy composite No. 4

In the areas of double bonds, the fluctuations in frequencies  $\nu = 1508.3\text{ cm}^{-1}$  ( $D = 0.32$ ,  $S = 14.6\%$ ) and  $\nu = 1705.1\text{ cm}^{-1}$  ( $D = 0.51$ ,  $S = 2.1\%$ ) were detected. The absorption band is available at the same frequency  $\nu = 1606.7\text{ cm}^{-1}$  ( $D = 0.45$ ,  $S = 11.5\%$ ).

Also, one band with optical density  $D = 0.65$  and peak area  $S = 11.7\%$  at frequency  $\nu = 2065.8\text{ cm}^{-1}$  was detected in the areas of triple bonds. Such a band indicates the presence of double bonds of valence vibrations  $\text{--C=C--}$ ,  $\text{--C=N--}$ , and  $\text{--C=O--}$  groups.

The following absorption bands characterize the high-frequency areas:

- optical density  $D = 0.43$  and peak area  $S = 20.3\%$  at frequency  $\nu = 2929.9\text{ cm}^{-1}$ ;
- optical density  $D = 0.50$  and peak area  $S = 2.9\%$  at frequency  $\nu = 3356.1\text{ cm}^{-1}$ .

The absorption bands have higher optical densities and smaller peak areas than materials No. 2-3.

For epoxy composite material No. 5, the following absorption bands shifted to higher values were found in the region of deformation oscillations (Figure 5):  $\nu = 569.0\text{ cm}^{-1}$  ( $D = 0.37$ ,  $S = 5.7\%$ );  $\nu = 767.7\text{ cm}^{-1}$  ( $D = 0.43$ ,  $S = 15.5\%$ );  $\nu = 829.4\text{ cm}^{-1}$  ( $D = 0.32$ ,  $S = 29.7\%$ );  $\nu = 1037.7\text{ cm}^{-1}$  ( $D = 0.33$ ,  $S = 25.0\%$ );  $\nu = 1182.4\text{ cm}^{-1}$  ( $D = 0.31$ ,  $S = 19.4\%$ );  $\nu = 1246.0\text{ cm}^{-1}$  ( $D = 0.31$ ,  $S = 19.3\%$ );  $\nu = 1456.3\text{ cm}^{-1}$  ( $D = 0.34$ ,  $S = 9.8\%$ ).

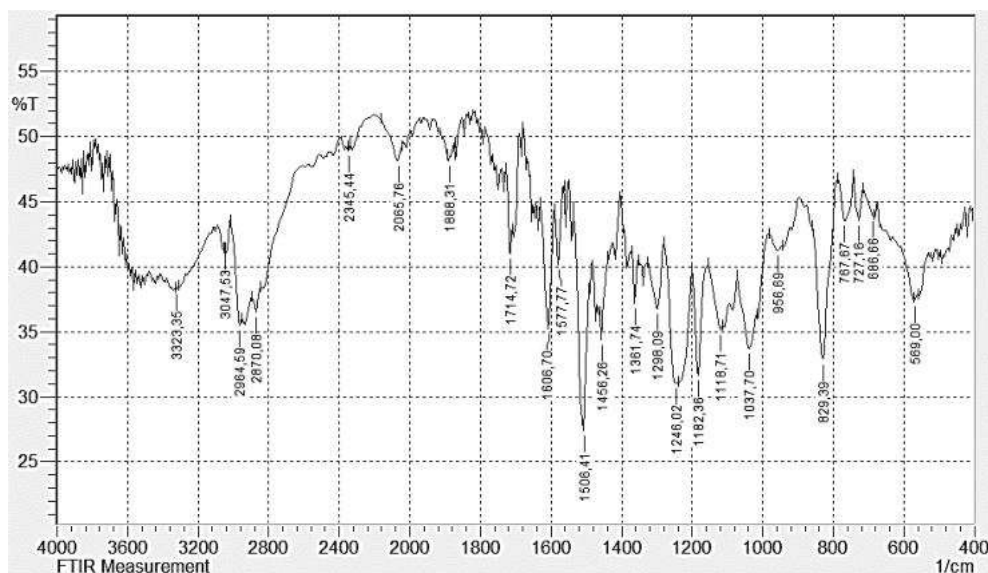


Figure 5 – IR spectrum of epoxy composite No. 5

In the areas of valence oscillations, the following absorption bands at frequencies were found:  $\nu = 1506.4\text{ cm}^{-1}$  ( $D = 0.27$ ,  $S = 21.4\%$ );  $\nu = 1714.7\text{ cm}^{-1}$  ( $D = 0.41$ ,  $S = 6.3\%$ ). They correspond to the area of the double connections absorption band at the same frequency  $\nu = 1606.7\text{ cm}^{-1}$  ( $D = 0.35$ ,  $S = 16.8\%$ ), comparing the IR spectrum of the epoxy composite material No. 4.

In the areas of triple bonds, absorption bands with optical density  $D = 0.48$  and peak area  $S = 36.86\%$  were detected at frequencies  $\nu = 2065.76\text{ cm}^{-1}$  and with optical density  $D = 0.48$  and peak area  $S = 4.15\%$  at frequencies  $\nu = 2345.44\text{ cm}^{-1}$ .

The high-frequency areas are characterized by absorption bands with optical density  $D = 0.36$  and peak area  $S = 21.4\%$  at frequency  $\nu = 2964.6\text{ cm}^{-1}$ , as well as optical density  $D = 0.38$  and peak area  $S = 7.2\%$  at frequency  $\nu = 3323.4\text{ cm}^{-1}$ .

## 5 Discussion

The areas of triple bonds of epoxy composite No. 1 are characterized by increased optical density and low peak areas, indicating unreacted functional groups. Absorption bands in these areas are associated with oscillations in which stretching of the corresponding bonds is observed. Double, more stable bonds indicate a complete crosslinking of the epoxy composite material [13, 14].

The content of the gel fraction of unmodified epoxy polymers after heat treatment is the lowest (91.7%), which

indicates the formation of a system with insufficient crosslinking of the polymer matrix.

The absorption bands of epoxy composite No. 2 are identical to those of the epoxy polymer sample composition No. 1, slightly shifted in frequency towards higher values. The absorption bands of the epoxy composite sample No. 2 are characterized by lower optical density and a larger peak area compared to the bands of the epoxy polymer (sample No. 1). This indicates the formation of a higher number of crosslinking nodes of the polymeric material  $-N-H-$ ,  $-O-H-$ , and  $-C-H-$ , as well as valence vibrations of  $-C-C-$ ,  $-C-O-$ , and  $-C-N-$  groups, which is achieved by introducing a finely dispersed filler in the form of an active type  $TiO_2$  powder.

The shift of the absorption bands on the IR spectrogram of the epoxy composite material composition No. 2 indicates its higher degree of structuring (93.2%) than the unfilled epoxy polymer composition No. 1 (91.7%).

The absorption bands of epoxy composite No. 3 have lower optical densities and larger peak areas compared to the epoxy polymer No. 1 and lower peak areas compared to the epoxy composite No. 2. A decrease in optical density indicates the formation of a more significant number of crosslinking bonds of the epoxy polymer material [15].

The obtained results indicate that introducing polyvinyl chloride as a modifying additive (epoxy polymer composition No. 3) increases the degree of structuring of epoxy polymers.

However, after comparing with the epoxy composite material of composition No. 2, a smaller number of formed chemical and physical crosslinking bonds of this epoxy polymer (composition No. 3) is observed.

Simultaneously, the content of the gel fraction is 92.5 %, which indicates a better interaction between macromolecules of epoxy resin and the surface of the filler than the interaction between macromolecules of epoxy resin and polyvinyl chloride.

The identity of most values of the wave numbers of epoxy composite No. 4 absorption bands with the wave numbers of epoxy composite No. 2 is observed. The uniformity of wave values occurs much less when compared with epoxy polymer No. 3.

However, these frequencies have higher optical density values and smaller peak areas. This fact indicates the presence of a significant number of  $-\text{CH}_2-$ ,  $-\text{CO}-$ , and  $-\text{CN}-$  valence,  $-\text{CH}-$ ,  $-\text{NH}-$  pendulum,  $-\text{OH}-$ ,  $-\text{CH}-$  deformation vibrations, as well as methylene  $-\text{CH}_2-$  and methyl  $-\text{CH}_3-\text{C}-$  groups in material, which is probably caused by the content of a modifying additive (polyvinyl chloride) and an active filler (fine  $\text{TiO}_2$  powder) with a large number of free radicals. This composition of the epoxy composite material ensures the formation of a structure with a gel fraction content of 94.9 %, which is associated with the dominant influence on the processes of  $\text{TiO}_2$  powder structuring. This indicates the activation of the course of physicochemical processes due to introducing a modifier and finely dispersed filler into the epoxy polymer system, significantly affecting the polymer matrix crosslinking.

The obtained lower values of optical density and larger peak area on the spectrum of epoxy composite No. 5 indicate a higher degree of structuring ( $G = 96.8 \%$ ) of epoxy composite material No. 5, compared to material No. 4. This indicates a complete passage of reactions in the material of composition No. 5, more complete than those of composition No. 4, with the formation of a more significant number of crosslinking nodes of the matrix, in which double and triple bonds are involved.

## References

1. Hosier, I.L., Vaughan, A.S., Swingler S.G. (2002). Effects of measuring technique and sample preparation on the breakdown strength of polyethylene. *IEEE Transactions on Dielectrics and Electrical Insulation*, Vol. 9(3), pp. 353-361, <https://doi.org/10.1109/TDEI.2002.1007697>
2. Haussonne, F.J.-M. (1995). Review of the synthesis methods for AIN. *Materials and Manufacturing Processes*, Vol. 10(4), pp. 717-755, <https://doi.org/10.1080/10426919508935062>
3. Bernard, M.C., Duval, S., Joiret, S., Keddami, M., Ropital, F., Takenoutia, H. (2002). Analysis of corrosion products beneath an epoxy-amine varnish film. *Progress in Organic Coatings*, Vol. 45(4), pp. 399-404, [https://doi.org/10.1016/S0300-9440\(02\)00126-1](https://doi.org/10.1016/S0300-9440(02)00126-1)
4. Gwon, J.G., Lee, S.Y., Chun, S.J., Doh, G.H., Kim, J.H. (2010). Effects of chemical treatments of hybrid fillers on the physical and thermal properties of wood plastic composites. *Composites Part A: Applied Science and Manufacturing*, Vol. 41(10), pp. 1491-1497, <https://doi.org/10.1016/j.compositesa.2010.06.011>
5. Rong, M.Z., Zhang, M.Q., Ruan, W.H. (2006). Surface modification of nanoscale fillers for improving properties of polymer nanocomposites: a review. *Materials Science and Technology*, Vol. 22(7), pp. 787-796, <https://doi.org/10.1179/174328406X101247>

## 6 Conclusions

Epoxy polymers containing an epoxy oligomer and a hardener (polyethylene polyamine) have absorption bands corresponding to double and triple chemical bonds in the range of valence vibrations. The areas of triple bonds are characterized by increased optical density and low peak areas, indicating unreacted functional groups. This affects the formation of an epoxy polymer system with a low content of the gel fraction (91.7 %), which is associated with an insufficient number of chemical bonds between the end groups of the component macromolecules and incomplete structuring of epoxy polymers.

The absorption bands of the epoxy composite material containing  $\text{TiO}_2$  powder have a lower optical density and a larger peak area than those of the epoxy polymer system "epoxy oligomer – polyethylene polyamine". This indicates the formation of more chemical bonds due to the introduction of finely dispersed  $\text{TiO}_2$  active powder.

The decrease in optical density for polyvinyl chloride-modified epoxy polymers indicates a more complete structure of the system than for unmodified epoxy polymers. However, a smaller number of formed chemical bonds was recorded compared to the epoxy composite containing finely dispersed titanium oxide powder, on the surface of whose particles there is a significant number of active centers. This indicates a better interaction between the epoxy resin's macromolecules and the filler's surface than the interaction between the macromolecules of the epoxy resin and polyvinyl chloride.

The epoxy composite system, consisting of a modified epoxy polymer binder and titanium oxide filler, contains a significant amount of valence ( $-\text{CH}_2-$ ,  $-\text{CO}-$ , and  $-\text{CN}-$ ), pendulum ( $-\text{CH}-$ ,  $-\text{NH}-$ ) and deformation ( $-\text{OH}-$ ,  $-\text{CH}-$ ) vibrations, as well as methylene  $-\text{CH}_2-$  and methyl  $-\text{CH}_3-\text{C}-$  groups. This ensures an increase in the content of the gel fraction to 94.9 %, which is associated with the activation of the course of physicochemical processes due to the introduction of polyvinyl chloride and an active filler (fine  $\text{TiO}_2$  powder) with a large number of free radicals into the epoxy polymer system.

6. Fronza, B.M., Lewis, S., Shah, P.K., Barros, M.D., Giannini, M., Stansbury J.W. (2019). Modification of filler surface treatment of composite resins using alternative silanes and functional nanogels. *Dent Mater*, Vol. 35(6), pp. 928-936, <https://doi.org/10.1016/j.dental.2019.03.007>
7. Moonart, U., Utara, S. (2019). Effect of surface treatments and filler loading on the properties of hemp fiber/natural rubber composites. *Cellulose*, Vol. 26, pp. 7271-7295, <https://doi.org/10.1007/s10570-019-02611-w>
8. Shah, A.R., Prabhakar, M.N., Wang, H., Song, J. (2018). The influence of particle size and surface treatment of filler on the properties of oyster shell powder filled polypropylene composites. *Polymer Composites*, Vol. 39(7), pp. 2420-2430, <https://doi.org/10.1002/pc.24225>
9. Sham, M.L., Li, J., Ma, P.C., Kim, J.-K. (2009). Cleaning and functionalization of polymer surfaces and nanoscale carbon fillers by UV/ozone treatment: A Review. *Journal of Composite Materials*, Vol. 43(14), P. 1537-1564, <https://doi.org/10.1177/0021998308337740>
10. Park S.-J. (2020). Effect of ozone-treated single-walled carbon nanotubes on interfacial properties and fracture toughness of carbon fiber-reinforced epoxy composites. *Composites Part A: Applied Science and Manufacturing*, Vol. 137, 105937, <https://doi.org/10.1016/j.compositesa.2020.105937>
11. Zhou, Y., Yao, Y., Chen, C.-Y., Moon, K., Wang, H., Wong, C. (2014). The use of polyimide-modified aluminum nitride fillers in AIN@PI/Epoxy composites with enhanced thermal conductivity for electronic encapsulation. *Scientific Reports*, Vol. 4, 4779, <https://doi.org/10.1038/srep04779>
12. Buketov, A., Stukhlyak, P., Maruschak, P., Panin, S., Menou, A. (2016). Physical and chemical aspects of formation of epoxy composite material with microfilling agent. *Physical Key Engineering Material*. Vol. 712, pp. 143-148, <https://doi.org/10.4028/www.scientific.net/KEM.712.143>
13. Moraes, L.G., Rocha, R.S., Menegazzo, L.M., Araújo, E.B., Yukimito, K, Moraes, J.C. (2008). Infrared spectroscopy: A tool for determination of the degree of conversion in dental composites. *J Appl Oral Sci*, Vol. 16(2), pp.145-149, <https://doi.org/10.1590/s1678-77572008000200012>
14. Buketov, A.V., Saprionov, A.A., Buketova, N.N., Brailo, M.V., Marushak, P.O., Panin, S.V., Amelin, M.Yu. (2018). Impact toughness of nanocomposite materials filled with fullerene C60 particles. *Composites: Mechanics, Computations, Applications. An International Journal*, Vol. 9(2), pp. 141-161, <https://doi.org/10.1615/CompMechComputApplIntJ.v9.i2.30>
15. Saprionov, O.O., Buketov, A.V., Saprionova, A.V., Sotsenko, V.V., Brailo, M.V., Yakushchenko, S.V., Maruschak, P.O., Smetankin, S.O., Kuinich, A.G., Kulinich, V.G., Poberezhna, L. (2020). The influence of the content and nature of the dispersive filler at the formation of coatings for protection of the equipment of river and sea transport. *SAE Int. J. Mater. Manf.*, Vol. 13(1), pp. 81-92, <https://doi.org/10.4271/05-13-01-0006>





Uysal M. U. (2023). Effects of cryogenically treated CFRP composite on the buckling behavior in the adhesively bonded beam. *Journal of Engineering Sciences*, Vol. 10(1), pp. D1-D7, doi: 10.21272/jes.2023.10(1).d1

## Effects of Cryogenically Treated CFRP Composite on the Buckling Behavior in the Adhesively Bonded Beam

Uysal M. U.<sup>[0000-0003-1618-3203]</sup>

Yildiz Technical University, Department of Mechanical Engineering, Yildiz Campus, Besiktas, 34349 Istanbul, Turkey

### Article info:

Submitted: March 7, 2023  
Received in revised form: May 5, 2023  
Accepted for publication: May 12, 2023  
Available online: May 15, 2023

### \*Corresponding email:

[mineuslu@yildiz.edu.tr](mailto:mineuslu@yildiz.edu.tr)

**Abstract.** Carbon fiber reinforced plastic (CFRP) composite materials have favorable mechanical and physical properties such as low density, high strength-to-weight ratio, high fatigue resistance and high creep behavior, and high stiffness. Thanks to these unique properties, they produce aircraft parts such as outer flaps, carry-through structures, and center wing boxes and automotive parts such as body panels, engine components, and structure members. However, studies have been continuously performed on improving the properties of CFRP composite materials. Recently, investigation of the effects of cryogenic (LN<sub>2</sub>) cooling on the mechanical behavior and characteristic of these composite materials is getting a popular and important issue. In this sense, this study aims to examine the buckling behaviors of adhesively bonded beam-produced cryogenically treated carbon fiber reinforced plastic (Cryo-CFRP), CFRP, steel, and aluminum. Therefore, a new finite element model was adopted to evaluate the buckling capacity of Cryo-CFRP composite material in the adhesively bonded beam. The model is a supported adhesive beam subject to two opposite-edge compressions until the material buckles. The elastic, homogeneous adhesive was used in the assembly. Finite element models for the adhesively bonded beam having four different adherents (CRFP, Cryo-CFRP, steel, and aluminum) were established by ANSYS® software. The critical buckling loads of the adhesively bonded beam were predicted, and their mode shapes were presented for the first six modes. The effects of the usage of Cryo-CFRP on the critical buckling load were investigated. Among the adherents' materials, the highest critical buckling load was determined for Cryo-CFRP/Steel adhesively bonded beam as 23.6 N. This value was obtained as 22.3 N for CFRP/Steel adherent samples. Thus, the critical buckling load was increased by 5.6 % when one adherent steel was constant and the other adherent material changed from CFRP to Cryo-CFRP. Also, the critical buckling load increased by 3.7 % when using a cryogenically treated Cryo-CFRP/Aluminum couple instead of a CFRP/Aluminum couple in the sandwich beam. The findings demonstrated that the cryogenic treatment positively affects the buckling behavior in the adhesively bonded beam.

**Keywords:** buckling behavior, finite element method, process innovation, environmentally-friendly materials construction.

## 1 Introduction

Carbon fiber composites, particularly those with polymeric matrices, have become the dominant advanced composite materials for aerospace, automobile, sporting goods, and other applications due to their high strength, high modulus, low density, and reasonable cost [1]. For applications requiring high strength and stiffness, as required by aerospace applications, carbon fiber reinforced plastics (CFRP) made using carbon fibers for reinforcing plastic resin matrices have become popular because their properties make them especially attractive.

CRFP composites have been increasingly used in the aerospace industry to build more reliable and fuel-efficient aircraft. Currently, fuel cost is calculated to be around 32 % of the airlines' operating cost, whereas it was 14 % in 2003 [2]. Airlines have reacted to this financial pressure by replacing older aircraft with a new generation of aircraft that are more fuel efficient. This efficiency partly comes from the increased use of sophisticated materials [3].

## 2 Literature Review

Studies have been continuously performed on improving the properties of CFRP composite materials. Recently, investigation of the effects of cryogenic (LN<sub>2</sub> – Liquid Nitrogen) cooling on the mechanical behavior and characteristic of these composite materials is getting a popular and important issue. Cryogenic treatment studies the behavior of materials at relatively low temperatures and examines the use of cryogenic coolants. The advantages of using the cryogenic treatment and machining techniques over the conventional methods were summarized by Pušavec et al. [4]. Cryogenic coolants can considerably reduce the high temperatures generated due to the continuous friction between the tool and the workpiece [5]. The LN<sub>2</sub> is the most commonly used cryogenic coolant in machining applications [6]. The LN<sub>2</sub> is a non-flammable, non-toxic, environmentally friendly gas. It has also been that cryogenically treated parts have improved surface integrity and fatigue resistance [7]. Researchers have previously investigated the effect of using cryogenically treated materials. Most of the work was conducted on metals such as steel, nickel, and titanium alloys. Minimal work has been conducted on cryogenically treated composite materials.

Kim and Donaldson [8] studied the mechanical properties of carbon fiber, and exposure to cryogenic temperatures with load can produce an actual rate of damage accumulation in the composite which may alter their material properties. They claimed that thermomechanical properties, such as transverse modulus, shear modulus, transverse shear modulus, and transverse strength, increased when the temperature was reduced. Drilling experiments were performed under dry and dipped cryogenic conditions using solid carbide drills and investigated the mechanical behaviors of composite materials [9]. A temperature-dependent micromechanical model, including the law of temperature-dependent Young's modulus of polymer, investigated the transverse mechanical properties of unidirectional CFRP composites at different temperatures [10]. The cryogenic temperature characteristic of several carbon fiber-reinforced composite materials was investigated and summarized in detail related to its mechanical and thermal aspects by Reed and Golda [11], who reported that Young's modulus and tensile strength of carbon fiber-reinforced composites increase as the temperature decreases. The challenges related to cryogenic experimental testing and analysis were introduced. The behavior of composite materials at low and cryogenic temperatures and the mechanical properties of the composite were reviewed. The material properties addressed are tensile, compressive, and shear strength; elastic modulus and stress-strain behavior; mechanical and thermal fatigue response; thermal expansion and thermal conductivity [12].

As it can be concluded from the literature, up to the authors' knowledge, no studies have looked into the impact of cryogenic treatment on buckling behaviors. The buckling behavior of adhesively bonded beams has been reported in the literature, but as stated, this is not the case

in a beam model formed by CFRP bonding of metal materials treated with cryogenic treatment. Determining the mechanical behavior of a bonded beam, especially the buckling behavior, is a stabilization problem, and determining beam life and critical buckling load is essential. Local deflections in the beam in advanced modes during buckling are essential for strength and adhesively bonded beam life. In this sense, this paper aims to examine the buckling behaviors of adhesively bonded beam produced cryogenically treated carbon fiber reinforced plastic (Cryo-CFRP), CFRP, steel, and aluminum. Thus, a new finite element model was adopted to estimate the buckling capacity of Cryo-CFRP composite material in the adhesively bonded beam.

## 3 Research Methodology

### 3.1 Description of the adhesively bonded beam geometry

It is known that using adhesive bonding in composite beams is more advantageous than mechanical fastening as the number of parts is reduced, and the drilling of components is eliminated. Bonded beams can be widely used for non-critical and lightly loaded structures and reliably at very high loads, often in primary aircraft structures. Also, the science and technology of adhesive-bonded joints are well understood. Pramanik et al. reviewed comprehensive knowledge regarding joining CFRP and aluminum alloys in available literature in terms of available methods, bonding processing, and mechanism and properties. The methods employed comprise adhesive to only CFRP and aluminum alloys. Besides adhesive bonding and welding, other joining methods require the penetration of metallic pins through joining parts; therefore, surface preparation is unimportant [13]. Ramaswamy et al. experimentally investigated interlocked hybrid joining technology using carbon-fiber thermoplastic composite and aluminum adherents loaded at quasi-static.

The mechanical response and damage progression were compared to baseline adhesive joints to quantify performance improvements [14]. The paper critically reviews adhesives and their various adhesion, categorization, and functions. The benefit of adhesive joining was explained. Requirements for excellent bonding, including an appropriate selection of adhesive and superior design for joining, surface cleansing, and wetting, were defined. The review clearly indicates the various theories involved in adhesion: mechanical interlocking, chemical bonding, and weak boundary layer. Bond failure modes and their mechanism were elaborated briefly [15]. Carneiro Neto et al. [16] studied the numerical evaluation of bonded joints with combined loading (traction and shear) using the finite element method, comparing the results obtained with the experiments performed at the same configurations. Considering adhesively bonded joints with the same bonded area but with different linear dimensions, the mechanical strength can be different, which characterizes the shape and adhesive type factor. Therefore, adhesives are increasingly

used, and they also play an important role in joining technologies of composite beams. One of the most important advantages is that they provide uniform stress distribution, simplicity, and flexibility in manufacturing. They provide structural integrity by combining materials with different mechanical and thermal properties and are investigated using the finite element method. He [17] reviewed recent work relating to finite element analysis of adhesively bonded joints in terms of static loading analysis, environmental behaviors, fatigue loading analysis, and dynamic characteristics of the adhesively bonded joints. Accurate and reliable modeling of adhesively bonded joints is still a difficult task as the mechanical behavior of these joints is not only influenced by the geometric characteristics of the joint but also by different factors and their combinations.

It is needed to address the performance of adhesive-adherent combinations and to combine environmental and thermal studies of adhesively bonded joints. It is also essential to validate the predicted mechanical behavior of adhesive bonding structures from FEA against experimental test results. Little work in these areas has been undertaken. The output obtained from the FEA of adhesively bonded joints includes differences in the basic mechanical properties, thermal behavior, and occurrence of high-stress gradients in certain regions of the joints. Marchione [18] investigated the numerical study of the stress distribution in the adhesive layer under buckling conditions. It is possible to predict the critical load value for each single analyzed combination through numerical analysis once the critical load is determined. The results show that small adhesive thicknesses can reduce the stress peaks with the same critical load value using structural adhesives with low elastic modulus (e.g., silicones). An adhesive joint must survive longer than the estimated working life of the entire structural system. Panda et al. [19] reviewed the factors which affect the durability of an adhesive joint and the approaches to improve the durability of a joint. Thakare and Dhumne [20] reviewed the design and analysis of adhesive-bonded joint by finite element analysis regarding static loading analysis, fatigue loading analysis, and dynamic characteristics of the adhesively bonded joints. The computational analysis comprises stress and buckling analysis.

The buckling behavior of adhesively bonded structures is included in the literature, but this is not the case with a beam model formed by bonding cryogenically treated metal materials with CFRP, such as appearances. In this context, this article aims to investigate the buckling of beams by bonding cryogenically treated steel and aluminum with carbon fiber-reinforced plastic.

Fig. 1 shows the adhesively bonded beam sandwich geometry and its dimensions. The length of the beam  $L = 100$  mm, the width of the beam is 10 mm, and the thickness of the one adherent panel is 1.4 mm. Adhesive thickness  $b = 0.2$  mm, and the total thickness of the adhesively bonded sandwich beam  $h = 3$  mm.

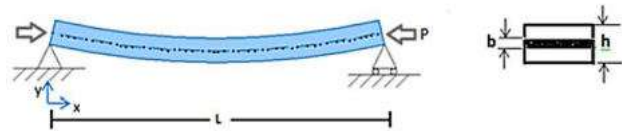


Figure 1 – Boundary conditions and dimensions for a simply supported adhesively bonded beam

Four different types of adherent material were used, and the adherent materials were chosen as Cryo-CFRP, CFRP, steel, and aluminum. One type of adhesive was used in this study. Loctite-Hysol 9464 was chosen for all adhesive bonds. The material properties of adhesive and adherent materials are shown in Tables 1-2.

Table 1 – Material properties of adhesive material [21]

Properties	Loctite-Hysol 9464
Shear Strength, MPa	22.0
Peeling Strength, MPa	10.5
Viscosity, Pa·s	270
Elastic Modulus $E$ , GPa	1.75
Shear Modulus $G$ , GPa	0.65
Poisson's ratio $\nu$	0.376
Density $\rho$ , kg/m <sup>3</sup>	1000

Table 2 – Material properties of adherent materials [22-24]

Properties	Cryo-CFRP	CFRP	Steel St37	Aluminium 2024
Ultimate Tensile Strength, MPa	668.49	688.84	370	469
Elastic Modulus $E$ , GPa	29.497	28.071	210	73
Poisson's ratio $\nu$	0.1	0.1	0.3	0.33
Density $\rho$ , kg/m <sup>3</sup>	1600	1600	8000	2780

In this study, four different adhesively bonded sandwich beam types were modeled. First, the upper panel was chosen as CFRP material and the lower panel was chosen as steel, so a type 1 adhesively bonded sandwich beam was created. Similarly, four different adhesively bonded sandwich beam types were created, as shown in Table 3.

Table 3 – Adhesively bonded sandwich beam types

Type	Upper Panel	Lower Panel
1	CFRP	Steel, St37
2	Cryo-CFRP	Steel, St37
3	CFRP	Aluminium 2024
4	Cryo-CFRP	Aluminium 2024

The model is a supported adhesive beam subject to two opposite-edge compressions until the material buckles. The buckling behaviors of the Cryo-CFRP adhesively bonded sandwich beam and the buckling loads were studied. The elastic buckling analysis was used for the corresponding buckling shapes. The force  $P = 1$  N was applied, and the response was calculated, ignoring the significant displacements effect and time-varying load.

### 3.2 Finite element model

The numerical model of the simply supported cryogenically treated carbon fiber reinforced plastic Cryo-CFRP (CFRP, steel, and aluminum) adhesively bonded sandwich beam patterns is developed using the ANSYS® software. The finite element program enables the prediction of buckling load and global behavior of the sandwich beam. SOLID95 is suitable for analyzing plates and adhesive layers.

The CONTA174 contact element (8-node and high order quadrilateral element) was selected to obtain the contact pairs in the finite element model. There were two contact pairs; one between the upper layer of adherent and adhesive and the other between the bottom layer of adherent and adhesive. TARGE170 was used for overlap surfaces of adherents and represented various target surfaces for the contact elements in the adhesive layer.

The Cryo-CFRP adhesively bonded sandwich beam's numerical model was divided into finite elements satisfying (3200 mesh elements) the equilibrium and compatibility at each node. Then, mesh convergence was applied. In the adhesively bonded beam, finite element analysis must be repeated to obtain the optimal convergence rate and adequate penetration by changing the defined normal penalty stiffness factor (FKN).

The contact surface is more deformable than the target surface. Therefore, the penalty method was selected as the contact algorithm. The penetration has to be as low as possible for the desired converged solution. Moreover, this is valid at high contact stiffness values. Fig. 2 shows the element types used in finite element modeling.

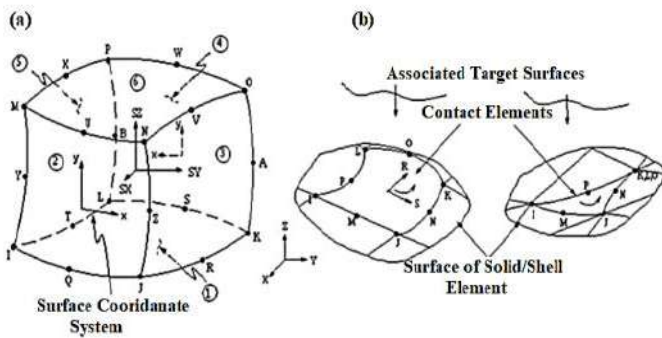


Figure 2 – Element Types: a – Solid95; b – Contal174; c – Targe170

### 4 Results and Discussion

This study supported four adhesively bonded sandwich beams as simply supported. These beams were subjected to two opposite-edge compressions until the adhesively bonded beam buckled. Then the sandwich beams were numerically modeled based on finite elements.

The adhesively bonded sandwich beam structure comprised two layers and a thin adhesive layer in between. Four types of adhesively bonded sandwich beams were modeled: CFRP/Steel, Cryo-CFRP/Steel, CFRP/Aluminum, and Cryo-CFRP/Aluminum panel pairs. These

panels had adhesive interlayers assumed to be linear-elastic homogeneous isotropic.

Elastic buckling analysis predicted the critical buckling load on the sandwich beams. The influences of the cryogenic treatment on the critical buckling load were presented in Fig. 3. The critical buckling loads of the sandwich beam structure panels were examined, and these loads were compared with the non-cryogenically treated CFRP sandwich structure beams. The non-cryogenically treated CFRP in the sandwich structure panels was compared to the first mode. The critical buckling load was 22.3 N for sample type 1 (CFRP/Steel). This value was determined as 3.9 N for sample type 3 (CFRP/Aluminum). As seen in Fig. 3a, the critical buckling load increased by 5.6 % when the cryogenically treated Cryo-CFRP/Steel pair was used instead of CFRP/Steel pair in the sandwich beam. This increment was calculated as 3.7 % for Cryo- CFRP/Aluminum pair was used instead of CFRP/Aluminum pair. These results presented that cryogenically treated Cryo-CFRP composite material panels responded much better against buckling.

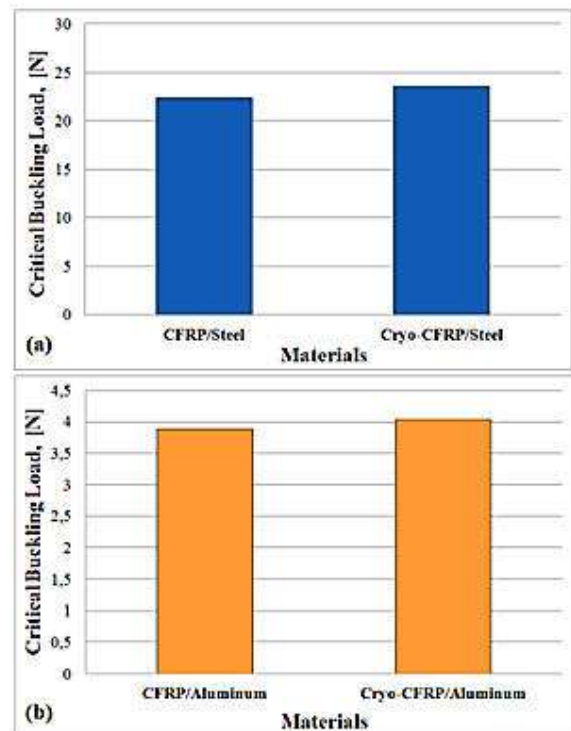


Figure 3 – Critical buckling load according to all adherent material pairs in the sandwich structure

In Fig. 4, the adherent pairs' buckling loads can be seen for each mode. Generally, the buckling load increases as the mode number increases. The buckling load increases approximately three times between mode 1 and mode 2 for the Cryo-CFRP/Steel and CFRP/Steel sandwich beam. For instance, the critical buckling load is 23.5 in mode 1, and 72.5 – in mode 2 for Cryo-CFRP/Steel sandwich beam (Fig. 4a).

As seen in Fig. 4b, when the comparison is made for the Cryo-CFRP/Aluminum sandwich beam in terms of buckling load in mode 2 and mode 1, the differences account for 198.5 %. This increment was calculated as 100.6 % between mode 3 and mode 2, and 68.8 %, 44.5 %, and 4.9 % for between mode 4 and mode 3, mode 5 and mode 4, and mode 6 and mode 5, respectively.

Also, in Table 4, the buckling loads of all samples are given for 6 modes collectively. The critical buckling loads are 3.9 N for aluminum and 22.3 N for steel in beams where CRRP bonds are formed by choosing steel and aluminum as metal materials. The cryogenically treated effect is also seen for both metal materials. Table 4 shows the critical buckling load values of 4.0 N for the Cryo-CRRP/Aluminum sample and 23.6 N for Cryo-CRRP/Steel samples. It was observed that the cryogenically treated process increased strength and positively affected buckling behavior.

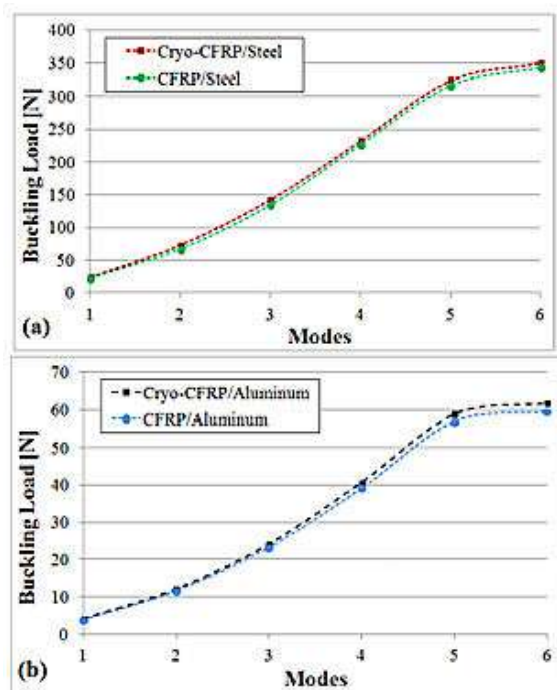


Figure 4 – Effects of the cryogenically treated CFRP material on the buckling loads for the first six modes

Table 4 – Buckling loads for six modes, N

Materials	Mode					
	1	2	3	4	5	6
CFRP/Steel	22.3	66.8	134.4	226.5	316.9	343.2
Cryo-CFRP/Steel	23.6	72.5	141.8	231.9	323.9	349.8
CFRP/Aluminium	3.9	11.6	23.3	39.3	57.0	59.5
Cryo-CFRP/Aluminium	4.0	12.0	24.1	40.7	58.8	61.7

The maximum out-of-the-plane deflection of the Cryo-CFRP/Steel adhesively bonded sandwich beam for the first six modes was presented in Fig. 5. As is known, two buckles in the adhesively bonded beam were created in mode 2. The mode shapes were similar to the other adherent materials in beams.

The deformations on  $x$  and  $y$  directions ( $U_x$  and  $U_y$ ) in Cryo-CFRP/Aluminum adhesively bonded sandwich beam for six modes were given in Fig. 6-7. In the buckling analysis, the stresses are not considered, and no large deflections exist. However, there are buckles, and their locations are changed based on each mode. For mode 1, the critical buckling load is 3.9 N, and the maximum deformation on the  $y$  direction ( $U_y$ ) is determined as 0.265 mm. For modes 2, 3, and 4, there are 2, 3, and 4 buckles, respectively. The maximum values of  $U_y$  are 0.192 mm, 0.144 mm, and 0.114 mm, respectively. However, in mode 5, the adhesively bonded beam has become stable.

Figures 5-7 show the deflections that occur because of buckling in the glued beam model for 6 modes. For mode 1 and other modes where the critical buckling load is determined, the position of both  $U_x$  and  $U_y$  directions on the beam is determined and presented by the finite element method. It is expected that a total of two buckles will occur in mode 2. At mode 5, the beam is close to the stable position.

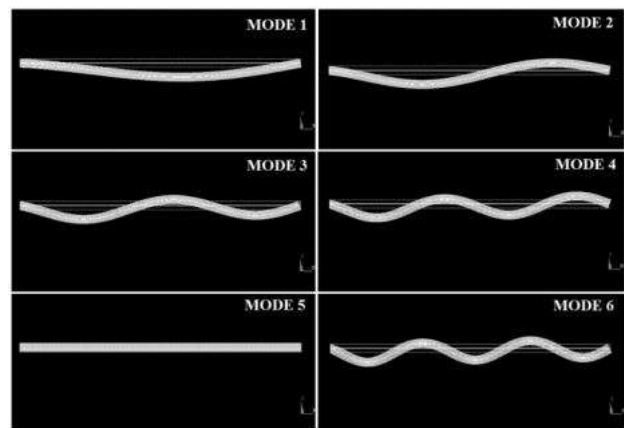


Figure 5 – Out of the plane deflections in Cryo-CFRP/Steel adhesively bonded beam for the first six modes

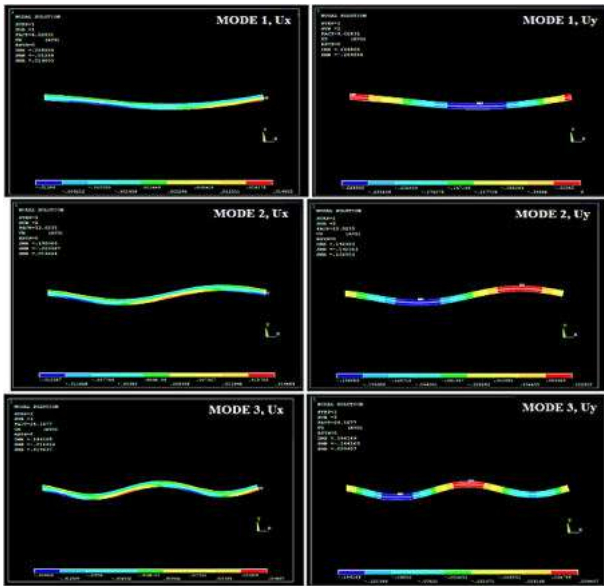


Figure 6 – The deformations on x and y directions ( $U_x$  and  $U_y$ ) in Cryo-CFRP/Aluminum adhesively bonded beam for modes 1-3

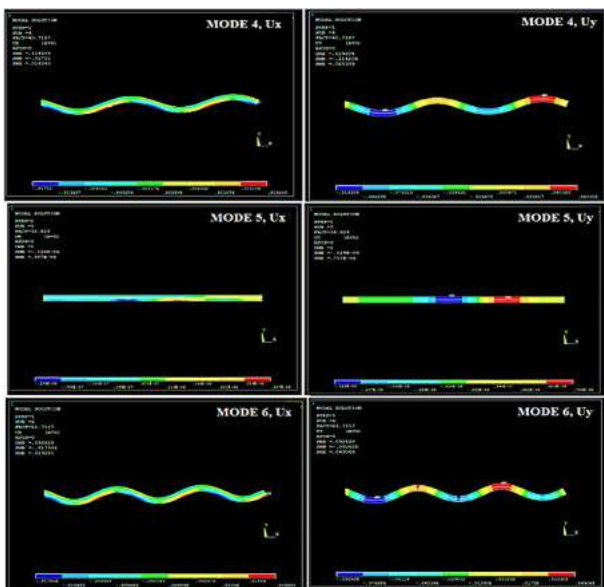


Figure 7 – The deformations on x and y directions ( $U_x$  and  $U_y$ ) in Cryo-CFRP/Aluminum adhesively bonded beam for modes of 4-6

## 5 Conclusions

In this study, the buckling problem in the Cryo-CFRP adhesively bonded beams subjected to opposite edge compression until buckling was investigated in detail by using the developed finite element model. Four types of adhesively bonded beams were built up for buckling analysis. These models were CFRP/Steel, Cryo-CFRP/Steel, CFRP/Aluminum, and Cryo-CFRP/Aluminum.

The obtained results revealed that critical buckling was affected by cryogenically treated materials. The aluminum CFRP/Aluminum adherent selection provided the lowest critical buckling load. Critical buckling load increased by 3.7 % when using a cryogenically treated Cryo-CFRP/Aluminum couple instead of a CFRP/Aluminum couple in the sandwich beam. This increase was calculated as 5.6 % when the Cryo-CFRP/Steel couple was used instead of the CFRP/Steel couple.

The highest critical buckling load was also determined for the Cryo-CFRP/Steel among all the adherent materials. Besides, it was seen that cryogenically treated CFRP panels had the highest buckling load in all steel and aluminum beam structures when comparing the obtained results from the numerical investigation. The presented comparative results can be helpful in the buckling behavior of Cryo-CFRP adhesively bonded sandwich beams.

## Nomenclature

$b$	Adhesive Thickness, mm;
$E$	Elastic Modulus, GPa;
$h$	Total Thickness of Adhesively Bonded Sandwich Beam, mm;
$L$	Length of Sandwich Beam, m;
$\rho$	Density, kg/m <sup>3</sup> ;
$\nu$	Poisson's ratio;
CFRP	Carbon Fiber Reinforced Plastic;
Cryo	Cryogenic;
LN <sub>2</sub>	Liquid Nitrogen;
$U_x$	Deformation on x direction, mm;
$U_y$	Deformation on y direction, mm.

## References

- Chung, D. D. L. (1994). *Carbon Fiber Composites*. Butterworth-Heinemann, Newton, MA, USA.
- Köse, Y., Aktan, C. (2022). Analysis of cost structures and cost control strategies of airlines: an empirical study on a hypothetical airline company. *Journal of Aviation*, Vol. 6(1), pp. 42-49, doi: 10.30518/jav.1024489.
- Karpat, Y., Deger, B., Bahtiyar, O. (2012). Drilling thick fabric woven CFRP laminates with double point angle drills. *Journal of Materials Processing Technology*, Vol. 212(10), pp. 2117-2127, doi: 10.1016/j.jmatprotec.2012.05.017.
- Pušavec, F., Stoić, A., Kopač, J. (2009). The role of cryogenics in machining processes. *Tehnicki Vjesnik*, Vol. 16(4), pp. 3-10.
- Dixit, U. S., Sarma, D., Davim, J. P. (2012). *Environmentally Friendly Machining*. Springer, New York, NY, USA.
- Yildiz, Y., Nalbant, M. (2008). A review of cryogenic cooling in machining processes. *International Journal of Machine Tools and Manufacture*, Vol. 48(9), pp. 947-964, doi: 10.1016/j.ijmactools.2008.01.008.

7. Seliger, G., Khraisheh, M. M., Jawahir, I. S. (2011). *Advances in Sustainable Manufacturing*. Springer Berlin, Heidelberg, Germany.
8. Kim, R. Y., Donaldson, S. L., Experimental and analytical studies on the damage initiation in composite laminates at cryogenic temperatures. *Composite Structures*, Vol. 76, pp. 62-66, doi: 10.1016/j.compstruct.2006.06.009.
9. Kim, D., Ramulu, M. (2004). Cryogenically treated carbide tool performance in drilling thermoplastic composites. *Transactions of the North American Manufacturing Research Institute of SME*, Vol. 32, pp. 79-85.
10. Yuan, X. W., Li, W. G., Xiao, Z. M., Zhang, Y. M. (2023). Prediction of temperature-dependent transverse strength of carbon fiber reinforced polymer composites by a modified cohesive zone model. *Composite Structures*, Vol. 304, 116310, doi: 10.1016/j.compstruct.2022.116310.
11. Reed, R. P., Golda, M. (1997). Cryogenic composite supports: a review of strap and strut properties. *Cryogenics*, Vol. 37, pp. 233-250, doi: 10.1016/S0011-2275(97)00004-0.
12. Sapi, Z., Butle, R. (2020). Properties of cryogenic and low temperature composite materials – a review. *Cryogenics*, Vol. 111, 103190, doi: 10.1016/j.cryogenics.2020.103190.
13. Pramanik, A., Basak, A. K., Dong, Y., Sarker, P. K., Uddin, M. S., Littlefair, G., Dixit, A. R., Chattopadhyaya, S. (2017). Joining of carbon fibre reinforced polymer (CFRP) composites and aluminium alloys – a review. *Composites Part A: Applied Science and Manufacturing*, Vol. 101, pp. 1-29, doi: 10.1016/j.compositesa.2017.06.007.
14. Ramaswamy, K., O’Higgins, R. M., Corbett, M. C., McCarthy, M. A., McCarthy, C. T. (2020). Quasi-static and dynamic performance of novel interlocked hybrid metal-composite joints. *Composite Structures*, Vol. 253, 112769, doi: 10.1016/j.compstruct.2020.112769.
15. Bharti, S. (2018). Adhesives and adhesion technologies: a critical review. *American Journal of Polymer Science and Technology*, Vol. 4(1), pp. 36-41, doi: 10.11648/j.ajpst.20180401.13.
16. Neto, R. M. C., Sampaio, E. M., Assis, J. T. (2019). Numerical and experimental analysis of bonded joints with combined loading. *International Journal of Adhesion and Adhesives*, Vol. 90, pp. 61-70, doi: 10.1016/j.ijadhadh.2019.02.002.
17. He, X. (2011). A review of finite element analysis of adhesively bonded joints. *International Journal of Adhesion and Adhesives*, Vol. 31(4), pp. 248-264, doi: 10.1016/j.ijadhadh.2011.01.006.
18. Marchione, F. (2021). Analytical stress analysis in single-lap adhesive joints under buckling. *IJE Transactions B: Applications*, Vol. 34(2), pp. 313-318, doi: 10.5829/IJE.2021.34.02B.02.
19. Mittal, K. L., Panigrahi, S. K. (2020). *Structural Adhesive Joints: Design, Analysis and Testing*. John Wiley & Sons, Inc., Hoboken, NJ, USA.
20. Thakare, N. B., Dhumne, A. B. (2015). A review on design and analysis of adhesive bonded joint by finite element analysis. *International Journal of Mechanical Engineering*, Vol. 2(4), pp. 17-20, doi: 10.14445/23488360/IJME-V2I4P104.
21. Loctite Corporation. (2008). Loctite Epoxy Catalogue, Technical Data Sheet Hysol Products, CT, USA, 2008.
22. Morkavuk, S., Koklu, U., Bağcı, M., Gemi, L. (2018). Cryogenic machining of carbon fiber reinforced plastic (CFRP) composites and the effects of cryogenic treatment on tensile properties: A comparative study. *Composites Part B: Engineering*, Vol. 147, pp. 1-11, doi: 10.1016/j.compositesb.2018.04.024.
23. Yuksel, M. (2001). *Materials Science Volume 1*. The Chamber of Mechanical Engineering Press, Istanbul, Turkiye.
24. Taskaya, S., Zengin, B., Kaymaz, K., Askin, M. (2019). Elastic stress analysis of St 37 and St 70 steels in finite element method. *International Journal of Materials Science and Applications*, Vol. 8(6), pp. 103-108, doi: 10.11648/j.ijmsa.20190806.12.



Voropay A. V., Menshykov O. V., Povaliaiev S. I., Sharapata A. S., Yehorov P. A. (2023). Modeling a viscoelastic support considering its mass-inertial characteristics during non-stationary vibrations of the beam. *Journal of Engineering Sciences*, Vol. 10(1), pp. D8-D14, doi: 10.21272/jes.2023.10(1).d2

## Modeling a Viscoelastic Support Considering Its Mass-Inertial Characteristics During Non-Stationary Vibrations of the Beam

Voropay A. V.<sup>1</sup>[0000-0003-3396-8803], Menshykov O. V.<sup>2</sup>[0000-0003-2869-3307], Povaliaiev S. I.<sup>1</sup>[0000-0001-9027-0132], Sharapata A. S.<sup>1</sup>[0000-0003-0823-9262], Yehorov P. A.<sup>1</sup>[0000-0001-6616-9966]

<sup>1</sup> Kharkiv National Automobile and Highway University, 25, Yaroslava Mudrogo St., 61002 Kharkiv, Ukraine;

<sup>2</sup> School of Engineering, University of Aberdeen, AB243UE Scotland, United Kingdom

### Article info:

Submitted: February 27, 2023  
 Received in revised form: May 10, 2023  
 Accepted for publication: May 16, 2023  
 Available online: May 19, 2023

### \*Corresponding email:

[voropay.alexey@gmail.com](mailto:voropay.alexey@gmail.com)

**Abstract.** Non-stationary loading of a mechanical system consisting of a hinged beam and additional support installed in the beam span was studied using a model of the beam deformation based on the Timoshenko hypothesis with considering rotatory inertia and shear. The system of partial differential equations describing the beam deformation was solved by expanding the unknown functions in the Fourier series with subsequent application of the integral Laplace transform. The additional support was assumed to be realistic rather than rigid. Thus it has linearly elastic, viscous, and inertial components. This means that the effect of a part of the support vibrating with the beam was considered such that their displacements coincide. The beam and additional support reaction were replaced by an unknown concentrated external force applied to the beam. This unknown reaction was assumed to be time-dependent. The time law was determined by solving the first kind of Volterra integral equation. The methodology of deriving the integral equation for the unknown reaction was explained. Analytic formulae and results of computations for specific numerical parameters were given. The impact of the mass value on the additional viscoelastic support reaction and the beam deflection at arbitrary points were determined. The research results of this paper can be helpful for engineers in designing multi-span bridges.

**Keywords:** Timoshenko multi-span beam, additional viscoelastic support, non-stationary vibration, concentrated mass, Volterra integral equation.

## 1 Introduction

In engineering and construction, there are many complex mechanical systems consisting of a large number of elements. The approach based on the choice of the central element of the study and taking into account the influence of objects interacting with it using concentrated or distributed forces can be used to build a model of the system in this case.

It is not always known in advance which system parameters significantly influence the stress-strain state, especially under dynamic loading [1]. Therefore, the maximum number of parameters, which at the same time do not overcomplicate the model, should be taken into account.

Thus, in this paper, the Timoshenko-type beam model, taking into account the viscoelastic and mass parameters of intermediate supports, is proposed to study the deformed state of widespread multi-span beams.

## 2 Literature Review

Beam-like structural elements are widely applied for engineering purposes of mankind. From experience, the Timoshenko hypothesis-based models considering rotatory inertia and shear provide good results for beams [2, 3]. Nevertheless, the classical models, i.e., Euler-Bernoulli beams, are still used for simplification when solving problems involving modeling nonlinear properties of the beam material [4] or in complex identification problems [5].



The paper [4] presents vibration analysis of a simply supported beam with a fractional order viscoelastic material model. The studies show that the selection of appropriate damping coefficients and fractional derivative order of the damping model enables us to fit more accurately the dynamic characteristics of the beam in comparison with using the integer order derivative damping model.

A new method to identify the viscoelastic boundary conditions of Euler–Bernoulli beams under forced response is presented in [5]. The capability of identifying complex boundary conditions under high levels of noise might open the door for the proposed method to be considered in real-life applications of structural health monitoring and model updating with boundary conditions of beam-like structures such as bridges.

For mechanical systems, including structural elements in the form of beams under non-stationary loads, auxiliary restrictions are sometimes imposed on the displacements of specific beam parts (e.g., displacement magnitude) in addition to the robustness requirements. In such cases (i.e., bridges), using additional supports for beams is advisable.

Vibrations of multi-span beams with additional elastic supports under pulse and traveling loads are considered in [6].

Non-stationary direct and inverse problems for multi-span beams with additional elastic supports are solved in [7]. Similar problems in viscoelastic settings are studied in [8].

Implementation of the time-weighted residual method for simulation of flexural waves in multi-span Timoshenko beams subjected to various external loads: from stationary loads to accelerating moving masses considered in [9]. Experimental studies of the dynamic response of multi-span beams under the action of moving masses, among which is [10], is also known.

The paper [11] study extends a frequency domain modified spectral element method (SEM) from single-span beams to multi-span beams subjected to moving point forces. The Timoshenko beam model represents each span. The time history of the moving point force is transformed to the frequency domain as a series of quasi-static or stationary point forces acting on the beam simultaneously. The dynamic responses are obtained by superposing the individual dynamic responses excited by each quasi-static point force. Note that in this work, a similar problem has already been solved at a high level, but each additional support is, in fact, absolutely rigid.

The assumption about the absolute rigidity of the supports is also used by authors in [12] in the analysis of the dynamic behavior of a Rayleigh multi-span uniform continuous beam system traversed by a constant moving force or uniformly distributed loads.

Manipulating the dynamic response of a multi-span bridge due to organizational arrangements is considered in the article [13], namely by managing the entry time of the crossing trains (in other words, moving loads).

The analytical solution uses the Euler–Bernoulli beam model. For comparisons, a two-dimensional numerical finite element modeling based on the Timoshenko beam element that includes the effect of the shear force is also presented there.

This solution is more complex because of the number of pavement bridge layers. However, it does not consider the properties of additional supports, is the model considered in [14].

In paper [15], the multi-span Timoshenko beams are investigated, and the interpolation modifies the mode shapes of the beams functions to model the vibration modes of the multi-span beams. Hamilton's principle is applied to establish the equation of motion of the structure, and the natural circular frequencies and the free vibration responses of the multi-span beams are obtained. Note that in this work, only free vibrations are considered.

The uniform formulation of dynamic vibration analysis of multi-span beams is presented by using an efficient domain decomposition method in the paper [16]. The domain decomposition method divides the structure into several equal sections. Next, the artificial spring is used to simulate the multi-span beam's complex boundaries and continuity conditions. Finally, the admissible displacement functions are expanded through Jacobi orthogonal polynomials, and the free and forced vibration characteristics of multi-span beam structures can be obtained using Rayleigh–Ritz method.

The paper [17] investigates multi-step Timoshenko beams coupled with rigid bodies on springs. Additional purely elastic supports are considered when In works [16, 17].

Note that in the case of modeling complex multilayer objects, along with beams, more complex objects are used, called strips or strip plates [18]. However, using an object as a strip significantly complicates the model and, in our case, will not give visible refinements of the solution.

The results of the present paper are based on those for non-stationary deforming of mechanical systems consisting of beams and plates having concentrated viscoelastic supports additional to the main support along its edge. Solutions to direct problems for beams and plates with additional supports are found in [19, 20].

After analyzing the existing publications, we conclude that the problem of studying non-stationary oscillations of multi-span beams is quite relevant. At the same time, absolutely rigid supports are most often considered in well-known publications. The proposed model makes it possible to describe the behavior of real mechanical objects more accurately. In addition, introducing additional supports, considering their characteristics can be used to reduce unwanted vibrations, such as in [21, 22].

### 3 Research Methodology

#### 3.1 Problem settings

A mechanical system consists of a hinged elastic isotropic beam and an additional concentrated viscoelastic support contacting the beam at some point (Figure 1).

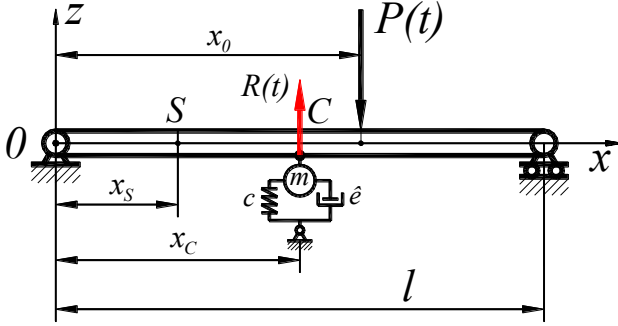


Figure 1 – Beam with additional support loading scheme

The additional support is assumed to be installed transversally to the beam, and its lower end is hinged. The stiffness and damping ratios are considered constant. Transverse pulse load  $P(t)$  is applied to the beam at some point, which excites non-stationary vibrations of the beam and additional support.

The impact of the additional viscoelastic support on the beam is modeled by a non-stationary external unknown force (the beam and additional support reaction taken with the opposite sign) applied to the beam at the point of its contact with the support. When solving the problem, we assume the point of the load application as well as the point of contact with the additional support to be arbitrary, i.e., they can be any points of the beam except for its ends.

The displacements of the points of the beam under the simultaneous action of the system of two forces (i.e., the given function  $P(t)$  and the unknown function  $R(t)$ , which is the time-dependent reaction of the beam and additional support considering its mass-inertia characteristics) are to be determined.

#### 3.2 Analytical solution

The system of Timoshenko beam partial differential equations, which considers the appropriately chosen initial and boundary conditions that describes non-stationary deformation processes, is of the form (see [2]):

$$\begin{cases} G'b_b h_b \left( \frac{\partial^2 w}{\partial x^2} - \frac{\partial \psi}{\partial x} \right) = \rho b_b h_b \frac{\partial^2 w}{\partial t^2} - P(x, t) + R_C(x, t); \\ EI \frac{\partial^2 \psi}{\partial x^2} + G'b_b h_b \left( \frac{\partial w}{\partial x} - \psi \right) = \rho \cdot I \frac{\partial^2 \psi}{\partial t^2}, \end{cases} \quad (1)$$

where  $h_b$  is the beam thickness;  $b_b$  is the beam width;  $l$  is the beam length;  $G' = k' \cdot G$ ;  $k'$  is the shear

coefficient;  $I = b_b h_b^3 / 12$ ;  $w$  describes the beam middle plane deflection;  $\psi$  stands for the rotation angle;  $\rho$ ,  $E$ ,  $\nu$  are the elastic constants of the beam material;  $t$  is the time. We also remind that  $P(x, t)$  and  $R_C(x, t)$  are the exciting load and the reaction of the beam and additional support interaction, respectively.

The system is solved by expanding the unknown functions, namely the displacements and rotation angles, into corresponding Fourier series with time-dependent coefficients. Then a system of ordinary differential equations can be derived for the expansion coefficients, which can be solved, for instance, by using the integral Laplace transform [23]. In this case, after applying the inverse transform, the solutions can be written as convolution-type Duhamel's integrals, which allows for obtaining analytic representations for the kernels of integral equations.

By solving the system of differential equation (1) for zero initial and hinge boundary conditions, we arrive at the following analytic formula for the deflection functions:

$$w(x, t) = \int_0^t P(\tau) K_P^W(x, t - \tau) d\tau - \int_0^t R(\tau) K_R^W(x, t - \tau) d\tau, \quad (2)$$

where  $K_i^W(x, t)$  are the corresponding kernels of Duhamel's integrals (i.e., convolutions):

$$K_i^W(x, t) = \sum_{k=1}^{\infty} \frac{C_{ik}}{\Delta_k} \cdot \sin \frac{k\pi \cdot x}{l} \sum_{p=1}^2 \Omega_{pk} \cdot \sin \omega_{pk} t.$$

In the equalities above, we adopt the following notations:

$$a = \frac{G'}{\rho}, \quad b = \frac{G' h_b^2}{\rho \cdot 12}, \quad d = \frac{E}{\rho}, \quad \lambda_k = \pi \frac{k}{l},$$

$$C_{ik} = \frac{2}{\rho \cdot l \cdot b_b \cdot h_b} \cdot \sin \frac{k\pi \cdot x_i}{l},$$

$$\Delta_k = \sqrt{(\lambda_k^2 (a + d) + b)^2 - 4 \cdot a \cdot d \cdot \lambda_k^4},$$

$$\Omega_{1k} = \omega_{1k} - \frac{d \cdot \lambda_k^2 + b}{\omega_{1k}}; \quad \Omega_{2k} = -\omega_{2k} + \frac{d \cdot \lambda_k^2 + b}{\omega_{2k}}.$$

The eigenfrequencies are given by the formula:

$$\omega_{1k} = \sqrt{0.5 [(\lambda_k^2 (a + d) + b) + \Delta_k]};$$

$$\omega_{2k} = \sqrt{0.5 [(\lambda_k^2 (a + d) + b) - \Delta_k]}.$$

Similar relations can be derived for total displacements, normal rotation angles, and deformation.

In the general case, the additional support can be represented as a combination of mass, stiffness, and damping impact (Figure 1). The formula gives the beam and additional viscoelastic support reaction considering inertia phenomena:

$$R_i(t) = m \frac{d^2 w_i(t)}{dt^2} + \kappa \frac{dw_i(t)}{dt} + c \cdot w_i(t), \quad (3)$$

where  $c$  is the additional support stiffness ratio, N/m;  $\kappa$  is the damping, N·s/m;  $m$  stands for the mass-inertia characteristic of the additional viscoelastic support, kg;  $w_i(t)$  describes the beam deflection at the point of the contact with the additional support, m.

For the case under consideration, the functions of deflections at a point are to be derived. Applying the direct Laplace integral transform to (3) for the zero initial condition, we get the formula:

$$R_i(s) = m_i \cdot s^2 \cdot w_i(s) + \kappa_i \cdot s \cdot w_i(s) + c_i \cdot w_i(s). \quad (4)$$

From (4), the Laplace transform of the deflection functions can be easily found:

$$w_i(s) = \frac{R_i(s)}{m_i \cdot s^2 + \kappa_i \cdot s + c_i}. \quad (5)$$

Applying the inverse Laplace transform by the convolution theorem, we arrive at the following expression for the deflection at the point of application of the viscoelastic support reaction considering its mass:

$$w_i(t) = \int_0^t K_{\beta}^W(t-\tau)R(\tau)d\tau, \quad (6)$$

where  $K_{\beta}^W(t) = \frac{1}{m_i} \frac{1}{\omega_{CDi}} \cdot e^{-\frac{\kappa_i}{2m_i}t} \cdot \sin(\omega_{CDi} \cdot t)$  is the

finite difference kernel of the convolution type integral accounting for viscous, elastic, and mass-inertia characteristics of the additional support at the  $i$ -th point, and  $\omega_{CDi} = \sqrt{c_i/m_i - 0.25 \cdot \kappa_i^2/m_i^2}$  is the eigenfrequency corresponding to the  $i$ -th additional viscoelastic support considering its mass.

Below is an example of solving the problem for one additional support.

Note that (6) is similar to (2) in its structure. Substituting the coordinate of the point of contact with the additional support  $x_C$  for the variable  $x$  in the beam deflection  $w(x, t)$ , we can equate the deflections obtained by the two formula:  $w(x_C, t) = w_i(t)$ .

Hence the right-hand parts of relations (2) and (6) are also equal for  $x = x_C$ . Then after gathering all the known summands in the right-hand part of the equality and keeping all the unknown ones in its left-hand part, we arrive at a first-kind Volterra equation with respect to the unknown reaction  $R(t)$ :

$$\int_0^t [K_R^W(t-\tau) + K_f(t-\tau)]R(\tau)d\tau = \int_0^t K_P^W(t-\tau)P_0(\tau)d\tau. \quad (7)$$

By discretization, integral equation (7) is transformed into a system of linear algebraic equations (SLAE) [24], which can be written in the form:

$$\mathbf{A}_R^* \mathbf{R} = \mathbf{w}_P, \quad (8)$$

where the vector  $\mathbf{R}$  corresponds to the change of the reaction  $R(t)$  in time; the vector  $\mathbf{w}_P$  is the change in deflection time at the point of contact with the additional support excited solely by the external force  $P(t)$

$w_P = \int_0^t K_P^W(t-\tau)P(\tau)d\tau$ ; the matrix  $\mathbf{A}_R^*$  corresponds to

the sum of the kernels  $K_R^W(t-\tau) + K_f(t-\tau)$ .

Finally, the beam and additional support reaction force  $R(t)$  is found taking into account the support mass-inertia characteristics, which allows determining the components of the deflection of the beam at all points in time considering the impact of two independent loads  $P(t)$  and  $R(t)$  rather than the presence of additional supports.

## 4 Results and Discussion

Consider a specific example of modeling non-stationary transverse vibrations of a beam with additional support. Let, for simplicity purposes, the beam be hinged at its ends and have only additional support attached to the downward side of the beam at an arbitrary point between its ends. The additional support is modeled to be realistic, considering elastic, viscous, and various mass-inertia characteristics.

When undeformed, the midline of the beam is assumed to coincide with the  $Ox$  axis of the cartesian coordinate system. The computations are carried out for the following parameters:  $\rho = 7890$  kg/m<sup>3</sup>,  $\nu = 0.3$ , and  $E = 2.07 \cdot 10^{11}$  Pa, which corresponds to the alloy steel beam mechanical constants; the beam length  $l = 0.80$  m; the beam thickness  $h_b = 0.04$  m; the beam width  $b_b = 0.05$  m.

The coordinates of the point of the exciting load application  $x_0 = 0.50$  m, of the point at which the additional viscoelastic support is attached to the beam  $x_C = 0.40$  m (i.e., the middle of the beam), the point at which the change of the deflection in time is studied  $x_{S1} = 0.20$  m.

The additional support stiffness ratio is  $c_1 = 1.0 \cdot 10^7$  N/m, and the ratio of the linear viscous damping is assumed to be  $\kappa_1 = 1.0 \cdot 10^3$  N·s/m; the number of the terms in the corresponding Fourier series is 100.

The general scheme of the geometry chosen for the computational example is shown in Figure. 1.

The computations are carried out for three cases, namely:

1) the minimal possible value of the mass-inertia characteristic, since in the case of the mass less than the value  $m_{\min} = \kappa_1^2 / (4 \cdot c_1)$ , the natural frequency corresponding to the additional viscoelastic support considering its mass  $\omega_{CD_i} = \sqrt{c_i / m_i - 0.25 \cdot \kappa_i^2 / m_i^2}$  becomes complex. For the values of the parameters ( $c_1, \kappa_1$ ) adopted above we have  $m_{\min} = 0.025$  kg. We choose  $m_1 = 0.0251$  kg for our computations;

2) the mass  $m_2 = 1.0$  kg;

3) the mass  $m_3 = 2.5$  kg.

Figure 2 shows the external force  $P(t)$  exiting the deformations (i.e., non-stationary vibrations) of the beam with additional support. We point out that in Figure 2, the force (in N) is plotted along the vertical axis, and time in seconds is plotted along the horizontal axis.

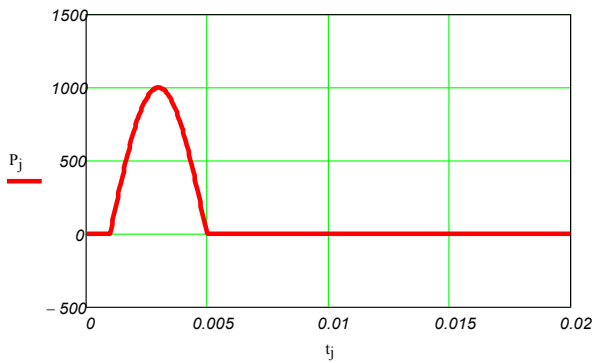


Figure 2 – Exiting load  $P(t)$

In Figure 3, the beam deflections  $w(x_{S1}, t)$ ,  $w(x_{S2}, t)$  and  $w(x_{S3}, t)$  are caused by the influence of only an external perturbing force (illustrate the case – a beam without additional support).

We point out that in Figure 3 the deflection in meters is plotted along the vertical axis, and time in seconds is plotted along the horizontal axis.

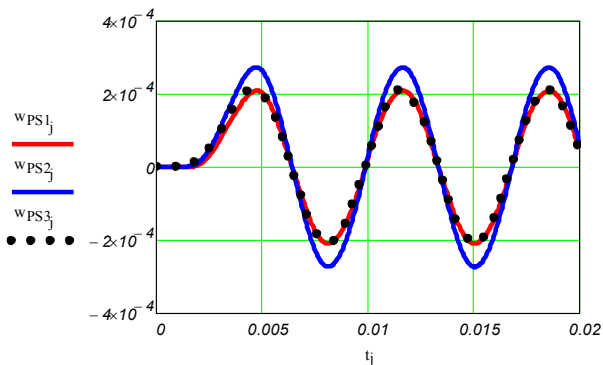


Figure 3 – Deflection of beam point are caused by the influence only of  $P(t)$

In Figure 4, the external force  $P(t)$  and the reaction of the additional support  $R(t)$  determined by solving matrix equation (8) are shown for the masses  $m_1 = 0.0251$  kg,  $m_2 = 1$  kg, and  $m_3 = 2.5$  kg. We point out that in Figure 4, the force (in N) is plotted along the vertical axis, and time in seconds is plotted along the horizontal axis.

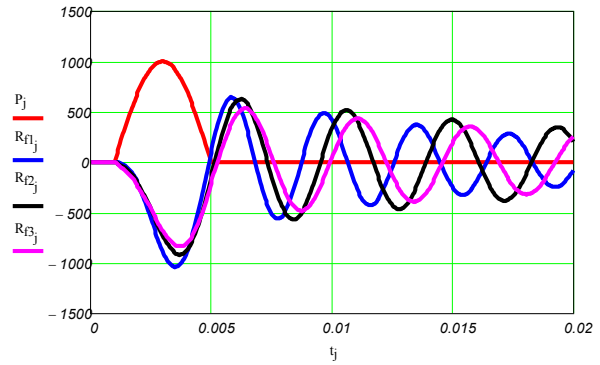


Figure 4 – Exiting load  $P(t)$  and reaction determined  $R(t)$

In Figure 5, the beam deflections  $w(x_{S1}, t)$ ,  $w(x_{S2}, t)$  and  $w(x_{S3}, t)$  are shown for the four cases, namely, for the case when the impact of the additional support is not considered and for the three cases of mass-inertia characteristics of the additional support listed above.

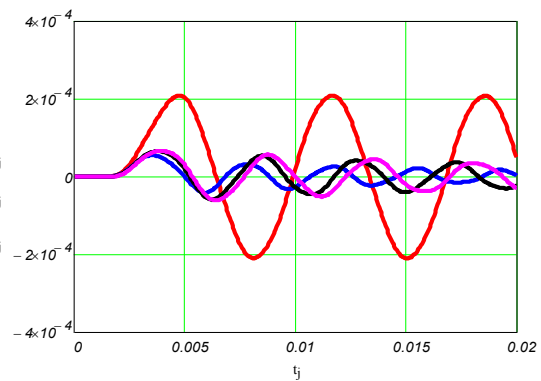


Figure 5 – Deflection of beam point are caused by the influence of  $P(t)$  and  $R(t)$

We point out that in Figure 5, the deflection in meters is plotted along the vertical axis, and time in seconds is plotted along the horizontal axis. Also, we can see that the impact of the mass on the deflection amplitudes is insignificant (there is a strong dependence of the amplitudes on the elastic and viscous component parameters). Nevertheless, changing the mass results in an essential change in the curve phase characteristics. Increasing the mass leads to increasing the vibration period, which is logical since the system inertia grows with its mass.

## 5 Conclusions

The article proposes an original approach to model the impact of additional viscoelastic support considering its mass-inertia characteristics by an independent non-stationary external force: the beam and additional support reaction.

Solving the first-kind integral Volterra equation determines the unknown non-stationary load. Modeling non-stationary vibrations of beams with additional supports based on the approach developed in the paper

allows obtaining stable analytic and numerical solutions to the problems of mechanics of deformable solids without using iteration schemes.

The impact of the mass on the deflection amplitudes is insignificant (if the mass is not very large). The phase characteristics of the vibrations are changed when the additional support's mass is considered. Increasing the mass leads to increasing the vibration period.

## References

1. Smetankina, N.V., Shupikov, A.N., Sotrikhin, S.Yu., Yareschenko, V.G. (2008). A noncanonically shape laminated plate subjected to impact loading: Theory and experiment. *Journal of Applied Mechanics*, Transactions ASME, Vol. 75, No 5. Pp. 051004-1–051004-9. <https://doi.org/10.1115/1.2936925>.
2. Timoshenko, S. P. (1937). *Vibration problems in engineering*. D. Van Nostrand Company INC. 497 p.
3. Filippov, A.P., Kokhmanyuk, S. S., Yanyutin, Ye. G. (1978). *Deformation of structural elements under impact and impulse loads*. Kyiv, Naukova dumka. 184 p.
4. Freundlich, J. (2013). Vibrations of a Simply Supported Beam with a Fractional Viscoelastic Material Model – Supports Movement Excitation. *Shock and Vibration*, 20, Article ID 126735, <https://doi.org/10.3233/SAV-130825>.
5. Qiao, G, Rahmatalla, S. (2019). Identification of the viscoelastic boundary conditions of Euler-Bernoulli beams using transmissibility. *Engineering Reports*, 1:e12074, <https://doi.org/10.1002/eng2.12074>.
6. Kokhmanyuk, S. S., Yanyutin, Ye. G., Romanenko, L. G. (1980). *Vibrations of deformable systems under pulse and moving loads*. Naukova Dumka, Kyiv.
7. Yanyutin, Ye. G., Gnatenko, G. O., Grishakin, V. T. (2007). Solving non-stationary direct and inverse problems for beams with additional elastic supports. *Mashynoznavstvo*, 8, pp. 18–23.
8. Yanyutyn, Ye. G., Grishakin, V. T. (2008). Identification of mobile load for viscoelastic beams. *Bulleting of the National Technical University “Kharkiv Polytechnic Institute”*. 47, pp. 178–184.
9. Borji, A., Movahedian, B., Boroomand, B. Implementation of time-weighted residual method for simulation of flexural waves in multi-span Timoshenko beams subjected to various types of external loads: from stationary loads to accelerating moving masses. (2022). *Archive of Applied Mechanics*, 92 (4), pp. <https://doi.org/10.1007/s00419-021-02103-z>.
10. Dan Stancioiu, Huajiang Ouyang, John E. Mottershead, Simon James, Experimental investigations of a multi-span flexible structure subjected to moving masses, *Journal of Sound and Vibration*, Volume 330, Issue 9, 2011, Pages 2004-2016, ISSN 0022-460X, <https://doi.org/10.1016/j.jsv.2010.11.011>.
11. Taehyun, K., Usik, L. (2017). Dynamic analysis of a multi-span beam subjected to a moving force using the frequency domain spectral element method. *Computers & Structures*. 192, pp. 181–195. <https://doi.org/10.1016/j.compstruc.2017.07.028>.
12. Szyłko-Bigus, O., Śniady, P., Zakeś, F. (2019). Application of Volterra integral equations in the dynamics of a multi-span Rayleigh beam subjected to a moving load. *Mechanical Systems and Signal Processing*, Vol. 121, pp. 777-790, ISSN 0888-3270, <https://doi.org/10.1016/j.ymssp.2018.11.056>.
13. Vesali, F., Rezvani, M.A., Shadfar, M. (2023). Attuned dynamic response of double track Multi-span railway bridges under the delayed entry of a second train. *Journal of Vibration Engineering and Technologies*. <https://doi.org/10.1007/s42417-023-00884-x>.
14. Liu, S., Jiang, L., Zhou, W., Xilin, C., Zhang, Y. (2021). Dynamic response analysis of multi-span bridge-track structure system under moving loads. *Mechanics Based Design of Structures and Machines*.
15. Zhao, Z., Wen, S., Li, F., Zhang, C. (2018). Free vibration analysis of multi-span Timoshenko beams using the assumed mode method. *Archive of Applied Mechanics*, Vol. 88, no. 7, pp. 1213–1228. <https://doi.org/10.1007/s00419-018-1368-8>.
16. Cong Gao, Fuzhen Pang, Haichao Li, Hongfu Wang, Jie Cui, Jisi Huang. (2021). Free and Forced Vibration Characteristics Analysis of a Multispan Timoshenko Beam Based on the Ritz Method. *Shock and Vibration*, Vol. 2021, Article ID 4440250. <https://doi.org/10.1155/2021/4440250>.
17. Chen, X., Zeng, X., Liu, X. and Rui, X. (2020). Transfer matrix method for the free and forced vibration analyses of multi-step Timoshenko beams coupled with rigid bodies on springs. *Applied Mathematical Modelling*, 87, pp. 152–170.
18. Kantor, B.Ya., Smetankina, N.V., Shupikov, A. N. (2001) Analysis of non-stationary temperature fields in laminated strips and plates. *International Journal of Solids and Structure*. Vol. 38, No 48/49, pp. 8673-8684. [https://doi.org/10.1016/S0020-7683\(01\)00099-3](https://doi.org/10.1016/S0020-7683(01)00099-3).

19. Voropay, A.V., Povaliaiev, S.I., Yehorov, P.A. (2022) Simulation of intermediate viscoelastic support under non-stationary vibrations of Timoshenko beams. *Bulletin of the National Technical University "KhPI". Series: Mathematical modeling in engineering and technology*, №1, pp. 36-44 (2022). <https://doi.org/10.20998/2222-0631.2022.01.05>.
20. Voropay, A. V., Yegorov, P. A. (2020). The influence of mass and inertial characteristics of an additional viscoelastic support in the non-stationary deforming of a rectangular plate. *Bulletin of the National Technical University "Kharkiv Polytechnic Institute"*, 1, pp. 15–23. <https://doi.org/10.20998/2222-0631.2020.01.02>.
21. Yang, F., Sedaghati, R., Esmailzadeh, E. (2021). Vibration suppression of structures using tuned mass damper technology: A state-of-the-art review. *Journal of Vibration and Control*, 28 (7-8), pp. 812-836. <https://doi.org/10.1177/1077546320984305>.
22. Zhang, L., Chen, Q., Zhang, R., Lei, T. (2023). Vibration control of beams under moving loads using tuned mass inerter systems. *Engineering Structures*, 275, art. no. 115265. <https://doi.org/10.1016/j.engstruct.2022.115265>.
23. Beerends, R. J., Ter Morsche, H. G., Van Den Berg, J. C., Van De Vrie, E. M. (2003). *Fourier and Laplace Transforms*. Cambridge University Press. 458 p. ISBN: 0521534410, 9780521806893.
24. Voropay, A., Gnatenko, G., Yehorov, P., Povaliaiev, S., Naboka, O. (2022). Identification of the pulse axisymmetric load acting on a composite cylindrical shell, inhomogeneous in length, made of different materials. *Eastern-European Journal of Enterprise Technologies*, 5(7 (119), pp. 21–34. <https://doi.org/10.15587/1729-4061.2022.265356>.



Lymarenko A., Kurgan V., Bazhanova A., Khamray V., Ponomarenko A., Karabegović I. (2023). The stress state of a thick-walled hydraulic press cylinder with concentrators. *Journal of Engineering Sciences*, Vol. 10(1), pp. D15-D19, doi: 10.21272/jes.2023.10(1).d3

## The Stress State of a Thick-Walled Hydraulic Press Cylinder with Concentrators

Lymarenko A.<sup>1</sup>[0000-0002-1806-3128], Kurgan V.<sup>1\*</sup>[0000-0003-3153-7313], Bazhanova A.<sup>1</sup>[0000-0001-9189-4529], Khamray V.<sup>1</sup>[0000-0002-1365-6979], Ponomarenko A.<sup>1</sup>[0000-0003-4642-4696], Karabegović I.<sup>2</sup>[0000-0001-9440-4441]

<sup>1</sup>Odessa Polytechnic National University, 1, Shevchenko Ave., 65044 Odessa, Ukraine;

<sup>2</sup>Academy of Sciences and Arts of Bosnia and Herzegovina, 7, Bistrik St., 71000 Sarajevo, Bosnia and Herzegovina

### Article info:

Submitted: March 1, 2023  
 Received in revised form: May 11, 2023  
 Accepted for publication: May 22, 2023  
 Available online: May 26, 2023

### \*Corresponding email:

[kurgan@op.edu.ua](mailto:kurgan@op.edu.ua)

**Abstract.** The article deals with modeling and calculations of volumetric machine-building structures with complex geometry. The relevance of the work lies in the fact that its methodology and results can help design massive structural elements complex in shape, including cylinders of powerful hydraulic presses. Attention is paid to the problems of reducing the metal content of machine-building products and the safe conditions of their operation. Theoretical and applied work is based on numerical methods using analytical solutions to assess the reliability of computer calculation results. The choice of research method is because analytical solutions for massive parts of such a configuration are too complex for numerical implementation. Experimental methods are too expensive and not so universal as to sort out possible variants of shapes and sizes. For the actual model of the press, the capabilities of the finite element method implemented in the ANSYS multipurpose complex were selected and rationally used. The results of the calculations are summarized in the table and shown on the graphs of the stress distribution. Based on the performed calculations (with a reliability check based on the formulas of the theory of elasticity for simplified calculation schemes), conclusions were made to ensure a more even distribution of stresses and a reduction in the metal content of the product.

**Keywords:** theory of elasticity, finite element analysis, hydraulic press, cylinder, stress-strain state.

## 1 Introduction

The need to perform a verification calculation of the cylinder strength is because the main cylinder of the D-0843 press has recently undergone structural changes. The shape of the main cylinder of the press is quite complex.

During the test, the internal pressure in the cylinder is 40 MPa, and the load by axial forces in the places where the cylinder is attached to the press columns is evenly distributed along the length of the four side brackets.

During the development of projects of previous models, there was no sufficiently reliable and precise method of calculating three-dimensional details. Therefore, methods were used that made it possible to determine stresses in structural elements very approximately.

In addition, the material of the cylinder (Steel 1.0501, EU) has low mechanical characteristics,

and therefore, taking into account the insufficient quality of the production of such thick-walled parts, the allowable stresses were assumed to be low enough.

## 2 Literature Review

The control of the position of the main drive of the press in terms of flatness is considered [1], and the design of the hydraulic press is described [2]. A methodology for calculating the total service life of a structure is presented [3], applicable to actual engineering structures [4].

Determination of the critical buckling load obtained by the energy method is compared using ANSYS finite element analysis [5] with different mounting conditions [6].

Numerical calculations were carried out using ANSYS Mechanical 19.0 software [7]. The stress-strain state of a cylindrical shell with a circular cutout is considered [8]. The stress distribution over the cutout contour and the wall thickness of the shell is investigated

[9], as well as the geometric nonlinearity, which determines its stress-strain state [10].

A method of calculating the strength, reliability, and resource of cast parts operating under conditions of variable loads of a random nature has been developed [11]. The three-dimensional model of the supporting system of the vehicle is considered [12].

Two different finite element packages of different complexity are used for verification [13]. The object of industrial engineering with a change in wall thickness is considered [14]. The stress-strain state of the traverse of the hydraulic press was investigated using the finite element method [15].

The influence of the structural parameters of the cylinder on stress, deformation, and margin of safety is studied. Analysis of FE of the CAD model is carried out in the ANSYS software [16]. Linear and non-linear finite element methods were introduced in [17]. Moreover, the finite element method is presented as the primary tool for predicting and modeling the physical behavior of complex engineering systems [18].

### 3 Research Methodology

After considering various methods for studying the stress-strain state of massive bodies, including through laboratory tests in polarized light, it was concluded that the calculation of the strength of the main cylinder should be performed using the finite element method.

To assess the reliability of the results obtained on a personal computer using two programs that implement the finite element method (the specialized program “Prism” and the multipurpose package ANSYS), the stress in the elements of the ideal schematic cylinder (Figure 1) was determined using the foundations of the theory of elasticity [19].

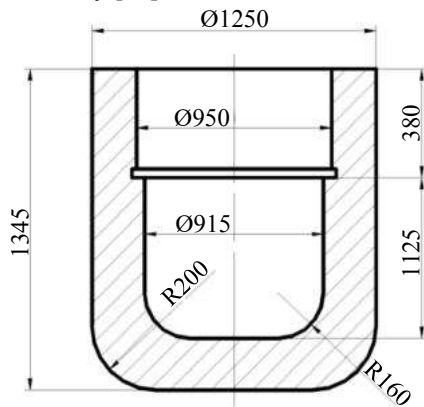


Figure 1 – Schematization of the cylinder

In such calculations, the cylinder is considered a body of rotation without brackets, holes, or supports. In the lower part, the cylinder connects to the bottom as a round plate, which is considered rigidly fixed on the contour, the radial transition with rounding from the cylinder wall to the bottom is not considered.

### 4 Results and Discussion

Determination of stresses in the cylinder wall is realized using the Lamé solution. The input data is as follows: the radius of the inner surface of the cylinder  $r_1 = 0.4575$  m; the radius of the outer surface of the cylinder  $r_2 = 0.6250$  m; the internal pressure of the liquid is taken as a single, dimensionless one ( $p = 1.0$ ) since all stresses are within fractions of this unit.

Calculation formulas and the value of unit stress on the inner surface of the cylinder wall (Figure 2) are as follows:

– radial normal stress:

$$\sigma_r = -p = -1; \quad (1)$$

– normal circular stress in the direction tangent to the cylindrical surface:

$$\sigma_t = p \cdot (r_2^2 + r_1^2) / (r_2^2 - r_1^2); \quad (2)$$

equivalent stress according to the 4th energy theory of strength:

$$\sigma_{equiv} = \sqrt{\sigma_r^2 + \sigma_t^2 + \sigma_y^2 - \sigma_t \sigma_r - \sigma_t \sigma_y - \sigma_r \sigma_y}. \quad (3)$$

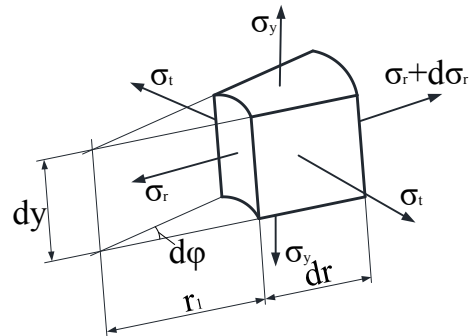


Figure 2 – The stressed state of the thick-walled cylinder element

Determination of stresses in the center of the bottom. We consider the bottom of the cylinder as a round plate, rigidly clamped on the contour and loaded with a uniform unit dimensionless pressure  $p$ .

Initial data is as follows: plate radius  $r_1 = 0.4575$  m; plate thickness  $h = 0.22$  m.

Radial bending moment:

$$M_r = \frac{pr_1^2}{16} \left[ 1 + \mu \cdot \frac{(3+\mu)r^2}{r_1^2} \right], \quad (4)$$

and circumferential bending moment:

$$M_t = \frac{pr_1^2}{16} \left[ 1 + \mu \cdot \frac{(3+\mu)r^2}{r_1^2} \right], \quad (5)$$

where  $r$  is the current radius vector of a point in a circular plate.





In the study of the stress-strain state of the cylinder based on the “PRISMA” software, one of the four identical (due to biaxial symmetry) parts of the D-0843 cylinder was discretized into finite elements. The X, Y, and Z coordinates of each 312 nodes were determined 36 elements; selected boundary conditions of their interaction and load in nodes; calculations were carried out on a computer.

The results of determining the equivalent stresses using the ANSYS and the “PRISMA” software packages are shown in Table 1.

Table 1 – Comparison of numerical calculation results in the “PRISMA” and ANSYS programs

No. of nodes “Prism”	$\sigma_{equiv}$ , MPa at $R_{pres} = 32$ MPa	No. of nodes “ANSYS”	$\sigma_{equiv}$ , MPa at $R_{pres} = 32$ MPa
3	61.5	8225	50.2
97	42.6	8227	65.9
90	40.3	8330	52.1
286	86.1	20 728	66.0
285	97.6	20 727	80.5
307	111.0	20 726	81.5
306	128.6	20 725	83.5
1	101.8	1460	83.8
96	104.0	1513	111.4
88	95.0	1507	121.2
140	89.6	1499	111.3

## 5 Conclusions

Analyzing the stresses obtained from the cylinder calculation allows for summarizing the following conclusions. The strength of the cylinder walls is ensured. However, there is an uneven distribution of stresses along the height of the cylinder, which does not satisfy the conditions of uniform strength of the structure. The strength of the flat part of the bottom is ensured, which follows from a comparison of the maximum stresses with the yield strength.

Some discrepancies in the distribution features of  $\sigma_{equiv}$  according to the two methods are, to a certain extent, caused by the fact that during the calculations in “ANSYS”, the internal pressure  $p$  was considered to be spread from the bottom to the annular groove, where the wall thickness changes. When using the “PRISMA” program in connection with the “manual” breakdown, it was impossible to isolate too small volumetric elements in the groove zone and the lower tides of the supporting ribs.

## 6 Acknowledgment

The authors appreciate the Department of Machine Dynamics and Mechanical Engineering and the “Presmash” industrial association.

## References

- Kogler, H., Ladner, K., Ladner, P. (2022). Flatness-based control of a closed-circuit hydraulic press. In: *Irschik, H., Krommer, M., Matveenko, V.P., Belyaev, A.K. (eds) Dynamics and Control of Advanced Structures and Machines. Advanced Structured Materials. Springer, Cham*, Vol 156, [https://doi.org/10.1007/978-3-030-79325-8\\_10](https://doi.org/10.1007/978-3-030-79325-8_10)
- Stishov, S.M. (2019). A small laboratory hydraulic press with a force of 20 tons. *Instrum Exp Tech*, Vol. 62, pp. 708-709, <https://doi.org/10.1134/S0020441219040213>
- Tomerlin, D., Kozak, D., Damjanović, D. et al. (2022). Structural life analysis method applied to hydraulic press welded frame construction. *Weld World*, Vol. 66, pp. 2595-2607, <https://doi.org/10.1007/s40194-022-01375-5>
- Wegener, K. (2019). Forming presses (hydraulic, mechanical, servo). In: *Chatti, S., Laperrière, L., Reinhart, G., Tolio, T. (eds) CIRP Encyclopedia of Production Engineering. Springer, Berlin, Heidelberg*, [https://doi.org/10.1007/978-3-662-53120-4\\_16695](https://doi.org/10.1007/978-3-662-53120-4_16695)
- Ramasamy, V., Basha, A.M.J. (2017). Multistage hydraulic cylinder buckling analysis by classical and numerical methods with different mounting conditions. In: *Saha, A., Das, D., Srivastava, R., Panigrahi, P., Muralidhar, K. (eds) Fluid Mechanics and Fluid Power – Contemporary Research. Lecture Notes in Mechanical Engineering. Springer, New Delhi*, [https://doi.org/10.1007/978-81-322-2743-4\\_85](https://doi.org/10.1007/978-81-322-2743-4_85)
- Salam, M.A. (2022). Hydraulic cylinders. In: *Fundamentals of Pneumatics and Hydraulics. Springer, Singapore*, [https://doi.org/10.1007/978-981-19-0855-2\\_7](https://doi.org/10.1007/978-981-19-0855-2_7)
- Lubecki, M., Stosiak, M., Gazińska, M. (2021). Numerical and experimental analysis of the base of a composite hydraulic cylinder made of PET. In: *Strzyzek, J., Warzyńska, U. (eds) Advances in Hydraulic and Pneumatic Drives and Control 2020. NSHP 2020. Lecture Notes in Mechanical Engineering. Springer, Cham*, [https://doi.org/10.1007/978-3-030-59509-8\\_36](https://doi.org/10.1007/978-3-030-59509-8_36)
- Sigova, E.M., Doronin, S.V. (2015). Stress-strain state of a cylindrical shell with a circular cutout. *Eng Res*, Vol. 35, pp. 481-484.
- Lepikhin, P.P., Romashchenko, V.A., Beiner, O.S. et al. (2018). Computational investigation of the effect of reinforcement schemes and angles on the stress-strain state and strength of composite cylinders under axisymmetric internal explosion. Part 1. Effect of the discretization spacings of the computational domain on the accuracy of determination of stress-strain state and strength. *Strength Mater*, Vol. 50, pp. 833-840, <https://doi.org/10.1007/s11223-019-00029-0>
- Boiko, A., Naidenko, E., Wang, Y. (2023). Vibration damping of lifting mechanisms. In: *Tonkonogiy, V., Ivanov, V., Trojanowska, J., Oborskyi, G., Pavlenko, I. (eds) Advanced Manufacturing Processes IV. InterPartner 2022. Lecture Notes in Mechanical Engineering. Springer, Cham*, [https://doi.org/10.1007/978-3-031-16651-8\\_38](https://doi.org/10.1007/978-3-031-16651-8_38)

11. Ponomarenko, O., Yevtushenko, N., Berlizieva, T., Grimzin, I., Lysenko, T. (2023). A method for calculating the strength performance of cast parts. In: *Tonkonogyi, V., Ivanov, V., Trojanowska, J., Oborskyi, G., Pavlenko, I. (eds) Advanced Manufacturing Processes IV. InterPartner 2022. Lecture Notes in Mechanical Engineering. Springer, Cham*, [https://doi.org/10.1007/978-3-031-16651-8\\_45](https://doi.org/10.1007/978-3-031-16651-8_45)
12. Bazhanova, A., Nemchuk, O., Lymarenko, O., Pitera, V., Sherstiuk, O., Khamrai, V. (2022). Diagnostics of stress and strained state of leaf springs of special purpose off-road vehicles. *Diagnostyka*, Vol. 23(1), 2022111, <https://doi.org/10.29354/diag/147292>
13. Sitharam, T., Govindaraju, L. (2021). *Theory of Elasticity*. Springer, Singapore, <https://doi.org/10.1007/978-981-33-4650-5>
14. Orobey, V., Nemchuk, O., Lymarenko, O., Romanov, O., Tkachuk, K. (2021). Diagnostics of the strength and stiffness of the loader carrier system structural elements in terms of thinning of walls by numerical methods. *Diagnostyka*, Vol. 22(3), pp. 73-81, <https://doi.org/10.29354/diag/141313>
15. Nemchynov, S. (2017). Finite element modeling of the stress-strain state of the traverse of the hydraulic press. *Computer Modeling: Analysis, Management, Optimization*, Vol. 1(1), pp. 37-40.
16. Agarwal, A., Seretse, O.M., Pitso, I. (2022). Optimal space filling design based finite element analysis of hydraulic cylinder. In: *Palani, I.A., Sathya, P., Palanisamy, D. (eds) Recent Advances in Materials and Modern Manufacturing. Lecture Notes in Mechanical Engineering. Springer, Singapore*, [https://doi.org/10.1007/978-981-19-0244-4\\_52](https://doi.org/10.1007/978-981-19-0244-4_52)
17. Gasser, C.T. (2021). The finite element method. In: *Vascular Biomechanics. Springer, Cham*, [https://doi.org/10.1007/978-3-030-70966-2\\_4](https://doi.org/10.1007/978-3-030-70966-2_4)
18. Erdogan, M., Ibrahim, G. (2006). *The Finite Element Method and Applications in Engineering Using ANSYS®*. Springer, New York, USA. <https://doi.org/10.1007/978-0-387-28290-9>.
19. Pisarenko, G., Kvitka, O., Umansky, E. (2004). *Resistance of Materials*. Vyscha Shkola, Kyiv, Ukraine.



*machines*

an Open Access Journal by MDPI



## Innovations in the Design, Simulation, and Manufacturing of Production Systems

Guest Editors:

**Prof. Dr. Vitalii Ivanov**

Department of Manufacturing Engineering, Machines and Tools, Sumy State University, 40007 Sumy, Ukraine  
ivanov@tmvi.sumdu.edu.ua

**Prof. Dr. Ivan Pavlenko**

Department of Computational Mechanics named after V. Martsynkovskyy, Sumy State University, 40007 Sumy, Ukraine  
i.pavlenko@cm.sumdu.edu.ua

**Dr. Katarzyna Antosz**

Department of Manufacturing Processes and Production Engineering, Rzeszow University of Technology, Aleja Powstańców Warszawy 12, 35-959 Rzeszów, Poland  
katarzyna.antosz@prz.edu.pl

Deadline for manuscript submissions:

**31 March 2024**



[mdpi.com/si/165601](https://mdpi.com/si/165601)

### Message from the Guest Editors

Dear Colleagues,

Design, simulation, and manufacturing are integral stages of a machine's production. Design engineering focuses on the creative process of developing innovative systems and units, ensuring process intensification, productivity, flexibility, and efficiency. The importance of this stage implies modern approaches in the CAx technologies, ensuring digitalization of the design process, which is an integral part of Industry 4.0. This Special Issue welcomes articles on innovative solutions in designing machine tools, mechatronic devices, robotic systems, flexible manufacturing systems, transport machines and systems, reconfigurable machines, fixture and tooling design, rotary machines and drive units, etc. Verification of the created products is mandatory before the manufacturing stage. The developed design should be checked in a virtual environment based on the operating conditions. For this purpose, numerical simulation and experimental studies can be applied. The reliability of the virtual and experimental studies should be justified in terms of quality requirements. The above-mentioned processes make it possible to proceed to the manufacturing stage.

**Special** Issue



Javanbakht T. (2023). Optimization of graphene oxide's characteristics with TOPSIS using an automated decision-making process. *Journal of Engineering Sciences*, Vol. 10(1), pp. E1-E7, doi: 10.21272/jes.2023.10(1).e1

## Optimization of Graphene Oxide's Characteristics with TOPSIS Using an Automated Decision-Making Process

Javanbakht T.

Department of Computer Science, University of Quebec in Montreal,  
201 President Kennedy St., Montreal, H2X 3Y7 Quebec, Canada

### Article info:

Submitted: March 8, 2023  
Received in revised form: May 6, 2023  
Accepted for publication: May 15, 2023  
Available online: May 18, 2023

### \*Corresponding email:

[javanbakht.taraneh@courrier.uqam.ca](mailto:javanbakht.taraneh@courrier.uqam.ca)

**Abstract.** The present study focuses on a new application of TOPSIS to predict and optimize graphene oxide's characteristics. Although this carbon-based material has been investigated previously, its optimization with this method using an automated decision-making process has not been performed yet. The major problem in the design and analysis of this nanomaterial is the lack of information on comparing its characteristics, which has led to the use of diverse methods that have not been appropriately compared. Moreover, their advantages and inconveniences could be investigated better once this investigation provides information on optimizing its candidates. In the current research work, a novel automated decision-making process was used with the TOPSIS algorithm using the Łukasiewicz disjunction, which helped detect the confusion of properties and determine its impact on the rank of candidates. Several characteristics of graphene oxide, such as its antibiofilm activity, hemocompatibility, activity with ferrous ions in hydrogen peroxide, rheological properties, and the cost of its preparation, have been considered in its analysis with TOPSIS. The results of this study revealed that the consideration of the criteria of this nanomaterial as profit or cost criteria would impact the distances of candidates from the alternatives. Moreover, the ranks of the candidates changed when the rheological properties were considered differently in the data analysis. This investigation can help improve the use of this nanomaterial in academic and industrial investigations.

**Keywords:** process innovation, energy optimization, prediction, TOPSIS, algorithm.

## 1 Introduction

Graphene oxide (GO) is a substantial two-dimensional nanomaterial that was prepared using the oxidation of graphene after the discovery of this nanomaterial by Novoselov et al. in 2004 [1]. It is among the carbon-based materials with various applications in science and engineering [2].

The physical properties of GO are comparable with those of graphene by removing the functional groups from its surface. The presence of the functional groups makes GO hydrophilic and dispersible in water, whereas graphene has hydrophobic properties [2].

Different GO sizes from nm to mm can be obtained using different sonication periods [3]. The optimization of the characteristics of GO is an important procedure required for the improvement of its design and manufacture.

## 2 Literature Review

The physicochemical, mechanical, and biological characteristics of GO, such as its activity with ferrous ions in hydrogen peroxide [4], rheological properties [5], antibiofilm activity [6], hemocompatibility [7, 8], and the cost of its preparation [9] with or without polymers have been carried out, previously. These properties of GO were chosen in this investigation for their optimization with the Technique for Order of Preference by Similarity to the Ideal Solution (TOPSIS). As indicated in the mentioned studies, the GO production with the less defective reduced product was performed in hydrogen peroxide [4], and the indicated properties significantly impacted the quality of GO [5]. Moreover, the practical value of GO was revealed in killing bacteria related to its surface physical properties [6]. It has been revealed that the interactions between the hematological entities, such as blood cells, and GO would influence the efficacy of its biomedical applications [7].

It is worth noting that the production of GO using less costly procedures for energy storage and conversion applications would be required [8]. The consideration of these properties of GO can lead to the energy optimization of its design and preparation.

The thickness of a single-layer GO flake measured with atomic force microscopy typically ranges between 1.0 nm and 1.4 nm [10, 11], which is above the thickness value measured for graphene (0.7 nm [12]). The thickness of GO can change according to its preparation procedure. No detailed investigation on the impact of the thickness of GO on its correlative characteristics has been done yet. Therefore, its thickness has not been considered for optimization in the current study.

TOPSIS is a method that considers the profit and cost criteria and optimizes the candidates. This has been done by considering their distances from the alternatives for comparative analysis using different methods [13], decision-making processes [14], and financial performance evaluation [15]. All these analysis procedures have included the advantages of TOPSIS. Universality is an advantage of this method [16]. The simplicity of computation and presentation is its other advantage [17].

The selection of the best process for removing color with the use of adsorbent materials [18], the improvement of the GO dispersion properties [19], the selection of graphene oxide nanocomposites [20], the optimization of the mixture proportions of graphene oxide [21] and the evaluation of the performance on reduced graphene oxide synthesized [22] have been performed with the TOPSIS method. However, no study has been done on the optimization of the physicochemical, mechanical, and biological characteristics of GO previously. For the first time, the optimization of this nanomaterial based on these characteristics is investigated in the current paper.

The objectives of this study have been to determine the results of the optimization of the characteristics of GO. For this, the unmodified and modified TOPSIS methods have been used.

The results of this study reveal the impact of the criteria of this nanomaterial as profit or cost criteria on the distances of each candidate from the alternatives. The ranking of the candidates can be affected by different considerations of its characteristics in several analyses. This investigation can help improve the use of this nanomaterial for further applications in science and engineering.

### 3 Research Methodology

#### 3.1 TOPSIS method

The following TOPSIS algorithm in Python was used for the optimization of GO: <https://github.com/Glitchfix/TOPSIS-Python/blob/master/topsis.py>.

Figure 1 presents the flowchart of the steps of the unmodified and modified TOPSIS methods. The modification step in the evaluation matrix, including the Łukasiewicz disjunction, does not exist in the unmodified TOPSIS algorithm but is used in its modified version.

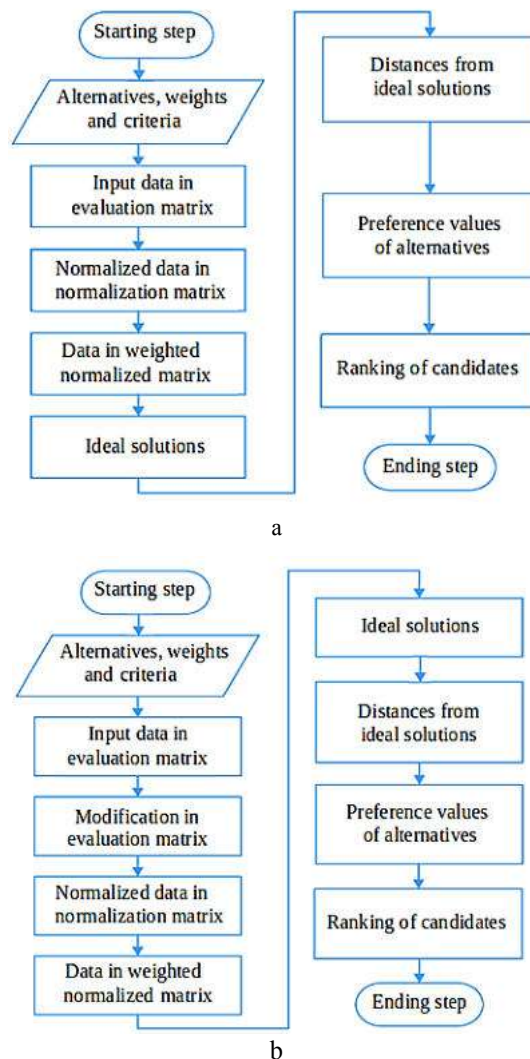


Figure 1 – The flowchart of the research steps with unmodified (a) and modified (b) TOPSIS

The other steps are in common in the two procedures. The Łukasiewicz disjunction in the modified TOPSIS method enables the algorithm to perform automated decision-making to distinguish the categories of graphene-based materials.

The activity of GO with ferrous ions in hydrogen peroxide [4], its rheological properties [5], antibiofilm activity [6], hemocompatibility [7, 8], and the cost of its preparation [9] have been optimized with TOPSIS in the current study.

The results with TOPSIS were obtained as described previously for data pre-processing [23] and ranking similarity [24].

#### 3.2 Modified TOPSIS

The modified TOPSIS using the Łukasiewicz disjunction optimized the GO candidates with a novel automated decision-making process. This method sets the maximum value acceptable in the TOPSIS algorithm to 1.0. Therefore, this procedure detected and analyzed the confusion in considering the GO properties. The modified TOPSIS algorithm was required to determine how the rank of the GO samples would change when the individual confused their properties with those of the other graphene-based samples, such as the reduced GO.

## 4 Results

Table 1, in three parts, shows the terms, their corresponding values of fuzzy membership degrees for the properties of GO samples, and their average values.

Table 1 – Terms, their related membership degrees of the characteristics of GO samples, and average values

Candidates/criteria	Antibiofilm activity	Hemo-compatibility	Activity in hydrogen peroxide	Rheological properties	Cost
C <sub>1</sub>	low	medium	medium	low	low
C <sub>2</sub>	medium	medium	medium	medium	medium
C <sub>3</sub>	medium	low	high	medium	high
Values of the characteristics					
Candidates/criteria	Antibiofilm activity	Hemo-compatibility	activity in hydrogen peroxide	Rheological properties	Cost
C <sub>1</sub>	0.2, 0.3, 0.4	0.4, 0.5, 0.6	0.4, 0.5, 0.6	0.2, 0.3, 0.4	0.2, 0.3, 0.4
C <sub>2</sub>	0.4, 0.5, 0.6	0.4, 0.5, 0.6	0.4, 0.5, 0.6	0.4, 0.5, 0.6	0.4, 0.5, 0.6
C <sub>3</sub>	0.4, 0.5, 0.6	0.2, 0.3, 0.4	0.7, 0.8, 0.9	0.4, 0.5, 0.6	0.7, 0.8, 0.9
Average values					
Candidates/criteria	Antibiofilm activity	Hemo-compatibility	Activity in hydrogen peroxide	Rheological properties	Cost
C <sub>1</sub>	0.3	0.5	0.5	0.3	0.3
C <sub>2</sub>	0.5	0.5	0.5	0.5	0.5
C <sub>3</sub>	0.5	0.3	0.8	0.5	0.8

The weight value of 0.5 is chosen for the criteria. In the next step, the criteria matrix of GO samples is determined. In the criteria matrix, all the characteristics of GO, apart from its cost, are considered as profit criteria. This last one is considered as a cost criterion. Therefore, the terms “true” and “false” are indicated in this matrix for the first and last criteria, respectively.

In the next step, the vector normalization of data for the GO samples is performed.

Tables 2, 3 show the results of the normalization procedure and the multiplication of weights with the normalized data, respectively.

The determination of the alternatives is performed in the next step. Table 4 shows the values of the alternatives for GO samples.

Table 2 – Data in normalized decision matrix

Candidates/criteria	Antibiofilm activity	Hemo-compatibility	Activity in hydrogen peroxide	Rheological properties	Cost
C <sub>1</sub>	0.3906	0.6509	0.4683	0.3906	0.3030
C <sub>2</sub>	0.6509	0.6509	0.4683	0.6509	0.5051
C <sub>3</sub>	0.6509	0.3906	0.7493	0.6509	0.8081

Table 3 – Data in weighted normalized decision matrix

Candidates/criteria	Antibiofilm activity	Hemo-compatibility	Activity in hydrogen peroxide	Rheological properties	Cost
C <sub>1</sub>	0.0781	0.1302	0.0937	0.0781	0.0606
C <sub>2</sub>	0.1302	0.1302	0.0937	0.1302	0.1010
C <sub>3</sub>	0.1302	0.0781	0.1499	0.1302	0.1616

Table 4 – The alternatives for GO samples

Candidates/criteria	Antibiofilm activity	Hemo-compatibility	Activity in hydrogen peroxide	Rheological properties	Cost
A <sup>+</sup>	0.1302	0.1302	0.1499	0.1302	0.0606
A <sup>-</sup>	0.0781	0.0781	0.0937	0.0781	0.1616

The distances from the alternatives for the GO samples are obtained in the next step.

Table 5 shows the values of distances from the alternatives for GO samples. Then, we performed the analysis of the similarity coefficients of the GO samples.

Table 6 shows the similarity coefficient ( $CC_i$ ) values and the ranking of the GO samples according to their worst similarity.

Table 5 – The distances from the alternatives for GO samples

Candidates	$d_i^*$	$d_i^-$
C <sub>1</sub>	0.0926	0.1136
C <sub>2</sub>	0.0692	0.1087
C <sub>3</sub>	0.1136	0.0926

Table 6 –  $CC_i$  and the ranking of GO samples

Candidates	$CC_i^*$	Ranking
C <sub>1</sub>	0.5509	2
C <sub>2</sub>	0.6109	1
C <sub>3</sub>	0.4491	3

Figure 2 shows the results of Table 6. The values of the distances from the best and worst alternatives and similarity coefficients ( $CC_i$ ) of the GO samples are presented in black, red, and green, respectively.

Considering that the rheological properties of GO samples could be their cost criteria, the term “false” was chosen for these properties instead of the term “true” in the criteria matrix of the GO samples. Tables 7 to 11 show the results obtained with the TOPSIS method after this modification.

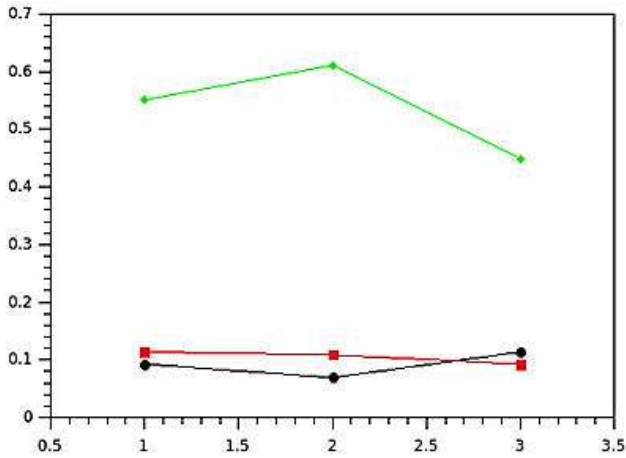


Figure 2 – The values of the distances from the alternatives and similarity coefficients ( $CC_i$ ) of GO samples

Table 7 presents the data of the normalized decision matrix for the GO samples. Table 8 presents the data of the weighted normalized decision matrix for the GO samples.

Table 9 presents the alternatives for the GO samples. Table 10 shows the distances from the alternatives for the GO samples. Table 11 shows the similarity coefficient values and the ranking of the GO samples.

Figure 3 shows the results of Table 11.

Table 7 – Data in the normalized decision matrix

Candidates/criteria	Antibiofilm activity	Hemo-compatibility	Activity in hydrogen peroxide	Rheological properties	Cost
C <sub>1</sub>	0.3906	0.6509	0.4683	0.3906	0.3030
C <sub>2</sub>	0.6509	0.6509	0.4683	0.6509	0.5051
C <sub>3</sub>	0.6509	0.3906	0.7493	0.6509	0.8081

Table 8 – Data in the weighted normalized decision matrix

Candidates/criteria	Antibiofilm activity	Hemo-compatibility	Activity in hydrogen peroxide	Rheological properties	Cost
C <sub>1</sub>	0.0781	0.1302	0.0937	0.0781	0.0606
C <sub>2</sub>	0.1302	0.1302	0.0937	0.1302	0.1010
C <sub>3</sub>	0.1302	0.0781	0.1499	0.1302	0.1616

Table 9 – The alternatives for GO samples

Candidates/criteria	Antibiofilm activity	Hemo-compatibility	Activity in hydrogen peroxide	Rheological properties	Cost
A <sup>+</sup>	0.1302	0.1302	0.1499	0.0781	0.0606
A <sup>-</sup>	0.0781	0.0781	0.0937	0.1302	0.1616

Table 10 – The distances from the alternatives for GO samples

Candidates	$d_i^*$	$d_i^-$
C <sub>1</sub>	0.0766	0.1250
C <sub>2</sub>	0.0866	0.0954
C <sub>3</sub>	0.1250	0.0766

Table 11 –  $CC_i$  and the ranking of GO samples

Candidates	$CC_i^*$	Ranking
C <sub>1</sub>	0.6200	1
C <sub>2</sub>	0.5241	2
C <sub>3</sub>	0.3800	3

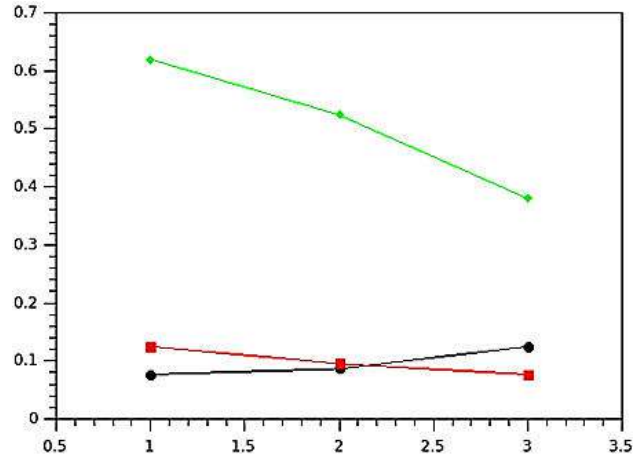


Figure 3 – The values of the distances from the alternatives and similarity coefficients ( $CC_i$ ) of GO samples

The values of the distances from the best and worst alternatives and similarity coefficients ( $CC_i$ ) of the GO samples are presented in black, red, and green, respectively.

As revealed by the obtained results in this paper, the ranking of the GO samples is influenced by modifying the consideration of their characteristics as profit or cost criteria. In the first ranking, the ranks 2, 1, and 3 were obtained for the first, second, and third candidates. In the second series of analysis, when these nanomaterial's rheological properties were considered cost criteria, the ranks 1, 2, and 3 were obtained for the first, second, and third candidates, respectively. Moreover, the values of distances from the alternatives and those of their similarity coefficients that determined their ranks also changed following this modification.

In another series of analyses, the modified TOPSIS algorithm with the Łukasiewicz disjunction was used to optimize the GO candidates with an automated decision-making process. In the analysis with the modified TOPSIS, the maximum value of the cost of GO in the evaluation matrix obtained in the algorithm's output for candidates 1 and 3 was 1.0. No other change was performed in the optimization. The data in the criteria matrix were like the ones used in the previous analysis.

Table 12 shows the results of the normalized decision matrix for the GO samples. Table 13 shows the results of the weighted normalized decision matrix for the GO samples.

Table 14 shows the values of the alternatives for the GO samples. Table 15 shows the values of distances from the alternatives for the GO samples. Table 16 shows the GO samples' similarity coefficients ( $CC_i$ ) and ranking.

Table 12 – Results of the normalized decision matrix

Candidates/criteria	Antibiofilm activity	Hemo-compatibility	Activity in hydrogen peroxide	Rheological properties	Cost
C <sub>1</sub>	0.3906	0.6509	0.4683	0.3906	0.6667
C <sub>2</sub>	0.6509	0.6509	0.4683	0.6509	0.3333
C <sub>3</sub>	0.6509	0.3906	0.7493	0.6509	0.6667



Table 13 – Results of the weighted normalized decision matrix

Candidates/criteria	Antibiofilm activity	Hemo-compatibility	Activity in hydrogen peroxide	Rheological properties	Cost
C <sub>1</sub>	0.0781	0.1302	0.0937	0.0781	0.1333
C <sub>2</sub>	0.1302	0.1302	0.0937	0.1302	0.0667
C <sub>3</sub>	0.1302	0.0781	0.1499	0.1302	0.1333

Table 14 – The alternatives for GO samples

Candidates/criteria	Antibiofilm activity	Hemo-compatibility	Activity in hydrogen peroxide	Rheological properties	Cost
A <sup>+</sup>	0.1302	0.1302	0.1499	0.0781	0.0667
A <sup>-</sup>	0.0781	0.0781	0.09365858	0.1302	0.1333

Table 15 – The distances from the alternatives

Candidates	$d_i^*$	$d_i^-$
C <sub>1</sub>	0.1016	0.0736
C <sub>2</sub>	0.0766	0.0993
C <sub>3</sub>	0.0993	0.0766

Table 16 –  $CC_i$  and the ranking of GO samples

Candidates	$CC_i^*$	Ranking
C <sub>1</sub>	0.4203	2
C <sub>2</sub>	0.5646	3
C <sub>3</sub>	0.4354	1

Figure 4 shows the results of Table 16. The values of the distances from the best and worst alternatives and similarity coefficients ( $CC_i$ ) of the GO samples are presented in black, red, and green, respectively.

The obtained results in the last series of analyses showed that the ranks of the GO samples depended on the values of their properties in the evaluation matrix.

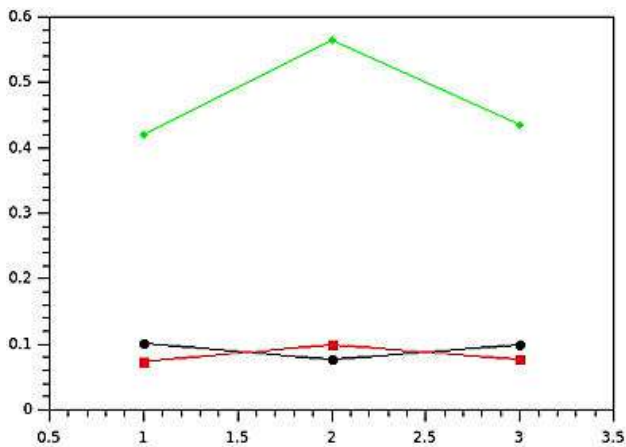


Figure 4 – The values of the distances from the alternatives and similarity coefficients ( $CC_i$ ) of GO samples

Figure 5 shows the values of the distances from the alternatives and similarity coefficients ( $CC_i$ ) of the first-ranked GO samples of the three series of analyses. The results for the first, second, and third analyses are represented in the left, middle, and right, respectively.

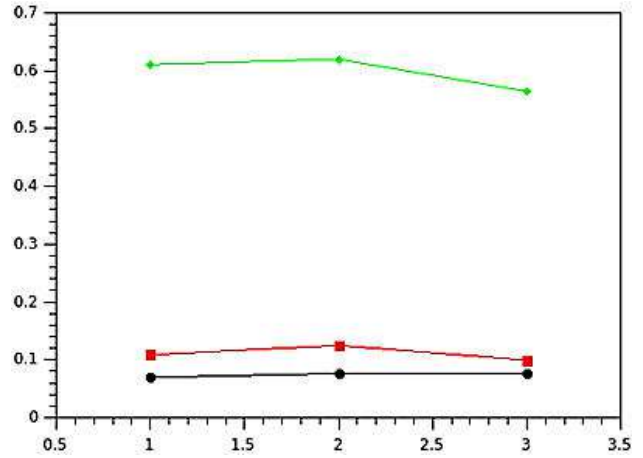


Figure 5 – The values of the distances from the alternatives and similarity coefficients ( $CC_i$ ) of the first-ranked GO samples of the three series of analyses

As shown in Figure 5, the lowest value of  $d_i^*$  and the highest value of  $d_i^-$  were observed for the first-ranked candidates of the first and second series of analyses, respectively. Moreover, the highest value of  $CC_i$  was observed for the first-ranked sample of the second analysis.

Further comparison of the obtained results showed that the distances of the GO samples from their ideal solutions and their ranks depended on the use of modified and unmodified TOPSIS algorithms. In the first series of analyses using the unmodified TOPSIS method, the second, first, and third samples had the first, second, and third ranks, respectively. In the second analysis series, when GO's rheological properties were considered cost criteria, the first, second, and third samples had the first, second, and third ranks, respectively. However, in the third series of analyses using the modified TOPSIS method, the second, third, and first samples had the first, second, and third ranks, respectively. These results showed the effect of the Łukasiewicz disjunction in the change of the ranking of candidates.

## 5 Discussion

The comparison of rankings obtained with the unmodified and modified TOPSIS methods revealed that the rank of the GO samples could change with the automated decision-making process using modified TOPSIS due to the confusion of the categories of samples by the individual. This showed that when the individual confused the properties of the GO samples with those of other graphene-based samples, this could change the ranks. Moreover, the results of ranking the GO samples obtained with the modified TOPSIS algorithm differed from both results obtained in the first and second series of analyses with unmodified TOPSIS.

The physical [25, 26], chemical [27, 28], and biological properties [29, 30] of different nanomaterials have been investigated in recent years. Further investigations are required for the optimization of the properties of these materials with TOPSIS.

The thickness of GO can have impact on the efficiency of certain devices such as solar cells [31]. Recently, the effects of the thickness of GO on some of its properties such as its friction [32] and hydrogen production [33] have been reported. However, these properties have not been correlated, yet. More investigations are required to optimize the correlated characteristics of this nanomaterial.

The current study, as the first optimization of the characteristics of GO using unmodified TOPSIS and an automated decision-making process with the modified algorithm, can help a better understanding of the characteristics of this nanomaterial for its further design and applications.

## 6 Conclusions

This paper presented for the first time the optimization of the chemical, rheological and biological characteristics and the cost of GO using the TOPSIS method. Two algorithms, unmodified and modified, were used in several series of analyses.

The impact of the characteristics such as the antibiofilm activity, hemocompatibility, activity with hydrogen peroxide, rheological properties, and the preparation cost of this nanomaterial on the candidates' ranking was investigated.

In the first series of analysis with unmodified TOPSIS, the values of the similarity coefficient of the first, second and third GO samples were 0.61, 0.55, and 0.45, respectively. These values in the second series of analysis with unmodified TOPSIS were 0.62, 0.52, and 0.38, respectively. In the third series of analysis with modified TOPSIS, the values were 0.44, 0.42, and 0.56, respectively.

The ranks of candidates were done according to these values, which helped optimize the samples considering their characteristics. The results obtained in this paper showed that the modification in the type of criteria would modify the ranks related to the changes in the values of the candidates' distances from the alternatives and those of their similarity coefficients. These results can be used for the comparative optimization of nanomaterials with applications in science and engineering.

## References

- Novoselov, K.S., Geim, A.K. et al. (2004). Electric field effect in automatically thin carbon films, *science*, vol. 306(5696), pp. 666-669. <https://doi.org/10.1126/science.1102896>.
- Perrozzzi, F. et al. (2015). Graphene oxide: from fundamentals to applications, *J. Phys.: Condens. Matter*, vol. 27, 013002. <https://doi.org/10.1088/0953-8984/27/1/013002>.
- Su, C.-Y., Xu, Y., Zhang, W., Zhao, J., Tang, X., Tsai, C.-H., Li, L.-J. (2009). Electrical and spectroscopic characterizations of ultra-large reduced graphene oxide monolayers, *Chem. Mater.*, vol. 21, pp. 5674-80. <https://doi.org/10.1021/cm902182y>.
- Piñas, J.A.V. et al. (2019). Production of reduced graphene oxide platelets from graphite flakes using the Fenton reaction as an alternative to harmful oxidizing agents, *Journal of Nanomaterials*, 736563.
- Shim, Y.H. et al. (2018). Tailored colloidal stability and rheological properties of graphene oxide liquid crystals with polymer-induced depletion attractions, *ACS Nano*, vol. 12(11), pp. 11399-11406.
- Javanbakht, T., Hadian, H., Wilkinson, K.J. (2020). Comparative study of physicochemical properties and antibiofilm activity of graphene oxide nanoribbons, *Journal of Engineering Sciences*, vol. 7(1), pp. C1-C8. <https://doi.org/10.21272/jes>.
- Kenry. (2018). Understanding the hemotoxicity of graphene nanomaterials through their interactions with blood proteins and cells, *J. Mater. Res.*, vol. 33(1), pp. 44-57.
- Kenry et al. (2015). Molecular hemocompatibility of graphene oxide and its implication for antithrombotic applications, *Small*, vol. 11(38), pp. 5105-5117. <https://europepmc.org/article/med/26237338>.
- Zhang, X. et al. (2015). Large-area preparation of high-quality and uniform three-dimensional graphene networks through thermal degradation of graphene oxide-nitrocellulose composites, *ACS Applied Materials and Interfaces*, vol. 7, pp. 1057-1064.
- Stankovich, S., Dikin, D.A., Piner, R.D., Kohlhaas, K.A., Kleinhammes, A., Jia, Y., Wu, Y., Nguyen, S.T., Ruoff, R.S. (2007). Synthesis of graphene-based nanosheets via chemical reduction of exfoliated graphite oxide, *Carbon*, vol. 45, pp. 1558-65. <https://doi.org/10.1016/j.carbon.2007.02.034>.
- Jung, I., Vaupel, M., Pelton, M., Piner, R., Dikin, D.A., Stankovich, S., An, J., Ruoff, R.S. (2008). Characterization of thermally reduced graphene oxide by imaging ellipsometry, *J. Phys. Chem. C*, vol. 112, pp. 8499-506. <https://doi.org/10.1021/jp802173m>.
- Gupta, A., Chen, G., Joshi, P., Tadigadapa, S., Eklund, P.C. (2006). Raman scattering from high-frequency phonons in supported n-graphene layer films, *Nano lett.*, vol. 6, pp. 2667-73. <https://doi.org/10.1021/nl061420a>.
- Sařabun, W., Wařróbski, J., Shekhovtsov, A. (2020). Are MCDA methods benchmarkable? A comparative study of TOPSIS, VIKOR, COPRAS, and PROMETHEE II methods. *Symmetry*, vol. 12(9), 1549. <https://doi.org/10.3390/sym12091549>.
- Hsu, L.-C. (2013). Investment decision making using a combined factor analysis and entropy-based TOPSIS model, *Journal of Business Economics and Management*, vol. 14(3), pp. 448-466. <https://doi.org/10.3846/16111699.2011.633098>.
- Bulgurcu, B. (2012). Application of TOPSIS technique for financial performance evaluation of technology firms in Istanbul stock exchange market. *Procedia*, vol. 62, pp. 1033-1040. <https://doi.org/10.1016/j.sbspro.2012.09.176>.
- Kochkina, M. V., Karamyshev, A. N., Isavnin, A. G. (2017). Modified multi-criteria decision making method development based on "AHP" and "TOPSIS" methods using probabilistic interval estimates. *The Turkish Online Journal of Design, Art and Communication TOJDAC*, pp. 1663-1674. <https://doi.org/10.7456/1070DSE/144>.
- Abidin, M. Z., Rusli, R., Shariff, A. M. (2016). Technique for order performance by similarity to ideal solution (TOPSIS)- entropy methodology for inherent safety design decision making tool, *Procedia Engineering*, vol. 148, pp. 1043-1050. <https://doi.org/10.1016/j.proeng.2016.06.587>.
- Azari, A. et al. (2022). Integrated fuzzy AHP-TOPSIS for selecting the best color removal process using carbon-based adsorbent materials: multi-criteria decision making vs. systematic review approaches and modeling of textile wastewater treatment in real conditions, *International Journal of Environmental Analytical Chemistry*, vol. 102(18), pp. 7329-7344.
- řimřek, B. et al. (2018). Improvement of the graphene oxide dispersion properties with the use of TOPSIS based Taguchi application, *Periodica Polytechnica Chemical Engineering*, vol. 62(3), pp. 323-335. <https://doi.org/10.3311/Ppch.11412>.

20. Awate, P.P., Barvem S.B. (2022). Graphene/Al6061 nanocomposite selection using TOPSIS and EXPROM2 multi-criteria decision-making methods, *Materials Today: Proceedings*, vol. 62(2). <https://doi.org/10.1016/j.matpr.2022.04.069>.
21. Korucu, H. et al. (2018). A TOPSIS-based Taguchi design to investigate optimum mixture proportions of graphene oxide powder synthesized by Hummers method, *Arabian Journal for Science and Engineering*, vol. 43, pp. 6033-6055. <https://doi.org/10.1007/s13369-018-3184-4>.
22. Korucu, H. (2022). Evaluation of the performance on reduced graphene oxide synthesized using ascorbic acid and sodium borohydride: Experimental designs-based multi-response optimization application, *Journal of Molecular Structure*, vol. 1268, 133715. <https://doi.org/10.1016/j.molstruc.2022.133715>.
23. Kobryń, A., Prystrom, J. (2016). A data pre-processing model for TOPSIS method, *Folia Oeconomica Stetinensia*, vol. 16(2), pp. 219-235. <https://doi.org/10.1515/fofi-2016-0036>.
24. Shekhovtsov, A., Sałabun, W. (2020). A comparative case study of the VIKOR and TOPSIS rankings similarity, *Procedia Computer Science*, vol. 176, pp. 3730-3740. <https://doi.org/10.1016/j.procs.2020.09.014>.
25. Djavanbakht T, Carrier V, André JM, Barchewitz R, Troussel P. (2000). Effets d'un chauffage thermique sur les performances de miroirs multicouches Mo/Si, Mo/C et Ni/C pour le rayonnement X mou, *Journal de Physique IV*, France, vol. 10, pp. 281-287. <https://doi.org/10.1051/jp4:20001031>.
26. Čitaković, N.M. (2019). Physical properties of nanomaterials, *Military Technical Courier*, vol. 67(1), pp. 159-171. <https://doi.org/10.5937/vojtehg67-18251>.
27. Bhawani, E. et al. (2020). Investigation on the synthesis and chemical properties of nanomaterials, *International Research Journal on Advanced Science Hub*, vol. 2(12), pp. 41-47. <https://doi.org/10.47392/irjash.2020.246>.
28. Javanbakht, T., Laurent, S., Stanicki, D., Frenette, M. (2020). Correlation between physicochemical properties of superparamagnetic iron oxide nanoparticles and their reactivity with hydrogen peroxide, *Canadian Journal of Chemistry*, Vol. 98(10), pp. 601-608. <https://doi.org/10.1139/cjc-2020-0087>.
29. Radu, N.N. et al. (2009). Biological properties of nanomaterials based on irridoidic compounds, *Proceedings of the International Society for Optical Engineering*, 7403. <https://doi.org/10.1117/12.828875>.
30. Javanbakht, T., Ghane-Motlagh, B., Sawan, M. (2020). Comparative study of antibiofilm activity and physicochemical properties of microelectrode arrays, *Microelectronic Engineering*, vol. 229, 111305. <https://doi.org/10.1016/j.mee.2020.111305>.
31. Mehrabian, M. et al. (2021). Simulating the thickness effect of the graphene oxide layer in CsPbBr<sub>3</sub>- based solar cells, *Materials Research Express*, 035509. <http://doi.org/10.1088/2053-1591/abf080>.
32. Kwon, S. et al. (2018). The effect of thickness and chemical reduction of graphene oxide on nanoscale friction, *J. Phys. Chem. B*, vol. 122(2), pp. 543-547. <https://doi.org/10.1021/acs.jpcc.7b04609>.
33. Gacka, E. (2021). Effect of graphene oxide flakes size and number of layers on photocatalytic hydrogen production, *Scientific Reports*, vol. 11, 15969. <http://doi.org/10.1038/s41598-021-95464-y>.



Tigariev V., Lopakov O., Rybak O., Kosmachevskiy V., Cioatǎ V. G. (2023). Design in modern information systems by applying cloud technologies. *Journal of Engineering Sciences*, Vol. 10(1), pp. E8-E13, doi: 10.21272/jes.2023.10(1).e2

## Design in Modern Information Systems by Applying Cloud Technologies

Tigariev V.<sup>1</sup>[0000-0001-8492-6633], Lopakov O.<sup>1</sup>[0000-0001-6307-8946], Rybak O.<sup>1</sup>[0000-0002-0250-3037],  
Kosmachevskiy V.<sup>1</sup>[0000-0002-3234-2297], Cioatǎ V. G.<sup>2</sup>[0000-0002-5578-2308]

<sup>1</sup> National University Odesa Polytechnic, 1, Shevchenko Ave., 65040 Odesa, Ukraine;

<sup>2</sup> Politehnica University Timisoara, 5, Revoluției St., 331128 Hunedoara, Romania

### Article info:

Submitted: February 18, 2023  
Received in revised form: May 12, 2023  
Accepted for publication: May 26, 2023  
Available online: May 29, 2023

### \*Corresponding email:

[volodymyr\\_t@ukr.net](mailto:volodymyr_t@ukr.net)

**Abstract.** In this study, the general algorithm and technology of design in advanced computer-aided design (CAD) software of the CAD-in-the-Cloud type using an information model (IM) was discussed in detail. Applying design systems of this type increases productivity and quality of the development and enables group work on the project. The proposed information model consists of three main components – working with Autodesk Fusion 360 on a computer, working with cloud capabilities, and designers’ collaboration through the cloud. Nevertheless, some IM elements may be missing in a particular design, or there can be options for applying the proposed steps in the design process. Developing customized respiratory protective equipment (face masks) in Autodesk Fusion 360 CAD family was considered as an example of the suggested IM application. Modern design and producing technologies enable the creation of masks according to individual anatomical characteristics of the human face. In this paper, the protective mask was created by applying modern cloud computing technologies using information models. Information models were adapted to the process of protective mask design. The model of a human headform was developed using the 3D scanning method. After applying retopology tools, a basis of the mask frame was created on the surface of a 3D model of a head. Building a solid model and testing the mask fame configuration under mechanical stresses due to facial expression changing was carried out in Autodesk Fusion 360 CAD software. Finally, the cloud module of the generative design was applied to determine the filtering element configuration.

**Keywords:** information model, CAD-on-the-cloud, CAD-in-the-cloud, mask, product innovation.

## 1 Introduction

Software technologies are developing very rapidly. Programs are becoming increasingly important in various design and manufacturing sectors, which causes increasing numbers of different applications for them. The widespread use of computer-aided design (CAD) systems allows for simulating the development of the information technology industry, leading to new trends and evolutions. Cloud services have become the only way to get through the crisis caused by the pandemic for many companies to keep working and cooperating with clients and partners. Their expenses have risen dramatically. When using cloud technologies, a designer can work with his team partners or independently on cloud servers at any time from any location by connecting to the cloud CAD platform. Basic parameters of the future product are laid at the design stage. The design process usually involves time-

consuming calculations and preparing varied documentation. There are advanced engineering tools that speed up the process and take product design to a higher level. Thanks to new technologies, it is possible to solve problems and expand design opportunities with the help of cloud CAD online platforms. The product is no longer a static object. The final product continues to evolve and expand functional capabilities after delivery. This presents new challenges for designers, engineers, and manufacturers by using cloud technologies.

## 2 Literature Review

Present-day design is hard to imagine without applying cloud technologies. Their capabilities extend to all the stages of project creation. The project itself is located on cloud storage as well. This increases the safety of all the project elements and access to them from

anywhere. Special modules for working in this mode using cloud design technologies are provided in multiple CAD systems. There are design systems whose functions are also moved into the cloud [1].

There are two main types of cloud CAD software: CAD-on-the-Cloud and CAD-in-the-Cloud.

CAD-on-the-Cloud allows for installing current CAD software to the cloud platform. Then designers can use their CAD programs via the Internet, just like laptops. Interaction takes place through the browser or as a remote client, and there is no need to download software on a personal computer. CAD programs and project files are stored online and work effectively in one place. Applying remote client software, CAD users can work with 3D design files as they do on their desktop computers in an office.

CAD-in-the-cloud is a cloud CAD program developed from scratch. This online form of design software became possible due to significant improvements in Internet speed, network bandwidth, and advanced capabilities of cloud infrastructure providers, such as AWS and Microsoft Azure. CAD-in-the-Cloud offers completely new applications developed and created exclusively for modern cloud infrastructure. An example of a cloud CAD platform is OnShape [2], which offers software for computer-aided design through the cloud with new features such as integrated data management and tools for real-time collaboration performance.

This type of CAD system has numerous additional features, including add-ons and plug-ins for modeling, possibilities of 3D printing, PLM, and many more niche solutions.

Cloud CAD means designers can access their files and project software from any location with a reliable Internet connection. This functionality allows them to work in an office, at home, or in the client's office.

The possibilities of virtual reality have become standard functions in CAD software. 3D models can be considered to exist in physical space due to virtual reality headsets. Many software providers have started to develop their products compatible with equipment for 3D viewing.

Nowadays, numerous program products actively use cloud technologies. They include the following software.

AutoCAD Web [3] is a reliable solution with basic AutoCAD commands required for easy editing and creating fundamental projects at an attractive price. AutoCAD drawing tools online in a simplified interface allows accessing and updating DWG™ files with any workplace arranging.

AutoCAD LT® [4] is CAD software architects, engineers, construction workers, and designers use to create 2D drawings and documentation. Design and sketching in a web browser on any computer allow reviewing, editing, commenting, and making CAD drawings in a simplified user interface.

CIDEON CLOUD CAD Integration (CCI) [5] combines data and structures of mechanical engineering (for example, assemblies and parts) in advanced cloud CAD systems, such as OnShape® [2], with SAP ERP or

SAP S/4HANA. CCI is developed on the platform SAP Cloud and fully integrates local and cloud SAP systems.

CMS IntelliCAD® [6] is intelligent, robust, and accessible fully functional CAD software compatible with hundreds of third-party solutions. CMS IntelliCAD also offers a complete set of tools for drawing, consistent with 2D and 3D AutoCAD®. It is a good choice for engineers, architects, consultants, and all the users of CAD drawings.

SkyCiv Structural 3D [7] is an entirely online cloud-based software for structural analysis that enables users to model, analyze and design complex 3D constructions.

Inventor® CAD program [8] provides professional-level instruments for 3D mechanical engineering, documenting, and modeling products with the possibility of using work elements in the cloud.

Creo [9] CAD software offers the most scalable packages and tools for 3D CAD product development in the modern market. Creo 7.0 includes breakthrough innovations in generative design, real-time simulation, multi-body design, additive manufacturing, and others using cloud design modules.

Autodesk Fusion 360 [10] combines design, electronics, and production into a single programming framework. This results in an integrated CAD, CAM, CAE, and PCB system on a shared development platform. Autodesk Fusion 360 CAD family includes EAGLE Premium, HSMWorks, Team Participant, and access to consumer services such as generative design, cloud modeling, and cloud rendering. Fusion 360 – Team Participant is intended for external users who can share their projects, review, and manage them through a cloud. This system contains the base kernel, which is installed on a computer, but the full advantage of many functions can be taken only by applying cloud capabilities.

The considered sources present selected examples of cloud technologies adoption to create different products. To obtain the maximum effect when using advanced methods of cloud design, it is necessary to develop algorithms and technologies for new features application in product creation and analysis.

This paper introduces a CAD-on-the-Cloud algorithm based on information model (IM) design in Autodesk Fusion 360, applying its cloud capabilities.

### 3 Research Methodology

Creating new objects in various spheres is currently done by applying design computer technologies using cloud platforms. Developing the algorithm for new object design with the help of computer technologies is to be based on information models. The information model generalizes the approach to design by applying different technologies. Examples of that are presented in papers [11-15]. IM allows optimizing the process of product design and analysis. Let us consider the information model for product design based on the CAD-on-the-Cloud type of CAD system. Autodesk Fusion 360 CAD family is used as CAD-on-the-Cloud software. When creating and analyzing the product model, it is necessary to perform several sequential and interconnected stages (Figure 1).

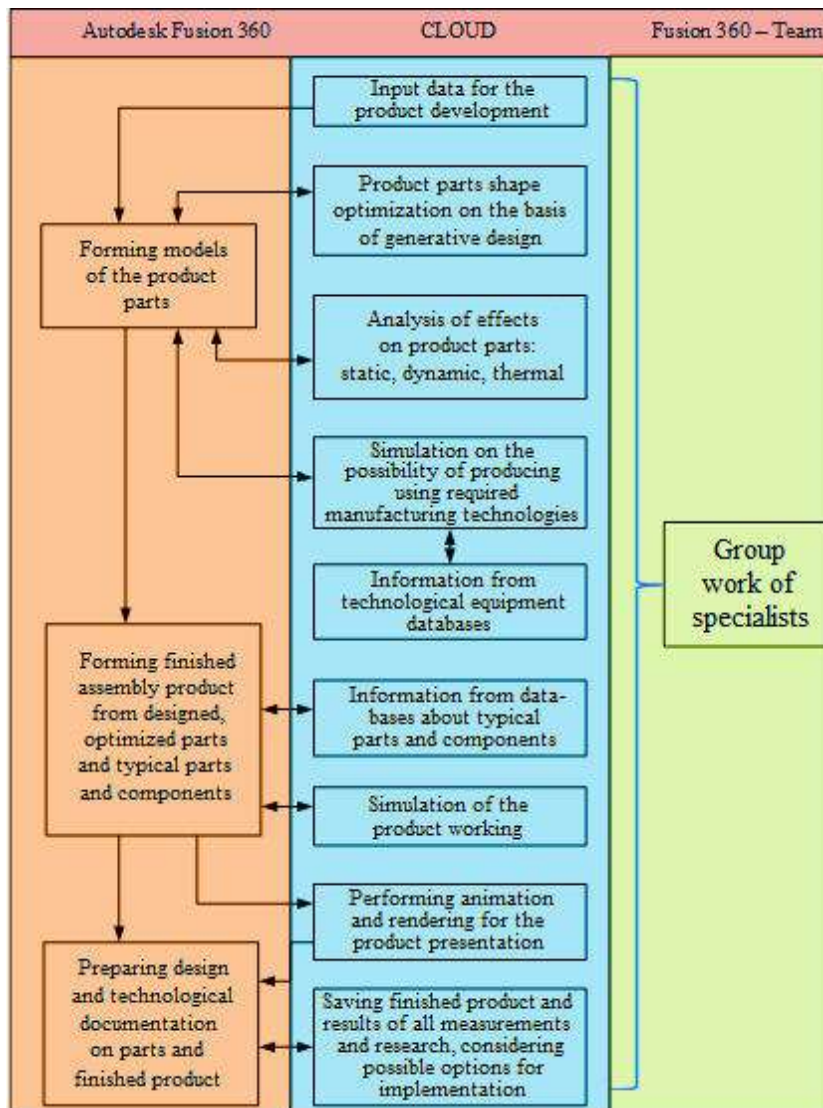


Figure 1 – Information model of design applying cloud technologies

The suggested information model consists of three major components: working with Autodesk Fusion 360 on a computer, working with cloud capabilities, and designers' collaboration through the cloud. Let us consider elements of the information model of design applying cloud technologies in detail.

1) input data for the product development should be presented in the form of an information set, for example, specifying the boundaries of an object in the form of a point cloud, the set of bounding surfaces, boundaries of the solid body. Input data is placed in cloud storage;

2) Autodesk Fusion 360 forms the required model of an object based on the obtained information;

3) the shape of the created part can be optimized in the cloud shape calculation module, which is based on generative design. As a result, the system optimizes the shape of an object the developer suggests. Otherwise, it offers its version. In this case, parts-producing technology is also considered;

4) it is possible to test the created model for the influence of different effects and stresses (static, dynamic, thermal) in cloud modules;

5) the finished model can be verified on the possibility of being produced with the help of required manufacturing technologies in the cloud module of technological processes simulation;

6) in order to carry out the creation and processing of parts simulation, it is necessary to use information about the equipment from the cloud data of the equipment manufacturers;

7) creating information about typical parts and components from cloud databases is used;

8) the finished product is assembled from designed and optimized parts and typical parts and components cloud databases;

9) working capacity of the created product is tested through its simulation;

10) to perform animation and rendering of the working product Autodesk Fusion 360 cloud service is applied;

11) results of all measurements and research, considering possible options for implementation, are saved in cloud storage of the entire project;

12) preparing design and technological documentation on parts and the finished product is made according to producing technologies;

13) in all stages of the design and research process, a group effort of various specialists in the Autodesk Fusion Team system is used.

The suggested information model allows considering the general approach to design, analysis, and simulation of production in CAD software of the CAD-on-the-Cloud type in the Autodesk Fusion 360 family.

#### 4 Results and Discussion

Creating customized respiratory protective equipment (face masks) during the coronavirus pandemic is highly topical nowadays. Available mask configurations do not consider the individual characteristics of a person wearing it. Therefore, it is critically important to create a mask according to the anatomical features of each person. Modern design and producing technologies enable the creation of masks considering the individual anatomical features of every human. The possibility of the protective mask design is presented considering the individual features of a person. The design is performed in Autodesk Fusion 360 based on the suggested application of IM cloud technologies. In the considered example, IM is adapted to the solved problem.

At the first stage of IM development, reverse engineering technology is applied to get input data. Thus, a real human head is scanned using a modern 3D scanner. As a result, we obtained a sufficiently high-quality mathematical model consisting of a 3D point cloud. The acquired cloud is a basis for virtual headform development in the computer modeling system. An extracted mathematical model of the headform as \*.obj file is imported into Fusion 360 software for further editing.

The following step in the process of 3D editing is the point phase. During this stage, it is necessary to reduce noise to decrease the number of scanned data points in homogeneous areas. The mesh model's density should be adjusted to obtain an acceptable quality model. This design approach implies inaccuracies in an object being 3D scanned, which has the form of open polygons. With the help of Fusion 360, the deficiencies are eliminated, and the density of the mesh model is changed. As a result, the complete mesh model of a human head is finalized.

In the next stage, the mask frame design is carried out. For this purpose, it is suggested to apply a retopology instrument. Retopology allows for creating a new geometry over an existing one by modifying its structure.

After applying retopology tools, new geometry of the mask configuration is put over a face using it as a basis. It allows placing a new object quite accurately and continuing to adapt it.

This toolbox helps design a mask frame's shape, which can be easily modified afterward. Based on the obtained mask frame configuration, the solid model of a mask is developed in Autodesk Fusion 360. This kind of work with model topology makes it possible to carry out different stress testing, select physical materials, define settings for 3D printing, and so on.

In the next stage, the mask structure is checked for reliability. The configuration of the mask frame consists of two major parts hingedly joined with each other. This allows to use of the mask regardless of changes in facial expression and speaking of the person wearing a mask. The mask frame's lower part is tight, close to the chin, and the upper part is fixed on the nose bridge.

Strains on all parts of the mask and their connections are simulated in Autodesk Fusion 360 software. It allows verifying the configuration's reliability under mechanical stresses along with its fixation on a face. Further, the material of the mask's basic structure is determined and tested for external forces impact and possible displacement due to facial expression changes during a conversation. After the testing is carried out in cloud-based modules, the shape of the mask structure can be corrected.

Then we define the filtering element type and determine how to fix it to the basic structure. Let us consider the simplest version with a replaceable multi-layered filtering element. The shape of the filtering element can be modeled in the cloud module of generative design by specifying boundary conditions in the form of a mask frame and space needed for normal breathing and facial expressions of a person. The filtering element is fixed to the basic structure using a sticky layer. An additional fixing element can be applied over the filter to provide a more reliable fixation. If necessary, mask configuration is adjusted considering the reliable attachment of the filtering element. It is possible to use separate filters as an implementation option, just as in the Pitta mask with one or two filters. To achieve this, we use cloud libraries of standard variants of filters. After the filtering element construction is defined, the technology of mask frame production is developed. The experiment chooses an additive technology using a 3D printer as a core technology. The printer type is chosen from the cloud libraries of equipment manufacturers. The technological process of creating an object based on a 3D printer can be simulated in Autodesk Fusion 360 program.

After using cloud computing technologies, the parameters of the required 3D printer are downloaded, and a mask frame-creating process is simulated. If errors occur during the simulation, the program suggests appropriate configuration corrections or adding extra fixing elements.

The resulting image of a mask with a filter put on a face is demonstrated in Figures 2-3.



Figure 3 – The designed mask with a single filter

To guarantee a more secure mask fixation, its version with ear hooks like those used in glasses is proposed. Variants with separate filtering elements are presented in Figure 3 (a single filter) and Figure 4 (a double filter).



Figure 4 – The designed mask with a double filter

Thus, this study suggests the general algorithm and technology of applying CAD software of the CAD-on-the-Cloud type during the design and analysis of product

creation in the form of IM. This IM can be adapted to the required work option with a particular task.

The presented information model is based on three main components – working with Autodesk Fusion 360 on a computer, working with cloud features of the software and collaboration of the designers through the cloud in Fusion 360 – Team Participant. As an example of IM applying, an approach to creating protective mask which considers individual characteristics of human face is discussed in detail. When designing a mask, an information model of the created object is used.

## 5 Conclusions

This study suggests the general algorithm and technology of applying CAD software of the CAD-on-the-Cloud type during the design and analysis of product creation as IM. This IM can be adapted to the required work option with a particular task. The presented information model is based on three main components – working with Autodesk Fusion 360 on a computer, working with cloud features of the software, and collaboration of the designers through the cloud in Fusion 360 – Team Participant.

As an example of an IM application, an approach to creating a protective mask that considers the individual characteristics of a human face is discussed in detail. An information model of the created object is used when designing a mask.

Information models include all the sequential stages of the mask creation design and analysis. Developing feasible options for protective masks with various replaceable filters is considered in detail. In this study of creating a mask model, cloud technologies were used: when modeling a mask frame based on retopology, when checking the mask design for reliability, a generative design module when optimizing the shape of the filter element, when developing technology and simulating the manufacture of a mask frame, when choosing technological equipment for mask manufacture, when preparing control programs for a 3D printer.

The proposed method of design using an information model can be applied to both single objects and assembled items. During the assembled items creation, it is possible to adapt IM elements for each of the product's components. Applying the presented IM reduces time and increases the constructed product's accuracy and reliability. This research is to be advanced by developing IM for CAD-in-the-cloud systems.

## References

1. Jiang, D. (2020). The construction of smart city information system based on the Internet of things and cloud computing. *Computer Communications*, Vol. 150, pp. 158-166, <https://doi.org/10.1016/j.comcom.2019.10.035>
2. Marion, T., Olechowksi, A., Guo, J. (2021). An analytical framework for collaborative cloud-based CAD platform affordances. *Proceedings of the Design Society*, Vol. 1, pp. 375-384, <https://doi.org/10.1017/pds.2021.38>
3. Sobociński, P., Strugała, D., Walczak, K., Maik, M., Jenek, T. (2021). Large-scale 3D web environment for visualization and marketing of household appliances. *Lecture Notes in Computer Science*, Vol. 12980, pp. 25-43, [https://doi.org/10.1007/978-3-030-87595-4\\_3](https://doi.org/10.1007/978-3-030-87595-4_3)



4. Simionescu, P. A. (2014). *Computer-Aided Graphing and Simulation Tools for AutoCAD Users*. Chapman and Hall/CRC, New York, USA, <https://doi.org/10.1201/b17904>
5. The CIDEON Cloud CAD to SAP Interface. Available online: <https://www.cideon.com/solutions/interfaces/cloud-cad-sap>
6. Wu, D., Terpenney, J., Schaefer, D. (2017). Digital design and manufacturing on the cloud: A review of software and services. *AI EDAM*, Vol. 31(1), pp. 104-118, <https://doi.org/10.1017/S0890060416000305>
7. Van Ameijde, J., Ma, C. Y., Goepel, G., Kirsten, C., Wong, J. (2022). Data-driven placemaking: Public space canopy design through multi-objective optimisation considering shading, structural and social performance. *Frontiers of Architectural Research*, Vol. 11(2), pp. 308-323, <https://doi.org/10.1016/j.foar.2021.10.007>
8. A-Ghamdi, S. A., Al-Rajhi, N. A., Al-Onaizy, N. M., Al-Khalifa, H. S. (2016). Using app Inventor 2 in a summer programming workshop: Improvements over previous years. *IEEE Global Engineering Education Conference, EDUCON*, pp. 383-388, <https://doi.org/10.1109/EDUCON.2016.7474582>
9. Hoque, A. S. M., Halder, P. K., Parvez, M. S., Szecsi, T. (2013). Integrated manufacturing features and design-for-manufacture guidelines for reducing product cost under CAD/CAM environment. *Computers and Industrial Engineering*, Vol. 66(4), pp. 988-1003, <https://doi.org/10.1016/j.cie.2013.08.016>
10. Tlhabadira, I., Daniyan, I. A., Machaka, R., Machio, C., Masu, L., Van Staden, L. R. (2019). Modelling and optimization of surface roughness during AISI P20 milling process using taguchi method. *International Journal of Advanced Manufacturing Technology*, Vol. 102(9-12), pp. 3707-3718, <https://doi.org/10.1007/s00170-019-03452-4>
11. Wu, D., Rosen, D. W., Wang, L., Schaefer, D. (2015). Cloud-based design and manufacturing: A new paradigm in digital manufacturing and design innovation. *CAD Computer Aided Design*, Vol. 59, pp. 1-14, <https://doi.org/10.1016/j.cad.2014.07.006>
12. Wagner, G. (2018). Information and process modeling for simulation. *Journal of Simulation Engineering*, Vol. 1(1), pp. 1-25, <https://articles.jsime.org/1/jsime-article-1-1.pdf>
13. Peffers, K., Tuunanen, T., Rothenberger, M. A., Chatterjee, S. (2007). A design science research methodology for information systems research. *Journal of Management Information Systems*, Vol. 24(3), pp. 45-77, <https://doi.org/10.2753/MIS0742-1222240302>
14. Schnabel, R., Wahl, R., Klein, R. (2007). Efficient RANSAC for point-cloud shape detection. *Computer Graphics Forum*, Vol. 26(2), pp. 214-226, <https://doi.org/10.1111/j.1467-8659.2007.01016.x>
15. Tang, P., Huber, D., Akinci, B., Lipman, R., Lytle, A. (2010). Automatic reconstruction of as-built building information models from laser-scanned point clouds: A review of related techniques. *Automation in Construction*, Vol. 19(7), pp. 829-843, <https://doi.org/10.1016/j.autcon.2010.06.007>



*materials*

an Open Access Journal by MDPI



## Novel Approaches in the Design, Simulation, and Manufacturing for Processes and Systems

Guest Editors:

**Prof. Dr. Vitalii Ivanov**  
ivanov@tmvi.sumdu.edu.ua

**Prof. Dr. Ivan Pavlenko**  
i.pavlenko@cm.sumdu.edu.ua

**Prof. Dr. Szymon Wojciechowski**  
szymon.wojciechowski@put.poznan.pl

**Dr. Jinyang Xu**  
xujinyang@sjtu.edu.cn

Deadline for manuscript submissions:  
**31 March 2024**

### Message from the Guest Editors

Dear Colleagues,

The application of novel approaches in the design, simulation, and manufacturing of engineering products ensures the effectiveness of manufacturing systems. Modeling the materials' structure leads to the production of a predetermined set of their properties and ensures the designed parts' reliability. This modeling is essential for cutting tools, fixtures and tooling, friction pairs, highly loaded parts of machines and equipment, etc. Implementation of the abovementioned issues must ensure the functionality and assigned operating parameters of the designed parts and units in terms of wear resistance, stress-strain modes and dynamic behavior, loading capacity, etc. Advanced material processing approaches can be applied (plasma deposition, electro spark, chemical-thermocycling treatment, strengthening, etc.). Additionally, novel approaches can be implemented in designing advanced materials (polymers, composites, ceramics, nanomaterials, etc.). At the design stage of materials, it is essential to predict the functional, rheological, and tribological properties using numerical simulation and experimental studies.



[mdpi.com/si/165101](https://mdpi.com/si/165101)

**Special** Issue



Antonyuk V. S., Bondarenko I. Iu., Vislouch S. P., Voloshko O. V., Bondarenko M. O. (2023). Heat exchange in a contact zone of nanoinstrumentation with elements of the microsystem technology. *Journal of Engineering Sciences*, Vol. 10(1), pp. F1-F6, doi: 10.21272/jes.2023.10(1).f1

## Heat Exchange in a Contact Zone of Nanoinstrumentation with Elements of the Microsystem Technology

Antonyuk V. S.<sup>1</sup>[0000-0003-0690-2411], Bondarenko I. Iu.<sup>2</sup>[0000-0002-5179-8329], Vislouch S. P.<sup>1</sup>[0000-0002-2204-2602],  
Voloshko O. V.<sup>1</sup>[0000-0002-1067-2615], Bondarenko M. O.<sup>3</sup>[0000-0002-5927-0326]

<sup>1</sup> National Technical University of Ukraine “Igor Sikorsky Kyiv Polytechnic Institute”, 37, Peremohy Ave., 03056 Kyiv, Ukraine;

<sup>2</sup> State Scientific Research Institute of Armament and Military Equipment Testing and Certification,  
164, Chornovil St., 18028 Cherkasy, Ukraine;

<sup>3</sup> Cherkasy State Technological University, 460, T. Shevchenka Blvd, 18006 Cherkasy, Ukraine

### Article info:

Submitted: February 24, 2023  
Received in revised form: May 8, 2023  
Accepted for publication: May 18, 2023  
Available online: May 23, 2023

### \*Corresponding email:

[victor.antoniuk@gmail.com](mailto:victor.antoniuk@gmail.com)

**Abstract.** Theoretical studies of physical processes and phenomena in the zone of physical interaction of nanoinstruments with the surfaces of elements of microsystem technology are carried out in work. Based on the conducted research, mathematical models of energy heat exchange in the zone of physical contact of nanometric dimensions were compiled, and their analytical solution was obtained using the Fourier method of separation of variables and Goodman’s integral method. Simultaneously, the energy components of the processes in the nanocontact zone were considered. The numerical solution of the mathematical model of energy heat exchange in the zone of physical nanocontact was carried out using a software application based on the finite element method. The results were checked according to the equivalent thermal scheme to confirm the adequacy and accuracy of the obtained models. As a result, the mechanisms of energetic interaction of the nanoinstrument with the surfaces of the elements of microsystem technology devices were clarified. It is shown that the use of the proposed method of equivalent thermal circuits for the evaluation of mathematical models of the energy interaction of nanoinstruments with the surfaces of microsystem technology device elements, as well as the further study of the distribution of thermal fields in the nanocontact zone, differs from other numerical and analytical methods in terms of sufficient accuracy and speed of calculations. At the same time, it was established that the discrepancy between the results of mathematical modeling and the results obtained according to the equivalent thermal scheme does not exceed 5-8 %.

**Keywords:** energy heat exchange, mathematical modeling, physical contact, thermal energy, process innovation, equivalent thermal circuit.

## 1 Introduction

The intensive development of modern microelectronics and microsystem technology requires modern engineering sciences and technologies to comply with strict requirements for further miniaturization, increasing the functionality and manufacturability of elements of microdevices and systems based on them [1].

Compliance with such requirements is due, first of all, to the qualitative and quantitative growth of indicators of operational parameters of these devices, such as [2]: operating speeds, frequencies, and duration of operation, with a simultaneous increase in indicators of their

reliability and accuracy. Simultaneous fulfillment of such mutually exclusive requirements is possible by observing the high stability of geometric shapes and sizes, as well as the physical and mechanical characteristics of microsystem technology devices in the process of their manufacture and operation [3, 4]. This, in turn, requires considering various physical processes that occur during the contact interaction between the elements of microsystem technology devices, both during their operation and during the manufacture and control of these elements with specialized nanoinstrumentation.

At the same time, physical processes (especially energy ones) that occur in the contact zone of nanometric

instruments with the surface are little studied and are limited by known laws, which are based on the laws of classical physics for macro-objects [5, 6].

## 2 Literature Review

The issue of mathematical modeling of energy processes in micro- and nanosystems was considered by many scientists, such as Awrejcewicz J., Belmiloudi A., Hegde V., Laurencot Ph., Nik K., Ravikumar H.M., Senturia S.D., Walker Ch. and others [7-10].

However, in the scientific works of these scientists, the thermodynamic processes that occur during contact in the zone of interaction of a nanometer-sized tool with elements of microsystem technology have not been investigated.

Thus, an urgent issue is developing a mathematical model of energy heat exchange in the zone of physical contact of nanometric instruments with the surfaces of elements of microsystem technology.

The work aims to increase the accuracy and speed of determining the parameters of stable operation of nanometric instrumentation during its contact with the surfaces of elements of microsystem technology by developing a mathematical model of energy heat exchange in the zone of their physical contact.

Therefore, in the presented work, mathematical (analytical and numerical) modeling of the energy interaction of nanoinstruments with the surfaces of elements of microsystem technology is carried out, and the results are confirmed by the method of equivalent thermal circuits.

Thermal calculations are based on a complex of nonlinear, non-stationary equations that consider the nanotool's shape, dimensions, and thermophysical characteristics and the surfaces with which the interaction occurs [11].

Simultaneously, only heat exchange by heat transfer was considered (convective and radiant types of heat exchange were not considered due to their insignificance). It also does not take into account the energy impact on the nanotool and the surface in the contact zone from the action of external electric and electromagnetic fields when conductive diamagnets are in contact or, in the case of dielectric diamagnets, due to their insignificant effect due to the additional neutralization of surface charges during the interaction of the nanotool with the surface [12].

Conducting thermal calculations consists of compiling and analytically solving mathematical models of heating individual elements of microsystem technology devices when a nanoinstrument acts on them with the involvement of the inverse integral Fourier transform method [13].

Among the elements for which thermal calculations were carried out [14] is the surface of the object of interaction, the tip of the tool, and the cantilever, to which the nanotool is attached.

## 3 Research Methodology

### 3.1 General formulation of a problem

The electrically conductive (Au-999 gold coating) surfaces of the conductive collector's rings ( $3 \times 3.0 \times 0.1$  mm) with an atomically smooth surface were chosen as model elements that were affected by the nanoinstrument. CSC38/No Al (Mikrotech) cantilever with a length of 12–18  $\mu\text{m}$  and a conical tip made of single-crystal (n-Si(111) silicon), with a radius of 8 nm and a tip angle of  $40^\circ$  placed at its end was chosen as the tool model. Such a tool can be used as a measuring tool in scanning probe microscopy and for surface modification of surfaces in nanoprocessing technologies. The energy scheme in the zone of contact of nanometric dimensions is shown in Figure 1.

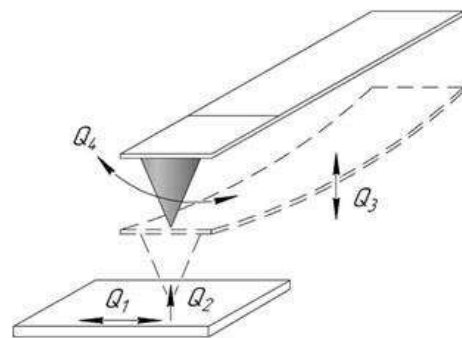


Figure 1 – Scheme of heat exchange in the zone of physical contact of nanometric dimensions (heat losses:  $Q_1$  – during mechanical friction of the nanotool on the interaction surface;  $Q_2$  – under the action of electromagnetic fields and electric charge;  $Q_3$  – when bending the nanotool;  $Q_4$  – when turning the nanotool)

### 3.2 Mathematical model of heating an interaction object

The thermal effect on the object of interaction (sample) is carried out by physical friction of the nanotool on its surface during the interaction of this sample in the contact mode. The total heat flow is uniformly distributed in the study area over the sample's surface (Figure 2).

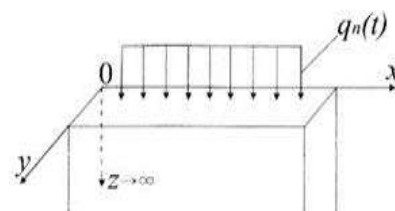


Figure 2 – Scheme of heating the working surface of the sample:  $q_n(t)$  – the surface heat flux density,  $\text{W/m}^2$

It is assumed that  $\partial T / \partial x = \partial T / \partial y = 0$  (heat distribution occurs only in the depth of the plate) and  $\delta = 2(a_0^2 \tau)^{1/2} \ll H$  (thermal effects are superficial, and heat exchange on the bottom side of the plate is not considered).

The equations of the mathematical model of sample heating (thick plates) have the following form:

$$C_V(T) \frac{\partial T}{\partial t} = \frac{\partial}{\partial z} \left[ \lambda(T) \frac{\partial T}{\partial z} \right], \quad t > 0, \quad 0 < z < +\infty. \quad (1)$$

$$\begin{aligned} -\lambda(T) \frac{\partial T}{\partial z} \Big|_{z=0} &= q_n(t); \quad T|_{t=0} = T_0; \\ T \rightarrow T_0, \quad \frac{\partial T}{\partial z} &\rightarrow 0, \quad z \rightarrow +\infty. \end{aligned} \quad (2)$$

Taking into account  $C_V(T)$  and  $\lambda(T)$ , as well as using the direct-inverse cosine Fourier transform along the  $z$  coordinate [15, 16], using the sequence of actions considered in [17], we find a general solution to the original problem:

$$T(z, t) = \left[ T_0^{v+1} + \frac{(v+1) a_0 q_{n0}}{\sqrt{\pi} \lambda_0} \int_0^t \frac{e^{-\frac{z^2}{4a_0^2(t-\tau)}}}{\sqrt{t-\tau}} d\tau \right]^{\frac{1}{v+1}}. \quad (3)$$

### 3.3 Mathematical model of heating a cantilever

During the operation of the nanoinstrument, a uniformly distributed heat flow arrives on the free (unfixed) surface of its cantilever  $q_n(t)$  (Figure 3):

$$q_n(t) \equiv q_{n0} = \frac{P_0}{R \cdot H}, \quad (4)$$

where  $P_0$  – the power of the heat flow acting on the cantilever from the outside, W.

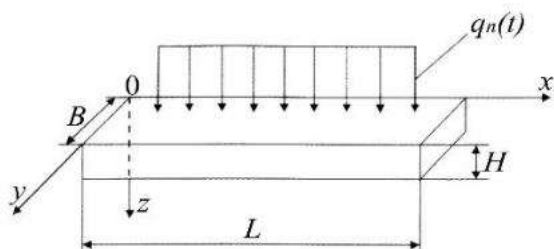


Figure 3 – Scheme of heating the free surface of the cantilever:  $B, H, L$  – width, thickness, and length of the cantilever, respectively, m;  $q_n(t)$  – the surface heat flux density,  $W/m^2$

As a model, a plate is considered, for which heat distribution occurs only deep into the plate:  $\frac{\partial T}{\partial x} = \frac{\partial T}{\partial y} = 0$ , as well as the depth of the zone of thermal influence  $\delta = H$ , i.e., heat exchange on the bottom side of the plate, is considered. When interacting with the plate, it is assumed that radiation heat exchange with the surrounding medium occurs on the plate's bottom side.

To find the values of  $T(z, t)$ , the following nonlinear equations of thermal conductivity are used [17]:

$$C_V(T) \frac{\partial T}{\partial t} = \frac{\partial}{\partial z} \left( \lambda(T) \frac{\partial T}{\partial z} \right), \quad t > 0, \quad 0 < z < H \quad (5)$$

with the initial condition

$$T|_{t=0} = T_0 \quad (6)$$

and boundary conditions

$$-\lambda(T) \frac{\partial T}{\partial z} \Big|_{z=0} = q_n(t); \quad \lambda(T) \frac{\partial T}{\partial z} \Big|_{z=H} = \varepsilon \bar{\sigma} (T_0^4 - T_c^4) \quad (7)$$

where  $T_c$  is the ambient temperature, K;  $\lambda(T)$ ,  $C_V(T)$  are thermal conductivity coefficient,  $W/(m \cdot K)$ , and volumetric heat capacity,  $J/(m^3 \cdot K)$ , of the plate material, respectively;  $\varepsilon$  is the blackness coefficient of the radiating

surface;  $\sigma = 5.67 \cdot 10^{-8} W/(m^2 \cdot K^4)$  is the Stefan–Boltzmann constant.

At the same time, empirical dependencies  $C_V(T) = C_{V0} T_V$ ,  $\lambda(T) = \lambda_0 T_n$  [18] are taken into account in equations (5)–(7).

To solve the formulated nonlinear thermal problem (5)–(7), the method of substitution of variables, the Goodman integral method [19], and the previously mentioned method of Fourier transformation [20] were applied for the function  $T(z, t)$  [17]:

$$\begin{aligned} T(z, t) = & \left\{ T_0^{v+1} + \frac{(v+1) q_{n0}}{\lambda_0} \left[ \frac{a_0^2 t}{H} + \frac{3z^2 - H^2}{6H} + \frac{2H}{\pi^2} \times \right. \right. \\ & \left. \left. \times \sum_{n=1}^{\infty} (-1)^{n+1} \frac{\cos \frac{\pi n z}{H}}{n^2} e^{-\left( \frac{\pi a_0 n}{H} \right)^2 t} \right] \right\}^{\frac{1}{v+1}}. \end{aligned} \quad (8)$$

### 3.4 Mathematical model of heating a tip of the nanoinstrument

A solid hemispherical element of radius  $R$  in a range of 8–10 nm made of silicon is considered as the tip of the tool (Figure 4).

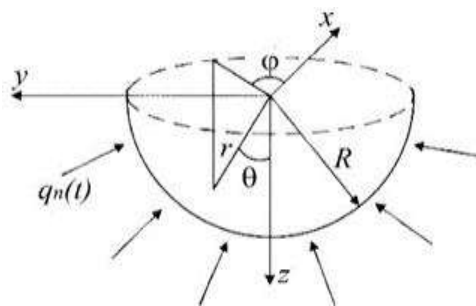


Figure 4 – Scheme of heating a hemispherical element:  $R$  – the radius of the element, m;  $q_n(t)$  – the surface density of thermal influence,  $W/m^2$ ;  $r, \theta, \varphi$  – spherical coordinates

The depth of penetration of the heat wave into the tip  $\delta = 2(a_0^2 \tau)^{1/2} = 5.78 \cdot 10^{-9}$  m. Since the depth of penetration of the heat wave into the tip of the tool is less than its radius ( $R > \delta$ ), it can be considered as a symmetric hemispherical element, the outer surface of which is heated by the heat flow arising as a result of the friction of this element on the surface of the sample. As a result, the total heat flow  $\partial T / \partial \varphi = \partial T / \partial \theta = 0$ , uniformly distributed over the surface, is formed. Convective and radiative heat losses are not considered.

Equations of the mathematical model of heat distribution in a hemispherical element have the form:

$$C_V(T) \frac{\partial T}{\partial t} = \frac{1}{r^2} \frac{\partial}{\partial r} \left[ r^2 \cdot \lambda(T) \frac{\partial T}{\partial r} \right], \quad t > 0, \quad 0 < r < R; \quad (9)$$

$$\begin{aligned} T|_{t=0} &= T_0; \quad \lambda(T) \frac{\partial T}{\partial r} \Big|_{r=R} = q_n(t); \\ \frac{\partial T}{\partial r} \Big|_{r=0} &= 0; \quad T|_{r=0} \neq \infty. \end{aligned} \quad (10)$$

Using the method of separation of variables (Fourier method [20]) and taking into account  $q_n(t) \equiv q_{n0} = \text{const}$ , as well as using the method of calculation according to formulas (1)–(3), the desired solution of the problem is obtained:

$$T(r, t) = T_0^{v+1} + \frac{(v+1)q_{n0}R}{\lambda_n} \left[ \frac{3a_0^2 t}{10R^2} - \sum_{n=1}^{\infty} \frac{2R \sin\left(\mu_n \frac{r}{R}\right)}{\mu_n^3 \cos(\mu_n R)} \cdot e^{-\left(\frac{\mu_n a_0}{R}\right)^2 \tau} \right] \quad (11)$$

where  $\mu_n$  – the root of the characteristic equation  $J(\mu) = 0$ .

## 4 Results

### 4.1 Numerical simulation results

For the numerical solution of the mathematical model of the process of heating nano-instruments and elements of microsystem technology, the finite element method was used, which has proven itself well, for example, in researching new instrumental materials [22, 23].

The solution of the mathematical model of the energy effect in the zone of interaction of the nano-instrument with the surface, as well as the study of the distribution of thermal fields, is implemented with the help of a software module [24]. The software module allows obtaining and investigating the thermal field distribution on the surface and in the volume of objects of nanometric dimensions with specified thermophysical properties.

Known values of geometric parameters and thermophysical characteristics of the materials from which both the elements of the nanometric tool and the objects with which this tool interacted and which are included in the expressions (3), (8), and (11) were used for the calculations. It was established that the most significant heat release occurs in the contact zone of the tool's tip with the surface (Figure 5).

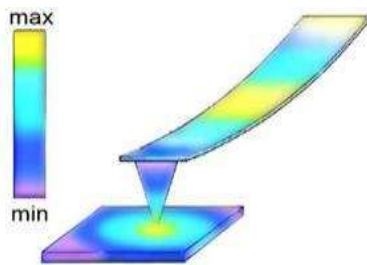


Figure 5 – Distribution of heat release in the zone of physical contact of nanometric dimensions (according to the results of analytical calculations)

### 4.2 Evaluation of the mathematical models

Mathematical heat exchange models were coordinated according to the heat balance scheme, in which the joint heat contribution was evenly distributed among all elements participating in heat exchange.

Simultaneously, the thermophysical properties of the materials from which these elements were not considered. An equivalent thermal scheme (Figure 6) was drawn up and investigated to assess the adequacy of the considered heat exchange models based on thermal resistances connected to a thermal network.

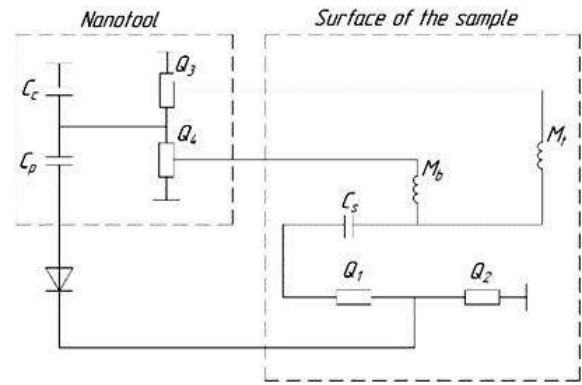


Figure 6 – Equivalent thermal scheme in the nanocontact zone (heat losses:  $Q_1$  – during mechanical friction of the tip of the tool on the examined surface;  $Q_2$  – under the action of electromagnetic fields and electric charge;  $Q_3$  – when bending the cantilever;  $Q_4$  – when the cantilever is twisted;  $C_c, C_p, C_s$  – specific heat capacities of the material of the cantilever, the tip of the tool, and the sample, respectively;  $M_b, M_t$  – energy dissipations resulting from the action of mechanical moments of bending and torsion of the cantilever)

Such a network simulates how heat flows are transferred into the nanocontact zone and provide an analogy of the heat flow with an electric current [25].

The diodes between the blocks on the equivalent thermal circuit are informative and determine the predominant direction of heat transfer between different functional blocks of the equivalent circuit.

After considering the features of the equivalent thermal scheme (Figure 6), the thermal models of heating in the nanocontact zone were compiled:

$$\begin{cases} C_s \left( \frac{dQ_1}{dt} + \frac{dQ_2}{dt} \right) = -\lambda_s(Q_1 + Q_2) + P_s; \\ \frac{C_s C_p C_c}{C_s C_p + C_s C_c + C_p C_c} \cdot \left( \frac{dQ_3}{dt} + \frac{dQ_4}{dt} \right) = -\lambda_c(Q_3 + Q_4) + P_c, \end{cases} \quad (12)$$

where  $C_p, C_s, C_c$  are coefficients of heat capacity of the materials of the tip of the tool, the sample, and the cantilever, respectively;  $\lambda_s, \lambda_c$  are thermal conductivity coefficients of sample and cantilever materials, respectively;  $P_s, P_c$  are heat losses on the sample and cantilever.

## 5 Discussion

System of differential equations (13) is the thermal model of heating individual elements in the contact zone of nano-instrumentation with the surfaces of elements of microsystem technology.

The numerical solution of these systems of equations was carried out in the “ELCUT” software application and made it possible to conclude the primary heat consumption and energy impact in the zone of contact of the nano-instrument with the surface.

It was established that the most significant heat release in the contact zone (about 70 %) occurs as a result of the friction of the nanotool on the surface, which is more than five times higher than the heat loss due to the bending of the cantilever, which fully confirms the results of the analytical calculation.

## 6 Conclusions

Thus, as a result of theoretical studies of thermophysical processes and phenomena that take place during the interaction of nanoinstruments with the surfaces of elements of microsystem technology, mathematical models of energy heat exchange in the zone of physical contact of nanometric dimensions were obtained, and their analytical solution was proposed.

A numerical calculation of the mathematical model of energy heat exchange in the zone of physical nanocontact was carried out. This calculation was carried out using the developed software application based on the finite element method.

The obtained analytical modeling results were checked using the equivalent thermal scheme, which allowed justifying the models' adequacy and accuracy. It is shown that the use of the proposed method of equivalent thermal

circuits for the evaluation of mathematical models of the energy interaction of nanoinstruments with the surfaces of microsystem technology device elements, as well as the further study of the distribution of thermal fields in the nanocontact zone, differs from other numerical and analytical methods in terms of sufficient accuracy and speed of calculations.

It was established that the most significant heat release in the contact zone occurs due to the friction of the nanotool on the surface, which is more than five times higher than the second most significant heat loss, which occurs due to the bending of the cantilever. This fully confirms the analytical calculation results, and the discrepancy between the results of mathematical modeling and the results obtained by the equivalent thermal scheme is 5-8 %.

## References

1. Manz, A., Becker, H. (2003). *Microsystem Technology in Chemistry and Life Sciences*. Springer Science & Business Media, London, UK.
2. Zhuoqing, Y. (2021). *Advanced MEMS/NEMS Fabrication and Sensors*. Springer, London, UK.
3. Bembenek, M., Makoviichuk, M., Shatskyi, I., Ropyak, L., Pritula, I., Gryn, L., Belyakovskiy, V. (2022). Optical and mechanical properties of layered infrared interference filters. *Sensors*, Vol. 22(21), 8105. DOI: 10.3390/s22218105
4. Hovorun, T.P., Pylypenko, O.V., Berladir, K.V., Dyadyura, K.O., Dunaeva, M.N., Vorobiov, S.I., Panda, A. (2019). Physical-mechanical properties and structural-phase state of nanostructured wear-resistant coatings based on nitrides of refractory metals Ti and Zr. *Functional Materials*, Vol. 26(3), pp. 548-555. DOI: 10.15407/fm26.03.548
5. Krukovskiy, S.I., Arikov, V., Voronko, A.O., Antonyuk, V.S. (2022). Features of low-temperature GaAs formation for epitaxy device structures. *Journal of Nano- and Electronic Physics*, Vol. 14(2), 02016(5pp). DOI: 10.21272/jnep.14(2).02016
6. Tatsiy, R.M., Pazen, O.Y., Vovk, S.Y., Ropyak, L.Y., Pryhorovska, T.O. (2019). Numerical study on heat transfer in multilayered structures of main geometric forms made of different materials. *Journal of the Serbian Society for Computational Mechanics*, Vol. 13(2), pp. 36-55. DOI: 10.24874/JSSCM.2019.13.02.04
7. Vasudha, H., Yellampalli, S., Ravikumar, H. M. (2020). Simulation, mathematical modeling, fabrication and experimental analysis of piezoelectric acoustic sensor for energy harvesting applications. *Microsyst. Technol.*, Vol. 26(5), pp. 1613-1623. DOI: 10.1007/s00542-019-04702-x
8. Belmiloudi, A. (2011). *Heat Transfer – Mathematical Modelling, Numerical Methods and Information Technology*. Physical Chemistry. IntechOpen, London, UK. DOI: 10.5772/569
9. Laurençot, P., Nik, K., Walker, C. (2021). Convergence of energy minimizers of a MEMS model in the reinforced limit. *Acta Appl. Math.*, Vol. 173, 9. DOI: 10.1007/s10440-021-00416-3
10. Krysko-Jr, V.A., Awrejcewicz, J., Yakovleva, T.V., Kirichenko, A.V., Jarzyna, O., Krysko, A.V. (2018). Mathematical modeling of MEMS elements subjected to external forces, temperature and noise, taking account of coupling of temperature and deformation fields as well as a nonhomogenous material structure. *Communications in Nonlinear Science and Numerical Simulation*, Vol. 72. DOI: 10.1016/j.cnsns.2018.12.001
11. Ralchenko, S., Andriienko, V. (2019). Features of thermal control of components of electrical engineering devices and systems. In: *Fourteenth International Scientific Conference "AVIA". Kyiv 23-25.04.2019*. Available online: <http://conference.nau.edu.ua/index.php/AVIA/AVIA2019/paper/view/5951/4479>
12. Bondarenko, M.A., Bilokon, S.A., Antonyuk, V.S., Bondarenko, I.I. (2014). Mechanism of origin and neutralization of residual triboelectricity at scanning of dielectric surfaces by a silicon probe of the atomic-force microscope. *Journal of Nano- and Electronic Physics*, Vol. 6(2), 02018(5pp).
13. Folland, G. B. (1995). *Introduction to Partial Differential Equations*. Princeton Univ. Press, Princeton, USA.
14. Andriienko, O., Ralchenko, S. (2019). Energy heat exchange in the zone of contact of the probe of an atomic force microscope with the surface under study. *Machines. Technologies. Materials*, Vol. XIII(11), pp. 495-499.
15. Parker, A. E. (2020). Solving linear first-order differential equations Bernoulli's (almost) variation of parameters method. *Differential Equations*. Available online: [https://digitalcommons.ursinus.edu/triumphs\\_differ/3](https://digitalcommons.ursinus.edu/triumphs_differ/3)
16. Lipschutz, S. (2017). *Schaum's Outline of Mathematical Handbook of Formulas and Tables*. McGraw Hill, London, UK.
17. Vaschenko, V.A., Kotelnikov, D.I., Lega, Yu.G., Krasnov, D.M., Yatsenko, I.V., Kirichenko, O.V. (2006). *Thermal Processes in the Electronic Processing of Optical Materials and Use of Products Based on Them*. Naukova Dumka, Kyiv, Ukraine.
18. Artale, P.H., Garra, R. (2001). Nonlinear heat conduction equations with memory: Physical meaning and analytical results. *J. Math. Phys.*, Vol. 58, 063501. DOI: 10.1063/1.4984583

19. Wood, A.S. (2001). A new look at the heat balance integral method. *Applied Mathematical Modelling*, Vol. 25(10), pp. 815-824. DOI: 10.1016/S0307-904X(01)00016-6
20. Grafakos, L., Teschl, G. (2013). On Fourier transforms of radial functions and distributions. *J. Fourier Anal. Appl.*, Vol. 19, pp. 167-179. DOI: 10.1007/s00041-012-9242-5
21. Kutz, M. (2011). *Plastics Design Library, Applied Plastics Engineering Handbook*. William Andrew Publishing, London, UK. DOI: 10.1016/B978-1-4377-3514-7.10045-5
22. Lewis, R.W., Nithiarasu, P., Seetharamu, K.N. (2004). *Fundamentals of the Finite Element Method for Heat and Fluid Flow*. John Wiley & Sons, Hoboken, USA.
23. Kattan, P.I. (2003). *The Linear Triangular Element*. Springer, Berlin, Germany. DOI: 10.1007/978-3-662-05209-9\_11
24. Milosan, I. (2015). Mathematical modeling by using a C++ software. In: *International Conference of Scientific Paper (AFASES 2015)*. Brasov 28-30.05.2015. Available online: [www.afahc.ro/ro/afases/2015/afases\\_2015/math/Milosan%20Ioan%201.pdf](http://www.afahc.ro/ro/afases/2015/afases_2015/math/Milosan%20Ioan%201.pdf)
25. Pulatov, A., Mamadaliev, B., Bekmurodov, J., Makhmudov, N. (2023). Application of the method of equivalent thermal circuits in the calculation of thermal modes of induction crucible furnaces in stationary and non-stationary modes. *AIP Conference Proceedings*, Vol. 2552, 040014. DOI: 10.1063/5.0111948





*Opyatyuk V. V., Kozlov I. L., Karchev K. D., Vistiak S. V., Kozlov O. I., Turmanidze R. (2023). Simulation of point defects formation in the fuel element of a nuclear power plant's wave reactor. Journal of Engineering Sciences, Vol. 10(1), pp. F7-F10, doi: 10.21272/jes.2023.10(1).f2*

## Simulation of Point Defects Formation in the Fuel Element of a Nuclear Power Plant's Wave Reactor

Opyatyuk V. V.<sup>1</sup>[0000-0002-4738-0712], Kozlov I. L.<sup>1\*</sup>[0000-0003-0435-6373], Karchev K. D.<sup>1</sup>[0000-0002-2666-1814], Vistiak S. V.<sup>1</sup>[0000-0002-9132-1541], Kozlov O. I.<sup>1</sup>[0000-0002-1834-6902], Turmanidze R.<sup>2</sup>[0000-0001-9003-6135]

<sup>1</sup> Odessa Polytechnic National University, 1, Shevchenko Ave., 65044 Odessa, Ukraine;

<sup>2</sup> Georgian Technical University, 77, Kostava St., 0175 Tbilisi, Georgia

### Article info:

Submitted: February 20, 2023  
 Received in revised form: May 10, 2023  
 Accepted for publication: May 21, 2023  
 Available online: May 30, 2023

### \*Corresponding email:

[kozlov\\_i.l.@ukr.net](mailto:kozlov_i.l.@ukr.net)

**Abstract.** This paper considers the point defects that influence the operation of a wave nuclear power reactor with a uranium fuel medium. The formed individual point defects or such defect groups can produce a perturbing effect on the stability of the nuclear reactor operating mode and involve its transition to an unstable state. Studies have been carried out on the effect on the characteristics of the nuclear burnup wave in a medium with neutron multiplication for 2D geometry. For the calculation, the uranium-thorium fissile medium has been considered. The parametric calculations were carried out with <sup>235</sup>U different enrichment percents and different values of neutron activation energy. At that, it was assumed that the wave (flow) reactor stable operation region is located in the range of activation energies from 10<sup>-3</sup> eV to 1 eV or in the region from 2 MeV to 8 MeV. When calculating the neutron flux intensity in a wave reactor, the influence of point defects and their aggregates on the decelerating elastically scattered neutrons' flux density and the flux density of decelerating non-elastically scattered neutrons was considered. The dependences of the point defects formation rate on the medium fissile temperature for several compositions of the uranium-thorium medium are obtained. As visually identified, the graphic materials obtained during the calculations are similar to the photos of fuel rods after the energy campaign.

**Keywords:** process visualization, defects spatial distribution, fuel rod damage mechanism, process innovation.

## 1 Introduction

This article continues the study of the theoretical mechanism for defects in spatial distribution. The given study includes numerical modeling on that mechanism basis and the obtained graphic material.

The study's relevance is determined by identifying the fuel assembly state and main behavior patterns, depending on the damaging nature and the operation duration.

This study aims to verify the results of calculations by the proposed mechanism on the material of fuel assembly cuts after the fuel campaign on actually operating power plants.

One of the reasons for the disturbing effect on the nuclear reactor operating mode stability and the decrease in the NPPs installed power factor (IPF) is the formation of defects in fuel elements of various reactors [1, 2].

The processes of the appearance of defects, depending on the processes occurring in fuel during the reactor operation, are considered in [3].

The dynamic aspects of forming point defects of the type substitution and intrusion during reactor operation are considered in [4, 5].

In most cases, the reason for the installed power factor (IPF) relatively low values is the static occurrence of damage to fuel assemblies (FA) through the formation of a defect in the fuel cladding [1].

Based on the results in the field of irradiated fuel assemblies post-reactor examinations [6-8], also taking into account the materials of defects study in the early stages of nuclear energy industry development [9-11], it should be noted that the main mechanisms of damage to fuel rods due to radiation growth, thermomechanical interaction between fuel and cladding, radiation and thermal creep, deflection of fuel rods (associated with

thermomechanical interaction in the bundle), and radiation-resulting decrease in plasticity.

## 2 Research Methodology

Due to the processes of heat intake and heat removal from the system to the medium, the reactor heating and the change in fuel component concentration are described by the following system of equations [4]:

$$\frac{dT}{dt} = \Phi \frac{QpC}{c_p m} e^{\frac{-E}{RT}} - a(T - T_\infty)S; \quad (1)$$

$$\frac{dC}{dt} = \frac{u}{V}(C_0 - C) - ze^{\frac{-E}{RT}}C, \quad (2)$$

where  $Q$  – the thermal reaction effect;  $\Phi = \Phi(E)$  – the rate of particle generation in the reaction;  $p$  – the reacting medium density;  $C_0, C$  – the initial and current concentrations of the fuel component, respectively;  $E$  – the activation energy, i.e., the energy that the neutron must have to react;  $T$  – reactor temperature;  $a$  – the heat transfer coefficient;  $T_\infty$  – the ambient temperature;  $V$  – the volume in which the reaction takes place;  $S$  – the surface area limiting the volume;  $c_p$  – the specific heat capacity at constant pressure;  $m$  – the reacting system mass;  $u$  – the burning nuclear fuel wave speed, or the rate of nuclear fuel components supply (in the case of a flow reactor).

It is known from previous works [12–14] that an appropriate equation also describes the neutron flux intensity in wave reactor temperature dynamics:

$$\Phi(E) = \Phi_1(E) + \Phi_2(E), \quad (3)$$

where  $\Phi_1(E)$  – an expression for the flux density of decelerating elastically scattered neutrons;  $\Phi_2(E)$  – an expression for the flux density of decelerating non-elastically scattered neutrons.

The PD concentration in the sample depends on spatial coordinates and time [3]. Therefore, it can be found from the solution of a system of two diffusion equations describing the migration of PD, which closes the general system of equations (1)-(5):

$$\frac{\partial C_V(r,t)}{\partial t} + \omega \nabla \vec{J}_V(\vec{r}, t) = -\alpha C_V(\vec{r}, t) C_I(\vec{r}, t); \quad (4)$$

$$\frac{\partial C_I(r,t)}{\partial t} + \omega \nabla \vec{J}_I(\vec{r}, t) = -\alpha C_V(\vec{r}, t) C_I(\vec{r}, t), \quad (5)$$

where  $C_V(r,t), C_I(r,t)$  – the concentrations of vacancies and interstitial atoms, respectively;  $J_V(r, t)$  and  $J_I(r, t)$  – the flux densities of vacancies and interstitial atoms;  $\omega \sim \alpha^3$  – the atomic volume;  $a$  – the lattice constant;  $\alpha$  – the PD mutual recombination coefficient.

Since the PD sources density is proportional to the rate of nuclear fission or the neutron flux density, considering the neutron capture cross-section (3).

Then, estimated computer calculations of the PD sources' density dependences on temperature can be carried out for several compositions, for example, a uranium-thorium fissile medium at a constant neutron flux density; the results are shown in Figure 1.

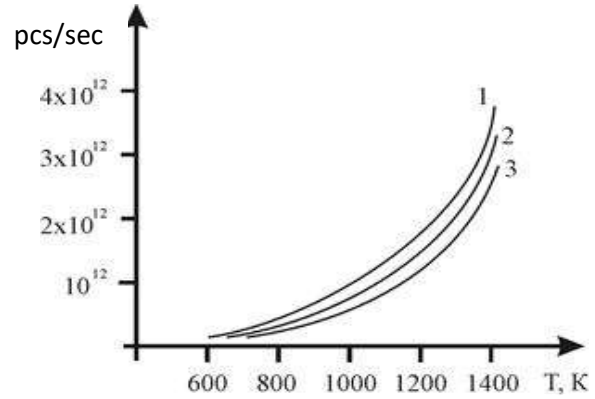


Figure 1 – Dependences of the rate of point defects formation on the medium fissile temperature for several compositions of the uranium-thorium medium (1-10 % Th; 2-5% Th; 3-1% Th) at a constant neutron flux density  $F = 10^{13}$  neutrons/(cm<sup>2</sup>·s)

Calculations were carried out for the wave (flow) reactor stable operation region, presumably located from  $10^{-3}$  eV to 1 eV or in the region from 2 MeV to 8 MeV.

When simulation, we use the following initial data:

$$\begin{aligned} E_u &= 5,5 \text{ MeV} = 5,5 \cdot 10^6 \cdot 1,6 \cdot 10^{-19} \text{ J}; & C &= 8,8 \cdot 10^{-13} \text{ J}; \\ E_{Th} &= 5,9 \text{ MeV} = 5,9 \cdot 10^6 \cdot 1,6 \cdot 10^{-19} \text{ J}; & C &= 9,44 \cdot 10^{-13} \text{ J}; \\ Q_u &= 204 \text{ MeV} = 204 \cdot 10^6 \cdot 1,6 \cdot 10^{-19} \text{ J}; & C &= 326,4 \cdot 10^{-13} \text{ J}; \\ Q_{Th} &= 190 \text{ MeV} = 190 \cdot 10^6 \cdot 1,6 \cdot 10^{-19} \text{ J}; & C &= 304 \cdot 10^{-13} \text{ J}. \end{aligned}$$

The calculations assumed that the thorium-specific heat capacity coincides with uranium's specific heat capacity.

It should be noted that the solution of this equations' system is associated with overcoming large computational difficulties due to the need to set boundary conditions on all PD drains, which, as a rule, are chaotically distributed over the sample volume. During the numerical simulation, these processes were not considered.

## 3 Results and Discussion

Later, an attempt was made to visualize the PD formation process. During the simulation, we considered the physical parameters of fuel energy-emitting elements' tablets (fuel elements) manufactured by powder metallurgy technology and their isotopic composition. The simulation was carried out according to such parameters as the total neutron flux, the point defects migration distance, and the size of a cell containing the active isotope. The simulation results are presented in a series of Figures 2-5 obtained using computer models.

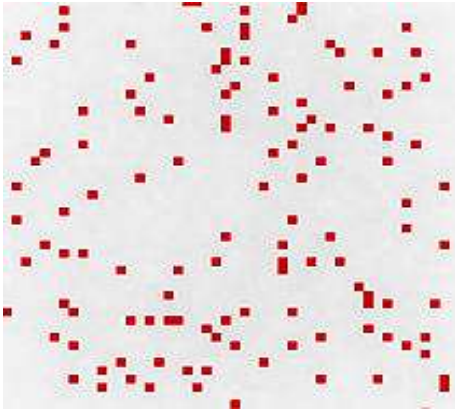


Figure 2 – Simulation of 2D chaotic placement of cells with an active isotope in a model fuel element (simulation size  $6000 \times 6000 \mu\text{m}$ ), the beginning of calculations; the active isotope containing cell size (highlighted in red) is  $\sim 100 \mu\text{m}$  per cell

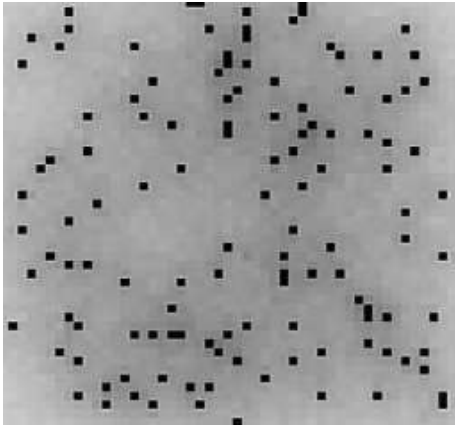


Figure 3 – Simulation of 2D chaotic placement of point defects (different grayscale) in a model fuel element (simulation size  $6000 \times 6000 \mu\text{m}$ ), end of calculations

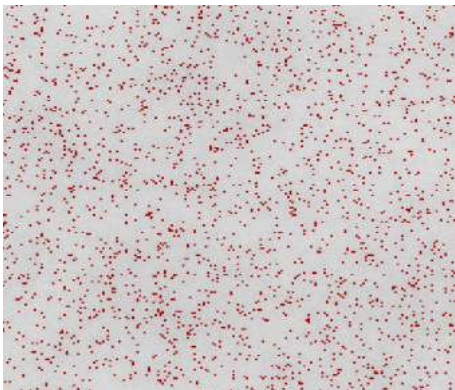


Figure 4 – Simulation of 2D chaotic placement of cells with an active isotope in a model fuel element (simulation size  $200 \times 200 \mu\text{m}$ ), the beginning of calculations; the active isotope containing cell size (highlighted in red) is  $\sim 1 \mu\text{m}$  per cell

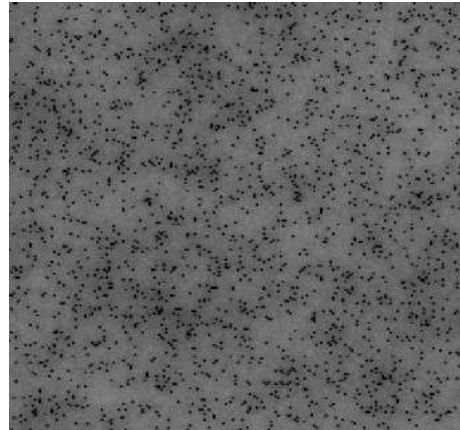


Figure 5 – Simulation of 2D chaotic placement of point defects (different grayscale) in a model fuel element (simulation size  $200 \times 200 \mu\text{m}$ ), end of calculations; the active isotope containing cell size (highlighted in black) is  $\sim 1 \mu\text{m}$  per cell

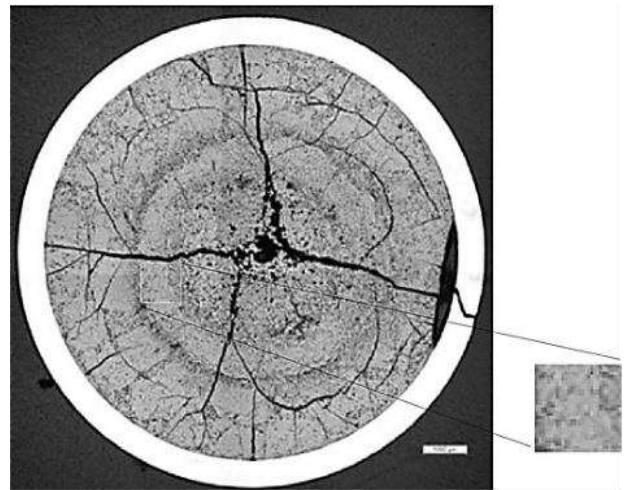


Figure 6 – Photo of the fuel rod after the fuel campaign (1), the same fuel element photo fragment, magnification by 10 (2); the results obtained allow us to state the correctness of the methodological and theoretical approach in modeling

It should be noted separately that the fuel tablet swelling and cracking processes were not considered in the simulation. These studies will be carried out further in the future.

Analysis of photos of fuel rods after the fuel campaign (Figure 6) showed their visual similarity with the graphic material obtained from numerical simulation carried out in the presented work (Figure 6 and, for example, Figure 5).

#### 4 Conclusions

As a result of the research work carried out, the following conclusions are formulated.

The point defects influencing the wave (flow) reactor operation with uranium-thorium fuel medium are considered. As a result of numerical simulation, the dependences of the point defects formation rate on temperature are obtained. These dependencies are power functions of temperature with an exponent equal to 4.

Numerical modeling was carried out, with calculation results visualization, the processes of a chaotic PD region formation, with a variation in the size of active isotope-bearing cells, from 1  $\mu\text{m}$  to 100  $\mu\text{m}$  per cell.

The resulting graphic material of 2D modeling of point defects formation is visually similar to photographs of fuel

element (TVEL) sections after the fuel campaign (excluding cracking and swelling).

The carried out visual similarity confirms the correctness of the theoretical approach applied in numerical modeling and allows for developing software for these processes simulation.

## References

1. Opyatyuk, V. V. (2016). The behavior of a flow reactor of ideal mixing near singular points and its effectiveness. *Combustion and Plasma Chemistry*, Vol. 14(3), pp. 182-188.
2. Smirnov, V. P., Markov D. V., Smirnov A. V. et al. (2006). VVER fuel: Result of post irradiation examination. *Fontevraud 6th International Symposium: Contribution of Materials Investigations to Improve the Safety and Performance of LWRs*, pp. 18-22.
3. Opyatyuk, V., Kozlov, I., Karchev, K. et al. (2023). Numerical modeling of point defect formation processes during the nuclear power plants operation. *Advanced Manufacturing Processes IV. InterPartner 2022. Lecture Notes in Mechanical Engineering. Springer, Cham*, pp. 530-539, [https://doi.org/10.1007/978-3-031-16651-8\\_50](https://doi.org/10.1007/978-3-031-16651-8_50)
4. Rusov, V. D., Tarasov, V. A., Sharf, I. V. et al. (2015). On some fundamental peculiarities of the traveling wave reactor. *Science and Technology of Nuclear Installations*, pp. 1-23, <https://doi.org/10.1155/2015/703069>
5. Rusov, V. D., Tarasov, V. A., Eingorn, M. V. et al. (2015). Ultraslow wave nuclear burning of uranium-plutonium fissile medium on epithermal neutrons. *Progress in Nuclear Energy*, Vol. 83, pp. 105-122, <https://doi.org/10.1016/j.pnucene.2015.03.007>
6. Luzzi, R., Vasconcellos, A. R., Ramos, J. G. et al. (2018). Statistical irreversible thermodynamics in the framework of Zubarev's nonequilibrium statistical operator method. *Theoretical and Mathematical Physics*, Vol. 194, pp. 4-29, <https://doi.org/10.1134/S0040577918010038>
7. Isihara, A. (2013). *Statistical Physics*. Academic Press, Amsterdam, Netherlands.
8. Balescu, R. (1975). *Equilibrium and Nonequilibrium Statistical Mechanics*. Brussels, Belgium.
9. Nosovsky A. V., Sharaevsky I. G., Fialko N. M., et al. . (2018). *Thermophysics of NPP Resource*. Chernobyl: In-t problem AES NAS of Ukraine, Kyiv, Ukraine.
10. Sharaevsky, I. G., Fialko, N. M., Zimin, L. B. et al. (2018). Features of diagnostics of unsuspected thermal, vibroacoustic and neutron processes in the first contour of nuclear reactors. *Problems of Nuclear Power Plants' Safety and of Chornobyl*, pp. 6-15, <http://dx.doi.org/10.31717/1813-3584.18.31.1>
11. Pavlov, S. V. (2013). Key results of VVER-1000 fuel assemblies post-irradiation examinations. *10-th International Conference on VVER Fuel Performance, Modeling and Experimental Support, 07-14.09.2013, Sandanski, Bulgaria*, pp. 213-227.
12. Tarasov, V. A., Borikov, T. L., Kryzhanovskaja, T. V. et al. (2007). The theory of dissipative structures of the kinetic system for defects of nonlinear physical system "metal + loading + irradiation". Part 1. *Problems of Atomic Science and Tecnology. Series: Physics of Radiation Effect and Radiation Materials Science*, Vol. 2(90), pp. 63-71, <http://dspace.nbu.gov.ua/handle/123456789/110649>
13. Tarasov, V. A., Borikov, T. L., Kryzhanovskaja, T. V. et al. (2007). The theory of dissipative structures of the kinetic system for defects of nonlinear physical system "metal + loading + irradiation". Part 2. *Problems of Atomic Science and Tecnology. Series: Physics of Radiation Effect and Radiation Materials Science*, Vol. 2(90), pp. 72-75, <http://dspace.nbu.gov.ua/handle/123456789/110648>
14. Tarasov, V. A., Borikov, T. L., Kryzhanovskaja, T. V. et al. (2007). The theory of dissipative structures of the kinetic system for defects of nonlinear physical system "metal + loading + irradiation". Part 3. *Problems of Atomic Science and Tecnology. Series: Physics of Radiation Effect and Radiation Materials Science*, Vol. 6(91), pp. 18-28, <http://dspace.nbu.gov.ua/handle/123456789/110649>



Spirin A., Borysiuk D., Tsurkan O., Tverdokhlib I., Veselovska N., Edl M. (2023). Ways of intensification of grass seed production. *Journal of Engineering Sciences*, Vol. 10(1), pp. F11-F19, doi: 10.21272/jes.2023.10(1).f3

## Ways of Intensification of Grass Seed Production

Spirin A.<sup>1</sup>[0000-0002-4642-6205], Borysiuk D.<sup>2</sup>[0000-0001-8572-6959], Tsurkan O.<sup>1</sup>[0000-0002-7218-0026], Tverdokhlib I.<sup>3</sup>[0000-0003-1350-3232], Veselovska N.<sup>3</sup>[0000-0001-9399-6721], Edl M.<sup>4</sup>[0000-0003-0761-7882]

<sup>1</sup> Separated Structural Unit “Ladyzhyn Professional College of Vinnytsia National Agrarian University”, 5, Kravchik Petro St., 24321, Ladyzhyn, Vinnytsia Region, Ukraine;

<sup>2</sup> Vinnytsia National Technical University, 95, Khmelnytske Hwy, 21021, Vinnytsia, Ukraine;

<sup>3</sup> Vinnytsia National Agrarian University, 3, Sonyachna St., 21008 Vinnytsia, Ukraine;

<sup>4</sup> University of West Bohemia, 8, Univerzitni St., 30614 Pilsen, Czech Republic

### Article info:

Submitted: March 6, 2023  
 Received in revised form: May 19, 2023  
 Accepted for publication: May 30, 2023  
 Available online: June 2, 2023

### \*Corresponding email:

[wnatalia@ukr.net](mailto:wnatalia@ukr.net)

**Abstract.** The main reason that restrains the development of seed production of perennial grasses is losses during harvesting, which depend on the agrotechnical properties of plants and the imperfection of existing means. There are no special grass seeds yet. Therefore, serial equipment with special devices is recommended for their collection. There are enough options for technologies for collecting grass seeds. In the article, six main options of technologies used in production were analyzed and compared according to the main indicators. The best results of a comprehensive comparison are those technologies that process the collected seed mass into a stationary one. The design of a device for wiping the seed mass was proposed to develop this direction of grass seed collection technologies. The article presents theoretical and experimental research results that allowed improving these devices based on rational design and operating parameters. Another way to intensify the production process of leguminous grass seeds is to combine the technological processes of wiping and separation in one machine. The analysis of various separating devices showed that machines with a rotating screen of cylindrical or conical shape are best suited for this purpose. The conducted theoretical studies confirmed the hypothesis that extending the time the material stays on the sieve by using a conical surface increases the yield of clean seeds and contributes to uniform loading of the sieve surface, improving the quality of the initial material. According to the research results, the design of the grating-separating block was proposed for the implementation of this scientific hypothesis. The theoretical and experimental studies presented in the article will allow for significantly intensifying the process of collecting grass seeds and outlining the further development of scientific research in this field.

**Keywords:** process technology, product innovation, grating device, wiping, separation.

## 1 Introduction

An indisputable axiom is that developed animal husbandry requires an appropriate production level of fodder crop seeds, especially alfalfa, and clover. This was stated repeatedly by various sources, including the authors [1], but judging by the unsatisfactory state of livestock breeding in Ukraine, the problem remains unresolved. It should be noted that, unlike other problems of agricultural production, several objective reasons restrain the development of the production of grass seeds.

The main reason restraining the development of seed production is the agrotechnical and physical-technical features of plants and, in fact, seeds. A characteristic feature of grass for seeds is their increased clogging (up to 60 %) by weeds of high humidity. During the collection of grass seeds, there is a significant difference in the humidity of individual parts of the plants. So, for example, the moisture content of clover seeds is within 12-35 %.

## 2 Literature Review

Some plants tend to lie down. Another feature of a physical and mechanical nature is the insignificant mass share of seeds in the total crop yield. So, for example, in [2], the use of rotary threshing-separating devices for collecting clover seeds is considered. At the same time, the instability of the flow of the technological process is observed, primarily due to the intensive formation of bundles from plant stems and, as a result, a rapid increase in energy consumption. It was concluded that the main way to overcome these problems is the improvement of grating surfaces, minimization of gaps, as well as the search for solutions to normalize stem mass.

Observing the rational parameters of the engine and main working organs is essential when collecting grass seeds with combined harvesters. Thus, in work [3], it is noted that when the engine speed is reduced by 10 %, the loss of the straw shaker and other working parts of the combine increases by 5 times. Therefore, during assembly, the engine speed should be maximum. At the same time, a significant conclusion is made that collecting grass seeds is the most complex labor- and energy-consuming operation in the technology of works on their production. It is noted that special harvesters for harvesting grass seeds do not yet exist. Therefore it is recommended to use serial harvesters equipped with special devices for their collection.

The works [3, 4] are devoted to the search for new solutions for the intensification of herb seed collection in Ukraine. They concluded that the main directions for improving the process of processing the seed mixture at the stationary plant are the intensification of the process of primary cleaning of the seed and its wiping from the beans, which provides an opportunity to increase the productivity of the technological line and reduce the labor intensity of the process.

All these features significantly complicate the performance of the most challenging and responsible operation in seed production – harvesting.

According to various estimates, under favorable weather conditions, the loss of biological harvest can reach 20 %, and it can even exceed 50 % in rainy weather.

All these noted facts, unfortunately, lead to the conclusion that the problem of collecting grass seeds remains unsolved. Despite several decades of work by many collectives, the issue of providing the fodder industry with high-quality forage seeds, especially legumes, remains relevant.

Collecting grass seeds is the most complicated part of their production. If the main issues with the cultivation of seed crops of alfalfa, clover, and other grasses have already been resolved [5, 6], then the issue of harvesting remains open [7]. That is, it can be said that the primary way of intensifying the production of grass seeds is, even, not to increase the yield of crops on the root but to reduce losses during their harvesting. Harvesters with special attachments are usually used to collect grass seeds. It should be noted that these tools do not always meet modern requirements. However, it should be noted that

this article is rather an exception from a number of quite normal studies. After all, most works, as a rule, are devoted to studying someone's constructive element.

In many cases, it is necessary to carry out repeated threshing of chaff. The characteristics of these plants again explain this.

This especially applies to alfalfa and clover. When harvesting, some beans are not threshed and fall into the chaff after cleaning the combine. Therefore, even using modern grain harvesters with appropriate devices requires including stationary elements. The authors have already considered the possible options for combining combined and stationary elements [8]. After summarizing the results of the analysis of the latest research on the cultivation and collection of grass seeds, it can be noted that there are many modernizations of harvesters, particular adaptations for them, stationary machines and equipment, and, accordingly, a significant number of possible combinations of them into actual technologies. The purpose of the work can be formulated based on the conducted analysis.

The research aims to increase the production of leguminous grass seeds by analyzing possible alternative technologies for collecting seeds and choosing rational options for specific agro-climatic conditions and technical capabilities of the farm.

## 3 Research Methodology

It was already noted above that in most cases, the harvesting of leguminous grass seeds by combine harvesters (even with special devices) exceeds agrotechnical requirements, so technologies are being developed in which the processing of the entire crop or part of it is transferred to a stationary plant. We refer to these technologies as stationary because mobile units, the main source of losses in combined technologies, are here replaced by stationary units.

Work on the improvement of stationary technologies has been carried out for a considerable time [9] in three main directions: harvesting the entire biological crop in the field and processing it at the stationary; harvesting part of the crop in the field (harvesting option) and processing it at the stationary; harvesting the non-threshed mixture in the field (an option is harvesting beans by threshing on soft modes) and processing it at the stationary.

The first technology ensures a minimum loss of seeds. However, in practice, it is hardly used due to high transport costs and difficulties with dosing the mass when feeding to the threshing floor. The low productivity of drying equipment and threshing devices necessitates transshipment operations. Long-term storage of wet mass can lead to its self-heating and loss of sowing qualities.

Storage of chopped biological harvest (or even better – combed seed part [10]) allows much better use of vehicles. Shredded or combed mass can be fed to the threshing floor more evenly and dosed. When collecting crushed mass with a field machine, even with the correct adjustment of the grinding device, there is increased seed damage.

Combing machines are free of these disadvantages, but the losses of the seed part slightly exceed agrotechnical requirements. Of course, after them, machines can be run for picking beans (for example [9]), but introducing an additional operation into the technology reduces its economic efficiency. However, this reduction in efficiency is offset by additional seed collection.

The third stationary technology provides significantly smaller volumes of transportation, drying, and threshing (or wiping) of material of uniform size and moisture content. This technology involves mainly using serial machines, devices, and equipment.

Processing beans, separated from the mixture, combed in the field, or collected in a hopper after “soft” threshing, is complicated with combined and stationary technologies. Their processing at the hospital is carried out either with a special grating device or a suitably prepared grain harvester. The use of combine harvesters is less efficient due to problems with loading them with the mixture and the need to pass the material through the combine twice to wipe the seeds entirely.

When analyzing technologies and technical means for their implementation, many indicators are considered: operational and energy costs, the productivity of units, their metal consumption, and the quality of execution of the technological process. According to the technology options, they differ significantly in terms of individual indicators, which makes it difficult to make the optimal decision when comparing them. For a better understanding of the advantages and disadvantages of technology, their comparison should be carried out according to complex indicators. The authors have already made a similar comparison for other technologies and machines [1]. In these works, the method of determining complex indicators is described in detail, so we will only give the result of technology evaluation.

Six of the most widespread technologies for collecting alfalfa seeds were compared according to the following individual indicators: operating costs (monetary units/ha), energy intensity (MJ/ha), metal intensity (kg/ha), and crop losses (kg/ha). The results of comparing technologies according to two comprehensive indicators are shown in the Table. 1 (where  $I_1$  and  $I_2$  are generalized indexes of the first and second kinds, respectively, defined in scientific work [1]).

Table 1 – Comparison of alfalfa seed harvesting technologies

Assembly technology	$I_1$	$I_2$
Direct combining	0.40	3.39
Separate combining	0.45	3.64
Threshing at the stationary biomass	0.47	3.82
Stationary threshing of unthreshed piles	0.51	4.01
Stationary processing of the combed seed pile	0.57	4.32
Stationary processing of the seed pile after “soft” threshing	0.61	4.51

From Table 1, the best results of a comprehensive comparison are those technologies that process the entire collected seed mass on a stationary basis. Of course, these results cannot and should not be taken as an absolute

verdict on the issue of the final choice of the best technologies, but they show the main direction of development of the ways of intensification of grass seed production.

The most “bottlenecks” in stationary technologies are wiping beans and separating the obtained material. With harvester technologies, the largest share of seeds is lost precisely because of unsatisfactory drying of beans because its degree does not exceed 70-75 %, even under favorable working conditions. This is the main reason for transferring part of the operations to the stationary.

Few modern serial machines for wiping the pile do not provide the necessary quality of work and have increased requirements for the composition of the pile, which causes a decrease in the efficiency of the entire technology.

The question of creating a universal grating device that would meet all the requirements has been around for a long time. Such a grating device should work in a wide range of changes in the fractional composition and moisture content of the seed mixture, be reliable in operation, provide the required quality of work, and not be very expensive and difficult to manufacture. It is also necessary to consider a particular farm’s seed production volume. Therefore, the universality of the grater device can only be talked about relatively, bearing in mind a certain range of their productivity. Over the past decades, a significant amount of work has been carried out on creating various structures of grating devices. Only according to the type of working body, they are divided into the following: hammer, drum hammer, drum pin, rotary hammer, rotary blade, screw, disk, screw disk, and roller. However, scientific research in this field continues.

The authors developed a design of a grating device with horizontal grating disks [1]. The scheme of the grating device is presented in Figure 1. The grating device includes a housing 6, in which a hopper 1 is installed with a loading neck 2 and a loading hole 3. In the space of the hopper, a finger activator 4 is installed, which has bars 5. The activator is mounted on the upper part of shaft 9, and the movable part is mounted on the lower part of the shaft grater disk 8. A fixed disk 7 is installed in the housing, which has a cup, the opening of which is a continuation of the loading neck.

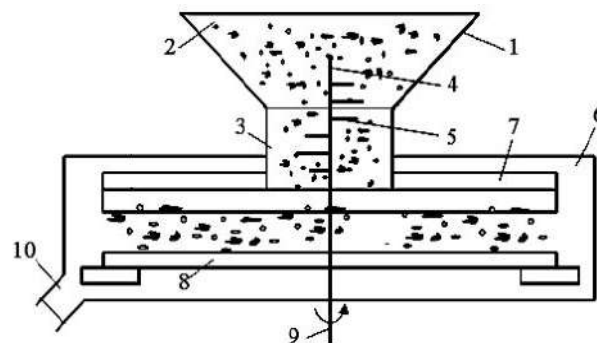


Figure 1 – Scheme of the grating device: 1 – hopper; 2 – loading neck; 3 – loading hole; 4 – activator; 5 – bar; 6 – body; 7, 8 – fixed and moving disk; 9 – drive shaft; 10 – output channel

The glass is made in the form of a hollow cylinder, on the outer side of which a threaded sleeve is wound. Beams are fixed to the lower surface of the fixed disk, installed radially on the disk in the form of rays. It was made in the form of reefs that have a notch. Ring protrusions are placed concentrically to the disk's axis in the spaces between the blades. The output channel 10 is placed in the lower part of the case.

In order to obtain new scientific data about the physical process of wiping seeds from beans and to study the patterns that occur in this process, theoretical and experimental studies were conducted on a laboratory installation, the structural scheme and general appearance of which is presented in Figure 2.

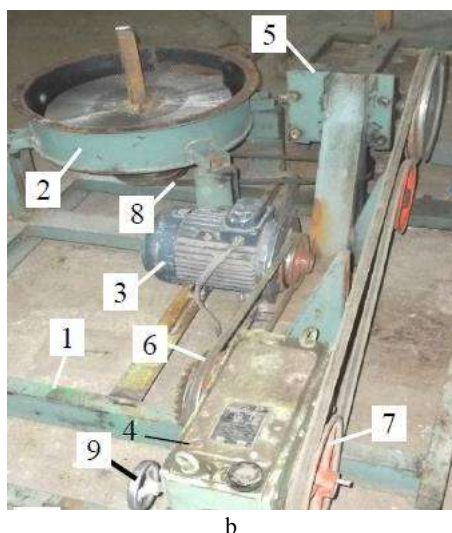
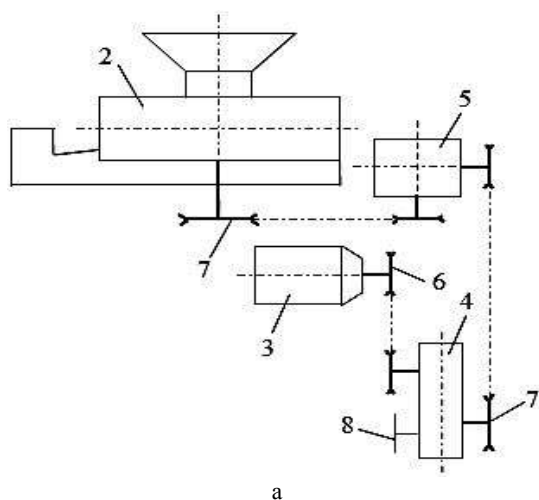


Figure 2 – Structural diagram (a) and general view (b) of the laboratory installation: 1 – frame; 2 – grating device; 3 – electric motor; 4 – speed variator; 5 – conical reducer; 6-8 – V-belt transmission; 9 – handle

The transportation of loose material in the space of the working channel of the grater device can take place in the form of movement of single particles of the rubbed seeds of the alfalfa mixture or their separate group under the influence of the forces of the carrier airflow in the form of

an aeromix [11]. In contrast, two main types of particle movement modes are possible: particles of loose material are carried by the airflow with the help of “jumps” and continuous flow [12].

Modes of movement of the flow of particles of bulk material are regulated, as a rule, by its main physical and mechanical properties, the main of which are density, particle size, coefficients of internal and external friction, and the uniformity of supply of bulk materials into the space of the working channel [13].

The energy consumption of the transportation process during the pneumatic method of moving the bulk medium primarily depends on the movement modes of the flow of particles of the bulk material. The flow speed is the dominant factor in the energy consumption of the transportation process, which is minimal during the wave and batch movement of the material in a quasi-liquid state [14].

The analysis of the modes of movement of flows of particles of loose materials shows that they are accompanied by their mutual movement, which is very complex [15, 16]. In order to formalize the process of movement of loose material, it is necessary to accept the restriction that its transportation takes place in the form of a continuous flow, and the particles of loose material in the process of movement retain their shape and mass.

In the grating device, due to the different speeds of the translational movement of the particles by mass  $m_n$  in the space of the working bed of the grating device, they have a relative shear speed of  $V_c$ . Due to the mutual contacts (collisions) of the particles, they acquire additional components of the translational speed  $V_n$  of chaotic movement, while the mass  $m_n$  participates in the portable rotational move together with the moving disk and at the same time relative to it - along the groove beat.

Consider the process of collision of two elements with mass  $m_n$ , which are located in the radial interaxial groove of the ball at a distance  $R_n$  from the axis of rotation of the disk, which rotates with an angular velocity  $\omega_n$ , while we consider that the material of the particles is elastic. The calculation scheme of the elastic collision process of two formalized spherical particles 1 and 2, by mass  $m_n$  is shown in (Figure 3).

The phenomenon of collision of two particles 1 and 2 by mass  $m_n$  occurs mainly in an oblique collision due to the mutual exchange of shock mass pulses (Figure 3). In contrast, shear flows of material occur, and the direction of the vectors  $\vec{u}_1$  and  $\vec{u}_2$  velocities of the colliding bodies is directed at the collision angle  $\beta_c$  to the horizontal axis of the Cartesian coordinate system.

We apply the kinetic theory of solid gases to solve the problem of shear flows that occur during the collision of two particles 1 and 2 by mass  $m_n$  [17]. In contrast, according to the theory of the movement of a granular medium [18], it is known that when the flow is sheared, the instantaneous speed of the particles is the sum of three related speed components: fluctuation speed, translational (averaged) and rotational speed.



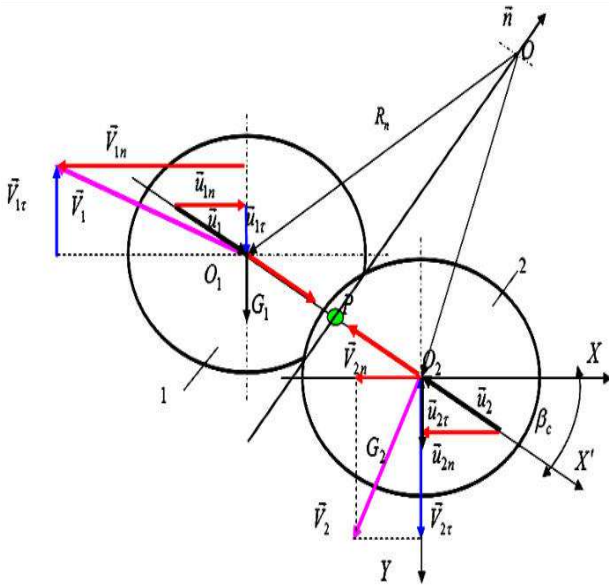


Figure 3 – Scheme for calculation of the collision of material particles by mass  $m_n$

According to the provisions of [19], the equation of state of the loose medium during its movement is written in the form:

$$p(x)\bar{\varepsilon}(x) = \chi \left( \frac{du}{dx} \right)^2. \quad (1)$$

The analysis of equation (1) shows that the product of the square of the speed of movement of the loose granular medium  $(du/dx)^2$  by the coefficient of the physical constant  $\chi$ , which is written in the right part, is identical to the specific value of the work spent on moving the layer of particles 1 and 2 by mass  $m_n$  based on  $1 \text{ m}^2$ . The left part of the product of the analog of hydrostatic pressure  $p(x)$  on the porosity of the granular medium  $\bar{\varepsilon}(x)$  is identical in the physical sense to the kinetic energy of the mutual chaotic movements of particles 1 and 2 by mass  $m_n$  due to the movement of the loose granular medium.

For the contact (collision) between particles 1 and 2 mass  $m_n$  to occur, the angle of collimation  $\beta_c$  (Figure 3) must be within the range from 0 to  $\pi/2$  rad.

Taking into account the fact that the movement of particles in the flow of the working bed of the grating device has a complex functional nature [9, 10], the total kinetic energy  $\sum K_m$  of the mutual movements of particles 1 and 2 by mass  $m_n$  is written as the sum of the kinetic energies of particles by mass  $m_n$ :

- in their relative translational displacement during shearing  $K_V, J$ ;
- for their chaotic movement  $K_C, J$ ;
- in transverse mass transfer  $K_T, J$ , namely

$$\sum K_m = K_V + K_C + K_T. \quad (2)$$

The kinetic energy of particles in their relative translational displacement in the direction of shear  $K_V$ , chaotic movement or fluctuation  $K_C$ , and transverse mass

transfer  $K_T$  of particles 1 and 2 by the mass  $m_n$  of the loose medium according to [20] is determined from the following expressions

$$\begin{cases} K_V = \frac{1}{2} m_n (\Delta X)^2 \left( \frac{du}{dx} \right)^2; \\ K_C = \frac{1}{2} m_n (u')^2; \\ K_T = \frac{1}{4} m_n l_c u' \frac{du}{dx}, \end{cases} \quad (3)$$

where  $m_n$  is the mass of a particle of alfalfa seeds, kg;  $\Delta X$  – a difference of coordinates of the centers of particles of adjacent layers of bulk environment, m;  $u'$  – particle fluctuation rate (m/s).

Taking into account that:

$$m_n = V_n \rho_v = \rho_v \pi d_n^3 / 6,$$

where  $V_n = \pi d_n^3 / 6$  – the volume of the  $i$ -th particle,  $\text{m}^3$ ;  $d_n$  – diameter of the  $n$  particle, m;  $\rho_v$  – the density of the seed particle,  $\text{kg}/\text{m}^3$ .

$$\Delta X = b_1 - b_2,$$

where  $b_1$  and  $b_2$  are the corresponding coordinate of the center of adjacent layers (particles) colliding with each other, m;

$$u' = 2l_c \gamma_n,$$

where  $l_c$  is the average distance between particles relative to their reduced mass, m;  $\gamma_n$  – average collision frequency of particles of a loose medium (1/s) and according to (3) can be written:

$$\begin{cases} K_V = \frac{1}{12} \pi d_n^3 \rho_v (b_1 - b_2)^2 \left( \frac{du}{dx} \right)^2; \\ K_C = \frac{1}{2} \frac{\pi d_n^3}{6} \rho_v (u')^2 = \frac{2\pi d_n^3}{3} \rho_v \gamma_n^2 l_c^2; \\ K_T = \frac{1}{4} \frac{\pi d_n^3}{6} \rho_v l_c u' \frac{dV}{dx} = \frac{1}{12} \pi d_n^3 \rho_v \gamma_n l_c^2 \frac{du}{dx}. \end{cases} \quad (4)$$

According to [21], the average collision frequency  $\gamma_n$  of the particles of the material of the loose medium is determined by the Ackerman-Shen method, while

$$\gamma_n = \frac{\tau}{E_k Z_n} \cdot \frac{du}{dx}, \quad (5)$$

where  $\tau$  is the shear stress, Pa;  $E_k$  – dissipation of the kinetic energy of a particle collision with one contact, J;  $Z_n$  – the number of particles per unit volume of the layer,  $1/\text{m}^3$ .

The dissipation of the kinetic energy  $E_k$  of the co-impact of one particle of the alfalfa seed mixture during its single contact is determined according to [22] by the Ackerman-Shen formula, namely

$$E_k = \frac{1}{12} \pi d_n^3 \rho_v \left( \frac{1-k^2}{4} + \frac{f(1+k)}{\pi} - \frac{f^2(1+k)^2}{4} \right) (u')^2, \quad (6)$$

where  $k$  is the recovery factor during impact;  $f$  – the coefficient of friction between particles.

At the same time, it is known that according to the Gauss hypothesis [22], the relationship between the magnitudes of tangential and normal impulses during impact is formed, similar to Coulomb's law for friction

$$\Delta u = -u'f(1+k), \quad (7)$$

where  $\Delta u$  is the change in the relative tangential velocity due to the impact, m/s.

The fluctuation rate  $u'$  of alfalfa mixture particles weighing  $m_n$  according to [2] characterizes the transverse quasi-diffusion coefficient  $D_{kd}$

$$D_{kd} = 0,5u'l_c. \quad (8)$$

At the same time, the coefficient of transverse quasi-diffusion  $D_{kd}$ , in turn, regulates the intensity of mutual movement of particles of a loose medium. In contrast, the intensity of the movement of particles increases in proportion to the coefficient of transverse quasi-diffusion  $D_{kd}$  and the gradient of the speed of translational movement of seeds in the direction of the shear speed  $du/dx$ .

From dependence (7), we determine the particle fluctuation rate, namely

$$u' = -\Delta u / f(1+k), \quad (9)$$

By substituting the value (9) into the dependence (6), we obtain the formula for determining the dissipation of the kinetic energy  $E_k$  of the collision of one alfalfa seed particle during its single contact

$$E_k = \frac{(\Delta u)^2}{12} \cdot \pi d_n^3 \rho_v \cdot \left( \frac{1-k}{4f^2(1+k)} + \frac{1}{\pi f(1+k)} - \frac{1}{4} \right). \quad (10)$$

According to (5) and (9), the average collision frequency  $\gamma_n$  of the particles of the loose medium will be determined

$$\gamma_n = \frac{48f^2\tau(1+k)}{(\Delta u)^2 d_n^3 \rho_v [\pi(1-k) + 4f - \pi f^2(1+k)] Z_n} \frac{du}{dx}. \quad (11)$$

By substituting the value of the average collision frequency  $\gamma_n$  of alfalfa seed particles or particles of a loose granular medium from equation (11) into dependence (4), we obtain:

$$K_c = \frac{2\pi d_c^2}{3d_n^3 \rho_v Z_n^2} \cdot \left( \frac{48f^2\tau(1+k)}{(\Delta u)^2 [\pi(1-k) + 4f - \pi f^2(1+k)]} \right)^2 \cdot \left( \frac{du}{dx} \right)^2; \quad (12)$$

$$K_r = \frac{4\pi d_c^2 f^2 \tau(1+k)}{(\Delta u)^2 [\pi(1-k) + 4f - \pi f^2(1+k)] Z_n} \cdot \left( \frac{du}{dx} \right)^2. \quad (13)$$

Thus, the total kinetic energy  $\sum K_m$  of mutual movements of particles of a loose granular medium or alfalfa seed particles after substituting the first equation from the system of equations (2) and equations (12) and (13) into dependence (2) and after the corresponding transformation and simplification of the expression, is defined by dependence

$$\begin{aligned} \sum K_m &= \frac{1}{12} \pi d_n^3 \rho_v (b_1 - b_2)^2 \left( \frac{du}{dx} \right)^2 + \\ &+ \frac{2\pi d_c^2}{3d_n^3 \rho_v Z_n^2} \left( \frac{48f^2\tau(1+k)}{(\Delta u)^2 [\pi(1-k) + 4f - \pi f^2(1+k)]} \right)^2 \left( \frac{du}{dx} \right)^2 + \\ &+ \frac{4\pi d_c^2 f^2 \tau(1+k)}{(\Delta u)^2 [\pi(1-k) + 4f - \pi f^2(1+k)] Z_n} \left( \frac{du}{dx} \right)^2 = \\ &= \frac{\pi}{12} \left( \frac{du}{dx} \right)^2 \left\{ \left[ d_n^3 \rho_v (b_1 - b_2)^2 \right] + 8 \frac{l_c^2}{d_n^3 \rho_v Z_n^2} \left( \frac{48f^2\tau(1+k)}{(\Delta u)^2 [\pi(1-k) + 4f - \pi f^2(1+k)]} \right)^2 + \right. \\ &\quad \left. + \frac{48f^2\tau(1+k)}{(\Delta u)^2 [\pi(1-k) + 4f - \pi f^2(1+k)] Z_n} \right\} = \\ &= \frac{\pi}{12} \left( \frac{du}{dx} \right)^2 \left\{ \left[ d_n^3 \rho_v (b_1 - b_2)^2 \right] + \frac{48f^2\tau(1+k)}{Z_n (\Delta u)^2 [\pi(1-k) + 4f - \pi f^2(1+k)]} \times \right. \\ &\quad \left. \times \left[ \frac{8}{d_n^3 \rho_v Z_n} \left( \frac{48f^2\tau(1+k)}{(\Delta u)^2 [\pi(1-k) + 4f - \pi f^2(1+k)]} \right) + 1 \right] \right\} \end{aligned} \quad (14)$$

or

$$\sum K_m = \frac{\pi}{12} \left( \frac{du}{dx} \right)^2 \left\{ \left[ d_n^3 \rho_v (b_1 - b_2)^2 \right] + \frac{48f^2\tau(1+k)}{Z_n (\Delta u)^2 [\pi(1-k) + 4f - \pi f^2(1+k)]} \times \right. \\ \left. \times \left[ \frac{8}{d_n^3 \rho_v Z_n} \left( \frac{48f^2\tau(1+k)}{(\Delta u)^2 [\pi(1-k) + 4f - \pi f^2(1+k)]} \right) + 1 \right] \right\}. \quad (15)$$

The obtained dependence (15) is a mathematical model that characterizes the total kinetic energy  $\sum K_m$  of the mutual movements of the particles of the loose granular medium, which is lost during a single collision of two spherical particles of the alfalfa seed mixture in the process of their movement to the periphery of the moving disk (or the output channel of the grating device). Depending on the speed components of the co-impact process, the physical and mechanical properties of alfalfa seeds and the conditions of the impact environment.

The mathematical model can be used for the analysis and analytical-empirical description of the state of the loose granular medium during the movement of alfalfa bean particles in the internal volumetric space of the working channel of the grating device.

Then, taking into account dependence (1), the known equation of the state of the loose granular medium  $p(x)\bar{\varepsilon}(x) = \chi(du/dx)^2$  during the movement of alfalfa seed particles can be written in the following form:

$$p\bar{\varepsilon} = \chi' \frac{\pi}{12} \left( \frac{du}{dx} \right)^2 \left\{ \left[ d_n^3 \rho_v (b_1 - b_2)^2 \right] + \frac{48f^2\tau(1+k)}{Z_n (\Delta u)^2 [\pi(1-k) + 4f - \pi f^2(1+k)]} \times \right. \\ \left. \times \left[ \frac{8}{d_n^3 \rho_v Z_n} \left( \frac{48f^2\tau(1+k)}{(\Delta u)^2 [\pi(1-k) + 4f - \pi f^2(1+k)]} \right) + 1 \right] \right\} \quad (16)$$

where  $\chi'$  is the coefficient of the physical constant, which is identical to the specific value of the work spent on moving the layer of particles per 1 m<sup>2</sup>;  $\bar{\varepsilon}$  – the average porosity of the granular medium.

The obtained dependences of the state of the loose medium (16) and (15) can be used for further analysis and justification of the parameters of the technological process of the grating device.

The program of experiments provided for, among other things, obtaining regression dependencies that characterize the change in the mass of the rubbed seeds, the degree of wiping of the seeds from the mixture, and the performance

of the grating device depending on the technological parameters of the process and the structural and kinematic parameters of the working bodies and the design of the fixed disk of the grating device. Laboratory experimental studies were carried out with stationary discs of four types. Variants of immovable discs are presented in Figure 4.



Figure 4 – Variants of execution of the stationary disk of the grating device: a – a disk with six balls fixed on it and flat plates installed in the space between the balls; b – a disk with three balls fixed on it and flat plates that, installed in the space between the balls; c – a disk with six fixed on it rings between which circular inserts with a diameter of 200, 250, and 300 mm, fixed from a rod with a diameter of 8 mm; d – a disk with 6 balls fixed on it, between which ring inserts made of a rod with a diameter of 6 mm, fixed in a circle with a diameter of 200, 250, and 300 mm

#### 4 Results and Discussion

The conducted studies showed that the best results of the wiping process (the maximum degree of wiping of the seeds) were obtained with option “d” of performing a stationary disk. This conclusion was made after analyzing the response surfaces of the change in the degree of wiping from the design of the fixed disk and the number of passes of the technological mass, which are presented in Figure 5. The approximating function, that is, the nature of the change in the degree of seed wiping from the alfalfa pile, is presented in the form of a mathematical model of a complete quadratic polynomial:

$$P_{4v}^{(21)} = 0.74 + 0.006 \cdot n + 4.9 \cdot k_n - 0.02 \cdot n \cdot k_n + 1.4 \cdot 10^{-5} \cdot n^2 - 0.28k_n^2, \quad (17)$$

where  $n$  is the rotation frequency of the moving disk, rpm;  $k_n$  – multiplicity of the wiping process [2]. Index “21” means the moisture content of the technological mass (21 %), and index “4” is the version of the fixed disk (option “d” in Figure 4).

Figure 5 presents the response surfaces for seed wiping.

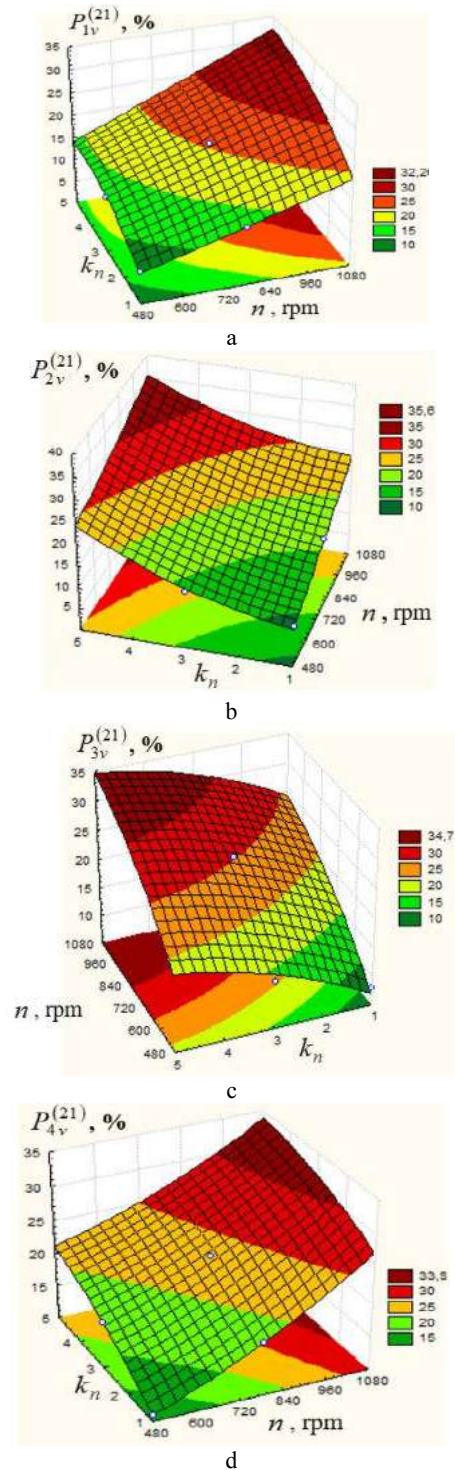


Figure 5 – Response surfaces of changes in the degree of seed wiping from the number of passes of the technological mass with a moisture content of 21 % and the frequency of rotation of the moving disk for various versions of the stationary disk: a – a disk with six balls fixed on it and flat plates, installed in the space between the balls; b – a disk with three balls fixed on it and flat plates installed in the space between the balls; c – a disk with six fixed on it rings between which circular inserts with a diameter of 200, 250, and 300 mm, fixed from a rod with a diameter of 8 mm; d – a disk with six balls fixed on it, between which ring inserts made of a rod with a diameter of 6 mm, fixed in a circle with a diameter of 200, 250, and 300 mm

The conducted experimental studies made it possible to determine the rational parameters of the wiping process: for the productivity of the grating device 0.8-6.6 kg/min, the diameter of the disks should be within 0.5-0.6 m, the rotation frequency of the moving disk 700-900 rpm, the diameter of the opening of the loading channel of the bunker is 0.11-0.15 m, the filling factor of the internal space of the working channel is 0.5-0.7.

One way to intensify the production process of leguminous grass seeds is to combine the technological processes of wiping and separation in one machine. The analysis of various separating devices showed that machines with a rotating screen of cylindrical or conical shape are best suited for this purpose. Such a combination was implemented in a grating-separating device [2], the technological scheme presented in Figure 6.

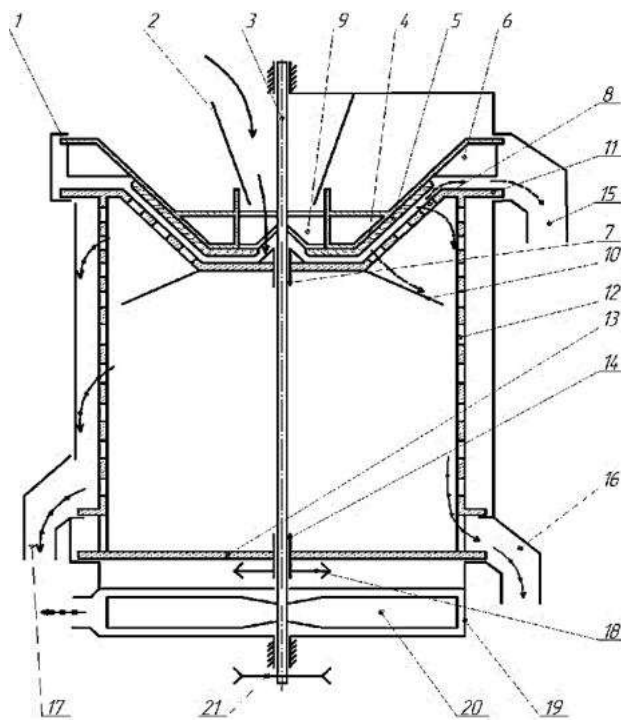


Figure 6 – Technological scheme of the grating-separating device: → heap; → coarse impurities; → grain part; → wiped grain; → unwiped grain; → air; 1 – casing; 2 – loading funnel; 3 – shaft; 4 – conical drum; 5 – beat; 6 – shoulder blades; 7 – bearing; 8 – tray; 9 – scrapers; 10 – scattering cone; 11 – ring; 12 – rotary sieve; 13 – disc; 14 – bearing support; 15 – a channel for removing the straw part of the pile; 16 – channel for removal of unwiped grain from beans; 17 – channel for removal of cleaned seeds; 18 – autonomous drive; 19 – fan; 20 – blades; 21 – drive

Laboratory studies of the grating-separation device of this design have shown one of its main shortcomings - insufficiently efficient use of the sieve surface. With this design, most seeds are removed from the upper part of the sieve, leaving the lower part empty. It is possible to increase the uniformity of the load on the separating surface by replacing the cylindrical sieve with a conical

one with a decrease in the radius of the cone in the direction of movement of the material [12].

Based on the results of the research, an expression was used to determine the speed  $V$ , m/s, of the seed supply depending on the time  $t$ , s, of the particle staying on the cone sieve and the length  $x$  (m) of the cone of the lattice-separation device:  $V = dx/dt$ .

The experiment results at the seed feeding speed for  $V = 0.1$  m/s, and  $V = 0.5$  m/s are presented in Figure 7 and Figure 8, respectively.

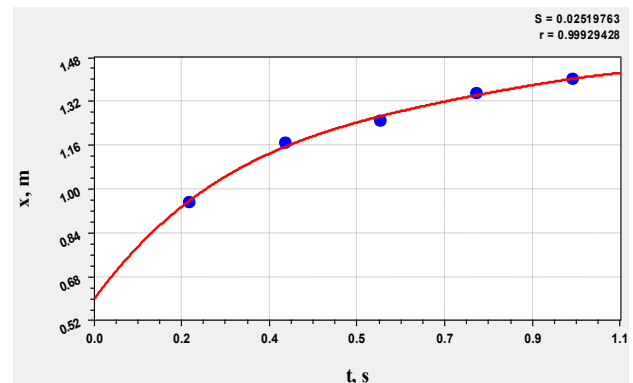


Figure 7 – Dependence of the seed residence time on the conical sieve on the length of the generating cone of the grating-separating device at  $V = 0.1$  m/s

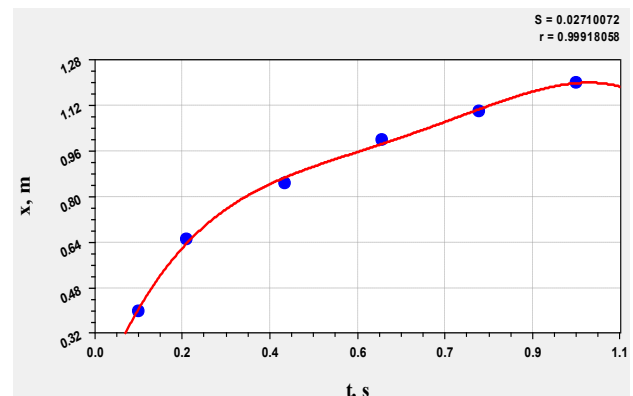


Figure 8 – Dependence of the seed residence time on the conical sieve on the length of the generating cone of the grating-separating device at  $V = 0.5$  m/s

The equations obtained based on the regression analysis of experimental data have the following form:

- at the seed feeding speed for  $V = 0.1$  m/s (Figure 7)

$$x = 0.5984127 + 2.3749339 \cdot t - 3.3715278 \cdot t^2 + 2.5810185 \cdot t^3 - 0.78125 \cdot t^4; \quad (18)$$

- at the seed feeding speed for  $V = 0.5$  m/s (Figure 8)

$$x = 0.034670173 + 4.5729655 \cdot t - 9.6638261 \cdot t^2 + 10.12661 \cdot t^3 - 3.8718052 \cdot t^4. \quad (19)$$

Therefore, extending the time the material stays on the sieve by using a conical surface increases the yield of clean seeds and contributes to the uniform loading of the sieve surface, improving the quality of the initial material.

## 5 Conclusions

The intensification of forage seed production, especially leguminous grasses, is held back by the imperfection of modern means of seed collection. All efforts in the field of harvesting should be focused on reducing losses during seed harvesting.

The analysis of literary sources and the authors' experience allows us to state that the main way to reduce seed losses during harvesting is the processing of the seed part of the crop at the hospital. According to the authors, the most promising technologies are harvesting the seed part by combing and threshing the mass in the "soft" mode to obtain a pile with unthreshed beans in the combine hopper.

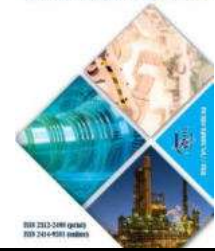
The most responsible operations in treating the seed pile at the hospital are wiping and separation. To implement the wiping process, we can recommend grating units of the original design similar to the one described in this article.

The obtained mathematical model for the total kinematic energy of mutual movements of particles of a loose granular medium during their movement with collisions in the working space of the grating device. The research results can be used to determine the device's rational parameters for wiping the alfalfa seed mixture.

The combination of wiping and separation operations in one machine appears to the authors to be a significant effect of intensification during the processing of grass seed piles at the stationary plant. The conducted theoretical and experimental studies show the prospects of such a direction.

## References

1. Spirin, A. V., Tverdokhlib I. V., Zamriy M. A. (2021). Determination of the operating mode of the centrifugal-gravity separator of the grating device. *Vibrations in Engineering and Technology*, Vol. 102, pp. 64-71, <https://doi.org/10.37128/2306-8744-2021-3-7>
2. Tverdokhlib, I. V. (2017). Increasing the efficiency of grass seed collection. *Bulletin of Mechanical Engineering and Transport*, Vol. 6, pp. 158-163, <https://vmt.vntu.edu.ua/index.php/vmt/article/view/111/102>
3. Antoniv, S. F., Rudnytskyi, B. O. (2017). Peculiarities of the technology of growing seeds of new and promising varieties of leguminous grasses in the conditions of the forest-steppe of Ukraine. *Agriculture and Forestry*, Vol. 49, pp. 70-76, <http://socrates.vsau.edu.ua/repository/getfile.php/19070.pdf>
4. Perepravo, N., Zolotarev, V., Sevcov, A., Ahlamov, J., Otrosko, S., Sarikov, N., Kosolapov, V., Marczuk, A., Caban, J. (2016). Improvement let harvesting methods of perennial seed grass. *Agricultural Engineering*, Vol. 20, pp. 167-173.
5. Molotkov, L. N., Ratmanov, M. V. (2018). Technologies for harvesting testicles of perennial grasses. *Proceedings of the 4th International Scientific and Practical Conference "Import Substitution Technology for Cultivation, Storage and Processing of Horticulture and Crop Production Products"*, Uman, Ukraine, pp. 63-64.
6. Moss, W. M., Guzzomi, A. L., Foster, K. J., Ryan, M. H., Nichols, P. G. H. (2021). Harvesting subterranean clover seed – Current practices, technology and issues. *Crop & Pasture Science*, Vol. 72, pp. 223-235, <https://doi.org/10.1071/CP20269>
7. Borisova, M. L., Dianov, L. V. (2015). Ways to reduce losses of seed mass of field crops during combine harvesting. *Fod and Agriculture Organization of the United Nations*, Vol. 31, pp. 85-88.
8. Sheychenko, V. O., Anelyak, M. M., Kuzmych, A. Y., Baranovskiy, V. M. (2016). Intensification of the process of collecting seeds of perennial grasses. *Technology, Energy, Transport of Agricultural Industry*, Vol. 94, pp. 29-33.
9. Boor, B., Lefebvre, N. (2021). *Harvest and Post-Harvest Handling of Herbs*. Research Institute of Organic Agriculture, Frick, Switzerland.
10. Solomka, O. V. (2017). *Justification of the Technological Process of Collecting Alfalfa Seeds by Combing Method*. National University of Life and Environmental Sciences of Ukraine, Kyiv, Ukraine.
11. Barth, W. (1958). Processes occurring during the transportation of solid and liquid particles in gases, taking into account the processes that occur during pneumatic transportation. *Chemie-Ing. Techn.*, Vol. 30, pp. 171-180.
12. Selger, G. (1956). Designs of agricultural blowers-conveyors. *Landtechn*, Vol. 1, pp. 2-10.
13. Gushchin, V. M. (1999). Modes of movement of air mixtures in a pneumatic transport pipeline. *Geotechnical Mechanics*, Vol. 13, pp. 71-76.
14. Gushchin, V. M. (2000). Restoration of the structure of the movement of air mixtures in a pneumotransport pipeline. *Bulletin of National Technical University of Ukraine "Kyiv Polytechnic Institute". Series "Engineering"*, Vol. 38, pp. 158-162.
15. Rosen, T. (2016). *Angular Dynamics of Non-Spherical Particles in Linear Flows Related to Production of Biobased Materials*. Royal Institute of Technology, Stockholm, Sweden.
16. Welshcof, G. (1962). *Pneumatische Forderung bei Grossen Fordergut-Konzentrationen*. Dusseldorf, Germany.
17. Savage, S. B. (1993). Mechanics of granular flows. In: *Hutter, K. (eds) Continuum Mechanics in Environmental Sciences and Geophysics. International Centre for Mechanical Sciences. Springer, Vienna*, Vol. 337, pp. 467-522, [https://doi.org/10.1007/978-3-7091-2600-4\\_6](https://doi.org/10.1007/978-3-7091-2600-4_6)
18. Shirko, I. V., Sakharov V. A. (1987). Phenomenological theory of movement of a granulated medium based on the methods of static mechanics. *Theoretical Foundations of Chemical Technology*, Vol. 21, pp. 661-668.
19. McLaren, C. P., Kovar, T. M., Penn, A., Müller, C. R. (2019). Gravitational instabilities in binary granular materials. *PNAS*, Vol. 116(19), pp. 9263-9268, <https://doi.org/10.1073/pnas.1820820116>
20. Pyven, M. V. (2015). Planning experiment in the study of the process of separation of grain mixtures by cylindrical vibrocentrifuges sieves. *Bulletin of Kharkiv National Technical University of Agriculture. Series "Technical Science"*, Vol. 156, pp. 5-11.
21. Shen, H. H., Ackermann N. I. (1982). Constitutive relationships for fluid-solid mixtures. *J. Eng. Mech. Div.*, Vol. 108, pp. 748-763.
22. Zbiciak, A., Kozyra, Z. (2014). Dynamics of multi-body mechanical systems with unilateral constraints and impacts. *Procedia Engineering*, Vol. 91, pp. 112-117, <https://doi.org/10.1016/j.proeng.2014.12.024>



The aim of the MANUFACTURING conference is to review the state of knowledge, present the results of scientific work, implementations and innovations, as well as to provide an international forum for the dissemination and exchange of experience in the field of design and machines building, manufacturing technologies, metrology, rapid prototyping and virtual reality as well as management and production management.

Additional goals of the MANUFACTURING conference are the integration of the scientific community with the economic environment, enabling the establishment of cooperation with partners from industry and business, as well as with domestic and foreign research and development centers.

The conference will be held in a traditional form.

There are two options for submission:

- a) **Full Paper** submission (oral or poster presentation during the conference, paper publication);
- b) **Extended Abstract** submission (oral or poster presentation, without paper publication).

**Paper submission deadline: November 3rd, 2023**

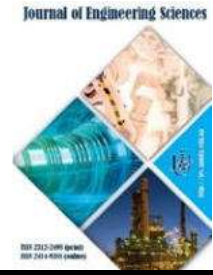
The conference proceedings will be published by **Springer** as **Lecture Notes in Mechanical Engineering** series. They will be submitted to, among others, **Web of Science**, **SCOPUS** and **Google Scholar**.



Faculty of Mechanical Engineering



PUT Foundation



## A Scheduling Model in Capturing Methane Gas from Methane Clathrates Deposits

Anyanwu U. O.<sup>1</sup>, Okafor O. C.<sup>2\*</sup>, Nkwor C. A.<sup>1</sup>

<sup>1</sup> Department of Mechanical Engineering, Federal Polytechnic Nekede, Owerri, Imo State, Nigeria;

<sup>2</sup> Department of Mechanical Engineering, Grundtvig Polytechnic, Oba, Anambra State, Nigeria

### Article info:

Submitted: December 15, 2022  
 Received in revised form: February 2, 2023  
 Accepted for publication: February 14, 2023  
 Available online: February 17, 2023

### \*Corresponding email:

[obiora.okafor@grundtvigpolytechnic.com](mailto:obiora.okafor@grundtvigpolytechnic.com)

**Abstract.** The execution of any project type, especially engineering-based projects, is usually time-based, efficiency-driven, and cost-effective. These factors are the deterministic parameters that engineer successful project completion. The application of scheduling models remains the best technique for achieving these three factors to their best degrees. Therefore, this study was centered on the impact study of applying the scheduling model in harvesting methane gas from methane clathrates deposits. Various data on gas hydrate reserves in the Niger Delta region of Nigeria were collected from relevant literature, studied, and analyzed. Such data includes the pictorial representation and description of the gas hydrate site in the Niger Delta region of Africa and various shapes and sizes of gas hydrate perimeters in the studied region positions of the gas reserves. The normal faults are projected on a bathymetric map of the study area and the bathymetric map of the Pockmark (with the stippled black line indicating the sea floor projection of a prominent N-S trending fracture in 3-D seismic data). As a type of scheduling model, the critical path method (CPM) was applied to develop the project's work sequence using the activity on node (AON) architectural technique and Primavera P6 software after carefully identifying the primary operations involved in the project and their respective sub-operations or work breakdown structure (WBS). The risks associated with each operation were meticulously identified, with their consequent impact and exposure matrix determined using probabilistic measures of 1-5 according to the degree of the risk. Mitigation strategies were recommended for all the identified risks. The cost benefits of the project were X-rayed using parameters such as net present value (NPV), project payback time, internal rate of return (IRR), and net cumulative cash flow. From the results obtained, the CPM schedule showed that the project execution would last approximately ten months. All the operations involved in the project execution plan were all critical, proving that each activity should be completed within the scheduled run period. Else, the entire project would be affected. Also, risks with a high exposure matrix of 25, 12, and 4 were mitigated to 5, 3, and 0 using the recommended strategies. In addition, the project yielded an NPV of \$20,736,951.04 for the run period of 22 years after the execution of the project, IRR of 14 %, and a payback time of 8 years (adding 2023- the year of project execution) provided the daily production rate is maintained within 60,000-65,000 MSCF/day. The cash flow and payback time will decrease if the daily production rate increases. Therefore, the application of CPM in extracting methane gas from gas hydrates positively affected the operation through the vivid insights provided in workflow pattern/methodology risks effects and cost benefits.

**Keywords:** operations research, critical path method, gas hydrate, project scheduling, risk management, cost analysis, energy efficiency.

## 1 Introduction

Gas hydrates are also called methane hydrates or, chemically, clathrates. As defined by [1], gas hydrates are ice-like crystalline lattices formed by combining water and methane molecules at low temperatures and high pressures. Large reserves of gas hydrates can be found under continental shelves and on land under permafrost. The percentage of organic carbon in gas hydrates is esti-

ated to be twice that in all other fossil fuels combined. The presence of gas hydrates in oceanic sediments was first postulated based on seismic observations. According to some estimates, gas hydrates represent one of the world's largest untapped energy reservoirs and have the potential to meet global energy needs for the next 1,000 years. Gas hydrates include combustible matter and are potentially one of the most critical energy resources for

the future. Gas hydrates are of considerable interest because of their potential as an energy resource and potential role in global climate change. Gas hydrates majorly contain methane gas. Methane is a thermogenic gas formed by decomposing organic matter due to geothermal heat and/or pressure [2].

Some developing countries that are seriously bedeviled by energy challenges stemming from electricity generation to heating and ventilation systems have huge reserves of gas hydrate that are untapped. For example, the Niger Delta region of Nigeria, which occupies the central part of West Africa's Gulf of Guinea, with a land area of about 75,000 km<sup>2</sup>, forms Africa's most extensive delta system. Its continental shelf holds a deposit of gas hydrate. The gas hydrate deposit in this region is primarily biogenic (formed by biological means). However, small amounts are thermogenic (heat-induced biological process) in nature. According to [3], the clathrates in this region have 99 % methane formation statistics up to the depth above 1500 m below sea level. This statistic proved that methane gas content's potential in clathrates is enormous. Exploiting methane gas from clathrates will in no small way boost the energy of Nigeria, since it is a sustainable energy source.

Applying the project scheduling technique (PST) in evaluating project cost and detailed planning for the execution of a project is a very imperative technique that should be used in the methane extraction process from gas hydrates [4]. PST also called network technique (NT) or network analysis (NA), entails a group of techniques for presenting information relating to time and resources to assist in planning, scheduling, and controlling projects. The info usually represented by a network includes the sequences, interdependencies, interrelationships, and criticality of various project activities. The three network techniques often used are the critical path method (CPM), program evaluation and review technique (PERT), and resource allocation and multi-project scheduling (RAMPS). But, CPM and PERT are considered the most convenient for application to various engineering projects.

Knowing the methane potential in Niger Delta region in Sub-Saharan Africa, it is crucial to demonstrate a workable network structure that details the cost-effectiveness of the project, risk analysis, list of activities to be performed, and their flow sequence. Therefore, this study focused on applying project scheduling in extracting methane gas from gas hydrate using the Niger Delta region in Sub-Saharan Africa as the case study. The cost-effectiveness of the extraction operation, risk analysis, and work plan modeling were carried out using CPM, risk analysis and decision criterion structure (RADCS), and Primavera 6. The data used for this research was obtained from the studies of many scholars on the existing Pockmarks described to have an approximately 600 m wide seafloor depression in deep waters situated in the Niger Delta zone offshore Nigeria. According to [5], pockmarks are subcircular or circular, or elliptical seafloor depressions known from shallow to deep-water areas worldwide. They can equally be regarded as craters (circular pits or depressions) in the seafloor caused by erupting gas or liquid. Pockmarks exist in diametric forms (tens to thousands of meters) and seafloor morphologies.

## 2 Literature Review

Many studies have employed project scheduling models to reveal the significant impact of PST applications in project planning and execution. Researchers [6] applied the project scheduling techniques in a real-life environment. They employed the CPM and PERT techniques in scheduling a project that aimed at expanding the production capacity of pure water at the Vlaamse Maatschappij voor watervoorziening (VMW) in Belgium. They proved that net present value (NPV) is schedule dependent. Their study showed that CPM and PERT had deficiencies in yielding their desired NPV. Hence they proposed some schedules that were combinations of the two. This led to the maximization of the NPV of the project under the restriction that each activity must have a certain amount of slack, if possible. In work [7], a study was carried out on a multi-agent system with application in project scheduling. They analyzed the implementation of a multi-agent system (MAS) considering two scheduling problems: time-constrained project scheduling problems (TCPS) and resource-constrained project scheduling problems (RCPS). They, therefore, developed and proposed an improved belief, desires, and intentions (BDI) based model. The model performed accurately from their findings. In addition, researchers [8] studied on aleatory uncertainty quantification of project resources and its application to project scheduling. Owing to the scanty literature on the uncertainty analysis of resource acquisition in project management, they employed the reliability theory to fill the literature gap through a take on a success-oriented view of acquiring the required resources for completing a project. They constructed the reliability block diagram (RBD) to quantify the aleatory uncertainty in resource acquisition by considering the supply of and demand for every resource and the probability that the resource is available when it is required. They also developed a new schedule sensitivity index which accounts for uncertainty in both time duration and resource acquisition of project activity. The effectiveness of the newly developed index in evaluating the relative importance of activities in stochastic project networks was also assessed. The result of their study showed that the new index yielded better performance due to its ability to capture uncertainty in both time duration and resource acquisition of project activity.

## 3 Research Methodology

### 3.1 Materials and tools

The materials and tools used in this study were essentially the gas hydrate reserve data obtained from the study site- Niger Delta region in Sub-Saharan Africa, analytical software (Microsoft Excel 2019 version), and project modeling software (Primavera 6). The extracted data from relevant literature includes the pictorial representation and description of the gas hydrate site in the Niger Delta region, various shapes and sizes of gas hydrate perimeters in the studied region, positions of the gas reserves, and the normal faults projected on a bathymetric map of the study area, the bathymetric map of the Pockmark and the methane gas constituent data.



Figure 1 depicts the photographic views of Pockmarks situated in the study site with clearly defined positions.

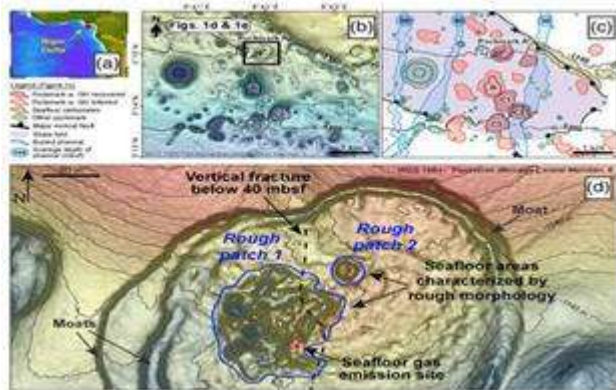


Figure 1 – Photographic views of Pockmarks: a – location of the pockmark field at the study site [5]; b – various shapes and sizes of Pockmarks; c – positions of the gas reserves and normal faults projected on a bathymetric map of the study area; d – the bathymetric map of the Pockmark [9]

Figure 1 a shows the study area where gas hydrate volume content is of the essence, and it is located at the West Africa margin continental slope off Nigeria in the transitional detachment zone of the Niger Delta. The area comprises a subcircular depression, called Pockmark, that is situated in the North-South extension of approximately 590 m and West-East of approximately 490 m, as shown in Figure 1 b-e.

The identified Pockmarks have gas hydrates widely distributed in a sediment body down to a depth of 34 mbsf at maximum [9-11]. Gas hydrates with gas-filled macro-pores in shallow sediments of the “Rough Patch 1” [9] point to their rapid formation from gaseous methane [12, 13].

In addition, Figure 2 shows the six pressure core areas of the studied site with the potential for methane gas hydrate reserves.

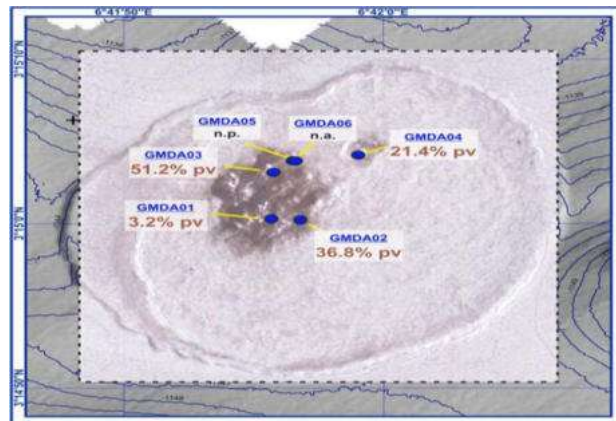


Figure 2 – The identified six pressure cores in the study site

The six pressure cores (GMDA01, GMDA02, GMDA03, GMDA04, GMDA05, and GMDA06) of methane gas hydrate are shown in their respective gas analysis results in Table 1.

Table 1 – Accumulated gas volumes, gas-sediment ratios (at ambient pressure), methane concentrations (average porosity 83 %), and calculated fractions of hydrates in sediment cores recovered by pressure coring (GHSat<sub>tr</sub>) [5]

DAPC core code	Core recovery, m	Total vol. of gas released, L	Volumetric gas-sediment ratio, total core, L/L	Conc. CH <sub>4</sub> total core, mol/dm <sup>3</sup>	Core vol. below sulfate zone, L	Hydrate saturation (sf) in pore vol. below sulphate zone GHSat <sub>tr</sub> , %
GMDA01	1.75	52.62	5.63	0.28	7.75	3.2
GMDA02	0.73	59.15	16.52	0.83	0.91	36.8
GMDA03	1.04	282.15	54.44	2.73	3.58	51.2
GMDA04	2.36	342.90	27.19	1.36	9.94	21.4
GMDA05	2.44	4.82	0.37	0.02	6.36	N/P**
GMDA06	2.05	4.10	0.37	0.02	N/A*	N/A
Average:						31.4

\* N/A– not analyzed; \*\* N/P – not presented.

### 3.2 Project scheduling assumptions

The scheduling of methane gas extraction processes of the identified six pressure cores of the test site from clathrates and analysis (cost and risk impacts) was based on the following assumptions.

1. The chosen technology proves to be a significant success.
2. Gas production rates were estimated from data obtained from gas wells in the same region.
3. Climatic conditions remain favorable over the project’s lifetime.
4. Tax, royalty, and discount rates do not change.
5. Gas obtained from the hydrates are primarily dry gases; no liquid is produced during production.
6. Contractors and staff contracts are renewed yearly with no salary increase.
7. Stability in gas prices fixed to a particular value and applied during costing.

Royalties will be taken as a variable operating cost and remain constant for the project.

### 3.3 Depressurization operation

Due to the cost and technological complexities involved in exploring gas hydrates, such as water circulation and carbon(iv)oxide injection, the depressurization method was employed in this scheduling project/study. The operation includes seismic analysis, drilling, engineering constructions, and extract distribution. The seismic analysis involves a mapping study to confirm the area has a large hydrate reserve.

Preparation of the rig site, suggestion/recommendation of the possible fluid type to be used in the drilling process, etc., are involved in the drilling and engineering phase of the work. Lastly is the methane gas distribution to purification points using fluid conveyors and pump drive systems.

Methane gas extraction operations done by depressurization were modeled using the CPM tool, as shown in

Figure 3.

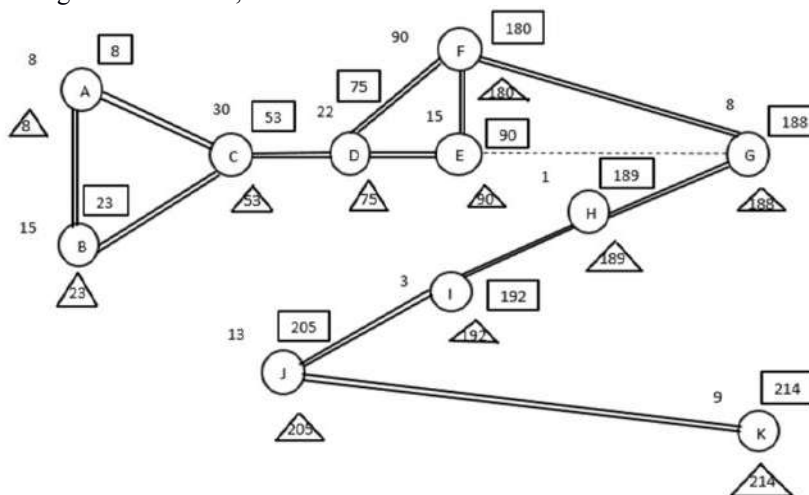


Figure 3 – Project scheduling using the CPM tool

From Figure 3, the project would last 214 working days as derived from the CPM scheduling model. The numerals without enclosures are the scheduled number of days the particular operation is expected to last, numerals with a rectangular enclosure represent the earliest finish time of the activity, and numerals with triangular enclosures are the latest finish time of the project. All the activities have double thick lines, representing the project's critical paths, while the thin broken lines show the dummy path

of the project flow. At the critical path, the earliest and latest finish times are equal, implying that the slack is zero and that each of the stated activities must be completed within the scheduled time. Otherwise, the project will be delayed beyond its completion time. The activities are represented with alphabets (A, B, C, D, E, F, G, H, I, J, and K) and enclosed with circles.

Table 2 shows the project description in detail.

Table 2 – The schedule of methane gas extraction from gas hydrates (Project name: GAS HYDRATE P006)

Major Operations	Sub-operations/work breakdown structure (WBS)	WBS, days
A: Premobilization/mobilization	Premobilization of all equipment	2
	Mobilization of personnel	2
	Mobilization of materials, tools, and equipment	4
B: Site preparations	Bush clearing of the site	3
	Excavation using heavy-duty machinery	5
	Building of tent structures for workers	3
	Electrification of the site	2
	Tent equipped with essential tools and materials	2
C: Seismic study	Mapping out the identified six pressure cores	9
	Data acquisition from the site	10
	Processing of the collected data using deconvolution, stacking or migration technologies	7
	Interpretation of the processed data	4
D: Good design and analysis	CAD modeling of the well	10
	Functional specifications	4
	Design of the drilling program	5
	Completion program design	3
E: Procurement of materials	Collection of quotations from suppliers	3
	Interaction with a few suppliers	2
	Decision and awarding of the supply contract	2
	Supply and inspection of items	8
F: Drilling and installation of good fittings	Metal casing construction for the well	10
	Installation of the drill casing	2
	Drilling	50
	An influx of fluid during the drilling operation	4
	Cementing work on the well	7
	Installation of tube structure into the drilled well	6
	Removal of the drilling pipes	2
	Installation of the blow-out preventer device (BOP)	5
	Installation of the wellhead for methane gas distribution	4
	G: Piping installation and RT	Installation of pipe networks to the Christmas tree
Installation of the needed fittings to the pipe		3
RT on all welded joints		1

Major Operations	Sub-operations/work breakdown structure (WBS)	WBS, days
H: Mechanical checks	Check all the piping connections, including the flanges (Torquing), pumps, etc.	1
I: Commissioning	Pressure test the piping network	3
J: Product movement	Movement of the extracted methane gas to the point of refining	13
K: Closeout/demobilization	Documentations- submissions of the reports etc.	7
	Demobilize all equipment	1

Table 3 clearly shows the duration summary of methane gas extraction from the gas hydrate project. The project was scheduled without consideration of uncertainties like public holidays, strikes, machine damages, etc. This is peculiar to the CPM technique, as it doesn't factor into consideration project uncertainties. But such uncertainties could be balanced off with the excluded days of the month (Saturdays and Sundays) to meet up with the earliest finish date of the project.

### 3.4 Project cost analysis

The project comprises capital cost analysis (CAPEX) and operating cost analysis (OPEX). The formulae, gas rates, and other parameters employed in the cost calculations were derived from [africaoilgasreport.com](http://africaoilgasreport.com), which used Nigeria as the case study.

Table 3 shows the applied factors which determine the project's cash inflow and cash outflows.

The capital cost analysis of the project is shown in Table 4.

Table 3 – Payable rates for the project execution ([africaoilgasreport.com](http://africaoilgasreport.com), 2021)

No.	Factors	Rate, %
1	Tax rate	30.00
2	Royalty rate	7.50
3	Discount rate	14.00
4	Inflation rate	3.45

The capital cost essentially comprises the cost of drilling one gas well (with all its accessories/components fitted) and the cost of LNG tanker for transporting extracted methane gas. Also, 30 % of the initial investment cost was used for risk contingencies. The total capital cost was derived by adding the initial investment cost to the 30 % risk contingency plan.

This cost analysis entails the fixed costs of the project execution processes. Table 5 shows the operating cost analysis of the project.

Table 4 – Capital cost analysis (CAPEX)

Operations	Specification	Unit Cost, USD	Total Cost, USD
Gas well drilling and installation of all its fittings/components	6 wells	25 million	150 million
LNG tanker (1)	29 tons (51,000 liters) capacity	70,200	70,200
Initial investment:			150,070,200
Contingency for risk at 30 % of initial investment:			45,021,060
Total CAPEX:			195,091,260

Table 5 – Operating cost analysis (OPEX)

Factors	Specification	Unit Cost, USD	Total cost, USD
Personnel salaries	15 permanent staff for 10 months	500 per month for each staff	75,000
Contractor salaries	20 contractors for 10 months	4000 per month for each staff	800,000
Maintenance cost of equipment	All machinery	2000 per month	20,000
Total fixed OPEX:			89,500 per month
			895,000

The derivation of the payback time of the project was obtained through a meticulous computation and analysis of some cost parameters like revenue, taxable income, tax paid, net cash flow (NCF), discount factor (DF), present

value (PV) and net current value (NPV). The formulae used in computing these parameters for 10 months are given thus:

$$\text{Revenue} = \text{avg. daily production rate} \left( \frac{\text{MSCF}}{\text{day}} \right) \times \text{gas price} \times 365 \text{ days}; \quad (1)$$

$$\text{Taxable income} = \text{revenue} - (\text{fixed cost} + \text{variable cost}); \quad (2)$$

$$\text{Tax paid} = \text{tax rate} \times \text{taxable income}; \quad (3)$$

$$\text{Net cash flow} = \text{Taxable income} - \text{Tax paid}; \quad (4)$$

$$\text{Discount factor} = (1 + r)^{-t}; \quad (5)$$

$$\text{Present value} = \text{Discount factor} \times \text{net cash flow}; \quad (6)$$

$$\text{Net present value} = \text{Sum of all present values} - \text{Initial investment}; \quad (7)$$

where r – the given discount rate; t – time in years.

### 3.5 Risk management

It is essential to carry out effective risk management for this project. This critical process helps plan a more realistic budget, identify possible alternatives, and ensure the project delivers its set goals. Hence, the project's risk management steps were used to determine the project threats and potential mitigation strategies.

Firstly, it is essential to identify any risk that could hinder the progress or completion of the project. This could be done in a round-table meeting of the management team alongside experts from different company divisions to ensure every section was duly covered. This storming session would further help prevent the team from limiting

its scope and dismissing risks prematurely. Risks were collected from different sources that could affect the project, including but not limited to organizational and management, economic, marketing, environmental, safety, and operational risks that could affect the project. All of these risks, after identification, were collected and recorded in the risk register form, as seen subsequently. As control measures were also taken, in trying to mitigate the risk, this risk register form was regularly updated.

Concerning the researched primary impact types, the impact types considered for this project include time, cost, safety, and environment. All of these have been highlighted in Table 6.

Table 6 – Impact estimate matrix

Severity	Primary Impact			
	Time	Cost, 1000 USD	Safety	Environment
Very High	> 6 months	> 2000	More than one fatality, including severe injuries	Maximum damage, including pollution to the environment
High	3-6 months	800–2000	One fatality, multiple minor and severe injuries	Serious damage, uncontrollable
Medium	3 months	200–800	No fatality, few minor and severe injuries	Minimal damage monitored and observed
Low	1-3 months	50–200	No fatality, few minor injuries	Little damage, put under control
Very Low	< 1 month	< 50	Zero fatality, zero severe injuries, zero minor injury	No damage to the environment of any sort

The risk exposure matrix was drawn up to help quantify each of the risks identified in the risk register. This will therefore help determine which risk to attend to first and the most suitable method to address such risk. Risk exposure was calculated simply by multiplication of the risk impact with the frequency of its occurrence (probability):

$$\text{Risk Exposure} = \text{impact} \times \text{Probability (frequency)}. \quad (8)$$

Another essential part of the risk management process is to lay out a mitigation plan or strategy for tackling the identified risks associated with the project model. Some techniques would be peculiar to individual risks. The aim of this step is also to employ the most cost-effective mitigation strategy in reducing individual risk exposure. Strategies such as: avoid, transfer, reduce and manage were all used depending on the risk type encountered.

Furthermore, it is imperative to continually monitor the risk to evaluate the efficiency/impact of the mitigation techniques put in place. Reviews like this end up aiding decisions on whether or not to abandon a mitigation strategy. Risk review also allows for opportunity response strategies to be looked into in the order of exploit, share, enhance, and ignore. Sharing the risk has proven to be a good tool for certain operations. Still, such cannot be applied due to the uncertainty surrounding the depressurization technology employed in this project modeling.

Primavera P6 version is an enterprise project portfolio management software. It includes project management, scheduling, risk analysis, opportunity management, resource management, collaboration, and control capabilities, and integrates with other enterprise software such as ORACLE and SAP's ERP system. The software tool was used to schedule the project's primary operations and the work breakdown structures to output the durations of

each activity, the start and finish dates of the project. Also, the software tool was equally employed to validate the critical nature of all the activities as given by the CPM architecture of figure 3. In addition, the sequential flow of operations is expected from the software's output through its GANTT chart for vivid comprehension of the pre and post activities of the project. This project was tagged, "Gas hydrate P006" in the software analysis. The parameters given in table 2 were used in preparing the schedule for the project.

## 4 Results and Discussion

### 4.1 Scheduling results using Primavera P6 software

The result of the project execution sequence performed with Primavera P6 software is vividly shown in Figures 4-5. The GANTT chart of the operations is also shown at the extreme right of Figures 4-5.

From Figures 4-5, the methane gas extraction operation from gas hydrates is expected to commence on January 9, 2023, and end on October 30, 2023. This implies that the project has an execution span of approximately ten months. The durations of each activity in the scheduling plan were also presented. In addition, the key activities of the project, as contained in the operation schedule, were: premobilization/mobilization, site preparations, seismic study, well design and analysis, drilling and installation of suitable fittings, piping installation, and radiographic testing (RT), mechanical checks, decommissioning, product movement, and close out/demobilization. The work breakdown structures (WBS)/sub-activities of these activities are shown equally in Figures 4-5. Radiographic testing (RT) is a non-destructive examination (NDE)

technique that involves using either X-rays or gamma-rays to view the internal structure of a component.

The GANTT chart shown at the extreme right of Figures 4-5 print the sequential flow of project operations and also indicates the critical nature of all the activities involved in the project. The red-colored GANTT chart indicates that all the operations are critical and that any delay in completing one activity would consequently affect the entire project. Each operation's zero float/slack values further validated the project schedule's critical nature. Also, from the GANTT chart, the black-colored lines indicate the summary of each operation. That is, it outputs the end period of the operation. The GANTT chart showed that the drilling work took the most significant percentage of the project execution duration. This was delineated by the long red rectangular bar from May 29, 2023, till August 4, 2023.

Furthermore, by meticulously following the project schedule shown in Figures 4-5, successful execution of

the project is assured. A failed project schedule results from poor adherence to the schedule plan and scope and univided description and comprehension of the project that necessitated the scheduling.

The identified risks associated with the project and their corresponding mitigation strategies are vividly outlined in Table 7. The probability boundary of the risk occurrence ranged from 1–5, and its impact on the project execution was also kept within 1–5. The risk exposures were computed by multiplying the probability and impact together.

From Table 7, the unmitigated risk is shown in the yellow and red colored columns. In contrast, the green colored column shows the mitigated risks – the result or the output of adopting the suggested risk mitigation strategies. A drastic drop in the risk exposure parameters could be observed from Table 7, hence endorsing a successful project completion following the planned schedule.

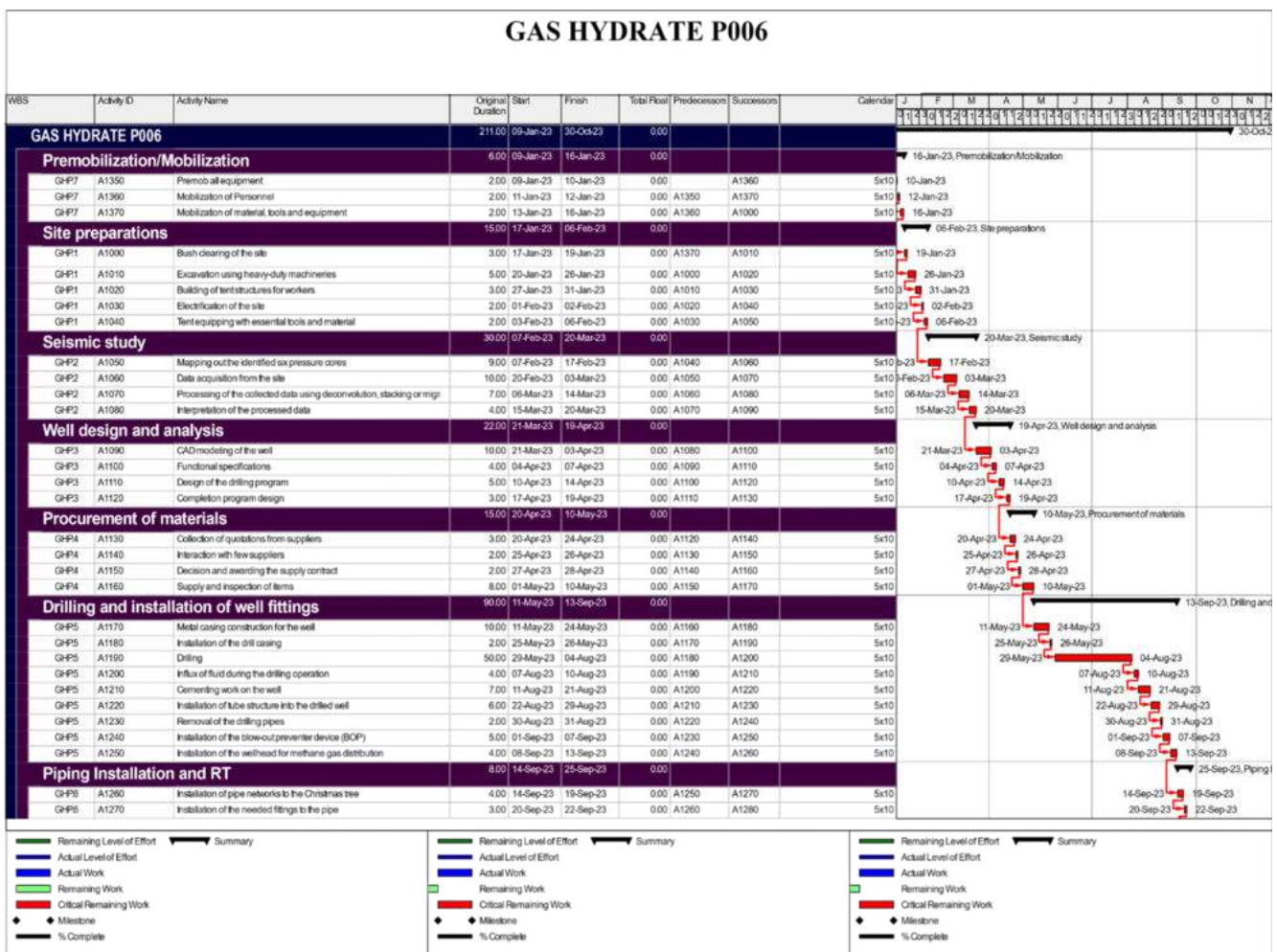


Figure 4 – Scheduling model of the project

## GAS HYDRATE P006

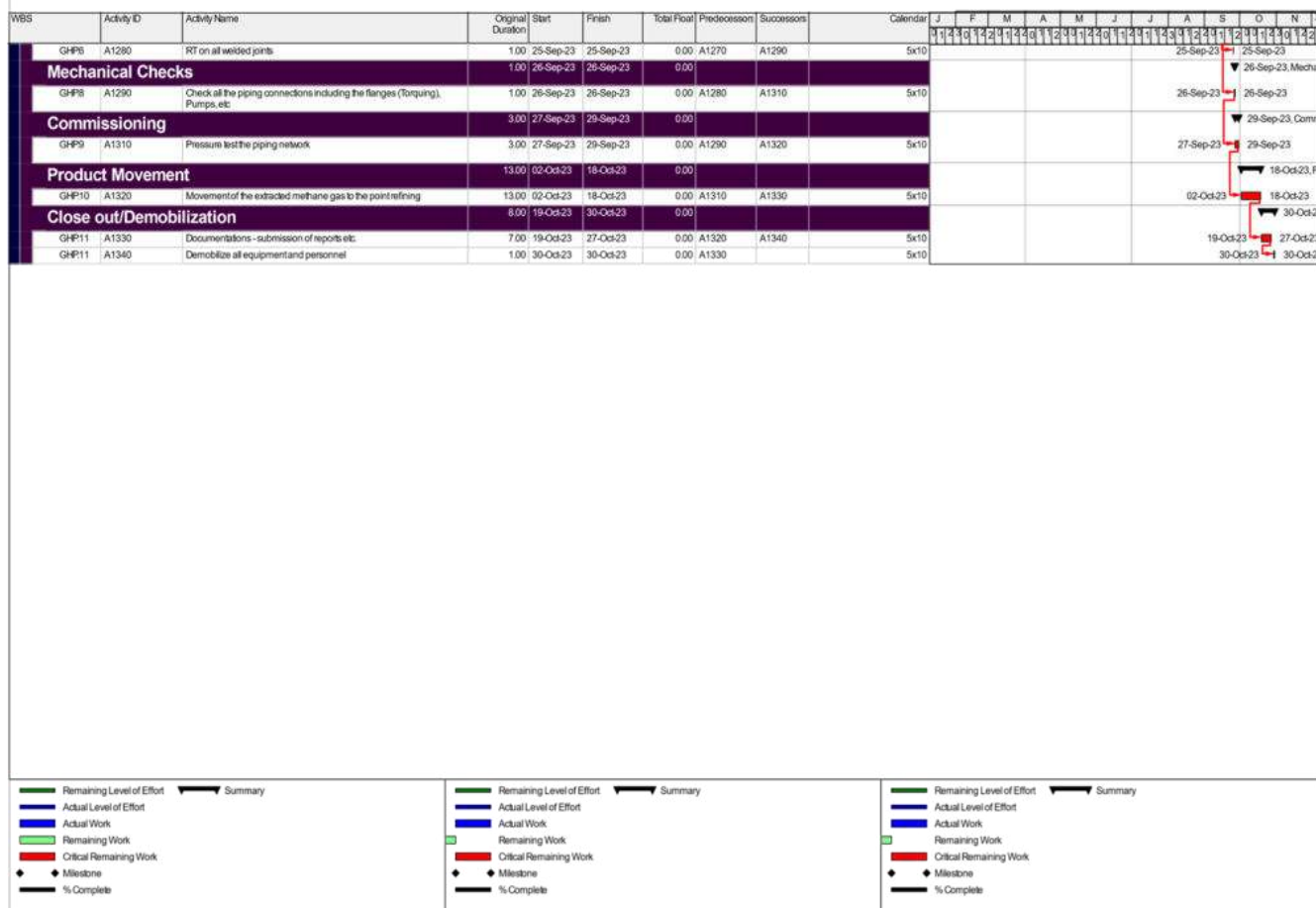


Figure 5 – The scheduling model of the project continues

Table 7 – Risk impact analysis

No.	Risk	Prob.	Imp.	Exp.	Mitigation	Prob.	Imp.	Exp.	By/when
<b>Project Framing phase</b>									
1	Misunderstanding of project objectives, resulting in the wrong framing process	1	5	5	Proper and detailed study and understanding of project aims and objectives	1	1	1	09/01/2023
2	Under or over-estimation of the project due to a lack of proper understanding of the depressurization method	3	3	9	External consultancy should be sought, and a comparison of budgets with in-house estimates	2	1	2	10/01/2023
3	Wrong selection of options during the option generation phase	3	4	12	Options should only be finalized after proper weighing of the pros and cons of each option	2	2	4	11/01/2023
4	The hiring of an incompetent and inexperienced workforce by the HR department	1	5	5	Proper screening and selection of qualified personnel with valuable experience	2	1	2	13/01/2023
5	Constant variation of project scope and inconsistency from framing team	3	4	12	The framing should be concluded only after detailed research has been done	4	1	4	15/01/2023
6	Members of the project team continually disagree with options generated at every stage	3	3	9	Any decision that warrants disagreement should be put to the vote after extensive analysis of the pros and cons	3	1	3	17/01/2023

No.	Risk	Prob.	Imp.	Exp.	Mitigation	Prob.	Imp.	Exp.	By/when
7	The company executives refuse to grant the project due to an unconvincing proposal	2	5	10	Proposals from previous projects should be sampled to identify what the executives need to see before granting the project	1	3	3	20/01/2023
<b>Project Appraisal phase</b>									
8	Failure to secure license due to inability to meet Japanese government requirements	5	5	25	The appraisal team must enquire about the license requirements and take all steps to meet them	1	4	4	23/01/2023
9	Japanese government increases the tax rate and amount of royalties to be paid	2	4	8	The team should factor this into estimation and set aside a sum from revenue for such scenarios	3	1	3	25/01/2022
10	Increase in cost and time of initial drilling of a gas well due to unfamiliar formation	3	3	9	The geology team should conduct exhaustive research on the formation, and the costing team should increase drilling cost by $\pm 5\%$ to cater for any uncertainty that might arise	2	1	2	27/01/2023
11	Delay in construction and delivery of FPSO vessel due to lack of raw materials and strike action by workers	3	5	15	FPSO construction should be done in a region of the world with sufficient raw materials and adequate and cooperative workers	1	3	3	30/01/2023
12	Poor scheduling by team resulted in improper management of resources and staff	5	4	20	Resource scheduling should be done as accurately as possible for effective resource management	2	2	4	02/02/2023
<b>Project Planning stage</b>									
13	Fluctuation of market gas price	3	4	12	The project team should draw up a sensitivity analysis using gas price changes to monitor revenue and cash flow differences.	1	1	1	04/02/2023
14	Nonavailability of clients to sell gas products to resulting in zero to low revenue and storage of excess gas products	5	3	15	Team should carry out aggressive marketing to attract enough clients to purchase gas	2	1	2	06/02/2023
15	Investors pull out of the project because of unproven technology	5	4	20	The project team should focus immensely on allaying the investors' fears by answering their questions satisfactorily.	1	1	1	09/02/2023
16	Failure to obtain clearance from environmental agencies due to paperwork complications	2	4	8	All paperwork should be submitted in duplicates or triplicates to get rid of any misunderstanding	1	2	2	12/02/2023
17	Inability to meet the supply demands of customers when production begins	3	3	9	Proper estimation of produced gas should be made to know the amount that will be available, avoiding disappointment	3	1	3	15/02/2023
<b>Execution and operation stages</b>									
18	Occurrence of the earthquake in the region resulting in damage to vessels and loss of lives	5	5	25	The vessel should be constructed with adequate technology that can withstand earthquakes	2	5	10	17/02/2023
19	Loss of containment on the vessel due to leakage of valves, excessive storage, or pressure loss.	4	4	16	Up-to-date monitoring of pressure gauges and stored gases should be sold to make space for more production, and engineers should constantly check safety valves and pipes	2	2	4	20/02/2023

No.	Risk	Prob.	Imp.	Exp.	Mitigation	Prob.	Imp.	Exp.	By/when
20	Failure of Depressurization technology due to inexperienced hands and lack of understanding of the process	4	5	20	Properly trained engineers hired initially alongside experts in the technology should be brought on board during the framing stage.	1	1	1	22/02/2023
21	Political instability in the region resulted in production hiatus	5	5	25	MoU, signed with the Japanese government to exclude the vessel and its operations from any form of political instability	1	2	2	24/02/2023
22	Presence of acid gases in produced gas results in extra processing	4	2	8	Chromatography tests should be conducted during the appraisal phase to account for the presence of acid gases in the gas, allowing for it to be catered for	3	1	3	26/03/2023
23	Failure of one or multiple wells during production as a result of sand production	3	5	15	Sand screens should be installed during well completions to help combat sand production	2	2	4	28/02/2023
24	Incurring fines as a result of waste spillage and unsatisfactory water treatment before flooding into the sea	2	5	10	Waste should be properly contained and treated before disposal; likewise, water should be treated in three (3) stages before flooding back into the sea	2	1	4	04/03/2023
25	Depletion of hydrate reserves quicker than initially expected	3	4	12	Provision should be made for decommissioning program to be possibly brought forward on the scheduling plan.	1	3	3	08/03/2023
26	Fire outage on the vessel	3	5	15	All firefighting and preventing systems should be properly installed, regularly tested, and maintained through frequent fire drills	2	1	2	14/03/2023
27	Damage to any processing equipment (compressor, drill bit, etc.)	4	3	12	Regular maintenance checks should be assigned to every piece of equipment, and faulty ones should be replaced immediately	3	1	3	17/03/2023
28	Delay in the transportation of gas to customers due to logistics	2	3	6	Issues regarding transportation should be identified, and backup plans created during the planning stage	1	1	1	20/03/2023
29	Emission of greenhouse gases during methane extraction and processing	4	4	16	Adopt processes that minimize the emission of these gases to the barest minimum, which must also meet agency requirements	2	2	4	22/03/2023
30	Loss of containment of stored gases as a result of liquid present in processed gases	2	4	8	Processing equipment should be adjusted to industry settings to ensure optimum performance, thus avoiding liquid carryover	1	2	2	26/03/2023
31	Investors begin to back out from the project due to it not making enough profit in the first year	4	5	20	The economics of the project should be presented to investors, identifying that the profits would still come later in the project's life	2	2	4	28/03/2023



## 4.2 Result of the risk impact analysis and mitigation strategies

A vivid pictorial visualization of the unmitigated and mitigated risk matrices is shown in Figures 6 a-b.

From Figure 6a, the risk matrix further explains that risks in the top right-hand corner with the red color re-

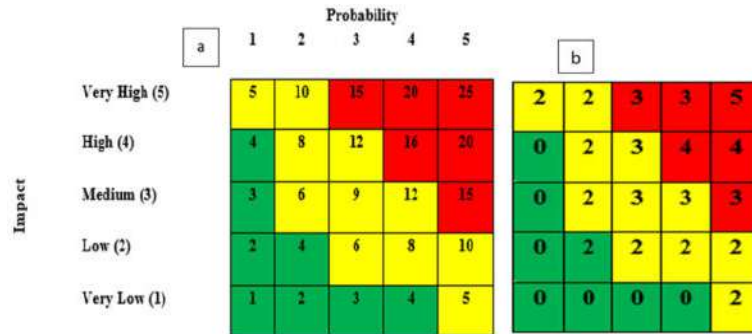


Figure 6 – Unmitigated (a) mitigated (b) risk matrices

Also, Figure 6b shows a spontaneous drop in the risk exposure matrix as a result of the application of the risk mitigation strategies. The most critical risks (red-colored cells) with a very high impact value of 25 were dropped to a minimum of 5. At the same time, the other risk matrices (yellow and green) were dropped from 12 and 4 to 3 and 0, respectively.

## 4.3 An impact of CPM scheduling on the project: Cost studies

The cost benefits of the application of the project scheduling (CPM) technique in the extraction of methane gas from gas hydrate reserves are determined or measured with some parameters such as net present value (NPV), the yielding time or payback time of the project and cash flow rate and internal rate of return (IRR). The results of these cost-deterministic parameters are vividly presented in Figures 7-11.

Figure 7 shows the variations in the generated revenue as the gas production rate changes. The revenues depicted in Figure 7 are only possible if the gas production rate is maintained between 60,000 to 65,000 MSCF/day. The revenues were also determined by fixing the gas price at \$2.073/MSCF.

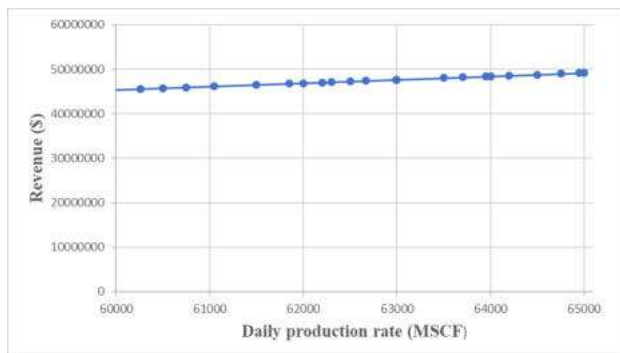


Figure 7 – Plot of revenue against daily production rate

From Figure 7, it can be observed vividly that as the daily production rate increases, the revenue also increases. This implies that there is a linear relationship between revenue and production rate.

quire urgent attention and cannot be accepted until they have been adequately dealt with to a manageable level.

Risks in the mid-region (shown in yellow) require attention only after the more urgent risks. The risks in the green zones represent tolerable risks that require minimal to zero mitigation.

Through a meticulous execution of the schedule plan obtained from the CPM analysis, the production is expected to start in 2024 and yield profits in 2030, hence a payback time of 8 years (adding 2023 – the year of project execution). This is shown in Figure 8.

From, Figure 8, a break-even is observed in 2030 when the operation enters profit in addition to the proportional increase in cash flow as the production year increases.

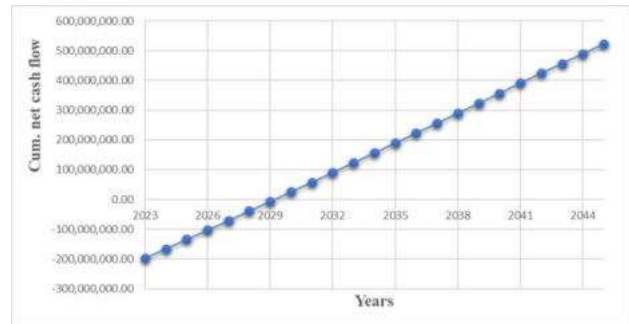


Figure 8 – Plot of cumulative net cash flow against years

This is only possible if the CPM scheduling is well applied (note that CPM assumes all operational and external variables to be efficient, giving no room for uncertainties).

The cash flows within the 22 years of production operation and the cash outflow in 2023 during the project execution phase are delineated in Figure 9.

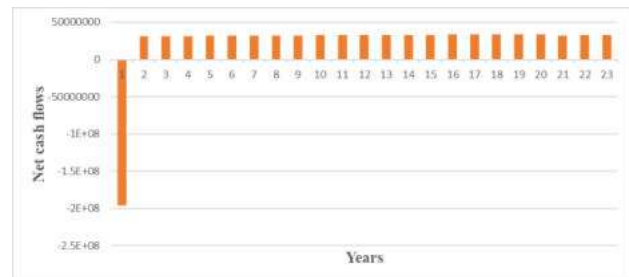


Figure 9 – Plot of net cash flows against years

Figure 9 shows that the cash inflows from year 2, 2024, to year 23 (2045) are approximately in the same

range for a production rate maintained between 60,000-65,000 MSCF/day.

Figure 10 depicts the plot of cumulative cash flow for a number of years.

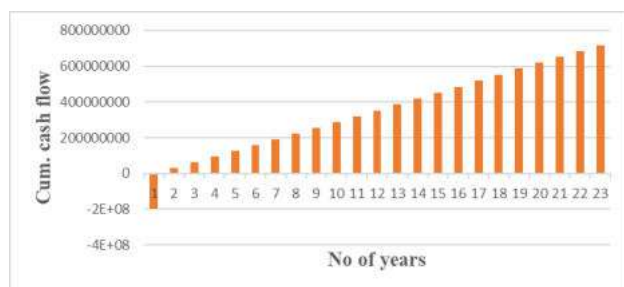


Figure 10 – Cumulative cash flow against a number of years

From Figure 10, the production operation appears to be efficient, as indicated by the excellent linear increment in the cash flows as the year increases. In addition, the net present value (NPV) obtained by subtracting the total current values (PV) from the initial investment sum of \$195,986,260.00 was derived from \$20,736,951.04 for the run period of 22 years after the execution of the project. This derived sum of NPV would increase as the run period increases, keeping all other production variables and the CPM scheduling plan fixed without any variations. In addition, the safety of this project is also assured and guaranteed by the value of the internal rate of return (IRR). IRR value is derived from the plot of NPV against discount rate, and the value is gotten at the point where NPV value is 0.

Figure 11 delineates the graphical plot of NPV against the discount rate.

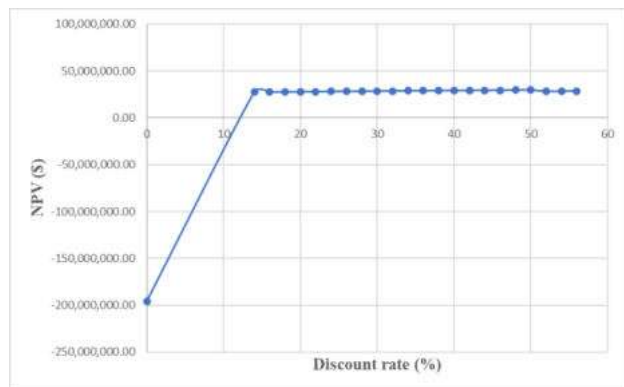


Figure 11 – Plot of NPV against discount rate

From Figure 11, the IRR value is derived from being 14%. This is, therefore, good for the project as it implies a faster rate for the project to break even and enter profit. From a 14–58% discount rate, an almost constant NPV is observed. This gives the value of NPV for the project, derived as \$20,736,951.04 for the run period of 22 years after the execution of the project.

## 5 Conclusions

The impacts of the scheduling technique in extracting methane gas from gas hydrates have been demonstrated in this study. It proved efficient to be used in any other projects requiring timely completion and efficient utilization of the available project resources. The project scheduling technique is a subset of operations research where project goals are met through careful design, description, comprehension, and application of scheduling models for the efficient execution of projects. The CPM schedule expressed that the project execution would last for approximately ten (10) months, from January 9, 2023, to October 30, 2023. All the operations involved in the project execution plan were critical, proving that each activity should be completed within the scheduled run period. Else, the entire project would be affected.

Furthermore, several identified risks that would hinder or affect the project were identified and appropriately mitigated using several strategies. Risks with a high exposure matrix of 25, 12, and 4 were mitigated to 5, 3, and 0 using the recommended strategies. This, therefore, ensured an efficient and timely completion of the project. In addition, the project yielded an NPV of \$20,736,951.04 for the run period of 22 years after the execution of the project, IRR of 14%, and a payback time of 8 years (adding 2023- the year of project execution) provided the daily production rate is maintained within 60,000-65,000 MSCF/day. If the daily production rate increases, the cash flow increases, and the payback time will decrease. In other words, the daily production rate determines the NPV, payback time, IRR, and cash flow rate value. The business model is safe once a linear relationship exists between the daily production rate and the deterministic cost factors – NPV, revenue, and cash flow rate. The application of CPM in extracting methane gas from gas hydrates positively affected the operation through the vivid insights provided in workflow pattern/methodology risks effects and cost benefits.

## References

1. Ayhan, D. (2017). *Methane Gas Hydrate*. Springer, New York.
2. Wilson, S., and Mortimer, S., (2020). Methane gas hazard. *Geological Society of London*, Vol. 29, pp. 457-478.
3. Francis, C., Nikolaus, B., Elke, K., Mathias, H. (2020). Methane production from gas hydrate deposits through injection of supercritical carbon(iv)oxide. *Energies*, Vol. 5, pp. 2112-2140.
4. Banga, T. R., Sharma, S. C. (2013). *Industrial Engineering and Management Including Production Management*. New AS Offset Press, Delhi, pp. 760-799.
5. Pape, T., Ruffine, L., Hong, W. L., et al. (2020). Shallow gas hydrate accumulations at a Nigerian deepwater pockmark – Quantities and dynamics. *Journal of Geophysical Research: Solid Earth*, Vol. 125, pp. 1-26.
6. Mario, V., Erik, D. (2017). The application of project scheduling techniques in a real-life environment. *Project Management Journal*, Vol. 34(1), pp. 30-42.

7. Nicoleta, C. B., Ruxandra, I. B., Radu-Loan, M. (2017). A multi-agent system with application in project scheduling. *Journal of Management and Marketing Challenges for Knowledge Society*, Vol. 6(4), pp. 573-590.
8. Seyed, A. Z., Jantane, D. (2021). Aleatory uncertainty quantification of project resources and its application to project scheduling. *Reliability Engineering and System Safety*, Vol. 211, pp. 1-15.
9. Sultan, N., Bohrmann, G., Ruffine, L., Pape, T., Riboulot, V., and Colliat, J. L. (2014). Pockmark formation and evolution in deep-water Nigeria: Rapid hydrate growth versus slow hydrate dissolution. *Journal of Geophysical Research: Solid Earth*, Vol. 119, pp. 2679-2694.
10. Wei, J., Pape, T., Sultan, N., Colliat, J.-L., Himmler, T., and Ruffine, L. (2015). Gas hydrate distributions in sediments of Pockmarks from the Nigerian margin – Results and interpretation from shallow drilling. *Marine and Petroleum Geology*, Vol. 59, pp. 359-370.
11. Taleb, F., Garziglia, S., and Sultan, N. (2018). Hydromechanical properties of gas hydrate-bearing fine sediments from in situ testing. *Journal of Geophysical Research: Solid Earth*, Vol. 123, pp. 9615-9634.
12. Bohrmann, G., Greinert, J., Suess, E., Torres, M. (1998). Authigenic carbonates from the Cascadia subduction zone and their relation to gas hydrate stability. *Geology*, Vol. 26(7), pp. 647-650.
13. Torres, M. E., Wallmann, K., Tréhu, A. M., Bohrmann, G., Borowski, W. S., Tomaru, H. (2004). Gas hydrate growth, methane transport, and chloride enrichment at the southern summit of Hydrate Ridge, Cascadia margin off Oregon. *Earth and Planetary Science Letters*, Vol. 226(1-2), pp. 225-241.



Sokolov S. (2023). Optimization of greenhouse microclimate parameters considering the impact of CO<sub>2</sub> and light. *Journal of Engineering Sciences*, Vol. 10(1), pp. G14-G21, doi: 10.21272/jes.2023.10(1).g2

## Optimization of Greenhouse Microclimate Parameters Considering the Impact of CO<sub>2</sub> and Light

Sokolov S.<sup>1</sup>[0000-0001-8707-4616]

<sup>1</sup> Sumy State University, 2, Rymskogo-Korsakova St., 40007 Sumy, Ukraine

### Article info:

Submitted: March 9, 2023  
 Received in revised form: May 5, 2023  
 Accepted for publication: May 12, 2023  
 Available online: May 16, 2023

### \*Corresponding email:

[s.sokolov@ksu.sumdu.edu.ua](mailto:s.sokolov@ksu.sumdu.edu.ua)

**Abstract.** The most critical parameters of the microclimate in greenhouses are air and soil temperature, air and soil moisture, plant illumination, and carbon dioxide (CO<sub>2</sub>) concentration in photosynthesis. New energy sources and resource-efficient management of microclimate parameters in greenhouses can be utilized to reduce greenhouse crop cultivation costs and increase profits. As the plant mass increase depends on photosynthesis, which involves the formation of glucose in the plant chloroplasts from water and carbon dioxide under the influence of light radiation, the saturation of greenhouses with carbon dioxide has become popular in recent decades. However, insufficient light slows down the process of glucose formation, while excessive light intensity negatively affects photosynthesis. Based on the experimentally proven Van Henten model of plant growth and using the MATLAB environment, a methodology was proposed, and the dependence between CO<sub>2</sub> concentration and leaf lettuce illumination power required for maximum photosynthesis was determined. It is equal to 0.57 ppm/(W/m<sup>2</sup>). Such dependence should be considered when designing control systems to reduce resource and energy costs for greenhouse crop cultivation while ensuring maximum yield.

**Keywords:** greenhouse gas, illumination, greenhouse effect, photosynthesis, energy efficiency, process innovation.

## 1 Introduction

The increasing population on Earth has led to a rise in demand for food products. However, using only natural conditions for crop cultivation is becoming insufficient. Therefore, the issue of growing crops in artificial conditions such as chambers and greenhouses is becoming more pressing. This allows for the cultivation of exotic crops and protects plants from adverse external climatic conditions in the winter and spring periods. The latest instruments and technologies expand the possibilities of achieving high yields. There are several directions in the pursuit of increasing yields, from developing genetically modified varieties, new disease and pest control methods and creating optimal conditions for plant growth. These achievements are effectively realized during plant cultivation in greenhouses. Additionally, creating favorable conditions for plants during greenhouse farming not only contributes to an increase in the yield of crops but also affects their quality. Such plant growth improvement is due to maintaining specific microclimate parameters in the greenhouse.

Most of the scientific research is focused on studying the impact of various factors on plant growth. These studies primarily identify qualitative dependencies, optimize control parameters, and various mathematical models. An essential task of horticultural engineering is optimal control of the microclimate parameters of the greenhouse. Such a task should not be based on intuition and results obtained from numerous experiments during plant cultivation. Instead, it should rely on certain principles of scientific optimization theory. Applying the optimal control theory allows for determining strategies for controlling microclimate parameters in greenhouse farming.

It should be noted that plant growth occurs through photosynthesis, which is a chemical reaction involving the formation of sugars from carbon dioxide and water in the presence of light. This reaction occurs in the leaves of plants, which are like small factories that use energy from the sun to produce food. Therefore, understanding the factors influencing photosynthesis is crucial for optimizing plant growth in greenhouses.

## 2 Literature Review

The process by which plants form sugars from water and carbon dioxide in the presence of light in chloroplasts is referred to as photosynthesis. During this process, free oxygen is released into the atmosphere. Despite its lack of color and odor, carbon dioxide is essential for maintaining life on Earth, with its concentration in the atmospheric air being approximately 0.004 % by volume or 400 parts per million (ppm). Although plants consume carbon dioxide during photosynthesis and release it during respiration, they consume much more gas than they exhale, creating a deficit of CO<sub>2</sub> in the air that limits the potential for further growth. The concentration of CO<sub>2</sub> in the air is not constant and depends on numerous factors, such as season, time of day, the presence of plants, water bodies, industrial enterprises, transportation, people, and animals, among others. Nevertheless, in the open air, the concentration of carbon dioxide varies only slightly.

A different state is characteristic of enclosed spaces, where during the day, while photosynthesis occurs, the concentration of CO<sub>2</sub> rapidly decreases, limiting glucose formation and slowing down plant growth. Experimental studies [1] confirm increased carbon dioxide consumption during photosynthesis, as 400 g of CO<sub>2</sub> is expended for every kilogram of cucumber harvest. Article [2] has shown a decrease in carbon dioxide concentration in greenhouse premises during the day by almost 2.0 times to 150-200 ppm. At night, the concentration of CO<sub>2</sub> rapidly increases due to the absence of the photosynthesis process in the absence of light and plant respiration, during which plants consume oxygen and release carbon dioxide. At this time, plants are already lacking oxygen, which can also harm their life processes. However, even in a closed environment, there is enough oxygen for plant respiration at night, and the problem remains only with carbon dioxide during photosynthesis in the daytime.

Increasing CO<sub>2</sub> concentration during the daytime to 800-1000 ppm has a favorable effect on crop yield. The study [3] considered the impact of carbon dioxide concentration on plant growth. A quantitative increase in biomass was found, and qualitative factors such as increased oxidative stress resistance of plants and increased concentration of minerals and vitamins in vegetables and fruits were improved. The review article on the influence of increasing carbon dioxide concentration on plants [4] concluded a 30 % increase in biomass for plants with C3 photosynthesis and a 10 % increase for plants with C4 photosynthesis with only a doubling of CO<sub>2</sub> concentration. However, research [2] found that the yield of C3 photosynthetic plants increased by 40-100 %, and C4 photosynthetic plants increased only by 10-25 %. Such differences in the effect of increasing carbon dioxide concentration on growth are due to different mechanisms of photosynthesis (C3, C4, CAM photosynthesis) [5]. Results of studies during pea cultivation [6] confirm a significant increase in plant mass with C3 photosynthesis with increased CO<sub>2</sub> concentration.

It should be noted that more than 90% of all plants in the world carry out C3 photosynthesis [5] without going

into detail on the mechanisms of photosynthesis. Only four crops, i.e., corn, millet, sorghum, and sugarcane, have C4 photosynthesis. For other plants, increasing CO<sub>2</sub> concentration significantly affects their development.

Further increases in carbon dioxide concentration initially led to an increase in yield, but after a certain optimum, it harmed their development. It should be noted that such dependence is averaged, but for most plants, the most significant increase in yield occurs at concentrations of carbon dioxide in the air within the range of 800 ppm to 1400 ppm. Further increase in CO<sub>2</sub> concentration harms plant development, and at a value of 1800 ppm, it becomes toxic to them.

The optimization of microclimate parameters in greenhouse farming has been an actual topic for almost half a century by the global scientific community. An example is in work [7], where greenhouse energy consumption is proposed to be optimized (to reduce energy costs by 27 %) by the proposed control scheme for microclimate parameters. In work [8], the optimization of greenhouse parameters is entrusted to neural networks, and in [9], mathematical models and experimental confirmations of optimization in growing lettuce are presented. Even though microclimate parameters of greenhouses include air temperature and humidity, soil moisture, illumination, CO<sub>2</sub> concentration in the greenhouse air, and soil acidity pH, research has mainly been conducted for temperature and humidity control and optimization. In [10], the feasibility of optimizing water consumption during greenhouse cultivation is demonstrated, and in [11], a mathematical model of optimal temperature and humidity control in the greenhouse depending on environmental weather conditions during rose cultivation is presented. In the study [12], a model in MATLAB environment is developed for controlling the heater's operation and window opening. The use of a Fuzzy controller for performing such functions is studied, and in [13], dynamic models and simulation results in MATLAB of temperature and humidity in the greenhouse depending on the season, solar radiation, wind speed, temperature, and humidity outside the greenhouse are presented.

The MATLAB environment contains a powerful package of programs that allows not only performing mathematical calculations and modeling technical systems but is also used as a computer graphic interface for controlling microclimate parameters [14].

In the study [15], four temperature control techniques in a greenhouse were compared: PI control, fuzzy logic control, artificial neural network control, and adaptive neuro-fuzzy control, and it was concluded that the latter controller is the most effective and fast. Although only thermal processes were modeled in [16], this work considers the type and orientation of the greenhouse, the temperature at different points of the greenhouse, environmental temperature, and the presence and absence of a thermal screen. It provides the results of testing the greenhouse model with experimental data and proposes implementing a temperature control system.

The direction of our research was determined by an experiment described in a project [17]. In this study, identical plants were selected for the experiment and sown in glass jars with the same amount of soil. These jars were placed on a windowsill. One jar was hermetically sealed without the addition of CO<sub>2</sub>. The latter's concentration was likely around 350-400 ppm. The second glass jar was sealed, and excess carbon dioxide was added. The drawback of this study is the lack of data on the concentration of this gas. The plants' height was measured every few days for three weeks. The experiment showed that the plants in the glass jar without the additional carbon dioxide content developed better than their excess, and it was concluded that excess CO<sub>2</sub> harms plant development, although initially, opposite results were expected.

The explanation for the experiment's results described above is the unknown carbon dioxide concentration in the second jar. It is possible that the concentration there exceeded 1800 ppm and thus was toxic to plant development. Another factor is that photosynthesis also requires light. Therefore, adding CO<sub>2</sub> without increasing the brightness will not affect photosynthesis processes. Furthermore, carbon dioxide molecules reflect sunlight, which is a hindering factor in photosynthesis.

Therefore, it can be concluded from the research in this study that a positive result in increasing crop yield through an increase in carbon dioxide concentration in a confined space (in this case, a greenhouse) can only be achieved with a proportional increase in the illumination of the surface of the plant leaves and enough water for photosynthesis. Moreover, to ensure resource-efficient management of CO<sub>2</sub> concentration and plant illumination, their optimum levels should be maintained to provide enough light specifically for photosynthesis, without excess, as noted in the study [18], as excessive light irradiation of tomatoes negatively affects photosynthesis processes.

A study [19] is attractive in terms of investigating the effect of carbon dioxide concentration on the rate of photosynthesis. This study proposes the main balance equations of the greenhouse microclimate model and provides the dependencies of the specific rate of crop photosynthesis on the concentration of carbon dioxide, the falling visible radiation and the temperature of the plant leaves. It was found that the maximum specific rate of photosynthesis occurred at a CO<sub>2</sub> concentration of 950 ppm, with sufficient light power for photosynthesis.

Modern control systems for monitoring the microclimate parameters of greenhouses and environmental balance, balancing the supply of nutrients, and lighting systems that use various types of light and renewable energy sources, have achieved high perfection. Despite the popularity of using industrial greenhouse farming, driven by their automation and latest technologies, some systems that significantly affect the yield of greenhouse crops are still in the early stages of development. The only factor limiting maximum plant growth is the amount of carbon dioxide in the greenhouse air, which is necessary for photosynthesis. Therefore, adding CO<sub>2</sub> offers potential opportunities for increasing

the yield of crops grown in greenhouses, but it is necessary to consider the advantages and disadvantages of increasing the concentration of carbon dioxide.

The quantity of carbon dioxide in the greenhouse is most often maintained constant [20], and the greenhouse lighting is turned on depending on the time of day. Such control leads to losses in the energy spent on lighting and excess carbon dioxide consumption. At the same time, climate control inside the greenhouse for growing a particular plant can be considered based on a model of the evolution of the crop over time as a function of the climate created inside the greenhouse. During the development of such models, it is necessary to have a clear understanding of the biological processes that occur in the plant.

Before the 1980s, the development of mathematical modeling of greenhouses was sluggish. However, as the world population grew and science and technology advanced, greenhouses became increasingly used to grow crops in unfavorable conditions. This led to increased commercial and scientific interest in organizing greenhouse farms. The commercial component of greenhouse farms influenced the expansion of greenhouses, the search for new materials, the implementation of new technologies, new equipment, and new scientific research. Consequently, the number of mathematical models overgrew from the 1980s. There was also a continuous improvement of mathematical models of greenhouses, with the discovery of new dependencies, patterns, and modeling methods. Various models describing greenhouses from different aspects, such as goals, precision, complexity, and transparency, emerged. Inadequate transparency of mathematical models led to the creation of new models. In pursuit of accuracy and comprehensiveness, models became increasingly complex, losing an understanding of critical processes. Therefore, among such a variety of models, without systematization, it is not easy to choose a mathematical model that meets specific requirements. Choosing the wrong initial model makes it impossible to obtain adequate results.

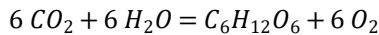
Regarding mathematical models of greenhouse farming, they have a typical structure but differ in various components and dependencies. Most models combine previously published elements of mathematical models, with only a small number containing new components.

To identify standard features of mathematical models of plant cultivation in greenhouses, review articles are emerging that analyze the commonalities and differences of models.

In the paper [21], more than 100 scientific publications on dynamic models describing climatic conditions in greenhouses were analyzed. Models were considered in terms of their purpose (theoretical or applied application), the set goal of controlling microclimate parameters (proportional-integral-derivative regulation, optimal, adaptive, robust, and predictive control), methods of parameter estimation, and the possibility of expanding the application of dynamic models of greenhouses to other objects.

### 3 Research Methodology

The concentration of carbon dioxide (CO<sub>2</sub>) in the air of greenhouses is a microclimate parameter that is not always considered. The starting point for investigating the need to control and regulate the concentration of CO<sub>2</sub>, which is one of the parameters of the greenhouse microclimate, was associated with the peculiarities of plant cultivation, specifically the process of photosynthesis. It is well known from biology that organic compounds are formed from carbon dioxide and water in plants under the influence of light energy with the participation of chlorophyll. This reaction has a chemical formula [24]:



Chlorophylls, which are found in plant chloroplasts, are primarily located in leaves. Each leaf cell contains 20-100 chloroplasts, which are structural components of cells that convert CO<sub>2</sub> into glucose C<sub>6</sub>H<sub>12</sub>O<sub>6</sub>.

Based on the above facts, it can be concluded that to increase crop yields, it is necessary to increase the amount of carbon dioxide and water. The amount of light should be sufficient for photosynthesis. Considering the resource-saving orientation of this work, it is essential to find an optimum between the amount of light required for photosynthesis and the concentration of CO<sub>2</sub>, considering the presence of chloroplasts, the number of which depends on the area of the plant's leaves.

We will assume that water is sufficient for photosynthesis and plant growth.

We will use a mathematical plant growth model and simulation modeling in MATLAB Simulink to identify the optimal dependence between carbon dioxide concentration and lighting. The initial conditions for choosing a mathematical model were as follows:

The purpose of mathematical modeling is to determine the optimal dependences between microclimate parameters to minimize material and energy costs for the cultivation of a unit of the crop.

The mathematical model should represent a dynamic carbon balance.

The selected microclimate parameters include air temperature in the greenhouse, concentration of carbon dioxide, and light intensity.

The model of the microclimate will consider some environmental climate parameters.

The growth model should consider plants' biological processes and microclimate parameters' effect on their speed.

To minimize biological processes considered in the growth's mathematical model, a plant that does not form flowers and does not require pollination will be selected. The growth modeling work was carried out for lettuce. Only the process of photosynthesis was considered from the biological processes that affect yield.

The plant yield will be assessed based on the plant's dry mass and the size of the leaves per unit of soil.

Economic indicators and elements of control systems are not the purposes of the presented mathematical modeling.

Based on critical scientific publications regarding new mathematical models of greenhouses, we will select and simplify a model with experimental verification of its adequacy. As the simplest model that satisfies most requirements, we will take the Van Henten mathematical model [25] in the first approximation.

Experimental studies were conducted to verify the adequacy of the model for the growth of lettuce. The lettuce was chosen as the greenhouse crop. According to Van Henten, the experimental results confirmed the mathematical model for lettuce growth with a high degree of correlation, with deviations not exceeding 5%. Such claims prompted the study of the Van Henten growth model, its analysis, and the identification of opportunities for improvement or simplification.

The increase in lettuce weight was assessed based on the dry mass of the lettuce, which was divided into two components: the structural component (X<sub>str</sub>) and the non-structural component (X<sub>nstr</sub>) of dry mass. The structural component consists of structural components such as cytoplasm and cell walls. The non-structural dry mass contains formations such as starch, glucose, and sucrose produced by the process of photosynthesis.

In the Van Henten model, it is considered that the processes of photosynthesis, respiration, and an increase in the mass of the structural component influence the increase in the non-structural component (X<sub>nstr</sub>). The increase in the mass of the structural component (X<sub>str</sub>) is proportional to its mass. Therefore, the Van Henten growth equations take the following form [25]:

$$\begin{aligned} \frac{dX_{nstr}}{dt} &= c_\alpha \times f_{photosyn} - v_{grow} \times X_{str} - f_{transp} - \frac{(1-c_\beta)}{c_\beta} \times v_{grow} \times X_{str}; \\ \frac{dX_{str}}{dt} &= v_{grow} \times X_{str}, \end{aligned} \quad (1)$$

where  $f_{photosyn}$  – the rate of plant mass increase due to photosynthesis;  $f_{transp}$  – reduction of plant mass in the process of exhaling carbon dioxide;  $v_{grow}$  – the specific growth rate of the structural component, [C<sup>-1</sup>];  $c_\alpha$ ,  $c_\beta$  – coefficients;  $v_{grow} \times X_{str}$  – reduction of the mass of the non-structural component due to its transformation into a structural one.

The coefficient  $(1 - c_\beta) / c_\beta$  considers the increase in mass losses due to synthesis and respiration during plant growth, i.e., its structural component. For lettuce,  $c_\beta$  is equal to 0.8, and  $(1 - c_\beta) / c_\beta = 0.25$ .

The coefficient  $c_\alpha$  is calculated assuming that carbon dioxide is transformed into glucose during photosynthesis, and the ratio of molecular weights of glucose and carbon dioxide is 30 / 44, i.e.,  $c_\alpha = 0.68$ .

At this stage of the research, the Van Henten equation for non-structural components can be simplified to the following form:

$$\frac{dX_{nstr}}{dt} = c_\alpha \times f_{photosyn} - \frac{v_{grow}}{c_\beta} \times X_{str} - f_{transp}. \quad (2)$$

The drawback of model (2) is the complexity of determining a plant's dry weight in real time. This can be overcome by transitioning from the dry weight of the plant

to the area of its leaves. The experimentally obtained formula for lettuce [25] is as follows:

$$S_{leaf} = (1 - c_T) \times k_{leaf} \times X_{str}, \quad (3)$$

where  $(1 - C_T)$  is a coefficient expressing the proportion of leaf mass in the total structural mass;  $k_{leaf}$  is the leaf area coefficient as the leaf area per dry structural plant component mass.

For lettuce,  $(1 - C_T) = 0.85$ , and it was experimentally determined that  $k_{leaf} = 0.075 \text{ [m}^2 \times \text{g}^{-1}\text{]}$ .

If the number of plants per unit area is  $n$ , the mass of one plant can be determined by dividing  $X_{str}$  by  $n$ , and then the expression (3) takes the following form [25]:

$$S_{leaf} = \frac{(1-c_T) \times k_{leaf} \times X_{str}}{n}. \quad (4)$$

Another drawback of growth model (2) is the complexity of separating structural components from non-structural ones. Such separation is essential for further use of the crop in the processing industry. As for lettuce, which this model is adapted for, it is usually consumed raw and sold by weight, without dividing into components. Therefore, in the model (2), we will move from the mass of structural ( $X_{str}$ ) and non-structural ( $X_{nstr}$ ) components to the total mass of the plant ( $X_{general}$ ), considering that:

$$X_{general} = X_{str} + X_{nstr}. \quad (5)$$

Experimental data from lettuce cultivation [25] revealed that the dry weight of one plant's structural component was 2.0 g, while the non-structural component was only 0.7 g. Therefore, the dry weight of the non-structural component represents approximately 25 % ( $0.7 \times 100 / 2.7 = 26 \%$ ) of the plant's total weight, and it can be stated that  $X_{str} = 0.75 \cdot X_{general}$ , and  $X_{nstr} = 0.25 \cdot X_{general}$ .

Estimation calculations of growth model (2) were made based on the results of the mathematical model and lettuce cultivation experiment [27], indicating that plant mass increase occurs exclusively due to photosynthesis. The loss of plant mass due to respiration can be neglected. In this case, the growth model's error for greenhouse conditions will not exceed 1%, and the model will take the following form:

$$\frac{dX_{general}}{dt} = c_\alpha \times f_{photosyn}. \quad (6)$$

It can be inferred from this model that the increase in plant mass occurs through photosynthesis, and the influence of other processes is insignificant, which is supported by biological research. The increase in weight of the non-structural component of the plant due to the process of photosynthesis can be described by the following empirical expression [25]:

$$f_{photosyn} = \{1 - \exp(-c_K \times k_{leaf} \times (1 - c_T) \times X_{str})\} \times f_{photosyn.max}, \quad (7)$$

where coefficient  $C_K$  is used to consider the orientation of the leaf. In the case of a plant with horizontally oriented leaves called pianophiles, the coefficient  $C_K$  equals 0.9.

In the case of a plant with vertically oriented leaves called electrophiles, the coefficient  $C_K = 0.3$ . As lettuce is

a more pianophile crop, we will choose  $C_K = 0.9$  because its leaves are situated in a horizontal plane.

The parameter  $f_{photosyn.max}$  represents the rate at which the plant mass increases due to photosynthesis in the case of complete coverage of the ground surface with leaves and is measured in  $[\text{g} \times \text{m}^{-2} \times \text{s}^{-1}]$ .

The coefficient  $(1 - C_T)$  expresses the proportion of the total structural mass that is made up of leaves. For lettuce,  $(1 - C_T) = 0.85$ . The  $k_{leaf} \times (1 - C_T) \times X_{str}$  multiplier is the leaf area index.

The expression in curly brackets in (7) demonstrates how many times the rate of plant biomass increase due to photosynthesis is lower than the maximum possible rate when leaves fully cover the soil. It considers the fact that leaves do not entirely cover the ground. When leaves fully cover the soil, this expression equals one.

As the rate of photosynthesis depends on the concentration of carbon dioxide, the intensity of light radiation, temperature, and leaf area, Van Henten proposed the following dependence [25]:

$$f_{photosyn.max} = \frac{c_{rad,phot} \times I_{light} \times g_{CO_2} \times \rho_{CO_2} \times (CO_2 - R)}{c_{rad,phot} \times I_{light} + g_{CO_2} \times \rho_{CO_2} \times (CO_2 - R)} \quad (8)$$

where  $C_{rad,phot}$  – light use efficiency, which is the fraction of radiation that is used in the process of photosynthesis  $[\text{g} \times \text{J}^{-1}]$ ;  $I_{light}$  – the power of photosynthetically active radiation per unit area of greenhouse surface, measured in watts per square meter  $[\text{W} \times \text{m}^{-2}]$ ;  $g_{CO_2}$  – the conductance of leaves to the diffusion of carbon dioxide through their surface, measured in meters per second  $[\text{m}/\text{s}]$ ;  $\rho_{CO_2}$  – the density of carbon dioxide gas, with a value of  $1.83 \cdot 10^{-3} \text{ [g} \times \text{m}^{-3}\text{]}$ ;  $CO_2$  – the concentration of carbon dioxide gas in the air, measured in parts per million  $[\text{ppm}]$ ;  $r$  – the compensation point for carbon dioxide, corresponds to photorespiration at high light intensities,  $[\text{ppm}]$ .

The compensation point depends on temperature as follows [25]:

$$r = C_R \times C_{comp}^{0.1T-2}, \quad (9)$$

where  $C_R$  – the compensation point of carbon dioxide at a temperature of 20 °C and is equal to 40 ppm;  $C_{comp}$  – coefficient, which considers the effect of temperature on the compensation points and has a value of 2.

The light use efficiency  $C_{rad,phot}$  can be calculated using the following formula, as described in [25]:

$$C_{rad,phot} = C_{eff} \times \frac{CO_2 - R}{CO_2 + 2R}, \quad (10)$$

where  $C_{eff}$  – the effective use of light during high carbon dioxide concentration and is equal to  $1.7 \cdot 10^{-5} \text{ [g} \times \text{J}]$ .

The conductivity of leaves for the diffusion of carbon dioxide through their surface,  $g_{CO_2}$ , consists of two physical conductivities and one chemical conductivity. The physical conductivities include the conductivity of the surface layer,  $g_{bound}$ , and the stomatal conductivity,  $g_{stom}$ , while the chemical conductivity is the conductivity of carboxylation,  $g_{carb}$ .

The dependence between the mentioned conductivities can be expressed as follows [25]:



$$\frac{1}{g_{CO_2}} = \frac{1}{g_{bound}} + \frac{1}{g_{stom}} + \frac{1}{g_{carb}}. \quad (11)$$

The conductivity of the leaf surface layer  $g_{bound}$  is determined by the wind speed and the temperature difference between the leaf and the greenhouse air. It has been experimentally determined that for lettuce, at a temperature difference of 5°C and a wind speed of 0.1 m/s, typical for a greenhouse,  $g_{bound} = 0.007 [m \times s^{-1}]$  [25].

The stomatal conductance  $g_{stom}$  depends on the plant's condition and the presence of stress factors. Without stress, the stomatal conductance of lettuce for carbon dioxide was experimentally determined to be 0.005  $[m \times s^{-1}]$ .

The conductivity of carboxylation  $g_{carb}$  depends on temperature. For lettuce, it reaches its maximum value  $g_{carb,max} = 0.004$  at a temperature of 17.5 °C and approaches zero at temperatures of 5 and 40 °C. For the temperature range of 5 °C to 40 °C, the conductivity of carboxylation can be described by the following expression [25]:

$$g_{carb} = c_{carb,1} \times T^2 + c_{carb,2} \times T + c_{carb,3}; \quad (12)$$

$$c_{carb,1} = -1,32 \times 10^{-5} [m \times s^{-1} \times ^\circ C^{-2}];$$

$$c_{carb,2} = 5,94 \times 10^{-4} [m \times s^{-1} \times ^\circ C^{-1}];$$

$$c_{carb,3} = -2,64 \times 10^{-3} [m \times s^{-1}].$$

## 4 Results

The resource efficiency of management is based on the regulation of greenhouse lighting depending on the concentration of carbon dioxide gas to obtain the maximum yield due to the maximum photosynthetic rate of the plant. It is assumed that plant illumination should be sufficient for photosynthesis, but solar radiation should also be considered. The control of lamp irradiance can be described using Equation (8), which represents a balance between the concentration of carbon dioxide gas ( $CO_2$ ) and the light intensity ( $I_{light}$ ) necessary for maximum photosynthesis. The relationship between them can be found by dividing the numerator and denominator by the factor  $C_{rad, phot} \times I_{light}$ :

$$f_{photosyn,max} = \frac{g_{CO_2} \times \rho_{CO_2} \times (CO_2 - R)}{1 + \frac{g_{CO_2} \times \rho_{CO_2} \times (CO_2 - R)}{C_{rad, phot} \times I_{light}}} \quad (13)$$

A relationship between the concentration of carbon dioxide ( $CO_2$ ) and the light intensity ( $I_{light}$ ) involved in photosynthesis can be obtained from this expression. The lack of data on the maximum rate of photosynthesis poses a problem for detecting such a relationship. We will implement expression (13) and perform modeling in Simulink (Fig. 1) to address this.

The subsystems used in this model are presented in Figures 2-5.

During the simulation, the relationship between the rate of photosynthesis and the power of light radiation was determined at different concentrations of carbon dioxide, which varied from 400 ppm to 1200 ppm with a step of 200 ppm (Fig. 6).

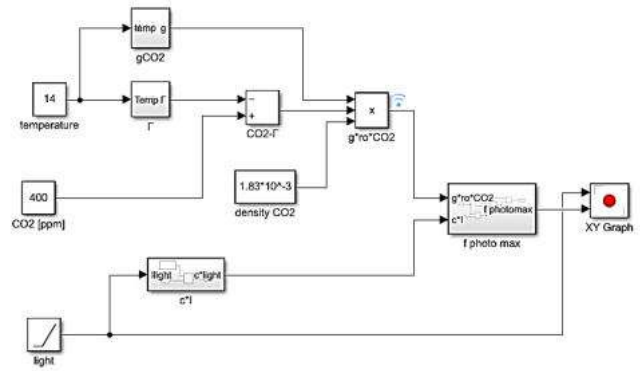


Figure 1 –MATLAB Simulink model for expression (13)

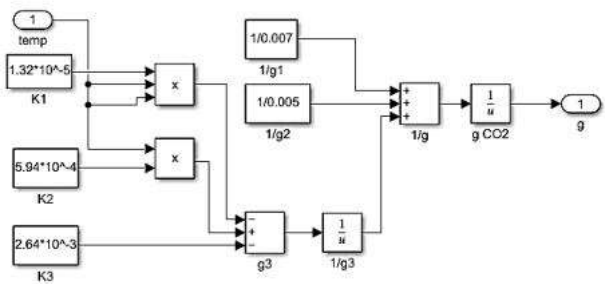


Figure 2 – Simulink subsystem for expressions (11) and (12)

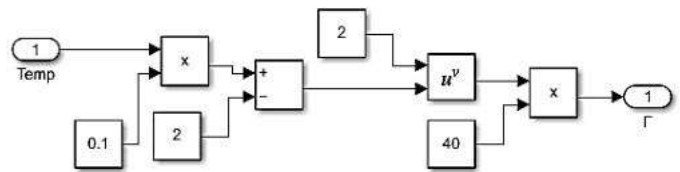


Figure 3 – Simulink subsystem. that implements expression (9)

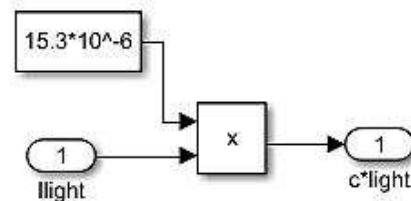


Figure 4 – Simulink subsystem that implements the product of the efficiency of light use and the power of light radiation

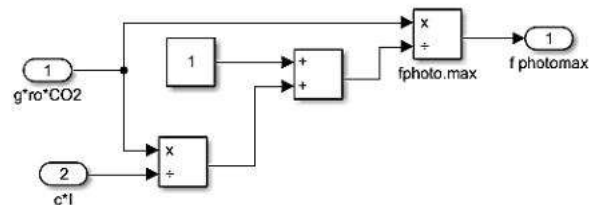


Figure 5 – Simulink subsystem that implements expression (13)

For each case, the value of light intensity at saturation was determined, indicating the impracticality of increasing the intensity as it had little effect on the rate of photosynthesis. The results of the study are presented in Table 1.

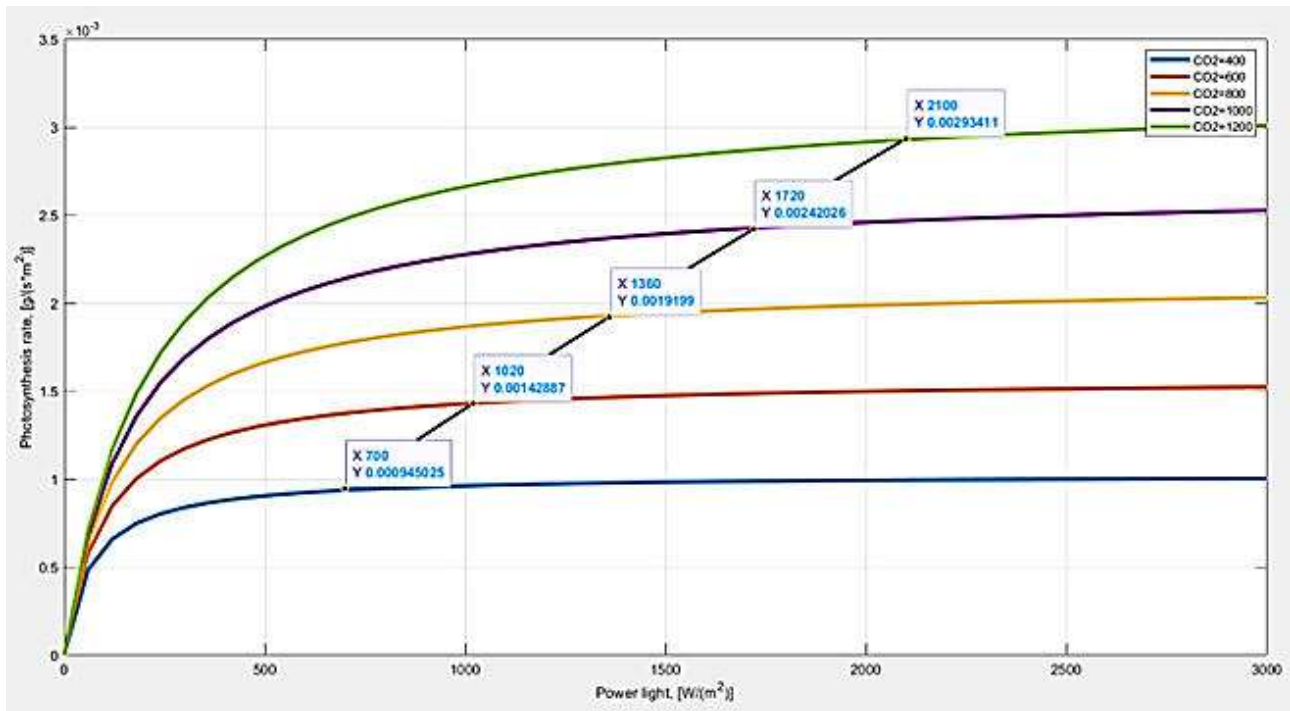


Figure 6 – Graphs of the dependence of the rate of photosynthesis on illumination at a CO<sub>2</sub> concentration of 400, 600, 800, 1000, and 1200 ppm

Table 1 – Results of modeling in MATLAB Simulink

CO <sub>2</sub> concentration, [ppm]	400	600	800	1000	1200
Light intensity, [W / m <sup>2</sup> ]	700	1000	1400	1700	2100
Ratio, [ppm × W <sup>-1</sup> × m <sup>2</sup> ]	0.57	0.6	0.57	0.59	0.57
Average light intensity, [W / m <sup>2</sup> ]	700	1020	1360	1720	2100
Relative error of the average, %	0.0	2.0	2.9	1.2	0.0

From Table 1, the ratio of carbon dioxide concentration to the light intensity that participates in photosynthesis ranges from 0.57 to 0.6 [ppm × W<sup>-1</sup> × m<sup>2</sup>]. An averaging line was plotted on the graphs of Fig. 6, corresponding to the plant photosynthesis rate's saturation.

From Fig. 6, it was determined that increasing the illumination intensity above the saturation point can change the photosynthesis rate by no more than 5%. Therefore, the light intensity per unit area of the greenhouse can be regulated according to the concentration of CO<sub>2</sub>, considering a coefficient of 0.57.

## 5 Conclusions

The simplified mathematical model and simulation in the MATLAB Simulink environment made it possible to establish the relationship between the concentration of carbon dioxide [ppm] and the lighting intensity in the greenhouse plant [W / m<sup>2</sup>], at which photosynthesis occurs at a maximum specific rate. A coefficient of 0.57 was determined for lettuce. The optimal specific photosynthesis rate for lettuce corresponds to a CO<sub>2</sub> concentration of 950 ppm at a specific lighting intensity of 542 [W × m<sup>-2</sup>]. The obtained relationship can be adjusted for other greenhouse crops and yield requirements, considering lighting costs. For lettuce, it can be increased to save energy. The proposed methodology can be used to investigate other relationships between microclimate parameters in the greenhouse, based on the energy balance equation or water vapor balance. The results will be used to develop and investigate a resource-saving microclimate control system in the greenhouse by controlling the supply of carbon dioxide depending on the leaf area of the plant and maintaining the optimum between lighting and CO<sub>2</sub> concentration parameters.

## References

1. Kläring, H. P., Becker, C., Wünsche, J. N., Lenz, R., & Dietrich, P. (2007). Model-based control of CO<sub>2</sub> concentration in greenhouses at ambient levels increases cucumber yield. *Agricultural and Forest Meteorology*, 143(3-4), 208-216. doi: 10.1016/j.agrformet.2006.12.002
2. Singh, H., Poudel, M. R., Dunn, B., Fontanier, C., & Kakani, G. (2020). Greenhouse carbon dioxide supplementation with irrigation and fertilization management of geranium and fountain grass. *HortScience*, 55(11), 1772-1780. doi: 10.21273/HORTSCI15327-20
3. Idso, S. B., & Idso, K. E. (2001). Effects of atmospheric CO<sub>2</sub> enrichment on plant constituents related to animal and human health. *Environmental and Experimental Botany*, 45(2), 179-199. doi: 10.1016/S0098-8472(00)00091-5
4. Streck, N. A. (2005). Climate change and agroecosystems: The effect of elevated atmospheric CO<sub>2</sub> and temperature on crop growth, development, and yield. *Ciência Rural*, 35(3), 730-740. doi: 10.1590/S0103-84782005000300041
5. Taub, D. R. (2010). Effects of rising atmospheric concentrations of carbon dioxide on plants. *Nature Education Knowledge*, 3(10), 21.
6. Kumari, M., Verma, S. K., Bhardwaj, S., Thakur, A., Gupta, R., & Sharma, R. (2016). Effect of elevated CO<sub>2</sub> and temperature on growth parameters of pea (*Pisum sativum* L.) crop. *Journal of Applied and Natural Science*, 8(4), 1941-1946. doi: 10.31018/jans.v8i4.1067
7. Ullah, I., Fayaz, M., Aman, M., Qadir, J., Ali, S., & Ahmad, S. (2022). An optimization scheme for IoT-based smart greenhouse climate control with efficient energy consumption. *Computing*, 104(1), 433-457. doi: 10.1007/s00607-021-00963-5
8. Su, Y., Xu, L., & Goodman, E. D. (2017). Nearly dynamic programming NN-approximation-based optimal control for greenhouse climate: A simulation study. *Optimal Control Applications and Methods*, 39(2), 638-662. doi: 10.1002/oca.2370
9. Van Henten, E. J. (2003). Sensitivity analysis of an optimal control problem in greenhouse climate management. *Biosystems Engineering*, 85(3), 355-364. doi: 10.1016/S1537-5110(03)00068-0
10. Stanghellini, C. (2014). Horticultural production in greenhouses: Efficient use of water. *Acta Horticulturae*, 1034, 25-32. doi: 10.17660/ActaHortic.2014.1034.1
11. Van Beveren, P. J. M., Bontsema, J., Van Straten, G., & Van Henten, E. J. (2015). Minimal heating and cooling in a modern rose greenhouse. *Applied Energy*, 137, 97-109. <https://doi.org/10.1016/j.apenergy.2014.09.083>
12. Caponetto, R., Fortuna, L., Nunnari, G., Occhipinti, L., & Xibilia, M. G. (2001). Soft computing for greenhouse climate control. *IEEE Transactions on Fuzzy Systems*, 9(4), 713-720. <https://doi.org/10.1109/91.890333>
13. Ben Ali, R., Aridhi, E., & Mami, A. (2015). Dynamic model of an agricultural greenhouse using Matlab-Simulink environment. In 2015 12th International Multi-Conference on Systems, Signals & Devices (SSD) (pp. 346-350). <https://doi.org/10.1109/STA.2015.7505185>
14. Katircioğlu, F. (2019). Control and monitoring of greenhouse system with Matlab GUI. *International Journal of Scientific and Technological Research*, 5(3), 95-100.
15. Atia, D., & Tolba, H. (2017). Analysis and design of greenhouse temperature control using adaptive neuro-fuzzy inference system. *International Journal of Advanced Research in Computer Science and Software Engineering*, 7(4), 34-48.
16. Taki, M., Ajabshirchi, Y., Ranjbar, F., Rohani, A., & Matloobi, M. (2016). Modeling and experimental validation of heat transfer and energy consumption in an innovative greenhouse structure. *Information Processing in Agriculture*, 3(1), 20-32. <https://doi.org/10.1016/j.inpa.2016.06.002>
17. USC. (n.d.). How do increased carbon dioxide levels affect plant growth? <https://csef.usc.edu/history/projects/J2321/>
18. O'Carrigan, A., Hinde, E., Lu, N., Xu, X.-Q., Duan, H., Huang, G., Mak, M., Bellotti, W., & Chen, Z.-H. (2014). Effects of light irradiance on stomatal regulation and growth of tomato. *Environmental and Experimental Botany*, 98, 65-73. <https://doi.org/10.1016/j.envexpbot.2013.10.007>
19. Effat, M. B., Shafey, H. M., & Nassib, A. M. (2015). Solar greenhouses can be promising candidate for CO<sub>2</sub> capture and utilization: Mathematical modeling. *International Journal of Energy and Environmental Engineering*, 6(3), 295-308. <https://doi.org/10.1007/s40095-015-0175-z>
20. Van Henten, E. J. (1994). Validation of a dynamic lettuce growth model for greenhouse climate control. *Agricultural Systems*, 45(1), 55-72. [https://doi.org/10.1016/S0308-521X\(94\)90280-1](https://doi.org/10.1016/S0308-521X(94)90280-1)
21. López-Cruz, I., Fitz-Rodríguez, E., Raquel, S., Rojano-Aguilar, A., & Kacira, M. (2018). Development and analysis of dynamical mathematical models of greenhouse climate: A review. *European Journal of Horticultural Science*, 83, 269-279. <https://doi.org/10.17660/eJHS.2018/83.5.1>
22. Katzin, D., van Henten, E. J., et al. (2022). Process-based greenhouse climate models: Genealogy, current status, and future directions. *Agricultural Systems*, 198, 104124. <https://doi.org/10.1016/j.agry.2022.104124>
23. Rezvani, S. M.-E.-D., Jafari, A., Ghoosheh, E. Z., et al. (2021). Greenhouse crop simulation models and microclimate control systems, a review. In *Next-Generation Greenhouses for Food Security*. IntechOpen. <https://doi.org/10.5772/intechopen.97361>
24. Blank, D. (2015). Global warming and global change: Facts and myths. *International Journal of Earth Science and Geophysics*, 1(4), 1-4. <https://doi.org/10.15436/2381-0697.15.004>
25. Van Henten, E. J. (1994). *Greenhouse climate management: An optimal control approach*. Wageningen University and Research.



Plotkin J., Levchenko N., Shyshkanova G., Levchenko S. (2023). Development of energy enterprises in the context of green transformation. *Journal of Engineering Sciences*, Vol. 10(1), pp. G22-G33, doi: 10.21272/jes.2023.10(1).g3

## Development of Energy Enterprises in the Context of Green Transformation

Plotkin J.<sup>1</sup>[0000-0001-9257-5933], Levchenko N.<sup>2,3\*</sup>[0000-0002-3283-6924], Shyshkanova G.<sup>2,4</sup>[0000-0002-0336-2803], Levchenko S.<sup>5</sup>[0000-0002-6569-909X]

<sup>1</sup> Hochschule für Wirtschaft und Recht Berlin (HWR Berlin), 52, Badensche St., 10825 Berlin, Germany;

<sup>2</sup> National University “Zaporizhzhia Polytechnic”, 64, Zhukovskogo St., 69063 Zaporizhzhia, Ukraine;

<sup>3</sup> Technical University of Berlin, 135, 17 Juni St., 10623 Berlin, Germany;

<sup>4</sup> Humboldt-Universität zu Berlin, 6, Unter den Linden St., 10099 Berlin, Germany;

<sup>5</sup> Information Technologies Department of the State Tax Service Main Department in Zaporizhzhia Region, 34, Dniprovska St., 69063 Zaporizhzhia, Ukraine

### Article info:

Submitted: March 9, 2023  
 Received in revised form: May 22, 2023  
 Accepted for publication: May 31, 2023  
 Available online: June 2, 2023

### \*Corresponding email:

[levchenkon65@gmail.com](mailto:levchenkon65@gmail.com)

**Abstract.** The article argues that the search for effective tools to ensure the economically secure future of energy companies and their development in the context of green transformation is necessary due to the speed of global transformations, the priority of reducing dependence on fuel and energy imports, the development of renewable energy sources, the instability of the environment for the functioning of energy companies (as a result of Russia's full-scale invasion of Ukraine) and their position both on the Ukrainian and European energy markets. The reality of the energy sector in the country and the steps for the recovery of the energy companies determined by the Economic Recovery Plan of Ukraine were analyzed. The evidence shows that the legislative amendments aimed at stabilizing the energy sector and solving key issues lack efficiency and cannot ensure the vital activity of energy enterprises and their development in the conditions of climate-neutral transformation. A methodology was proposed to assess the progress of the carbon-neutral development of energy companies, which should become the basis for attracting ESG investing. The vectors for creating a favorable environment for environmental, social, and governance (ESG) investing were identified as a unique opportunity to ensure the economically secure future of energy companies and their development in the context of green transformation.

**Keywords:** energy neutrality, decarbonization, sustainability reporting, green tariff, transitional payment mechanism, ESG investing, energy efficiency.

## 1 Introduction

The challenges associated with environmental degradation and climate change have emerged rapidly in recent years, raising serious concerns among the international community and policymakers seeking sustainable development. At the recent COP27 (Conference of the Parties) summit on environmental governance and climate change, countries that have ratified the United Nations Framework Convention on Climate Change (UNFCCC) decided to achieve net-zero carbon emissions, primarily through the reduction of fossil fuel power plants [1].

Ukraine did not stay on the sidelines either. As a result, the Government adopted the National Plan for the Reduction of Emissions (NPRE) from Large Combustion

Plants (LCP) – Thermal Power Plants (TPP) and Combined Heat and Power Plants (CHP) [2], the second nationally determined contribution of Ukraine to the Paris Agreement [3], adopted the National Energy and Climate Change Plan for the period up to 2030 [4], approved the Strategy for Environmental Security and Climate Change Adaptation for the period up to 2030 [5] and developed the Operational Plan for its implementation for the period 2022-2024 [6]. With their introduction, the volume of electricity generation by TPPs and CHPs in Ukraine gradually decreases. However, we consider it inappropriate to completely abandon TPP/CHP for the following four main reasons.

First, Ukraine does not have enough capacity for substations for receiving, distributing, and transforming electricity.

Second, the units of the nuclear power plants (NPPs) cannot increase their load during the day, as they work with a constant load and provide basic electricity consumption. Therefore, there needs to be an additional source of generation that can be used to meet the electricity demand generated during peak hours. This is what TPPs and CHPs do. Therefore, their importance in the energy system of Ukraine lies primarily in regulating the volume of power generation during the day, thus ensuring the stability of the country of the Economic Cooperation Organization (ECO).

Third, as the main driver for developing renewable energy sources (RES), solar energy is a low-efficiency and unstable type of energy with an average conversion efficiency not exceeding 20%. In addition, it requires large areas to house the equipment in the face of an ever-increasing scarcity of agricultural land. It is, therefore, unlikely that solar energy and other types of renewable energy will be able to replace fossil fuels 100%, even in the long term. An energy model that combines the development of RES, hydroelectric power plants (HEPS), combined heat and power (CHP), and innovative, safe nuclear technologies (in particular small modular reactors (SMR) and fast neutron reactors) could be a more realistic scenario for achieving climate goals [7].

Fourth, TPP simultaneously generates both electricity and heat, meeting the needs of consumers in heat supply.

Perhaps the only way to reduce carbon emissions from thermal power plants is to gasify them. However, this requires the implementation of large-scale and capital-intensive projects to reconstruct TPP/CHP equipment and construct flue gas cleaning plants from sulfur dioxide (CO<sub>2</sub>) and nitrogen oxides (NO<sub>x</sub>) emissions. However, unfortunately, NPRES [4] mechanisms and sources of their financing are not defined. The same mechanisms for financing projects for reconstruction/modernization of power generation facilities that were in effect before the introduction of the new electricity market have lost their relevance, and new ones have not been developed or implemented in national legislation. Therefore, it is evident that TPP/CHP do not have the necessary resources to finance the modernization of their equipment [8] since the marginal prices for electricity set by the national regulator do not provide the creation of funds necessary for implementing TPP/CHP gasification projects. On the contrary, they make it more and more difficult for the Ukrainian power industry to fulfill the tasks defined by the NPRES [4], the Nationally Determined Contribution (NDC) 2 to the Paris Climate Agreement [3], and the Association Agreement between Ukraine and the EU. The decommissioning of a part of the TPP/CHP units and/or their shutdown due to non-compliance with the provisions of the NPRES may lead to a shortage of generating capacities and, consequently, to a violation of the country's energy security [8, p. 11], which is in a rather critical state as a result of Russia's full-scale invasion of Ukraine.

As a result of missile attacks alone, as of the end of March 2023, up to 5 GW of generating capacity remains damaged in the United Energy System (UES) of Ukraine,

including 19 TPP units with a total capacity of 3.3 GW, four CHP units with a capacity of 1.1 GW, and eight HEPS hydroelectric units with a capacity of 0.54 GW. Part of the generating capacity is still under occupation. These are five TPPs with a total capacity of 10 GW and the largest, Zaporizhzhia NPP, with a total capacity of 6 GW [9].

The experience of foreign countries after the post-war reconstruction shows that the main source of financing for the modernization of TPP/CHP generating equipment should be foreign financial assistance. However, against the backdrop of a large number of statements and declarations of Western partners on financial support for the modernization of TPP / CHP generating equipment in Ukraine in the post-war years, the institutional mechanism and financial instruments for restoring the energy industry have not yet been determined. In particular, in May 2022, the European Commission announced the creation of a special financial mechanism, "Rebuild Ukraine", designed to provide financial support to Ukraine through grants and loans, but so far, such a mechanism has not been launched [1]. Therefore, understanding the complexity of this issue, there is an urgent need to find avant-garde ways to ensure the development of energy enterprises in the post-war years in the context of green transformation.

## 2 Literature Review

It is not only the complexity of the "green transformation" and the lack of funds for its financing but also the constant shifting of the attention of politics, business, and science to this area. This is evidenced by numerous speeches of government representatives and public organizations, publications of foreign and domestic researchers in scientific journals, and publications of experts and practitioners in mass media and blogs.

The existing climate threats and environmental pollution require humanity to reflect on the actual value of nature, UN Secretary-General António Guterres [10] emphasizes. Humanity will only ensure the well-being of the planet, and thus the well-being of present and future generations, if we understand its value and direct our ingenuity towards the transition to low-carbon production [11]. R. Flavio, M. Arroyo, and L. J. Miguel [12] emphasize that adequate financial support is critical for achieving carbon emission reductions, especially in the energy sector, under any of the energy-growth-environment nexus scenarios. In addition, government regulation plays an essential role in its formation by creating a favorable environment for attracting investment.

Mara Madaleno and Manuel Carlos Nogueira [13, p.33] emphasize that since energy is an essential source of economic growth in the world economy, sustainable economic growth can only be achieved by first creating the conditions necessary for expanding the production and consumption of "green" energy sources. Only in a sustainable way will it be possible to ensure the necessary

reduction of CO<sub>2</sub> emissions while increasing the amount of electricity generation, the demand for which is constantly growing.

They are fully supported by Hongyi Zhang, Hsing Hung Chen, Kunseng Lao, and Zhengyu Ren [14], as well as Zhuohang Li, Tao Shen, Yifen Yin, and Hsing Hung Chen [15], as well as Zahoor Ahmed, Michael Cary, Muhammad Shahbaz, Xuan Vinh Vo [16], which in the example of the United States is the second largest emitter of CO<sub>2</sub> environmental pollutant, where nearly 16 % of the world's energy production is consumed with only 4.3 % of the world's population (for comparison, China and India together consume about 28 % of the world's energy production, despite being home to 36 % of the world's population) have proven that public investment in renewable energy research and development and thermal power plant modernization is a helpful strategy for achieving better economic performance and environmental sustainability. As part of its efforts to combat climate change, the United States has increased its share of renewable electricity generation over the past two decades. However, the United States still generates most of its energy from fossil fuels, primarily due to a history of government subsidies that were put in place to artificially support domestic fossil fuel production. Whether these subsidies will continue is one of the most critical issues in US political discourse [16].

With the rapid development of renewable energy, regulating the load of the electric power system has become an important issue, and much research has been conducted on regulating the load using TPP [17]. Challenges related to environmental sustainability, security of energy supply, economic stability, and social aspects are identified on the way to a decarbonized energy sector [18]. Elisa Papadis and George Tsatsaronis [18] argues that a global carbon tax is the most promising instrument to accelerate the process of decarbonization. However, this process will be very challenging for humankind due to the high capital requirements.

I. P. Hayuduky [19] argues the need to form a global and national motivation system for sustainable low-carbon development of the country's economy and industries. The author emphasizes that achieving ambitious goals requires large amounts of investment. Nevertheless, the formation of such an investment potential is complicated by contradictions in the global anti-carbon policy when negative environmental consequences are global, and the financing of measures to reduce greenhouse gas emissions is sectoral [11].

Investments prioritizing environmental, social, and corporate responsibility are replacing the conventional investment paradigm, and the energy sector is one of the sectors most affected by this trend [20].

Thus, the European-Ukrainian Energy Agency director K. Polyakova [21] emphasizes that the energy industry has continued to fight for survival for more than a year. RES producers ended 2022 with a "green" tariff payment rate of 54 %. Debts for imbalances and debts under the "green" tariff for the current and previous years remain

the key issues important for the survival of the industry's enterprises. The analyzed sample in [22] includes over 500 publicly reported companies from different energy sectors, and the research methodology embeds robust regression models. The main results provide new insights into the modeling of firm performance through environmental, social, and governance (ESG) practices and entail that the environmental pillar of ESG negatively affects energy companies' financial performance.

Experts of the Razumkov Center [7] emphasize the complexity of the process of decarbonization of the energy industry of Ukraine and dwell in detail on the problems of attracting investments in the development of energy infrastructure to ensure the transition to carbon-neutral energy. It proposed a set of recommendations for energy decarbonization to ensure sustainable electricity production, energy security, and economic recovery of Ukraine [7]. The set is based on European experience in combating climate change and the "green" transition, as well as considering external challenges – the Carbon Border Adjustment Mechanism (CBAM) and the impact on the energy sector of military operations.

The work [23] presents the possibility of ensuring economic security by transforming the energy system towards renewable energy sources, including solar, wind, hydropower, and biofuels. This process is linked to the transition of economies to a less carbon-intensive and more sustainable energy system. The study [23] examines economic and policy incentives for clean energies, both direct and indirect.

Proposals are also coming from government officials, in particular with the submission to the Verkhovna Rada of 02.05.2023 for consideration of the draft law No. 3056-IX, which is aimed at improving the conditions for supporting the production of electricity from alternative energy sources by generating plants of consumers, taking into account the best global practices. And also a whole circle of scientists. In particular, the scientists of the IEP of the National Academy of Sciences of Ukraine, in the Report "Economically justified approach to the introduction of the National Plan for the reduction of emissions in Ukraine based on the experience of reducing emissions of harmful pollutants into the air by large combustion plants in Europe" considered the European experience of state support for TPPs/CHPs. It was emphasized that among the mechanisms that were used and continue to be used to support coal generation, the most significant in terms of financing is the transitional payment mechanism, which is currently used in Poland, Germany, Portugal, the Czech Republic, Greece, Italy, and contracts for difference, which are still used in Austria, Denmark, the Netherlands, and Great Britain.

O. V. Borysiak [24], based on the results of a study of the potential of energy enterprises under martial law, proposes to apply an integrated segmental approach to the development of a conceptual model for positioning "green" energy on the European energy market as a carbon-neutral product, which will contribute to the formation of additional resources for the modernization

of energy enterprises thanks to its export, in particular TPP and/or CHP.

There are also proposals regarding the replacement of the “green tariff” in Ukraine with a new model of Net billing, to which K. Bilousova [25] calls for discussion on the pages of “Ecopolitics”.

Therefore, we are convinced that the issue of the development of energy enterprises in the context of “green transformations” does not lose its relevance, and with the damage to energy infrastructure facilities as a result of russia’s full-scale invasion of the territory of Ukraine, they become even more relevant.

The goal is to determine the optimal path for the formation of Ukraine’s energy portfolio in the post-war years, taking into account the characteristics of the country’s energy mix, the consequences of russia’s full-scale invasion of Ukraine, and the possibility of attracting investments in the development of energy enterprises in the context of “green transformations”.

### 3 Research Methodology

The theoretical and methodological basis for realizing the research goal became the fundamental provisions of the modern science of public administration. In the research process, general scientific methods were used. In particular, methods of abstraction, induction and deduction, analysis and synthesis, abstract-logical, and graphic.

Among the special methods in the research process, the following were used: the method of sectoral mapping – when assessing the state of electric power enterprises, the decoupling analysis method – when determining the dynamism of the gap between the capital invested in the development of DTEK Group’s TPP/CHP and the number of carbon emissions; the method of harmonization – when searching for sources of financing for the “green” development of energy enterprises according to the decarbonization tasks set. Correlation regression analysis and the least square method were used for mathematical model construction, and scenario forecasts were found.

Sharing the values of the “European Green Deal” [26], with the adoption of which Europe declared its intention to become the first climate-neutral continent in the world by 2050, Ukraine announced its intention to cooperate with the EU in the direction of “greening” energy.

Currently, the EU is moving dynamically in this direction, as evidenced by the data in Table 1.

Ukraine is moving much more dynamically in this trend. During the analyzed period, it reduced GHG emissions (from the power industry) to 167.9 million tons, or in other words by 44 %. However, such positive indicators were achieved not due to the implementation of projects for the modernization of energy enterprises, but due to the reduction of production volumes and, therefore, the volumes of electricity consumption by industrial enterprises.

Table 1 – Dynamics of reduction of greenhouse gas emissions in EU countries and Ukraine during 2012-2021

Countries	Years									
	2012	2013	2014	2015	2016	2017	2018	2019	2020	2021
EU countries	3218.7	3146.0	2980.8	3043.7	3075.7	3095.7	3069.0	2931.5	2564.2	2728.2
Ukraine	299.1	286.5	246.8	195.1	215.6	187.9	196.7	185.5	172.9	167.9

There is no doubt that it is challenging to implement projects for modernizing power plants and, in particular, combined heat and power plants with investment needs above 4 billion EUR (Table 2) in the absence of the sources and mechanisms for their financing defined in the NRP [8], even if there is agreement on the issue of extending the terms of their implementation [1].

However, having received the status of a candidate for EU accession, Ukraine will continue to move in the direction of achieving the goals of the European Green Agreement, continuing the implementation of the principles and standards of European legislation, focusing on the future obligations of EU membership in cooperation with European partners.

In order to achieve the goals of decarbonization, a comprehensive approach and an effective recovery plan with an effective program for attracting investments, creating the basis for “green” modernization, and stimulating the development of renewable energy is necessary [7].

Table 2 – The need for capital investments for the reconstruction/modernization/technical re-equipment of power plants, considering the changes ensuring the implementation of the NPRE [8]

Years	Desulfurization	Denitrification	Dust cleaning	Amount
2020	97	42	15	154
2021	396	18	87	501
2022	193	18	135	346
2023	171	18	56	245
2024	135	185	75	395
2025	158	307	57	522
2026	138	102	51	291
2027	153	88	36	277
2028	203	78	31	312
2029	170	46	–	216
2030	156	69	–	225
2031	170	108	–	278
2032	143	114	–	257
2033	26	86	–	112
Total	2311	1 276	543	4130

Undoubtedly, one of the sources of financing the modernization of TPPs and CHPs should be the investment component of the electricity price. However, the electricity market has been liberalized, and wholesale and retail electricity markets have been created by analogy with European countries, namely: the market of bilateral contracts, the market of bilateral contracts at free prices, the day-ahead market, the balancing, and intraday market, did not bring the expected result. In addition, in connection with the state of war in the country, the CMU Resolution No. 838 of 22.07.2022 [27] extended the operation of the mechanism for ensuring the public interests in the process of functioning of the electric energy market, i.e., the operation of forced price restrictions.

Using this mechanism shows that price regulation measures on the electricity market should be limited and gradually phased out in the post-war years, ensuring generating companies' gradual financial recovery [28].

In order to accelerate the "greening" of the energy industry and stimulate the development of RES in Ukraine, the "green" tariff model has been introduced for many years. On the one hand, this has allowed a significant push for creating a new industry and the rapid development of small-scale generations. Thus, from 2018 to 2022, the total capacity of household installations for producing energy from solar radiation will increase more than fivefold and, by the beginning of 2022, will amount to 1205 MW (about 45 thousand units) [29].

On the other hand, this model has a number of limitations and shortcomings that have led to abuses and do not allow to ensure the stability and sustainability of the development of "green" generation:

firstly, the introduction of the "green" tariff did not promote self-sufficiency and energy independence, but rather the targeted sale of electric energy at a higher tariff;

secondly, such a model leads to a number of technical challenges and distorts the ideology of support for small-scale generation from renewable energy sources in order to bring clean "green" energy closer to consumers;

thirdly, the mechanism for supporting RES generation is currently regulated only for households (up to 30 kW) and energy cooperatives (up to 150 kW) [29].

For this reason, the issues of modernization of coal-fired power plants have so far been of secondary importance.

Among the models of "greening" of coal-fired power generation, which have been used for many years in foreign practice, in particular in Poland, Germany, Portugal, the Czech Republic, Greece, Italy, and are still used in Austria, Denmark, the Netherlands, Great Britain, etc., there is a transitional payment model [8, p.88].

The results of calculations of transitional payment volumes carried out by IEP of NASU are summarized in Table 3.

Table 3 – Calculations of transitional payment volumes for three options for the distribution of charges between household and non-household consumers [8, pp. 156-164].

Years	Household consumers (permanent payment per month, UAH)			Non-household consumers (transitional payment rate per 1 kW, UAH)		
	Alternative options for charging a transitional fee					
	30/70	50/50	70/30	30/70	50/50	70/30
1	0.662006	1.103343	1.544680	0.003704	0.002645	0.001587
2	2.871502	4.785837	6.700171	0.016065	0.011475	0.006885
3	4.828002	8.046671	11.265339	0.027010	0.019293	0.011576
4	6.873052	11.455086	16.037120	0.038451	0.027465	0.016479
5	9.166880	15.278133	21.389386	0.051284	0.036632	0.021979
6	11.848635	19.747725	27.646815	0.066287	0.047348	0.028409
7	13.404559	22.340931	31.277304	0.074992	0.053566	0.032139
8	14.964699	24.941166	34.917632	0.083720	0.059800	0.035880
9	15.635138	26.058564	36.481989	0.087471	0.062479	0.037488
10	15.829102	26.381836	36.934570	0.088556	0.063254	0.037953
11	15.458041	25.763402	36.068763	0.086480	0.061772	0.037063
12	13.703937	22.839895	31.975853	0.076667	0.054762	0.032857
13	12.228129	20.380214	28.532300	0.068410	0.048865	0.029319
14	10.545707	17.576178	24.606649	0.058998	0.042141	0.025285
15	8.251878	13.753131	19.254383	0.046165	0.032975	0.019785
16	5.570123	9.283539	12.996955	0.031162	0.022259	0.013355
17	4.014199	6.690332	9.366465	0.022457	0.016041	0.009625
18	2.454059	4.090098	5.726137	0.013729	0.009807	0.005884
19	1.783620	2.972700	4.161780	0.009978	0.007127	0.004276
20	1.589657	2.649428	3.709199	0.008893	0.006352	0.003811
21	1.298712	2.164519	3.030327	0.007266	0.005190	0.003114
22	0.843319	1.405532	1.967745	0.004718	0.003370	0.002022
23	0.362627	0.604379	0.846130	0.002029	0.001449	0.000869



Its difference lies in the fact that when the TPP/CHP receives bank loans to implement modernization projects, a clear schedule of fixed income for the entire project life cycle is established. Therefore, researchers from the Institute of Economics and Forecasting of the National Academy of Sciences of Ukraine recommended implementing this model in Ukraine. In the report [8], they provide calculations of the amount of transitional payment for three options for the distribution of charges between household and non-household consumers:

- option 30/70, where 30 % of the transitional payment is charged to household consumers and 70 % to non-household consumers;

- the 50/50 option, where 50 % of the transitional payment is charged to household consumers and 50 % to non-household consumers;

- the 70/30 option, where 70 % of the transition payment is collected from household consumers and 30 % from non-household consumers [8].

The transitional payment model provides for financing the repayment of loans taken out by thermal power plants

for implementing environmental projects. Therefore the term of its operation should be set to the term of repayment of loans taken out by plant operators for the implementation of environmental projects according to the requirements of the NPRE [8].

However, this model can be used to implement projects to modernize coal-fired power plants. In this case, obtaining bank loans will only increase the cost of projects requiring significant investments.

At present, energy companies have a unique opportunity to attract ESG investments and thereby ensure the economically secure future of energy companies [19]. A clear example of this is the companies of the DTEK Group, which have set an ambitious goal in their strategy - to become a carbon-neutral company, a leader in decarbonization in Central and Eastern Europe.

DTEK started its decarbonization journey in 2012 by constructing the first 3 MW wind turbine at the Botievska wind farm. Today, DTEK manages 1 GW of green generation (Table 4) [30-32].

Table 4 – Dynamics of electricity production indicators by DTEK Group (Ukraine) during 2012-2021 by types of generation

Characteristics	Years									
	2012	2013	2014	2015	2016	2017	2018	2019	2020	2021
Electricity production in total, billion kWh	47.6	53.0	47.8	38.3	39.5	37.1	34.7	29.8	26.2	25.4
Including wind and sun power plants, billion kW/year	–	–	–	–	0.7	0.6	0.6	1.4	2.4	2.6
Including TPP and CHP, billion kW/year	47.6	53.0	47.8	38.3	40.1	36.5	34.1	28.4	23.8	21.4

DTEK Group’s ambition is to secure the interests of its stakeholders, who today expect companies to take responsibility for future generations by creating material goods and values. Therefore, the holding company has followed ESG principles recently and aims to attract ESG investments shortly.

However, investors making decisions about investing capital in implementing modernization and environmental protection projects need to study the background of ESG investments and follow up on previous investments in environmental measures with the effect of decoupling.

In order to determine the possibility of attracting ESG investment by DTEK Group, we will carry out sectoral

mapping according to the data in Tables 5-6 [30-32], which will provide an opportunity to determine the Group’s portfolio at this stage.

The data in Table 5 show that during the period studied, the DTEK Group is successfully developing and increasing its assets. The volumes of capital investments and environmental costs are also increasing (Table 6).

With the growth of capital investments, indicators of environmental pollution are also significantly reduced, which we can observe according to the data in Table 7 [30-32].

Table 5 – Dynamics of performance indicators of the DTEK Group Ukraine (2012-2021)

indicators	Years									
	2012	2013	2014	2015	2016	2017	2018	2019	2020	2021
Income, UAH billion	82.6	92.8	93.3	95.4	131.8	145.1	157.6	137.7	116.0	112.4
EBITDA, UAH billion	16.9	14.9	18.9	7.5	30.6	37.2	42.9	32.7	31.9	32.1
EBITDA margin, %	14.3	10.9	10.3	8.0	23.0	28.0	27.0	24.0	22.0	22.0
Net profit (loss), billion UAH	6.0	3.3	–19.7	–41.9	–1.2	4.6	12.4	12.6	–13.8	7.6
Assets, UAH billion	76.9	95.1	110.8	119.8	140.6	152.5	148.0	168.3	180.4	179.5
Capital investments, billion UAH	10.2	10.3	6.5	5.0	7.1	10.4	19.9	23.2	11.2	12.4
Taxes paid in Ukraine, billion UAH	9.8	10.4	12.8	14.1	17.9	22.5	26.7	23.4	20.2	19.8

Table 6 – Dynamics of ecoinvesting indicators of the DTEK Group Ukraine (2012-2021)

Indicators	Years									
	2012	2013	2014	2015	2016	2017	2018	2019	2020	2021
The volume of capital investments of DTEK:	10193	10310	6460	5015	7781	10388	19878	23180	11197	12445
DTEK Energo	7077	6698	4860	3570	6194	8416	6037	5186	1195	1896
Including mining and beneficiation of coal	3855	4212	3008	2460	3912	4552	4061	3804	3069	2165
Electricity generation	3222	2486	1852	1110	1357	2725	1511	1099	1874	2134
DTEK Networks	1495	1806	481	418	827	992	1932	3525	4853	4913
DTEK RES	1420	1562	153	7	8	370	9556	10968	36	2789
DTEK Naftogaz	201	119	940	947	932	1143	1685	2559	2524	2611
Environmental costs (excluding eco-tax), total, million UAH	548.5	976.0	777.2	822.5	858.4	1126.8	1378.3	1362.2	741.5	1080
Including capital costs, million UAH	–	370.8	203.2	101.9	111.9	349.2	299.7	371.8	250.5	344.9
Current costs, million UAH	–	526.5	507.9	659.7	672.6	732.4	1014.7	938.1	444.4	512.1
Additional costs, million UAH	–	78.7	66.1	60.9	73.8	46.1	62.9	52.3	46.6	44.8

Table 7 – Dynamics of pollution indicators of the DTEK Group Ukraine (2012-2021)

Indicators	Years									
	2012	2013	2014	2015	2016	2017	2018	2019	2020	2021
Gross greenhouse gas emissions (GHG), thousand tons	60688.4	62545.7	56339.1	47606.6	50266.8	43598.9	35725.5	31340.5	29951.3	29007.9
Pollutant emissions, thousand tons	1126.7	1090.9	724.3	554.7	–	863.8	771.8	723.1	607.8	592.9
Water intake volumes, m <sup>3</sup>	2193.9	2190.2	1985.9	1700.1	1816.5	1635.9	1375.2	1314.8	1136.6	1131.2
Land reclamation, ha	10.2	10.9	18.2	25.6	30.1	39.3	10.9	20.1	97.8	75.6
The total volume of waste generation, million tons	21.6	21.5	19.3	16.2	17.9	17.6	13.8	13.7	12.3	12.1
Including volume of waste processing, million tons	2.4	2.6	2.3	1.6	3.9	3.1	3.4	5.9	5.3	5.3

Using the indicator of capital investment and environmental pollution, the DTEK group will conduct a decoupling analysis, allowing us to determine the presence/absence of the decoupling effect. The decoupling effect is present in the case when, under the positive dynamics of economic growth, the indicators of negative environmental impact remain stable or show a tendency to decrease over the same period [11, 33].

According to the OECD methodology [34], the effect of decoupling is estimated by the Decoupling Index:

$$DecInd = \left( \frac{EP}{DF} \right)_{ending} \left( \frac{EP}{DF} \right)_{beginning}^{-1} = \frac{K_{EPending}}{K_{DFbeginning}}, \quad (1)$$

where  $EP$  – an indicator of the anthropogenic pressure on the environment (environmental pressure), natural units;  $DF$  – an indicator of economic growth (driving force), it is displayed most often through the gross internal product, monetary unit;  $K_{EP}$ ,  $K_{DF}$  – the rate of increase in the general indicators in the ending and base (beginning) periods of the pre-season (years), respectively.

Let us consider the following values to measure  $DecInd$ :  $K_{eco}$  – is a chain growth rate to the previous year of the polluting factor of the DTEK enterprise (negative

impact on the environment (NII)), %.  $K_{EV}$  – a chain growth rate to the previous year of the electricity production volumes, %.

$DecInd$  is calculated by a formula similar to formula (1):

$$DecInd(t) = \frac{K_{eco t}}{K_{EV t}}, \quad (2)$$

where  $t$  – the year;  $K_t$  – the chain growth rate of the corresponding indicator:

$$K_t = (T_t - 100)\%; \quad (3)$$

$T_t$  – the chain index of the corresponding indicator:

$$T_t = \frac{y_t}{y_{t-1}} \cdot 100\%; \quad (4)$$

$y_t$  – the value of the corresponding indicator in the considered year;  $y_{t-1}$  – the value of the corresponding indicator in the previous year.

The data from Table 7 allows for carrying out the decoupling analysis.

Table 8 – Categories of Decoupling Index by Tapio

Weak 0 < Decoupling Index < 0.8	Strong Decoupling Index < 0	Recessive	Expansive
Positive Decoupling-effect		1.2 > Decoupling Index > 0.8 Coupling effect	
Observed if the condition of simultaneous growth of economic growth rates and NII, but when the growth rates of the former exceed the latter	Observed if conditions of growth of economic growth rates and a simultaneous decrease in rates of NII	Observed if the rate of economic growth and NII tend to decrease	Observed if the rate of economic growth and NII tend to increase
Negative Overcoupling effect		Decoupling Index > 1.2	
Observed if the rate of economic growth and the rate of change of NII tend to decline, but when the rate of decline of economic growth exceeds the rate of decline of NII	Observed if the rate of economic growth tends to decline and the rate of change in NII to increase	Decoupling-effect observed if with a simultaneous decline in economic growth and NII, but when the rate of decline in NII exceeds the rate of decline in economic growth)	Overcoupling-effect observed if the rate of economic growth and the rate of change of NII tend to increase, but when the growth rate of the latter exceeds the former

To describe the decoupling effect of transportation by rail, we will use the classification of decoupling types according to P. Tapio [33]. Depending on the density of the relationship between economic growth and the rate of nature of the Decoupling Index, researchers distinguish four subcategories and eight logical degrees (Table 8).

Let us denote:  $T_{GHG}$  is an index of gross greenhouse gas emissions, %;  $T_Z$  is an index of pollutant emissions, %;  $T_W$  is an index of water intake volumes, %;  $T_G$  is an index of volumes of unprocessed waste.

#### 4 Results and Discussion

Applying the chain growth indices of the corresponding indicators calculated according to formula (4), we offer the following formula for finding the integral indicator of the growth rates of NII, using the geometric mean, that is, a number that can be used to replace each of these numbers so that their product does not change:

$$T_{Integ} = \sqrt[4]{T_{GHG} \cdot T_Z \cdot T_W \cdot T_G} \quad (5)$$

Guided by formula (3), let us find an integral indicator of the growth rate of negative factors, %:

$$K_{Integ} = (T_{Integ} - 100)\% \quad (6)$$

We propose to calculate the integral  $DecInd$  by a formula similar to formula (2):

$$DecInd_{Integt} = \frac{K_{Integt}}{K_{EVt}} \quad (7)$$

Similarly to (7), we make a notation of  $K_{Inv}$  is the chain growth rates compared to the previous year according to the volume of capital investments in DTEK, %.

$$DecInd_{Integt} = \frac{K_{Integt}}{K_{Invt}}$$

The calculation results are summarized in Table 9 and Figure 1.

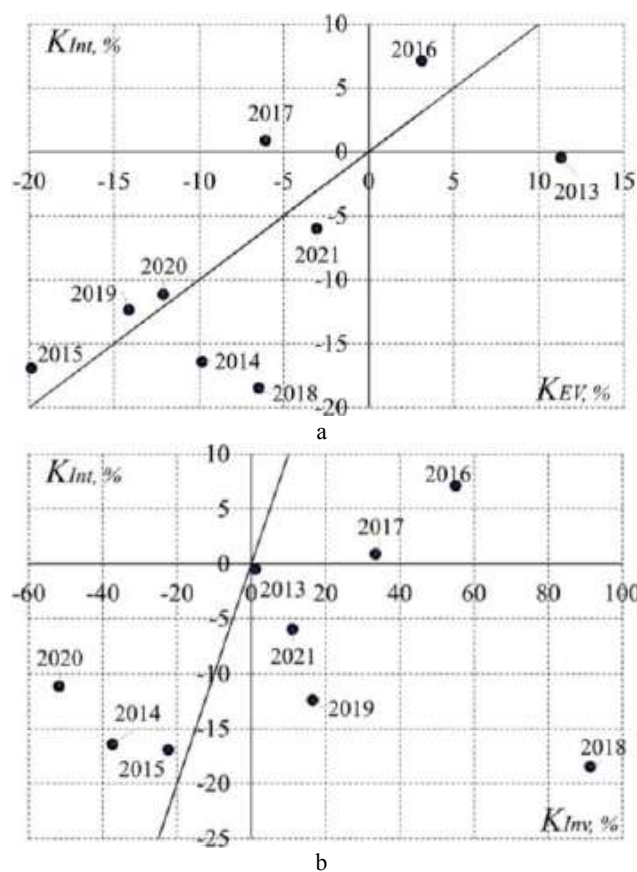


Figure 1 – The dynamics of growth indices of the integral indicator of polluting factors of the DTEK from the volume of electricity production (a) and capital investment (b)

According to the classification of types of decoupling according to P. Tapio [33], the trend of growth rates of electricity generation volumes and the integral indicator of environmental pollution is accompanied by a recessive coupling-effect since both the indicators of electricity production volumes and the indicators of environmental pollution during the analyzed period show a decline. Besides, almost at the same speed.

Table 9 – Decoupling Index Dynamics of DTEK (2013-2021)

Year	Decoupling Index relative to the volumes of electricity production					Integral Decoupling Index relative to investments
	GHG	emissions of pollutants	volumes of water intake	volumes of unprocessed waste	Integral	
2013	0.2698	-0.2801	-0.0149	-0.1377	-0.0430	-0.4254
2014	1.0114	3.4251	0.9507	1.0246	1.67457	0.4400
2015	0.7799	1.1782	0.7241	0.7103	0.8527	0.7576
2016	1.7835	6.9144	2.1852	-1.311643836	2.2691	0.1289
2017	2.1832	-4.6075	1.6363	-0.5878	-0.1441	0.0261
2018	2.7916	1.6464	2.4634	4.37101	2.8580	-0.2024
2019	0.8692	0.4468	0.3110	1.7704	0.8768	-0.7454
2020	0.3669	1.3199	1.1219	0.8490	0.9230	0.2157
2021	1.0316	0.8028	3.1436	2.8071	1.9638	-0.5380

The trend of growth rates of capital investments and the integral indicator of environmental pollution is also accompanied by a recessive coupling effect, but at a faster rate, which shows that with each unit of capital investment in the modernization of TPPs and CHPs of the DTEK Group, the amount of environmental pollution is rapidly reduced.

Regression analysis methods are used to identify implicit and veiled relationships between observation data.

In this case, linear regression does not adequately approximate the experimental data. Thus, the challenge is to find a nonlinear multiple regression equation that fits the empirical points well, preferably in the best possible way. The model specification is proposed to be carried out by the method of directed enumeration using the method of least squares (LSM) [35]. The approximation quality is estimated using the coefficient of determination (the closer to one, the better) and the average approximation error (the closer to zero, the better). The contribution of each independent variable to the variation of the studied (predicted) dependent variable is determined based on the constructed regression equation.

As is well known [36], LSM works well when the number of experiments sufficiently exceeds (by about an order of magnitude) the estimated components of the regression equation. The deterioration of the ratio between the number of estimated coefficients and the number of experiments has negative consequences for the following reasons. First, the variances of the estimates of the values of the elements of the vector of coefficients located on the main diagonal of the covariance matrix of the estimation errors increase. Second, it reduces the degrees of freedom, which is equal to the difference between the number of experiments and estimated parameters, leading to an expansion of the confidence intervals covering the actual values of the regression equation coefficients. The consequence is an increase in the probability of accepting the hypothesis of the insignificant factors for which the calculated confidence intervals cover zero. Thus, the cumulative effect of these causes under conditions of lack of initial data reduces the adequacy of the model.

Promising possibilities arise when using artificial orthogonalization of the results of a passive experiment [11, 35]. The set of results of statistical data on DTEK reports forms a passive experiment. At the same time, the corresponding matrix of initial data is not orthogonal, which excludes the possibility of independent evaluation of the influence of each of the factors and their interactions, which ensures the elimination of insignificant components of the regression equation.

First, we convert the scaling (normalization) of the actual values of the factors to the interval (0; 1] according to the formula:

$$X_i^* = X_i / X_{\max}$$

where  $X$  – the considered factor;  $i = \overline{1,10}$  – an observation number.

The technology of processing the results of a passive experiment [36] is used, which makes it possible to establish a relationship between the values of greenhouse gas emissions (the determining parameter of the studied complex system) and a large number of supposedly influencing factors in a situation where the total number of experiments is not enough to build an adequate model. This enabled it to independently filter out insignificant factors and interactions, simplifying the estimated regression equation's structure and increasing its accuracy. Thus, we limited ourselves to only four factors that most impact greenhouse gas emissions.

As a result, a multifactor nonlinear dependence was constructed:

$$GHG^* = 0.1814 - 0.2158 \cdot \sqrt{S^*} - 0.0594 \cdot I^{*3/2} + 1.0273 \cdot E^* \quad (8)$$

where  $GHG^*$  – gross emissions of GHG;  $S^*$  – environmental costs (excluding eco-tax);  $I^*$  – investments in the modernization of the DTEK group (capital investments);  $E^*$  – electricity production; symbol “\*” means that we are considering normalized dimensionless quantities.

The coefficients of the multivariate nonlinear regression (8) after the initial linearization were found in matrix form by the generalized least squares method.

According to model (8), we can see that the growth of electricity production causes an increase in greenhouse gas emissions. They are in a direct linear relationship. The minus sign before investments in modernization and environmental costs shows that gross greenhouse gas emissions decrease when these parameters increase.

The obtained coefficient of determination for this model is  $R^2 = 0.986$ . It is close to 1, indicating sufficient density between the variables.

The calculated value of the Fisher coefficient according to the sample data is  $F = 143.46$ , and the critical value of the Fisher coefficient is  $F_{kr} = 4.76$  according to the degrees of freedom 6, 3, and the significance level.

According to Fisher's test,  $F > F_{kr}$  showed that with a reliability of 95 %, it is assumed that the proposed mathematical model is adequate to the statistical data, and based on the accepted model, economic analysis can be carried out.

The average approximation error  $\bar{A} = 2.88$  %. Thus, the regression values differ from the corresponding empirical values by an average of 2.88 %, which can be considered a good enough result.

To implement the emission reduction program, by 2030, it is necessary to reduce by 25 % relative to the value for 2019 [31, 32], i.e., 23505.38 thousand tons, while the production of electricity for 2030 is planned in the amount of 27 000 million kWh [31, 32]. To achieve this goal, forecast values of environmental costs are proposed, which amount to 2292 million UAH. and investments in the modernization of the DTEK group (capital investments), 20 851 million UAH on average per year.

The dependence graph (8) is shown in Figure 2 at a constant volume of electricity production.

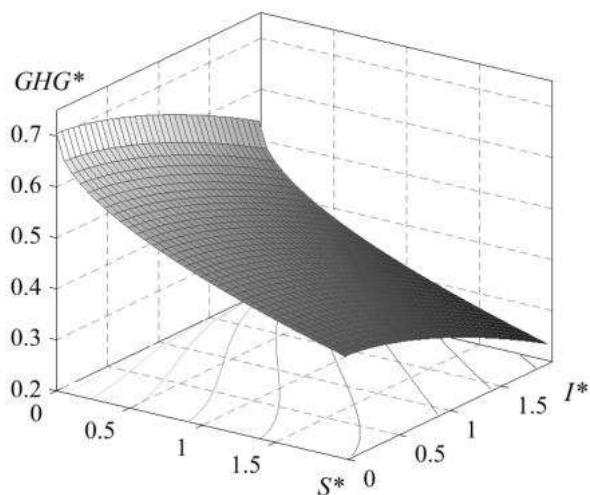


Figure 2 – The surface of the dependence of GHG emission volumes on investments in modernization and environmental costs at a constant volume of electricity production of the DTEK group

For fixed values of the forecast value of environmental costs, 2292 million UAH and the planned 27 000 million kWh electricity production is built according to model (8) graph of the dependence of gross greenhouse gas emissions on the amount of capital investments (Figure 2).

The reliable zone for this regression is constructed for the level of significance  $\alpha = 0.05$  (Figure 3), and the critical value of the Student's coefficient according to the table of values is equal to  $t_{kr} = 2.365$ .

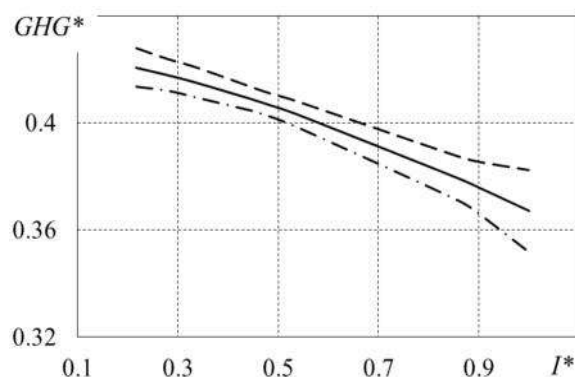


Figure 3 – Regression confidence zone of the dependence of GHG emission volumes on investments in modernization at a constant environmental cost and constant volume of electricity production

That is, for the forecast value, the confidence interval for the forecast, calculated with reliability  $p = 95$  %, is  $22\ 009.27 \leq GHG_{pr} \leq 23\ 909.81$ .

## 5 Conclusions

Thus, according to the achieved results, it was established that the high pace of global transformations, the priority of reducing dependence on fuel and energy imports, the development of RES, and the commitment to reduce carbon emissions require immediate measures for the modernization of energy enterprises and, therefore, the implementation of large-scale and capital-intensive projects for the reconstruction of TPP/CHP equipment and construction of facilities for cleaning flue gases from emissions of sulfur dioxide, and nitrogen oxides. The mechanisms and sources of financing are not defined in the NPRE. Unfortunately, however, the mechanisms and sources of their financing are not defined in the NPSV.

The exact financing mechanisms for projects of reconstruction/modernization of power generation facilities that were in operation before the introduction of the new electricity market have lost their relevance, and new ones have not been developed or introduced into the national legislation.

Therefore, it is evident that TPPs/CHPs do not have the necessary resources to finance the modernization of their equipment because the limited prices for electricity established by the National Regulator do not ensure the creation of funds necessary for the implementation of projects for the gasification of their TPPs/CHPs, on the contrary, they make the situation more difficult for the

performance by the electric power industry of Ukraine of the tasks defined by the NPRE.

Using the method of sectoral mapping, an assessment of the country's energy reality and the reconstruction of the power industry in the post-war years were carried out. It is well established that the regulatory changes introduced by the Government to stabilize the industry and solve critical problems are insufficiently effective and unable to ensure the viability of energy enterprises and their further development in the context of "green transformations".

Alternative options for financing the development of energy companies in the context of "green

transformation" were considered. It is well established that a unique opportunity for implementing TPP/CHP modernization projects is the inclusion of ESG investments. It is emphasized that the decision to provide ESG investments in global practice is made based on the results of studying the background of the development of companies, accompanying their previous investments with the decal effect and their compliance with ESG principles. Based on DTEK Group's data, the readiness of energy companies to attract ESG investments has been proven.

## References

1. Levchenko, S. (2023). Ensuring economic security of thermal power plants with accelerated decarbonization of the energy industry. *Economic Herald of State Higher Educational Institution "Ukrainian State University of Chemical Technology"*, Vol. 17 (1), pp. 27-35, <http://dx.doi.org/10.32434/2415-3974>
2. National plan to reduce emissions from large combustion plants. Order of the CMU from 08.11.2011 No. 796-p. Available online: <https://zakon.rada.gov.ua/laws/show/796-2017-%D1%80#Text>
3. On the approval of the Updated Nationally Determined Contribution of Ukraine to the Paris Agreement. Order of the CMU from 30.07.2021 No. 868-p. Available online: <https://zakon.rada.gov.ua/laws/show/868-2021-%D1%80#Text>
4. About the National Energy and Climate Change Plan for the period up to 2030. Order of the CMU from 29.12.2021 No. 1803-p. Available online: <https://zakon.rada.gov.ua/laws/show/1803-2021-%D1%80#Text>
5. Strategy for environmental security and adaptation to climate change for the period up to 2030. Order of the CMU from 20.10.2021 No. 1363-p. Available online: <https://zakon.rada.gov.ua/laws/show/1363-2021-%D1%80#Text>
6. Operational plan for the implementation in 2022-2024 of the Strategy for Environmental Security and Adaptation to Climate Change for the period up to 2030. Order of the CMU from 20.10.2021. No. 1363-p. Available online: <https://zakon.rada.gov.ua/laws/show/1363-2021-%D1%80#Text>
7. Omelchenko, V., Chekunova, S., Bilyavskiy, M., Khytryk, T., Konechenkov, A., Mishchenko, M., and Doborovolskyi, D. (2022). *Decarbonization of Ukrainian Energy (Economics): The Impact of Russian Aggression, Ambitious Goals, and Potential Opportunities for Ukraine in the Postwar Years*. Razumkov Center, Kyiv, Ukraine.
8. Report "Economically justified approach to the introduction of the National plan for reducing emissions in Ukraine based on the experience of reducing emissions of harmful pollutants into the air by large incineration plants in Europe" (2020). *IEPr of NASU*. Available online: [https://vse.energy/docs/Report\\_NP%20.pdf](https://vse.energy/docs/Report_NP%20.pdf)
9. Vlasenko, Yu. (2023). 5 GW of generation in the Ukrainian energy system remain damaged as a result of russian missile attacks – information from the First Deputy Minister of Energy. Available online: <https://interfax.com.ua/news/economic/899696.html>
10. Still time to reverse damage to 'ravaged' ecosystems, declares UN chief, marking World Environment Day (2021). Available online: <https://news.un.org/en/story/2021/06/1093382>
11. Dvignun, A., Datsii, O., Levchenko, N., Shyshkanova, G., Platonov, O., and Zalizniuk, V. (2022). Increasing ambition to reduce the carbon trace of multimodal transportation in the conditions of Ukraine's economy transformation towards climate neutrality. *Science and Innovation*, Vol. 18 (1), pp. 96-111, <https://doi.org/10.15407/scine18.01.096>
12. Arroyo, F. R. M., Miguel, L. J. (2020). Low-carbon energy governance: Scenarios to accelerate the change in the energy Matrix in Ecuador. *Energies*, Vol. 13(18), 4731, <https://doi.org/10.3390/en13184731>
13. Madaleno, M., Nogueira, M.C. (2023) How renewable energy and CO<sub>2</sub> emissions contribute to economic growth, and sustainability – An extensive analysis. *Sustainability*, Vol. 15, pp. 33-47, <https://doi.org/10.3390/su15054089>
14. Zhang, H., Chen, H. H., Lao, K., Ren, Z. (2022). The Impacts of resource endowment, and environmental regulations on sustainability – Empirical evidence based on data from renewable energy enterprises. *Energies*, Vol. 15, 4678, <https://doi.org/10.3390/en15134678>
15. Li, Z., Shen, T., Yin, Y., and Chen, H. H. (2022). Innovation input, climate change, and energy-environment-growth nexus: evidence from OECD and Non-OECD countries. *Energies*, Vol. 15(23), 8927, <https://doi.org/10.3390/en15238927>
16. Ahmed Z., Cary, M., Shahbaz, M., Vo, X. V. (2021). Asymmetric nexus between economic policy uncertainty, renewable energy technology budgets, and environmental sustainability: Evidence from the United States. *Journal of Cleaner Production*, Vol. 313, 127723, <https://doi.org/10.1016/j.jclepro.2021.127723>
17. Papadis, E., Tsatsaronis, G. (2020). Challenges in the decarbonization of the energy sector. *Energy*, Vol. 205, 118025, <https://doi.org/10.1016/j.energy.2020.118025>

18. Fan, X., Ji, W., Guo, L., Gao, Z., Chen, L., Wang, J. (2023). Thermo-economic analysis of the integrated system of thermal power plant and liquid air energy storage. *Journal of Energy Storage*, Vol. 57, 106233, <https://doi.org/10.1016/j.est.2022.106233>
19. Hayduky, I. P. (2017). Low-carbon development: global motivation tools. *Investments: Practice and Experience*, Vol. 2, pp. 22-26.
20. Nitlar, T., Kiattisin, S. (2022). The impact factors of Industry 4.0 on ESG in the energy sector. *Sustainability*, Vol. 14(15), 9198, <https://doi.org/10.3390/su14159198>
21. Polyakova, K. (2023). Green energy: Action plan for 2023. *Economic Truth*. Available online: <https://www.epravda.com.ua/columns/2023/01/24/696297>
22. Hurduzeu, G., Noja, G. G., Cristea, M., Drăcea, R. M., Filip, R. I. (2022). Revisiting the impact of ESG practices on firm financial performance in the energy sector: new empirical evidence. *Economic Computation & Economic Cybernetics Studies & Research*, Vol. 56(4), pp. 37-53, <http://dx.doi.org/10.24818/18423264/56.4.22.03>
23. Kharisova, A. Z., Shvayko, I. V., Shalina, O. I., Ostryakova, A. F., Singizov, I. Y. (2022). Ensuring economic security by modifying renewable energy systems. In: Popkova, E.G., Sergi, B.S. (eds) *Geo-Economy of the Future*. Springer, Cham, Switzerland, pp. 851-858, [https://doi.org/10.1007/978-3-030-92303-7\\_88](https://doi.org/10.1007/978-3-030-92303-7_88)
24. Borysiak, O. V. (2022). Innovative potential of energy enterprises and critical climate technologies within war conditions. *Innovative Economy*, Vol. 2-3, pp. 25-28, <https://doi.org/10.37332/2309-1533.2022.2-3.4>
25. Belousova, K. (2022). Ukraine to replace green tariff with a new Net billing model. Available online: <https://ecopolitic.com.ua/ua/news/v-ukraini-hochut-zaminiti-zelenij-tarif-na-novu-model-net-billing-shho-zminitsya/>
26. A European Green Deal, striving to be the first climate-neutral continent. *European Commission*. Available online: [https://ec.europa.eu/info/strategy/priorities-2019-2024/european-green-deal\\_en](https://ec.europa.eu/info/strategy/priorities-2019-2024/european-green-deal_en)
27. On Approval of the Regulation on Imposition of Special Duties on the Transmission System Operator to Ensure the Public Interests in the Process of Functioning of the Electric Energy Market. The CMU Resolution 838-2022-p of 22.07.2022. Available online: <https://zakon.rada.gov.ua/laws/show/838-2022-%D0%BF#Text>
28. Levchenko, S. (2022). Toolkit for providing economic and safe future of energy enterprises. *Economic Herald of State Higher Educational Institution "Ukrainian State University of Chemical Technology"*, Vol. 16(2), pp. 30-38, <https://dx.doi.org/10.32434/2415-3974-2022-16-2-30-38>
29. Vlasenko, Yu. (2022). How to provide 25% of energy from RES without support from the budget. *Economic Truth*. Available online: <https://www.epravda.com.ua/columns/2022/07/25/689577>
30. Reporting of DTEK financial and non-financial results 2012-2020. Available online: [https://dtek.com/investors\\_and\\_partners/reports](https://dtek.com/investors_and_partners/reports)
31. Financial statement DTEK 2021. Available online: <https://energo.dtek.com/en/ir/financial-statements-2021>
32. Sustainable Development DTEK. Available online: [https://dtek.com/sustainable\\_development/reportsesg](https://dtek.com/sustainable_development/reportsesg)
33. Tapio, P. (2005). Towards a theory of decoupling: degrees of decoupling in the EU and the case of road traffic in Finland between 1970 and 2001. *Transport Policy*. Vol. 12, pp. 137-151, <https://doi.org/10.1016/j.tranpol.2005.01.001>
34. Mensah, C. N., Long, X., Boamah, K. B., Bediako, I. A., Dauda, L., Salman, M. (2018). The effect of innovation on CO<sub>2</sub> emissions of OECD countries from 1990 to 2014. *Environmental Science Pollution Research*, Vol. 25, pp. 29678-29698, <https://doi.org/10.1007/s11356-018-2968-0>
35. Greene, W. H. (2018). *Econometric Analysis*. Pearson, New York, USA
36. Pal, M., Bharati, P. (2019). *Applications of Regression Techniques*. Springer Nature, Singapore, <https://doi.org/10.1007/978-981-13-9314-3>



The emergence of innovative technologies and new business models based on innovation, cooperation networks, and the enhancement of endogenous resources, are assumed to be a strong contribution to the development of competitive economies all around the world. Innovation and Engineering, focused on sustainability of resources, have a key role in this context.

ICIE is an event that is not based only in a purely academic but also technological and innovative dimensions, across the most diverse sectors of activity.

The objective of this conference is to make this moment an opportunity to show the set innovations and engineering achievements, as well as to transmit to all participants an overview about potentiating the foundations for the creation of networks of knowledge and entrepreneurial cooperation, involving Innovation, Engineering and Entrepreneurship stakeholders.

This edition is specially focused on new trends and evolutions in a context of a more advanced technology and innovation capacity, being able for creation of added value for economy and society, based in some basic principles as human wellbeing, environment and sustainability of resources.

The conference will be held on June 26th-28th, 2024, in Municipal Auditorium of Povoação, Municipal Garden Square 9650-410 Povoação – São Miguel Island Azores – Portugal.

Accepted papers will be published by **Springer** as **Lecture Notes in Mechanical Engineering** series. The books of this series are submitted to, among others, **ISI Proceedings (Web of Science)** and **SCOPUS**.

## **DEADLINES:**

**Full paper Submission:** January 15th, 2024;

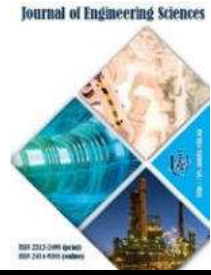
**Notification of Acceptance:** February 19th, 2024;

**Camera Ready:** February 26th, 2024;

**Registration:** March 11th, 2024;

**Conference days:** June 26th – 28th, 2024.





Javanbakht T. (2023). A novel automated decision-making process for analysis of ions and organic materials in drinking water. *Journal of Engineering Sciences*, Vol. 10(1), pp. H1-H7, doi: 10.21272/jes.2023.10(1).h1

## A Novel Automated Decision-Making Process for Analysis of Ions and Organic Materials in Drinking Water

Javanbakht T.

Department of Computer Science, University of Quebec in Montreal,  
201 President Kennedy St., Montreal, H2X 3Y7 Quebec, Canada

### Article info:

Submitted: December 5, 2022  
Received in revised form: February 6, 2023  
Accepted for publication: February 20, 2023  
Available online: February 24, 2023

### \*Corresponding email:

[javanbakht.taraneh@courrier.uqam.ca](mailto:javanbakht.taraneh@courrier.uqam.ca)

**Abstract.** This paper applies a novel automated decision-making process with TOPSIS to analyze ions and organic materials in drinking water. The hypothesis was that the modified TOPSIS algorithm with the Łukasiewicz fuzzy disjunction would be appropriate to optimize the drinking water samples. The maximum output values were set to one to apply the fuzzy disjunction. The concentrations of ions and organic materials in the drinking water samples were considered from the values for naturally occurring chemicals that would be of health significance. Materials with positive effects on the body were considered profit criteria, whereas other ones with negative impacts on human health were considered cost criteria. The analysis of samples with unmodified TOPSIS showed that profit criteria having high concentrations and cost criteria having low concentrations had the dominant effects on the candidates' ranking. The modified TOPSIS showed that the candidates' ranking in the second analysis series was the same as in the first. However, the value of 1.0 for the fourth candidate's concentration of nitrite, which resulted from the fuzzy disjunction in the algorithm of the modified TOPSIS, was attributed to the confusion of the drinking water and undrinkable water categories. The optimization results for drinking water samples could be applied in science and engineering based on the concentrations of their ions and organic materials with the automated decision-making process for their distinction from undrinkable water.

**Keywords:** drinking water, automated decision-making process, health public, environment.

## 1 Introduction

Access to drinking water in the environment is a key factor for human survival. The lack of this material in many regions has searched for drinking water a first-order task. For this purpose, many industries produce large-scale drinking water each year to overcome this challenge. However, diseases due to drinking polluted water cause more than 1 million deaths per year [1]. Therefore, the distinction and analysis of drinking water are crucial processes. This is a remaining need to search for water on the planets with primordial atmosphere [2-4]. The already applied approach is based on the registration of several photos obtained by satellites and their analysis by humans on Earth. At this level, all the tasks of gathering and analyzing the data are carried out by humans. However, the environmental conditions where drinking water would be searched would not always be

appropriate for humans because of the lack of atmosphere, polluted environment, and extreme temperatures. Therefore, developing an automated decision-making process that distinguishes drinking water from undrinkable water and performs appropriate analysis and optimization is urgently needed.

The Technique for Order of Preference by Similarity to Ideal Solution (TOPSIS) is a multi-criteria decision-making method with many applications in science and engineering [5-9]. This method ranks the candidates based on their distances from ideal solutions and closeness coefficients [10-14].

The characteristics of drinking water, such as its total dissolved solids, hardness, electrical conductivity, and cost, depend on the concentration of its ions [15-18]. Previous work presented the analysis of drinking water and undrinkable samples according to these characteristics with TOPSIS [7]. In the present paper, this method has

been used to analyze the concentrations of ions with a new perspective for science and environmental applications. For this purpose, the modified version of the TOPSIS method in a recently developed software has been used to optimize and rank candidates.

Appropriate amounts of minerals in drinking water are essential for human health. Calcium is essential as the extracellular mineral forms different skeleton parts, such as teeth and bones [19]. Magnesium has several functions, such as helping the muscle and nervous system and binding to targets in enzymatic reactions [20]. Boron is essential for bone and central nervous system growth, hormone regulation, and reducing the risk of cancer, arthritis, and heart disease symptoms. It also positively accelerates wound healing and reduces pain in gynecological diseases and kidney stones by decreasing cytokines [21]. Copper has several roles in the body, such as storing calcium in bones and repairing or building connective tissues [22]. Chlorine is converted to chloride in the body. Sodium and chloride are the principal cation and anions of the body, respectively [23]. These ions maintain an equilibrated sodium balance to maintain body volume and blood pressure system and regulate blood pressure [23, 24]. Therefore, these minerals are considered in the current work as profit criteria for the analysis with unmodified and modified TOPSIS methods. It has been shown that nitrite consumption harms human health, leads to methemoglobinemia, and increases cancer incidence by promoting the formation of potentially carcinogenic nitrosamines [25, 26]. Hence, this ion was considered a cost criterion for this investigation with TOPSIS.

This paper is aimed to analyze and optimize the drinking water samples according to the concentrations of their ions using the unmodified and modified TOPSIS methods, this second algorithm for performing an automated decision-making process. Three tasks have been performed with the developed software: 1. optimization of drinking water samples with unmodified TOPSIS, 2. modification of TOPSIS with the Łukasiewicz fuzzy disjunction for performing automated decision making, 3. optimization of drinking water samples with modified TOPSIS for their analysis and optimization.

The application of an automated decision-making process for detecting and analyzing ions in drinking water samples for their distinction from undrinkable water and their optimization has not been performed yet. The current research results on these issues can be applied in science and engineering.

## 2 Research Methodology

The standard concentrations of ions in drinking water were considered from the World Health Organization (WHO) guideline for naturally occurring chemicals, according to which these concentrations would be of health significance.

The concentrations of the ions and organic materials for health significance in the standard drinking water sample, which was the first sample or candidate indicated as C<sub>1</sub> in the TOPSIS matrices, would be as below: calcium (80 mg/L), magnesium (60 mg/L), boron (2.4 mg/L), copper (2 mg/L), sodium (50 mg/L), chlorine (5 mg/L), nitrite (3 mg/L), 1,2-dichlorobenzene (1 mg/L), monochloramine (2 mg/L), dichloroisocyanurate (40 mg/L), and toluene (1 mg/L). The second, third, and fourth samples were indicated as C<sub>2</sub>, C<sub>3</sub>, and C<sub>4</sub>, respectively. Their ions and organic materials concentrations were proportional to the first candidate's.

The TOPSIS code in Python presented on GitHub was used to analyze and optimize candidates as described previously [8, 9, 27].

The ions and organic materials determined the characteristics of drinking water samples, such as hardness, turbidity, etc. As the analysis of their concentrations was the aim of this paper, they were considered as criteria. Their concentration values were divided by 100 to adjust them between 0.0 and 1.0 and make them similar to fuzzy membership degrees for their use in the TOPSIS method.

The modified TOPSIS, including the Łukasiewicz fuzzy disjunction, was used in this paper, and this method was described previously [8]. The data analysis with the modified algorithm considered the members of drinking and undrinkable water categories. The category confusion due to humans' inappropriate consideration of the criteria that led to the inconsistency of their epistemic beliefs was analyzed as explained previously [8, 28].

The maximum value of 1.0, according to the Łukasiewicz fuzzy disjunction, was observed in the evaluation matrix in the output of TOPSIS [28].

## 3 Results

The first series of results were obtained with the unmodified TOPSIS algorithm.

Tables 1-2 show matrices of the triangular fuzzy data corresponding to the concentrations of ions and organic materials in the water samples and their average values.

Table 1 – Matrix of triangular fuzzy data for different water samples

Candidates/Criteria	Calcium	Magnesium	Boron	Copper	Sodium	Chlorine	Nitrite
C <sub>1</sub>	0.7, 0.8, 0.9	0.5, 0.6, 0.7	0.01, 0.02, 0.03	0.01, 0.02, 0.03	0.4, 0.5, 0.6	0.04, 0.05, 0.06	0.02, 0.03, 0.04
C <sub>2</sub>	0.1, 0.2, 0.3	0.1, 0.2, 0.3	0.1, 0.2, 0.3	0.1, 0.2, 0.3	0.4, 0.5, 0.6	0.4, 0.5, 0.6	0.05, 0.06, 0.07
C <sub>3</sub>	0.1, 0.2, 0.3	0.1, 0.2, 0.3	0.3, 0.4, 0.5	0.3, 0.4, 0.5	0.0, 0.1, 0.2	0.0, 0.1, 0.2	0.05, 0.06, 0.07
C <sub>4</sub>	0.3, 0.4, 0.5	0.2, 0.3, 0.4	0.3, 0.4, 0.5	0.7, 0.8, 0.9	0.0, 0.1, 0.2	0.0, 0.1, 0.2	0.00, 0.01, 0.02

Table 2 – Matrix of the mean values of triangular fuzzy data for different water samples

Candidates/Criteria	Calcium	Magnesium	Boron	Copper	Sodium	Chlorine	Nitrite
C <sub>1</sub>	0.8	0.6	0.02	0.02	0.5	0.05	0.03
C <sub>2</sub>	0.2	0.2	0.20	0.20	0.5	0.50	0.06
C <sub>3</sub>	0.2	0.2	0.40	0.40	0.1	0.10	0.06
C <sub>4</sub>	0.4	0.3	0.40	0.80	0.1	0.10	0.01

Tables 3-4 show the weight values applied for each criterion and the criteria matrix of different water samples, respectively.

Table 3 – Weight values applied for each criterion of different water samples

Alternatives/Values	Calcium	Magnesium	Boron	Copper	Sodium	Chlorine	Nitrite
C <sub>1</sub> -C <sub>4</sub>	0.5	0.5	0.5	0.5	0.5	0.5	0.5

Table 4 – Criteria matrix for different water samples

Alternatives/Values	Calcium	Magnesium	Boron	Copper	Sodium	Chlorine	Nitrite
C <sub>1</sub> -C <sub>4</sub>	True	True	True	True	True	True	False

Materials with positive effects on human health were considered profit criteria, whereas those with negative effects were considered cost criteria. Therefore, the term “true” was considered for all the criteria. The exception is those for which “false” was in the criteria matrix in TOPSIS.

Table 5 represents the distances from the best and worst alternatives ( $d_i^*$  and  $d_i^-$ ), the similarity coefficients ( $CC_i$ ), and the ranking of water samples.

Table 5 – The distances from the best and worst alternatives, similarity coefficients, and ranking of different water samples

Candidates	$d_i^*$	$d_i^-$	$CC_i$	Ranking
C <sub>1</sub>	0.1978	0.1518	0.4342	4
C <sub>2</sub>	0.1782	0.1551	0.4655	2
C <sub>3</sub>	0.2071	0.1090	0.3448	1
C <sub>4</sub>	0.1595	0.1751	0.5234	3

As shown in Tables 2, 5, sodium, chlorine, boron, and copper, having high concentrations, and nitrite having low concentrations, had the dominant effects on the candidates’ ranking. Therefore, the fourth candidate, C<sub>4</sub>, was ranked in a position better than the other candidates. Moreover, higher concentrations of boron, copper, and chlorine for the second candidate compared with those for the first candidate showed their effect on the preference of candidate C<sub>2</sub> to candidate C<sub>1</sub> in the ranking. The third candidate, C<sub>3</sub>, having lower concentrations of calcium, magnesium, and sodium and a higher concentration of nitrite, was ranked fourth.

Table 6 – Matrix of the mean values of triangular fuzzy data for different water samples

Candidates/Criteria	Calcium	Magnesium	Boron	Copper	Sodium	Chlorine	Nitrite
C <sub>1</sub>	0.8	0.6	0.02	0.02	0.5	0.05	0.03
C <sub>2</sub>	0.2	0.2	0.2	0.2	0.5	0.5	0.06
C <sub>3</sub>	0.2	0.2	0.4	0.4	0.1	0.1	0.06
C <sub>4</sub>	0.4	0.3	0.4	0.8	0.1	0.1	1.0

Table 7 – Criteria matrix for different water samples

Alternatives/Values	Calcium	Magnesium	Boron	Copper	Sodium	Chlorine	Nitrite
C <sub>1</sub> -C <sub>4</sub>	True	True	True	True	True	True	True

The weight values of 0.5 were applied for each criterion of water samples like the ones applied in the first series of analyses.

Tables 7-8 show the distances from the best and worst alternatives, the similarity coefficients, and the ranking of different water samples.

In the second series of this study, the modified TOPSIS algorithm, with the Łukasiewicz fuzzy disjunction, was used for performing the automated decision-making process, which allowed the appearance of the maximum value of 1.0 in the output.

These modifications were considered in the second series of this analysis: 1. The concentration of the nitrite ion in the fourth candidate was high (0.5 mg/L in place of 0.03 mg/L). 2. Nitrite was considered as a profit criterion like the other ions by the individual. Therefore, the term “true” was considered for all the criteria in the criteria matrix of TOPSIS. This was due to the confusion of the drinking and undrinkable water categories by the individual leading to the appearance of the value of 1.0 for the nitrite concentration for the last water sample (candidate C<sub>4</sub>). Also, this is due to the application of the Łukasiewicz fuzzy disjunction representing the high concentration of this ion and that of the candidate of the undrinkable water category. As the candidates’ membership degrees in this analysis were the concentrations of ions and organic materials in water samples, the addition of the concentration of nitrite for candidate C<sub>4</sub> with that of the undrinkable water sample from the undrinkable water category would be considered according to this fuzzy disjunction (0.5 mg/L + 0.5 mg/L = 1.0 mg/L). As the maximum value of concentrations in the modified TOPSIS algorithm was set to 1.0, this value appeared in the output of the modified TOPSIS.

The two modifications described in the second series of analyses are shown in Tables 6-7.

Table 8 – The distances from the best and worst alternatives, similarity coefficients, and ranking of different water samples

Candidates	$d_i^*$	$d_i^-$	$CC_i$	Ranking
C <sub>1</sub>	0.2391	0.1442	0.3762	4
C <sub>2</sub>	0.2083	0.1552	0.4269	2
C <sub>3</sub>	0.2335	0.1090	0.3183	1
C <sub>4</sub>	0.1595	0.2086	0.5667	3

The comparison of the rankings in the two series of analyses shows the same ranks for the candidates. However, the value of 1.0 appeared in the output of TOPSIS in the second series of analyses. The first rank for the fourth candidate ( $C_4$ ) would not be accepted due to the individual's mistake of considering nitrite in this water sample as a profit criterion, as this ion should have been considered as a cost criterion, as explained in this paper. This candidate would be considered drinking water in the first analysis series, whereas it would be considered undrinkable water in the second.

Boron and copper with excessive doses are harmful to human health and biological systems [29, 30]. Therefore,

Table 9 – Matrix of the mean values of triangular fuzzy data for different water samples

Candidates/ Criteria	Calcium	Magnesium	Boron	Copper	Sodium	Chlorine	Nitrite	1, 2-Dichloro- benzene	Monochlo- ramine	Dichloro- isocyanurate	Toluene
$C_1$	0.8	0.6	0.2	0.2	0.5	0.05	0.03	0.01	0.02	0.4	0.01
$C_2$	0.2	0.2	0.2	0.2	0.5	0.5	0.06	0.02	0.04	0.1	0.02
$C_3$	0.2	0.2	0.4	0.4	0.1	0.1	0.06	0.03	0.04	0.1	0.02
$C_4$	0.4	0.3	0.4	0.8	0.1	0.1	0.01	0.01	0.02	0.2	0.04

Table 10 – Weight values applied for each criterion of different water samples

Alternatives/ Values	Cal- cium	Magne- sium	Bo- ron	Cop- per	So- dium	Chlo- rine	Nit- rite	1, 2-Dichlo- robenzene	Monochlo- ramine	Dichloro- isocyanurate	Tolu- ene	1, 2-Dichloro- benzene
$C_1$ – $C_4$	0.5	0.5	0.1	0.1	0.5	0.5	0.1	0.1	0.1	0.1	0.1	0.1

Table 11 – Criteria matrix for different water samples

Alternatives/ Values	Calcium	Magnesium	Boron	Copper	Sodium	Chlorine	Nitrite	1, 2-Dichlo- robenzene	Monochlo- ramine	Dichloro- isocyanurate	Toluene
$C_1$ – $C_4$	True	True	False	False	True	True	False	False	False	False	False

Table 12 shows the distances from the best and worst alternatives, the similarity coefficients, and the ranking of different water samples.

Table 12 – The distances from the best and worst alternatives, similarity coefficients, and ranking of different water samples

Candidates	$d_i^*$	$d_i^-$	$CC_i$	Ranking
$C_1$	0.1616	0.1918	0.5427	2
$C_2$	0.1584	0.1939	0.5504	1
$C_3$	0.2372	0.0367	0.1339	4
$C_4$	0.2098	0.0608	0.2246	3

As shown in Table 12, the water samples' ranking was modified due to adding organic materials and considering boron and copper as cost criteria. Comparing the obtained results showed that candidate 4 was replaced with candidate 2 as the best candidate in the third analysis series. Moreover, candidate 2 was replaced with candidate 1 and candidate 1 with candidate 4. The rank of candidate 3 did not change in both analysis. These results showed the importance of considering criteria in analyzing candidates with TOPSIS. The presence of the ions and organic materials considered as cost criteria could affect drinking water quality. Their ranking with this method has been helpful for their comparison with the samples without organic materials.

Recently, the TOPSIS method modified by incorporating the Łukasiewicz fuzzy disjunction in a new software has shown its efficacy in providing a novel automated

these ions were considered cost criteria in the third analysis series. Moreover, some organic materials, such as 1, 2-dichlorobenzene, monochloramine, dichloroisocyanurate, and toluene, as cost criteria were also added to the entry data matrix, and their concentrations appeared in the evaluation matrix of TOPSIS.

Table 9 shows the matrix of the mean values of triangular fuzzy data for different water samples.

Table 10 shows the weight values matrix applied for each water sample criterion.

Table 11 shows the criteria for drinking water samples.

water analysis decision-making process [7]. The current work presents the results of the analysis of drinking water samples based on the concentrations of their ions and organic materials. These works are the first step required for a perspective change in the search for drinking water. The results of these investigations can be used in the next generation of robots helping them distinguish the confusion of the categories of drinking water and undrinkable water with the appearance of 1.0 in the output of TOPSIS.

## 4 Discussion

The proposed detection and analysis procedure proposed a new insight for the perspective change in science and engineering, which could help robots become independent of humans for predicting, detecting, and analyzing the target category, which was that of drinking water in this study. Therefore, their performance could be done independently from humans. In other words, the application of the proposed new software by robots, instead of the organizations' procedure of taking photos from other planets and analyzing them by humans, can provide automated detection and analysis of this important material in environmental conditions. This would not be appropriate for humans because of the lack of atmosphere, polluted environment, and extreme temperatures. Further investigations would be required to implement this software in the next generation of robots to search for drinking water on other planets.

TOPSIS is a decision-making algorithm. As categorization is the central process for decision-making in humans and it is before learning, in a perspective change for artificial intelligence, decision-making processes applying algorithms such as TOPSIS, including the issues of categorization, a cognitive disorder due to inconsistency in epistemic beliefs should be considered before machine learning. In other words, these issues should be implemented in new software in combination with this last method to advance science and engineering.

Previously, the properties of different nanomaterials [31-35], biomaterials [36-40], and construction materials [41, 42] were investigated for diverse applications in science and engineering. It has been revealed that nanoparticles [43, 44], polymers [45-48], and nanocomposites [49] would be used for water treatment, and more investigations could be performed for this application.

During recent years, TOPSIS has been used for the optimization and analysis of polymers [50-53], nanomaterials [54-56], and machine process or operation parameters [57-60]. More investigations would be required to develop this algorithm for the manufacturing optimization of materials and their preparation procedures for environmental studies.

## 5 Conclusions

The search for water in difficult environmental conditions is essential for human survival, for which a new perspective has been proposed in this paper.

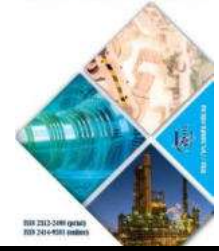
## References

1. Dawood, D. H., Sanad, M. I. (2014). Determination of ions (anion and cation) by ion chromatography in drinking water Talkha territory and some its villages, Dakahlia, Egypt, *J. Agric. Chem. and Biotechn.*, Vol. 5(9), pp. 215-226. DOI: 10.21608/jacb.2014.49898
2. Bell, J. F. (2010). Water on planets. *Highlights of Astronomy*, Vol. 15, pp. 29-44. DOI: 10.1017/S1743921310008161
3. Hubbard, G. S., et al. (2002). Following the water, the new program for Mars exploration. *Acta Astronautica*, Vol. 51(1-9), pp. 337-50. DOI: 10.1016/s0094-5765(02)00067-x
4. Nair, C. P. R., Unnikrishnan, V. (2020). Stability of the liquid water phase on Mars: A thermodynamic analysis considering Martian atmospheric conditions and perchlorate brine solutions. *ACS Omega*, Vol. 5(16), pp. 9391-9397. DOI: 10.1021/acsomega.0c00444
5. Hanine, M., et al. (2016). Application of an integrated multi-criteria decision making AHP-TOPSIS methodology for ETL software selection. *Springerplus*, Vol. 5, 263. DOI: 10.1186/s40064-016-1888-z
6. Azhar, N. A., et al. (2021). Multi-criteria decision making: A systematic review. *Recent Advances in Electrical & Electronic Engineering*, Vol. 14(8), pp. 779-801. DOI: 10.2174/2352096514666211029112443
7. Javanbakht, T. (2022). Automated decision-making with TOPSIS for water analysis. *Journal of Engineering Sciences*, Vol. 9(1), pp. H19-H24. DOI: 10.21272/jes.2022.9(1).h3
8. Javanbakht, T. (2022). Optimization of physical instruments' characteristics with TOPSIS, *Ukrainian Journal of Mechanical Engineering and Materials Science*, Vol. 8(3), pp. 1-9. DOI: 10.23939/ujmems2022.03.001
9. Javanbakht, T., Chakravorty, S. (2022). Prediction of human behavior with TOPSIS. *Journal of Fuzzy Extension and Applications*, Vol. 3, pp. 109-125. DOI: 10.22105/jfea.2022.326185.1197
10. Alguliyev, R., et al. (2020). Modified fuzzy TOPSIS + TFNs ranking model for candidate selection using the qualifying criteria. *Soft Computing*, Vol. 24(1), 681-695. DOI: 10.1007/s00500-019-04521-2
11. Varnamkhasti, M. J., et al. (2020). A new index for TOPSIS based on relative distance to best and worst points. *International Journal of Information Technology and Decision Making*, Vol. 16(03), pp. 695-719. DOI: 10.1142/S02196220200500145
12. Jumarni, R. F., Zamri, N. (2018). An integration of fuzzy TOPSIS and fuzzy logic for multi-criteria decision making problems. *Int. J. Eng. Tech.*, Vol. 7(2), pp. 102-106. DOI: 10.14419/ijet.v7i2.15.11362
13. Indahingwati, A., et al. (2018). Comparison analysis of TOPSIS and fuzzy logic methods on fertilizer selection. *International Journal of Engineering and Technology*, Vol. 7(2.3), pp. 109-114. DOI: 10.14419/ijet.v7i2.3.12630
14. Sadabadi, S. A., et al. (2020). A new index for TOPSIS based on relative distance to best and worst points. *International Journal of Information Technology and Decision Making*, Vol. 19(3), pp. 695-719. DOI: 10.1142/S02196220200500145
15. Clark, R. M., Goddard, H. (1977). Cost and quality of water supply. *Journal of American Water Works Associations*, Vol. 69(1), pp. 13-15. DOI: 10.1002/j.1551-8833.1977.tb02533.x
16. Büker, O., Stolt, K., Kroner, C., et al. (2021). Investigations on the influence of total water hardness and pH value on the measurement accuracy of domestic cold water meters. *Water*, Vol. 13, 2701. DOI: 10.3390/w13192701

The drinking water analysis in this work aimed to demonstrate and explain how to apply the automated decision-making process with modified TOPSIS in comparison with the unmodified algorithm for the prediction, analysis, and optimization of this material based on the concentrations of its ions and organic materials. The modified TOPSIS method was obtained using the Łukasiewicz fuzzy disjunction in this algorithm, according to which the maximum values of the membership degrees, the concentrations of ions, and organic materials of drinking and undrinkable water samples, were set to one. It was observed that the candidates' distances from the best and worst alternatives and similarity coefficients were different with the unmodified and modified algorithms. However, the same rankings were obtained for both of them. Moreover, the appearance of the value of 1.0 in the output of the modified algorithm corresponded to an individual's confusion about drinking and undrinkable water categories. This could be due to the inconsistency in his epistemic beliefs. The analysis revealed that adding organic materials to the list of the water's content led to a change in the candidates' ranking. With the new application of the TOPSIS method for predicting, detecting, and analyzing drinking water, this investigation could be applied in sciences and engineering.

17. Xianhong, Y., Shijun, L., et al. (2021). Application analysis of conductivity in drinking water quality analysis, *International Energy, Environment and Water Resources Conference. IOP Publishing*, Vol. 784, 012028. DOI: 10.1088/1755-1315/784/1/012028
18. Thirumalini, S., Joseph, K. (2009). Correlation between electrical conductivity and total dissolved solids in natural waters. *Malaysian J. Sci.*, Vol. 28(1), pp. 55-61. DOI: 10.22452/mjs.vol28no1.7
19. Aggarwal, P., et al. (2016). Role of calcium in human body – A review. *Bhavnagar University's Journal of Dentistry*, Vol. 6(1), pp. 30-34.
20. Khali, S., Alharthi, S. (2020). On-selective membrane sensor for magnesium determination in pharmaceutical formulations. *Int. J. Electrochem. Sci.*, Vol. 15, pp. 9223-9232. DOI: 10.20964/2020.09.39
21. Nikkhah, S., Naghii, M. R. (2019). Medicinal properties of boron supplementation on the prevention and treatment of diseases: A systematic review. *Complementary Medicine Journal*, Vol. 9(3), pp. 3760-3779.
22. Ali, S. F. A., et al. (2012). Determination of copper concentration in human blood serum by using flame atomic absorption spectroscopy (FAAS). *International Conference on Chemical Engineering and Pharmaceutical Sciences*, pp. 140-142, 2012.
23. Walker, W. F., Jonhston, I. (1971). *Water and Electrolyte Metabolism. The Metabolic Basis of Surgical Care, Elsevier, Netherlands.*
24. Burnier, M., et al. (2015). Salt, blood pressure and cardiovascular risk: what is the most adequate preventive strategy? A Swiss perspective. *Front. Physiol.*, Vol. 6, 227. DOI: 10.3389/fphys.2015.00227
25. Wang, Z., Shao, Y. (2018). Effects of microbial diversity on nitrite concentration in *pao cai*, a naturally fermented cabbage product from China. *Food Microbiology*, Vol. 72, pp. 185-192.
26. Lundberg, J. O., et al. (2018). Metabolic effects of dietary nitrate in health and disease. *Cell Metabolism*, Vol. 28(1), pp. 9-22.
27. Javanbakht, T. (2022). Analysis of nanoparticles characteristics with TOPSIS for their manufacture optimization. *Journal of Engineering Sciences*, Vol. 9(2), pp. C1-C8. DOI: 10.21272/jes.2022.9(2).c1
28. Javanbakht, T. (2022). *Modélisation et Traitement Informatique de L'inconsistance des Croyances Épistémiques*. PhD Thesis, University of Quebec in Montreal, Canada.
29. Tu, K. L., Nghiem, L. D., Chivas, A. R. (2010). Boron removal by reverse osmosis membranes in seawater desalination applications. *Separat. Purif. Technol.*, Vol. 75, pp. 87-101. DOI: 10.1016/j.seppur.2010.07.021
30. Jabłońska, B., et al. (2019). Natural and chemically modified post-mining clays – Structural and surface properties and preliminary tests on copper sorption. *Minerals*, Vol. 9, 704. DOI: 10.3390/min9110704
31. Javanbakht, T., Hadian, H., Wilkinson, K. J. (2020). Comparative study of physicochemical properties and antibiofilm activity of graphene oxide nanoribbons. *Journal of Engineering Sciences*, Vol. 7(1), pp. C1-C8. DOI: 10.21272/jes.2020.7(1).c1
32. Javanbakht, T. (2021). Investigation of rheological properties of graphene oxide and its nanocomposite with polyvinyl alcohol. *Ukrainian Journal of Mechanical Engineering and Materials Science*, Vol. 7, pp. 23-32. DOI: 10.23939/ujmms2021.01-02.023
33. Javanbakht, T., David, E. (2020). Rheological and physical properties of a nanocomposite of graphene oxide nanoribbons with polyvinyl alcohol. *Journal of Thermoplastic Composite Materials*, Vol. 35(5), 0892705720912767. DOI: 10.1177/0892705720912767
34. Javanbakht, T., Laurent, S., Stanicki, D. and Salzmann, I. (2021). Rheological properties of superparamagnetic iron oxide nanoparticles. *Journal of Engineering Sciences*, Vol. 8, pp. C29-C37. DOI: 10.21272/jes.2021.8(1).c4
35. Javanbakht, T., Laurent, S., Stanicki, D., Frenette, M. (2020). Correlation between physicochemical properties of superparamagnetic iron oxide nanoparticles and their reactivity with hydrogen peroxide. *Can. J. Chem.*, Vol. 98, pp. 601-608. DOI: 10.1139/cjc-2020-0087
36. Ghane-Motlagh, B., Javanbakht, T., et al. (2016). Physicochemical properties of peptide-coated microelectrode arrays and their *in vitro* effects on neuroblast cells. *Mat. Sci. Eng. C*, Vol. 68, pp. 642-650. DOI: 10.1016/j.msec.2016.06.045
37. Javanbakht, T., Ghane-Motlagh, B., Sawan, M. (2020). Comparative study of antibiofilm activity and physicochemical properties of microelectrode arrays. *Microelectronic Engineering*, Vol. 229, 111305. DOI: 10.1016/j.mee.2020.111305
38. Dimitriadis, E. K., Horkay, F., Maresca, J., Kachar, B., Chadwick, R. S. (2002). Determination of elastic moduli of thinlayers of soft material using the atomic force microscope. *Biophysical Journal*, Vol. 82(5), pp. 2798-2810.
39. Javanbakht, T., Sokolowski, W. (2015). Thiol-ene/acrylate systems for biomedical shape-memory polymers. *Shape Memory Polymers for Biomedical Applications*, Vol. 8, pp. 157-166. DOI: 10.1016/B978-0-85709-698-2.00008-8
40. Javanbakht, T., Laurent, S., Stanicki, D., David, E. (2019). Related physicochemical, rheological, and dielectric properties of nanocomposites of superparamagnetic iron oxide nanoparticles with polyethyleneglycol. *J. App. Polym. Sci.*, Vol. 136, pp. 48280-48290. DOI: 10.1002/app.48280
41. Kuzmin, S. A., Egorova, A. D., Krasilnikov, D. A., Emelianov, Z. V. (2019). Durability of construction materials modified by polymeric additives. *Procedia Structural Integrity*, Vol. 20, pp. 278-283. DOI: 10.1016/j.prostr.2019.12.152
42. Djavanbakht, T., et al. (2000). Effets d'un chauffage thermique sur les performances de miroirs multicouches Mo/Si, Mo/C et Ni/C pour le rayonnement X mou. *Journal de Physique IV*, Vol. 10, pp. 281-287. DOI: 10.1051/jp4:20001031
43. Fiorati, A., et al. (2020). Silver nanoparticles for water pollution monitoring and treatments: Ecosafety challenge and cellulose-based hybrids solution. *Polym.*, Vol. 12(8), 1635. DOI: 10.3390/polym12081635
44. Nagar, A., Pradeep, T. (2021). Clean water through nanotechnology: Needs, gaps, and fulfillment. *ACS Nano*, Vol. 14(6), pp. 6420-6435. DOI: 10.1021/acsnano.9b01730
45. Serajuddin, et al. (2020). Application of a polymer in drinking water treatment: A case study. *5th Intern. Conf. Civil Eng. Sustain. Dev.*, Vol. ICCESD-2020-4407, pp. 1-12.
46. Adeola, A. O., Nomngongo, P. N. (2022). Advanced polymeric nanocomposites for water treatment applications: A holistic perspective. *Polym.*, Vol. 14, 2462. DOI: 10.3390/polym14122462
47. Giwa, A., et al. (2019). Polymeric materials for clean water. *Springer*, pp. 167-190. DOI: 10.1007/978-3-030-00743-0
48. Khodakarami, M., Bagheri, M. (2021). Recent advances in synthesis and application of polymer nanocomposites for water and wastewater treatment. *J. Clean. Prod.*, Vol. 296, 126404. DOI: 10.1016/j.jclepro.2021.126404
49. Beyene, H. D., Ambaye, T. G. (2019). Application of sustainable nanocomposites for water purification process. *Sustainable Polymer Composites and Nanocomposites*, pp. 387-412. DOI: 10.1007/978-3-030-05399-4\_14

50. Ardhiyanto, N. K., et al. (2019). Multi responses optimization of plastic injection molding for biodegradable polymers using Taguchi method and TOPSIS. *AIP Conf. Proceed.*, Vol. 2097(1), 030064. DOI: 10.1063/1.5098239
51. Alaaeddin, M. H., et al. (2019). Polymer matrix materials selection for short sugar palm composites using integrated multi criteria evaluation method. *Compos. B: Eng.*, Vol. 176, 107342. DOI: 10.1016/j.compositesb.2019.107342
52. Narayanan, N. S., et al. (2019). Evaluation and optimization of surface roughness and metal removal rate through RSM, GRA, and TOPSIS techniques in turning PTFE polymers. *Adv. Manufact. Tech.*, Vol. 2019, pp. 595-605. DOI: 10.1007/978-981-13-6374-0\_65
53. Chohan, J. S., et al. (2020). Taguchi S/N and TOPSIS based optimization of fused deposition modelling and vapor finishing process for manufacturing of ABS plastic parts. *Materials*, Vol. 13(22), 5176. DOI: 10.3390/ma13225176
54. Yadav, R., Lee, H.-H. (2022). Fabrication, characterization, and selection using FAHP-TOPSIS technique of zirconia, titanium oxide, and marble dust powder filled dental restorative composite materials. *Polym. Adv. Tech.*, Vol. 33(1), pp. 3286-3295. DOI: 10.1002/pat.5780
55. Zhang, K., Zhan, J., Yao, Y. (2019). TOPSIS method based on a fuzzy covering approximation space: An application to biological nanomaterials selection. *Inform. Sci.*, Vol. 502, pp. 297-309. DOI: 10.1016/j.ins.2019.06.043
56. Loganathan, T. M., et al. (2021). Effect of *Cyrtostachys renda* fiber loading on the mechanical, morphology, and flammability properties of multi-walled carbon nanotubes/phenolic bio-composites. *Nanomat.*, Vol. 11(11), 3049. DOI: 10.3390/nano11113049
57. Shunmugesh, K., Panneerselvam, K. (2017). Optimization of machine process parameters in drilling of CFRP using multi-objective Taguchi technique, TOPSIS and RSA techniques. *Polym. Polym. Compos.*, Vol. 25(3), pp. 185-192.
58. Prahburam, T., et al. (2022). Optimization of operation parameters in machining of functionally graded metal matrix composite using TOPSIS. *Materials Today: Proceedings*, Vol. 62, pp. 429-433. DOI: 10.1016/j.matpr.2022.03.562
59. Sharma, A. K. (2021). EDM process parameters impact on MRR and TWR for titanium alloy [Ti6Al4V] and their optimization using Taguchi and TOPSIS method - An experiential analysis. *IOP Conf. Ser.: Mater. Sci. Eng.*, Vol. 1116, 012030. DOI: 10.1088/1757-899X/1116/1/012030
60. Patel, P. B., et al. (2015). Evaluation of FDM process parameter for PLA material by using MOORA-TOPSIS method. *International Journal of Mechanical and Industrial Technology*, Vol. 1(3), pp. 84-93.



# iATDI International Association for Technological Development and Innovations

## International Association for Technological Development and Innovations

(IATDI) is a non-government organization and a professional community established for fostering and promoting innovations to science, technology, and education.

### The main objectives:

- formation of the integrated relationship between individuals, local authorities and the private sector to improve the quality of human capital;
- pooling of intellectual potential of members for technological development and innovation;
- creating a network of partners with domestic and foreign higher education institutions and international organizations;
- co-organizing strategies in the context of implementing innovative scientific and educational projects, training highly skilled specialists, as well as an exchange of scientific information and academic staff.







## Copyright Agreement

We, the Authors of the Article publishing in the Journal of Engineering Sciences, in the case of acceptance for publication, transfer to Founders and Editorial Board the underlined rights:

- publishing this article in English and distribution of the printed version;
- English translation of the article and distribution of the hard copy of the translation;
- distribution of the electronic version of the article through any electronic means (by hosted on the official website of the Journal, in electronic databases, repositories, etc.).

### **We reserve the rights without the consent of the Editorial Board or Founders:**

- to use the article materials partially or in whole for educational purposes;
- to use the article materials partially or in whole to write own dissertations;
- to use the article materials for thesis preparing, conference materials, as well as for presentations;
- to post electronic copies (including the final electronic version downloaded from the official website of the Journal):
  - on the personal web-sources of all the co-authors (websites, webpages, blogs, etc.);
  - on the web-sources of authors working organizations (including electronic institutional repository);
  - on the International scientometric databases;
  - on non-commercial open-access sources.

In all cases, the presence of citations to the article or hyper-link to the electronic copy of the journal's official website is obligatory.

### **By this agreement, we also certify that the submitted article:**

- does not violate the copyrights of other persons or organizations;
- has not been published previously in other publishing houses and submitted for publication in other Journals.



## Dear Authors of the Journal of Engineering Sciences!

The Editorial Board of the Journal of Engineering Sciences pays special attention to the structure of the articles according to the **List of Scientific Professional Editions of Ukraine** (Category “B”, Minutes No. 1208 of 07.11.2018, Appendix No. 8). Only original articles by the authorship of up to 5 authors are accepted for publication according to the **Template** with the following elements:

- general statement of the problem and its relationship with the essential scientific or practical problems;
- analysis of the recent investigations and publications in the same research field;
- statement of the significance of the general problem that was not solved before;
- statement of the purpose of the research article;
- description of the initial data of the research with the justification of the achieved scientific results;
- conclusions and ways for further development of the research.

**All the articles are reviewed by the independent double-blind procedure.**

All the authors should send via e-mail [jes@teset.sumdu.edu.ua](mailto:jes@teset.sumdu.edu.ua) the electronic version of the following materials:

- article **in English** according to the **Template**;
- information about authors and their affiliation with the related address.

### ATTENTION!

If one of the mentioned components is not sent or there are many stylistic, orthographic, and grammatical errors, the article will not be considered by the Editorial Board and will not be reviewed.

### The minimum size of the materials:

1. Scientific – theoretical articles (up to 25,000 symbols; about 14 pages) that deal with the theoretical research and descriptions of physical laws concerning the investigated phenomena; theoretical generalizations and fundamental principles proved by the experimental research data.
2. Scientific-practical articles (up to 10,000 symbols; about 6 pages) that deal with scientific experiments and recent experience. They include the proposed methods for the experimental research or means to observe the studied phenomena. An essential part of these articles is the description of the achieved results and their explanation acquired in immediate interaction with the object of investigations, its significance, and practical implementations.
3. Scientific-methodological articles (up to 15,000 symbols; about 8 pages) that deal with the review of processes, methods, instruments for solving scientific and applied problems; the statement of the new methodology, results of which allow creating more precise methodology based on an up-to-date methodology for the implementation of discovered laws.

Ministry of Education and Science of Ukraine  
Sumy State University

# JOURNAL OF ENGINEERING SCIENCES

Scientific Journal

**Volume 10, Issue 1 (2023)**

**Відповідальний за випуск**

I. В. Павленко

**Комп'ютерне складання та верстання:**

Х. В. Берладір

**Обкладинка:**

В. О. Іванов

**Коректор:**

С. М. Симоненко

**Responsible for release:**

Ivan Pavlenko

**Computer design and typesetting:**

Khrystyna Berladir

**Cover page:**

Vitalii Ivanov

**Corrector:**

Svitlana Symonenko

---

Підписано до друку 30.06.2023. Формат 60x84/8.

Папір офс. Друк офс.

Ум. друк. арк. 20,01. Обл.-вид. арк. 27,20.

Наклад 100 прим. Замовлення №

Сумський державний університет, вул. Римського-Корсакова, 2, 40007, м. Суми, Україна

Свідоцтво про внесення суб'єкта видавничої справи до Державного реєстру

ДК № 3062 від 17.12.2007.

Надруковано у друкарні Сумського державного університету,  
вул. Римського-Корсакова, 2, 40007, м. Суми, Україна

**Editorial Board:** 2, Rymkogo-Korsakova St., 40007, Sumy, Ukraine; Apt. M-211  
**E-mail:** [jes@teset.sumdu.edu.ua](mailto:jes@teset.sumdu.edu.ua)  
**Website:** <https://jes.sumdu.edu.ua>

State registration certificate of the print mass-media No. 20499-10299 PR.